Chemical Vapour Deposition of Atomically Thin Tungsten Disulphide

A thesis submitted in partial fulfilment of the requirements for the award of the degree

Doctor of Philosophy

from

Imperial College London

by

Francesco Reale

Faculty of Engineering, Department of Materials

September 2017

DECLARATION OF ORIGINALITY

I, Francesco Reale, declare that this thesis, submitted in partial fulfilment of the requirements for the award of Doctor of Philosophy in the Department of Materials, Imperial College London, is the result of my own work unless otherwise referenced or acknowledged. I further state that the document has not been submitted for any qualification at any other academic institution.

Francesco Reale

September 2017

COPYRIGHT DECLARATION

"The copyright of this thesis rests with the author and is made available under a Creative Commons Attribution Non-Commercial No Derivatives licence. Researchers are free to copy, distribute or transmit the thesis on the condition that they attribute it, that they do not use it for commercial purposes and that they do not alter, transform or build upon it. For any reuse or redistribution, researchers must make clear to others the licence terms of this work"

ACKNOWLEDGEMENTS

I would like to express my gratitude to my supervisor Dr. Cecilia Mattevi for guiding, supporting and encouraging me throughout my post-graduate journey. I'd also like to acknowledge the examiners Prof. Norbert Klein and Prof. Cinzia Casiraghi for reviewing this work.

Thank you to my colleague Mr Pawel Palczynski for the insightful daily discussions and great help with Raman, PL and XPS spectroscopy characterization and data analysis.

To Dr. Peter Sherrell and Dr. Federico Pesci for their experimental help and support throughout, thank you, I could not have done it without you.

I would also like to acknowledge our collaborators Dr. Na Ni for TEM imaging, Dr. Iddo Amit, Prof. Monica F. Craciun and Prof. Saverio Russo for carrying out electrical measurements, and Dr Stefano Agnoli for XPS measurements.

Thank you to my lab and office mates, Maria Sokolikova, Kanudha Sharda, Cong Lu, Chiara Grotta, Aleksandra Krajewska, Emilia Donata, Julian Buchinger, Hao Wen, Jerome Nicolas, Francesca Tallia, Cyril Besnard, David Poussin, Shengyang Chen, Jonathan Ngiam, Luca Occhi, Gianmaria Matrone, Leonie Flückiger, Ezra Feilden, for the numerous discussions, coffee breaks and other little things that make the PhD journey a memorable experience.

I am also grateful to my dear friends Laura, Elizabeth, Annalisa, Aleksandra, Anastasia who constantly gave me the courage to face all the challenges that I have encountered throughout the course of the PhD program.

Last but not least, I would like to thank my family, Dad, Mum, Roberto, Paolo, Serena and Carmela for their love.

Funding for this research project was mainly provided by the EPSRC-Royal Society fellowship engagement (2013-2016) EP/L003481/1 "Tailoring the Electronic Properties of Semiconducting Transition Metal Dichalcogenides".

PUBLICATIONS

Reale, F.; Sharda, K.; Mattevi, C. From Bulk Crystals to Atomically Thin Layers of Group VI-Transition Metal Dichalcogenides Vapour Phase Synthesis. *Applied Materials Today* **3** (2016), 11–22.

Reale, F.; Palczynski, P.; Amit, I.; Jones, G. F.; Mehew, J. D.; Bacon, A.; Ni, N.; Sherrell, P. C.; Agnoli, S.; Craciun, M. F.; Russo, S.; Mattevi, C. High-Mobility and High-Optical Quality Atomically Thin WS_2. *Scientific Reports*, Accepted (2017). ArXiv:1707.07523.

Amit, I.; Octon, T. J.; Townsend, N. J.; Reale, F.; Wright, C. D.; Mattevi, C.; Craciun, M. F.; Russo, S. Role of Charge Traps in the Performance of Atomically Thin Transistors. *Advanced Materials* **29** (2017), 1605598.

Pesci, F. M.; Sokolikova, M. S.; Grotta, C.; Sherrell, P. C.; Reale, F.; Sharda, K.; Ni, N.; Palczynski, P.; Mattevi, C. MoS_2/WS_2 Heterojunction for Photoelectrochemical Water Oxidation. *ACS Catalysis* **7** (2017), 4990–4998.

Wakamura, T.; Reale, F.; Palczynski, P.; Guéron, S.; Mattevi, C., Bouchiat, H. Strong Spin-Orbit Interaction Induced in Graphene by Monolayer WS_2. Submitted.

ABSTRACT

Transition metal dichalcogenides (TMDs) are van der Waals layered materials that have been known and studied for decades in their bulk form for applications such as solid-state lubricants and catalysts. However, TMDs were largely unexplored in their two-dimensional, atomically thin form. Their unique optical and electrical properties due to their reduced dimensionality started to emerge only in the last decade. In particular, group VI-TMDs (i.e., MoS_2, WS_2, $MoSe_2$, WSe_2) have been recently attracting tremendous attention as emerging post-graphene materials owing to their direct band-gap in the visible range which opens many prospects for diverse optoelectronic devices. Among them, atomically thin tungsten disulphide (WS_2) has emerged as unique candidate for future nanotechnologies due to its superior optical, electrical and thermal properties.

Any envisioned application of WS_2 requires high-quality and large-area material obtainable via a scalable synthesis method. The chemical vapour deposition (CVD) of group VI-TMDs holds promise for the synthesis of high quality monolayered material extended over wafer-size areas. Nevertheless, the CVD growth of high-quality atomically thin WS_2 layers requires further development since film continuity and thickness uniformity are normally limited to a few tens of micron-sized areas. The most extensively used CVD method to synthesize WS_2 entails co-evaporation of tungsten oxide (WO_3) and sulphur (S) powders. This choice of precursors is mainly dictated by their low toxicity compared to halides/ organic precursors and effective replacement of O by S. However, due to the high sublimation temperature of WO_3, the growth has to be carried out at high temperatures in between 950-1070°C and low pressures.

In this work we demonstrate a novel facilitated CVD growth of high-quality atomically thin WS_2 by using a novel molecular precursor approach. This strategy involves reagents which are carbon-free, volatile and easily decomposable at low temperatures, allowing for the growth of mono- and bi-layered WS_2 crystals with lateral sizes of 300μm at temperatures as low as 750°C, and with superior optical and electrical properties than those of naturally occurring materials. The charge carrier mobilities that we report are also higher compared to the ones obtained using innovative synthesis procedures, such as CVD growth on reusable gold substrates or metalorganic CVD on different oxides. Further we demonstrate tunability of the optical and electrical properties of WS_2, inducing atomic doping with Indium.

TABLE OF CONTENTS

DECLARATION OF ORIGINALITY……1

COPYRIGHT DECLARATION……...2

ACKNOWLEDGEMENTS……...3

PUBLICATIONS……..4

ABSTRACT……5

TABLE OF CONTENTS……...6

1. TOPIC, AIMS AND OBJECTIVES……10

2. PROPERTIES OF GROUP VI-TRANSITION METAL DICHALCOGENIDES (TMDs)……...15

2.1. INTRODUCTION……...15

2.2. TMDs: DEFINITION AND STRUCTURE……16

2.3. PROPERTIES OF LAYERED TMDs……16

2.3.1. ELECTRONIC PROPERTIES……..18

2.3.2. OPTICAL PROPERTIES……..20

2.3.3. PHONON DISPERSION……...22

2.4. SYNTHESIS METHODS……24

2.5. APPLICATIONS OF TMDs……25

2.5.1. TMDs-BASED ELECTRONICS……...26

2.5.2. TMDs-BASED OPTOELECTRONICS – *P-N JUNCTIONS*……28

2.6. TRANSITION METAL-DOPED TMDs…….30

2.6.1. GROUP IV: Ti AND Zr…….32

2.6.2. GROUP V: V AND Nb……..34

2.6.3. GROUP VI: Cr……...35

2.6.4. GROUP VII: Mn AND Re…….36

2.6.5. GROUPS VIII-X: Fe, Co AND Ni…….38

2.6.6. GROUP XI: Cu……..40

2.7. CHEMICAL FUNCTIONALIZATION OF TMDs…….41

2.8. CONCLUSIONS…….44

3. VAPOUR PHASE SYNTHESIS OF WS_2: LITERATURE REVIEW……...45

3.1. INTRODUCTION……...45

3.2. BULK SINGLE CRYSTAL GROWTH BY CHEMICAL VAPOUR TRANSPORT…….....48

3.3. VAPOUR PHASE SYNTHESIS OF ATOMOCALLY THIN WS_2……51

3.3.1. CVD OF WS_2 THIN FILMS FROM METAL-ORGANIC PRECURSORS……..53

3.3.2. CHALCOGENIZATION OF PRE-DEPOSITED METAL-CONTAINING THIN FILMS……..54

3.3.2.1. CHALCOGENIZATION OF A PRE-DEPOSITED METAL THIN FILM……..54

3.3.2.2. CHALCOGENIZATION OF A PRE-DEPOSITED METAL OXIDE THIN FILM……55

3.3.3. VAPOUR PHASE REACION OF METAL AND CHALCOGEN PRECURSORS……...58

3.3.3.1. METAL AND CHALCOGEN PRECURSORS POWDERS……...58

3.3.3.2. METAL AND CHALCOGEN PRECURSORS IN GASEOUS PHASE…….81

3.4. VAPOUR PHASE SYNTHESIS OF METAL-DOPED WS_2…….88

3.5. CONCLUSIONS……97

4. CHARACTERIZATION TECHNIQUES……98

4.1. INTRODUCTION……...98

4.2. SCANNING ELECTRON MICROSCOPY (SEM)…….....98

4.3. ATOMIC FORCE MICROSCOPY (AFM)……100

4.4. TRANSMISSION ELECTRON MICROSCOPY (TEM)…….102

4.5. RAMAN AND PHOTOLUMINESCENCE (PL) SPECTROSCOPY……...104

4.6. X-RAY DIFFRACTION (XRD)……...106

4.7. X-RAY PHOTOELECTRON SPECTROSCOPY (XPS)…….……107

4.8. TRANSFER PROCEDURE…….….108

4.9. DEVICE FABRICATION AND ELECTRICAL MEASUREMENTS…….....109

4.10. CONCLUSIONS…….110

5. TUNGSTEN TRIOXIDE-BASED CVD SYNTHESIS OF WS_2……111

5.1. INTRODUCTION…….112

5.2. SULFUR TEMPERATURE: ≥250°C……...113

5.3. SULFUR TEMPERATURE: ~250°C……...115

5.4. SULFUR TEMPERATURE: ≤250°C……...118

5.5. CONCLUSIONS……...129

6. WATER-ASSISTED CVD SYNTHESIS OF WS_2……..130

6.1. INTRODUCTION…….130

6.2. RESULTS……..131

6.3. REACTION MECHANISM……..135

6.4. STRUCTURAL AND PHYSICAL CHARACTERIZATION……..139

6.4.1. STRUCTURAL CHARACTERIZATION……..139

6.4.2. PHOTOLUMINESCENCE……141

6.4.3. CHEMICAL PURITY AND STRUCTURAL DEFECTS……..……145

6.4.4. ELECTRICAL CHARACTERIZATION……....147

6.5. CONCLUSIONS……...150

7. CVD SYNHESIS OF INDIUM-DOPED WS_2…….……..151

7.1. INTRODUCTION……151

7.2. RESULTS……...153

7.3. PHYSICAL CHARACTERIZATION……...156

7.3.1. X-RAY DIFFRACTION……156

7.3.2. RAMAN AND PHOTOLUMINESCENCE……160

7.3.3. X-RAY PHOTOELECTRON SPECTROSCOPY……...162

7.4. CONCLUSIONS……...165

8. CONCLUSIONS AND FUTURE WORK……....165

APPENDIX……170

BIBLIOGRAPHY……..176

1) TOPIC, AIMS AND OBJECTIVES

The large-scale synthesis of semiconducting thin films forms the basis of modern-day electronics and optoelectronics. Further, a decrease in the films thickness to the ultimate limit of the sub-nanometre/ atomic length scale, a current limitation of traditional semiconductors (such as Si and GaAs), would be highly beneficial for the development of ultrathin and flexible electronics and photovoltaics. For this, tungsten disulphide (WS_2), which belongs to the family of group VI-transition metal dichalcogenides (TMDs) and can form stable three-atom-thick layers, has recently emerged as an ideal semiconducting material with unforeseen optical, electrical and mechanical properties. Nevertheless, the synthesis of atomically thin WS_2 with high crystal quality over large areas represents to date the biggest challenge to overcome in order to see any application of this material. Therefore, the aim of this PhD research project is to design a reproducible, safe and cost effective synthesis method to achieve a controllable large-area growth of single-layered WS_2 with high optical and electrical properties towards the scalable production of WS_2, and to further expand the potential of the material through metal doping.

As discussed in Chapter 2, TMDs are layered materials formed by triatomic sheets anchored together by van der Waals forces. The range of layered TMDs compounds extends up to at least 40, exhibiting different electrical properties ranging from insulating to semiconducting and metallic. Among them, the group VI of transition metals (W, Mo) sulphides and selenides has recently raised enormous interest. The appeal of MoS_2, WS_2, $MoSe_2$ and WSe_2 relies on their similitudes with silicon, but with several advantages that can enable flexible electronics and optoelectronics at smaller scales and new quantum electronics such as valleytronics. In the monolayered form, group-VI TMDs have a direct band gap in the visible-near IR range, carrier mobilities up to $1020 cm^2V^{-1}s^{-1}$, on/off ratios higher than 10^7 and subthreshold swing values below 100mV per decade. Further, TMDs-based devices can be built

onto virtually any substrate and single- and few-layered flakes can tolerate strain induced through flexible/ stretchable supports while also exhibiting photoluminescence tunability and piezoelectricity. In addition, due to different possible polymorphisms in TMDs, it has been shown that room temperature phase transitions from semiconducting to metallic can be induced by alkali metals, enabling low contact resistance and paving the way for new electronic device concepts. Finally, the modification of TMDs by metal doping can further extend their potential since it has been predicted that a number of properties can be tuned through compositional variation. Therefore, the group VI-TMDs can potentially lead to the development of a new nanoelectronics "beyond silicon" onto flexible and lightweight substrates.

As discussed in Chapter 3, atomically thin tungsten disulphide (WS_2) has recently proved to be one of the most promising materials within the group VI-TMDs. Theoretical models have predicted that WS_2 can exhibit ambipolar field-modulation behaviour and that it should have the highest mobility among the semiconducting TMDs due to a reduced effective mass. Indeed, room temperature electron mobility up to $234 cm^2 V^{-1} s^{-1}$ has recently been achieved in multilayered WS_2 by using gold contacts. Moreover, compared to the most studied MoS_2, monolayered WS_2 exhibits a nearly three times larger valence band splitting, which allows for an easier observation of the valley hall effect, and about twenty times higher photoluminescence emission, leading to optoelectronic devices with relatively high quantum efficiency. Further, vertical graphene/WS_2 heterostructures-based field effect transistors have shown a very large on-state current and an unprecedentedly high on/off ratio ascribable to a combination of tunnelling and thermionic transport. Finally, as a lubricant WS_2 exhibits a wider operation temperature range than other TMDs, indicating a stronger thermal stability. Therefore, these properties make WS_2 a unique candidate for future nanotechnologies, ranging from large area consumer electronics to quantum electronics.

The bottleneck of any application of WS_2 is the synthesis of this material over wafer-size areas and with controllable thickness. Among different possible preparation methods, the chemical vapour deposition (CVD) can lead to the synthesis of monolayered WS_2 and offer industrial scalability. However, up until now the large-scale growth of high-quality monolayered WS_2 films with spatial homogeneity and good electrical performance remains an unsolved challenge and it is yet to see its full realization. In Chapter 3 we review the progress that has been achieved over the last few years in the vapour-phase synthesis of atomically thin WS_2. Further, we discuss on how the growth of TMDs bulk crystals developed

during the '70s and '80s has led to the identification of physical/chemical mechanisms underlying the formation of these materials, which we have exploited to achieve single-layer synthesis of high-quality WS_2.

In Chapter 4 we discuss the state-of-art characterization techniques required to obtain critical information on the chemistry, morphology, crystal quality, optical and electrical properties of WS_2 atomic layers. A set of microscopic, spectroscopic, crystallographic and electrical techniques have been extensively used thought this work in order to correlate the structure and morphology of CVD-grown WS_2 samples with their optoelectronic properties.

The most extensively used vapour-phase synthesis method to synthesize mono- and few-layered WS_2 crystals is a one-step CVD process consisting in the co-evaporation of a W precursor and S powders in a horizontal tubular furnace in the presence of a carrier gas. In particular, WO_3 has seen a widespread use as W precursor due to its low toxicity compared to halides/organic compounds, easy handling and effective replacement of O by S. To date, atomically thin WS_2 flakes have been successfully synthesized through this WO_3-based CVD strategy by several research groups. Nevertheless, the reported synthesis conditions are often contradictory revealing lack of reliability and reproducibility issues. With the aim of shedding light on the basic principles that govern the growth mechanism of WS_2 atomic layers from WO_3 and S, in Chapter 5 we present a parametric study of the CVD reaction variables, such as reaction temperature and time, heating profile of sulphur, carrier gad flux, amount of precursors and precursors-substrate distance. As a result, we provide insights into the key factors that affect the WO_3-based CVD synthesis of WS_2 from the early stages of nucleation up to the formation of film-like continuous domains over hundreds of micron-sized areas, discussing how different growth conditions lead to different size, thickness and density of the WS_2 crystals. However, due to the high sublimation temperature and low vapour pressure of WO_3, the controlled evaporation and deposition of both precursors onto the substrate requires high temperatures (950°C) and low pressures. Further, the synthesis of WS_2 from WO_3 involves a topotactic transformation which typically yields to sparsely distributed WS_2 nuclei. These limitations, which often prevent a reproducible deposition of high-quality and large-area WS_2, have motivated the search for alternative W precursors which effectively decompose and undergo a complete sulfurization at molecular level.

In Chapter 6 we demonstrate a controlled CVD synthesis of mono- and bi-layered WS_2 over large areas exhibiting record room temperature-electron mobilities of 28cm^2/Vs and 52cm^2/Vs, respectively. These results have been achieved by employing a combination of precursors (H_2WO_4+NaCl) which leads to the formation of molecular W-containing intermediates (WO_xCl_y) with higher volatility than the most widely used tungsten oxides. Compared to the topotactic transformation of WO_3-based precursors, this CVD strategy allows for a large-area growth of atomically thin WS_2 crystals with higher crystal quality at lower temperatures (750°C). Further, the as-grown monolayered WS_2 exhibit superior optical quality compared to both exfoliated WS_2 and CVD-grown WS_2 onto SiO_2, with ultra-sharp photoluminescence linewidth (36meV) over submillimetre areas. Finally, the proposed molecular precursors-approach has some of the typical advantages of metal-organic CVD (such as lower growth temperatures and higher substrate coverages) but without employing oxy-carbon precursors of W, which are known to be toxic and to contaminate the final synthesis product.

Since two-dimensional materials offer a limited choice in terms of band-gaps (0eV for graphene, 5.8eV for monolayered hexagonal boron nitride and 1.64-2eV for monolayered group VI-TMDs), a number of experimental strategies, such as functionalization, strain, electrical gating and dielectric screening, have been attempted in order to tune the band gap of 2D materials. However, these experimental efforts did not lead to a significant broadening of the bad-gap range. In contrast to graphite and boron nitride, which are immiscible and did not allow for band-gap tuning in their alloys due to phase separations, it has been predicted that layered TMDs may have better intermiscibility and stability. As a result, several bulk TMDs alloys with tunable band-gaps, such as $Mo_{1-x}W_xS_2$ and $Mo_{1-x}W_xSe_2$, have been successfully prepared, thus suggesting good thermodynamic stability for the corresponding 2D alloys. Nevertheless, attempts to synthesized atomically thin TMDs alloys via conventional vapour-phase synthesis processes led to either small ternary domains or binary heterostructures. Therefore, as the aim of this PhD research project is to extend the properties of WS_2 atomic layers without sacrificing their lateral extension or the reproducibility and scalability of the synthesis process, a better strategy to expand the material potential would be doping through functionalization strategies (interaction with adlayers, atoms or molecules) or metal atoms incorporation. As it has been shown that the charge transfer doping through functionalization schemes rely on environmental conditions, surface adsorption, metal contacts and dielectric interfaces,

thus severely limiting the device working conditions, a more reliable doping through stable incorporation of non-volatile metal atoms is highly preferred. In Chapter 7 we demonstrate a successful incorporation of indium atoms into atomically thin WS_2 crystals, resulting in large-area In-doped WS_2 atomic layers exhibiting tunable optical properties and a semiconducting-to-metallic transition at high doping levels.

2) PROPERTIES OF GROUP VI-TRANSITION METAL DICHALCOGENIDES

2.1. INTRODUCTION

The group VI of transition metal dichalcogenides (TMDs) (MoS_2, WS_2, $MoSe_2$, WSe_2, $MoTe_2$, WTe_2) consists of van der Waals compounds formed by three-atom-thick layers of covalently bonded metal and chalcogen atoms [1]. Atomically thin layers of TMDs are being extensively investigated in recent years as they present complementary properties to graphene and unique optoelectronic characteristics compared to conventional low dimensional semiconductors [2][3]. While the bulk counterpart manifests an indirect electronic band gap, an individual layer presents a direct band gap in the visible-near IR range [4] which can enable applications in optoelectronic devices for light emission and detection. Further, monolayered sulphides and selenides show strong light absorption [2][5][6], valley polarization [7][8], second-harmonic generation [9], tightly bound excitons [10] and strong spin-orbit interaction [11][12] due to their intrinsic two-dimensional nature inherently free from dangling bonds and their particular d-orbitals configuration [1][13]. Finally, given their atomically thin nature, they are mechanically flexible and they can sustain tensile strain up to 20% [14][15]. These properties make two-dimensional (2D) TMDs very attractive materials for the next generation of optoelectronic devices and communication systems, which can be fabricated onto flexible and stretchable substrates. Further, the modification of TMDs by metal doping can eventually extend their potential since it has been shown that their electronic, optical, magnetic, morphological and tribological properties can be altered by compositional variation [16]. In this chapter, the structures and properties of the group VI of TMDs, the synthesis methods for preparing atomically thin layers and their doping with different metal atoms are reported and discussed.

2.2. TMDs: DEFINITION AND STRUCTURE

Since 1958, interest in the properties of TMDs started to arise and about 60 different compounds have been studied and categorized [1] with general formula MX_2, X being a chalcogen (S, Se, Te) and M a transition metal mainly from group IV, V and VI [1]. At least 40 of them are layered compounds and present strong in-plane bonding and weak out-of-plane interlayer (van der Waals) interactions (Fig. 2.1*a*). Each individual layer is three-atom-thick and has the form X-M-X, where a plane of metal atoms (M) is covalently bonded between two hexagonal planes of chalcogen atoms (X) [17][18] (Fig. 2.1*b*).

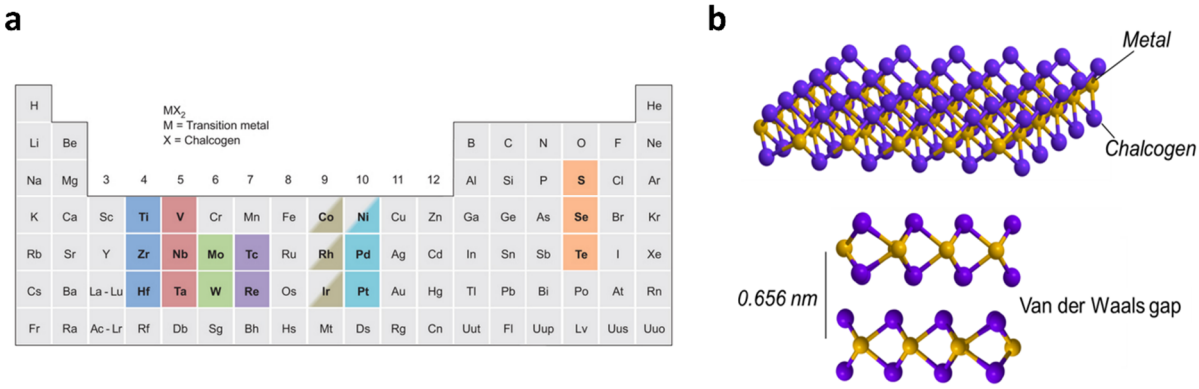


Figure 2.1 *(a) Highlighting of the three chalcogens (S, Se, Te) and transition metals which crystallize in the layered structure MX_2. Adapted from Ref. [17]. (b) Schematic of a typical MX_2 structure (chalcogen atoms in purple and metal atoms in yellow).*

Adjacent layers are weakly held together by means of van der Waals forces to form the bulk crystals in a variety of polytypes, which vary in stacking orders and metal elements coordination. The symmetry of the unit cell can be hexagonal (2H), rhombohedral (3R) or tetragonal (1T) (Fig. 2.2) while the metal atoms have trigonal prismatic or octahedral coordination [19]. The electronic properties of TMDs range from metallic to semiconducting and some of them are known to exhibit superconducting properties and charge density waves at low temperatures [19].

2.3. PROPERTIES OF LAYERED TMDs

Bulk crystals of TMDs show a range of mechanical, electronic, optical, chemical and thermal properties that have been studied for decades [20] for applications such as solid-state lubricants and catalyst.

On the contrary, investigation of the properties of their two-dimensional form has started only a few years ago when the stability in air of these atomically thin layers has been demonstrated. Since the isolation of graphene has sparked interest in layered compounds which can be disassembled into their elementary building blocks [21][22], recent advances in 2D materials preparation, manipulation and characterization have paved the way towards new developments for TMDs in their atomically thin form.

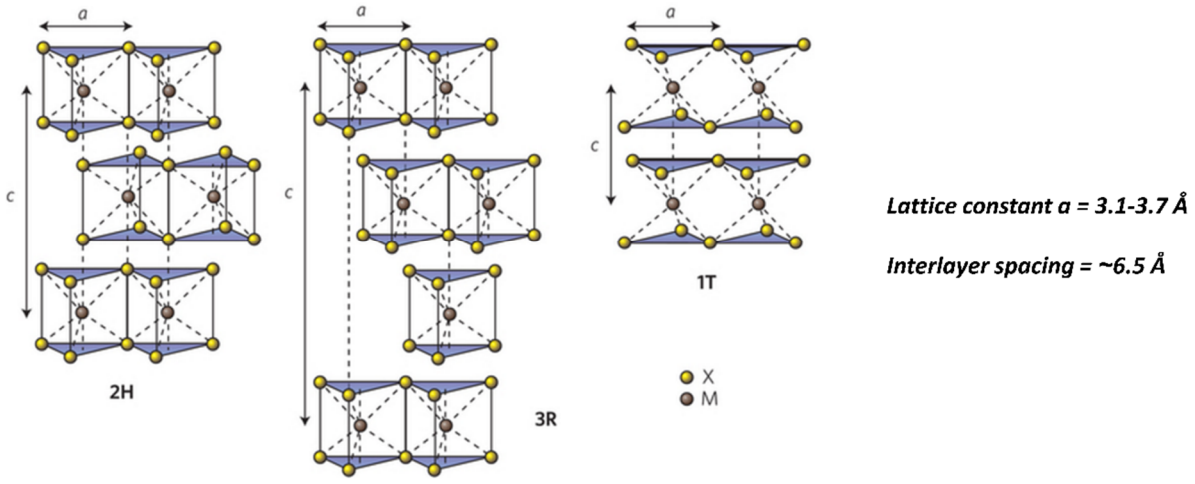


Figure 2.2 *Schematics of the TMDs structural polytypes (chalcogen atoms X in yellow and metal atoms M in dark grey): hexagonal symmetry 2H (two layers per repeat unit, trigonal prismatic coordination), rhombohedral symmetry 3R (three layers per repeat unit, trigonal prismatic coordination) and tetragonal symmetry 1T (one layer per repeat unit, octahedral coordination). The lattice constants a are in the range 3.1-3.7Å for different TMDs and the interlayer spacing is ~6.5Å. Adapted from Ref. [19].*

In particular, the semiconducting group VI-TMDs, sulphur and selenium based, have attracted increasing attention as they present complementary properties to graphene. In fact, the lack of a finite electronic band-gap in graphene hinders its applications as active component in transistors or optoelectronic devices. On the contrary, several TMDs in the monolayered form show a direct band-gap in the visible-near IR range (1.64-2eV) [23], opening opportunities in field-effect transistors (FETs), light harvesting, detection and emission. Finally, emerging telluride compounds of Mo and W have recently revealed complementary properties to the other sulphides and selenides [24]. $MoTe_2$ presents interchangeable metallic and semiconducting phases, the latter displaying a small band gap of 1.1eV [25][26], whereas WTe_2 exhibits an unforeseen large non-saturated magnetoresistance [27].

2.3.1. ELECTRONIC PROPERTIES

Both theoretical calculations and experimental characterizations have shown that layered group VI-TMDs are isostructural materials with very similar band structures [28]. Table 2.1 summarizes the electronic properties of semiconducting Mo and W dichalcogenides, reporting the band gap values in the bulk and monolayered form. As a representative case, Figure 2.3 shows the band structures of bulk, multi- and mono-layered WS_2 [28], recently emerged as one of the most promising group VI-TMDs (Chapter 3). In the bulk, the maximum of the valence band is at the Γ point, while the minimum of the conduction band is at the Λ point (halfway between Γ and K points). This identifies an indirect band-gap of 1.3eV which characterizes both the bulk material and the multilayered forms. Upon reducing the layer number to 4 (and then 2) it is possible to notice how the valleys of the conduction band at the Λ points progressively rise up. In the bilayered form a crossover between the conduction band minima at the Λ and K points occurs, thus shifting the indirect band-gap between the maximum of the valence band at Γ and the new lowest point of the conduction band at K. At the same time, the hill of the valence band at the K point is comparatively unaffected by the number of layers down to the monolayered form where it overcomes the maximum at the Γ point, thus establishing a direct band-gap at the K point.

	-S_2	**-Se_2**	**-Te_2**
Mo	Semiconducting: 1L: direct band-gap 1.8eV Bulk: indirect band-gap 1.2eV	Semiconducting: 1L: direct band-gap 1.5eV Bulk: indirect band-gap 1.1eV	Semiconducting: 1L: direct band-gap1.1eV Bulk: indirect band-gap 1.0eV
W	Semiconducting 1L: direct band-gap 2.1eV Bulk: indirect band-gap 1.3eV	Semiconducting 1L: direct band-gap 1.7eV Bulk: indirect band-gap 1.2eV	Semiconducting 1L: direct bandgap1.1 eV

Table 2.1*: Electronic characteristics of Mo and W dichalcogenides in the bulk and monolayered (1L) form. Adapted from Ref. [19].*

All MoX_2 and WX_2 compounds undergo a similar indirect-to-direct band-gap transition from the bulk to the monolayered form, covering a band-gap energy range of 1.1-1.9eV (Table 2.1) [19] and enabling several excitonic transitions [31]. In particular, the so called A and B excitons correspond to direct band-gap optical transitions at the K point of the Brillouin zone between the two maxima of the valence

band and the minimum of the conduction band, where the valence band splitting is due to spin-orbit coupling [19][31]. It is worth to note that these characteristics are significantly different from the behaviour reported in other low dimensional nanostructures obtained from indirect band-gap semiconductors such as silicon. In fact, the enhanced photoluminescence of Si nanocrystals compared to that of bulk Si originates from quantum confined electronic states with increased emission energy at decreased nanoparticle size [3] and not from allowed direct electronic transitions as in MoX_2 and WX_2 compounds.

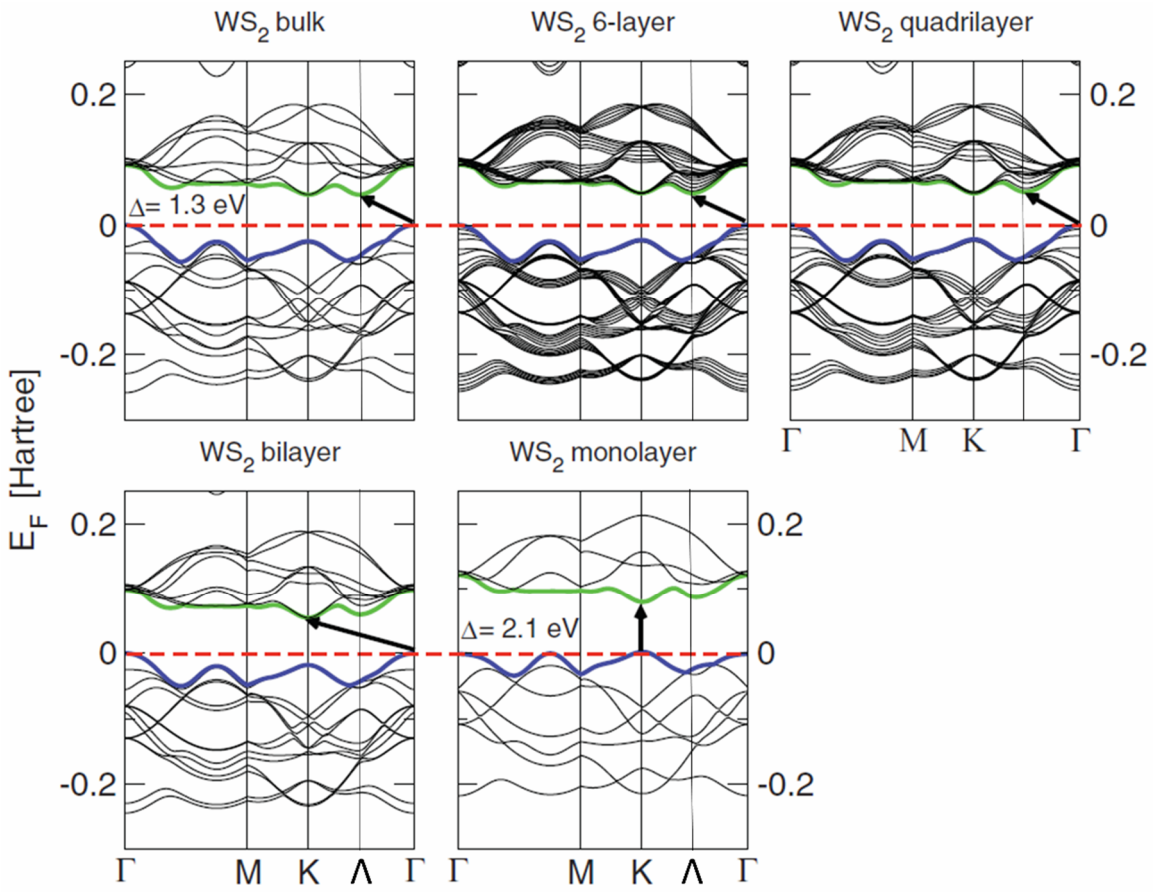


Figure 2.3 *Band structure of WS_2 in the bulk, multi- and mono-layered forms calculated from density functional theory (DFT) calculations. The horizontal dashed lines indicate the Fermi level and the arrows show the fundamental band-gap. The top of the valence band and the bottom of the conduction band are highlighted in blue and green, respectively. Adapted from Ref. [28].*

DFT calculations on MoS_2 have revealed that the conduction band states at the K point originate from strongly localized d orbitals at Mo atoms [3]. Since the metal atom sites are located in the middle of the sandwiched S-Mo-S unit cell, these states are relatively unaffected by interlayer coupling [3]. On

the contrary, the states near Γ and the indirect band-gap point originate from a linear combination of the d orbitals on Mo atoms and the anti-bonding p_z orbitals on S atoms [3]. These states display strong inter-layer coupling effect and their energies depend significantly on the number of layers [3].

2.3.2. OPTICAL PROPERTIES

Group VI-TMDs exhibit strong light-matter interactions as a result of the enhanced excitonic effect in two dimensional systems. Further, both indirect-to-direct band-gap transition and increase in band-gap energy from the bulk to the monolayered form result in variations in their photoluminescence, photoconductivity and absorption of light in the visible and near-infrared range.

Excitons are hydrogen-like bound states formed by a negatively charged electron and a positively charged hole due to Coulomb attraction, and they typically result from photo-excitations in semiconductors [29]. The recombination of the electron-hole pairs emits a photon which is observed as PL emission. In a typical bulk semiconductor crystal such as silicon, the large dielectric screening and small quasiparticle effective mass result in extremely small binding energies of the excitons [30]. This makes their bound behaviour at room temperature insignificant compared to the thermal fluctuations [30]. In contrast, bound exciton states play a key role in dictating the optical behaviour of 2D materials such as monolayered TMDs. Indeed, the strong Coulomb interaction due to the spatial confinement and the reduced dielectric screening compared to bulk crystals, make the excitons bound even at room temperature and with binding energies of hundreds of meV [30]. Further, the two dimensional nature of monolayered TMDs makes the excitons largely tunable thought a number of external stimuli such as light, electric fields, magnetic fields and strain [30]. Therefore, these properties can potentially lead to the development of several 2D photonic devices for next-generation optoelectronics, such as excitonic LEDs, lasers, optical modulators and coupling in an optical cavity [30].

The photoluminescence (PL) intensity of MoS_2 crystals onto SiO_2 increases by a factor of 10^4 from the bulk to the monolayered form [2]. The PL spectrum of single-layered MoS_2 exhibits a peak centered at ~1.9eV (Fig. 2.4*a*) due to the A exciton, which decreases in intensity increasing the number of layers (Fig 2.4*b*). An additional peak at ~1.4-1.6eV due to the indirect band-gap luminescence appears for the

multi-layered structures (Fig. 2.4*b-c*) [2]. The photoconductivity of TMDs is also affected by their band structure features and it has been shown that the photocurrent of MoS_2 increases in steps with photon energy corresponding to the direct and indirect band-gap energies [19]. As expected, the photoconductivity of 1L MoS_2 near 1.8eV is about 3 orders of magnitude higher than that of 2L MoS_2 around 1.6eV [19].

The optical absorption spectrum of MoS_2 (Fig. 2.5*a*) shows two main peaks corresponding to the A and B excitons (Fig. 2.5*b*) [19][31]. Further, a strong absorption at higher energies (called C peak for MoS_2, WS_2 and $MoSe_2$) arises from nearly degenerate exciton states corresponding to the region of the Brillouin zone where the valence and conduction bands are nested [32].

It has been shown that ~1nm thick-MoS_2, WS_2 and $MoSe_2$ can absorb up to 5-10% incident sunlight in the visible range [33], thus achieving absorptions one order of magnitude higher than Si and GaAs (two of the most commonly used absorbers in solar cells) of comparable thickness. Such an absorbance is equivalent to that of ~20nm thick-Si or ~5nm thick-GaAs. The strong absorption in monolayered TMDs has been attributed to dipole transitions between localized d orbitals (which contribute to absorbances up to 2-5%) and to excitonic coupling of such transitions (which increase the absorbance further up to 5-10%) [33].

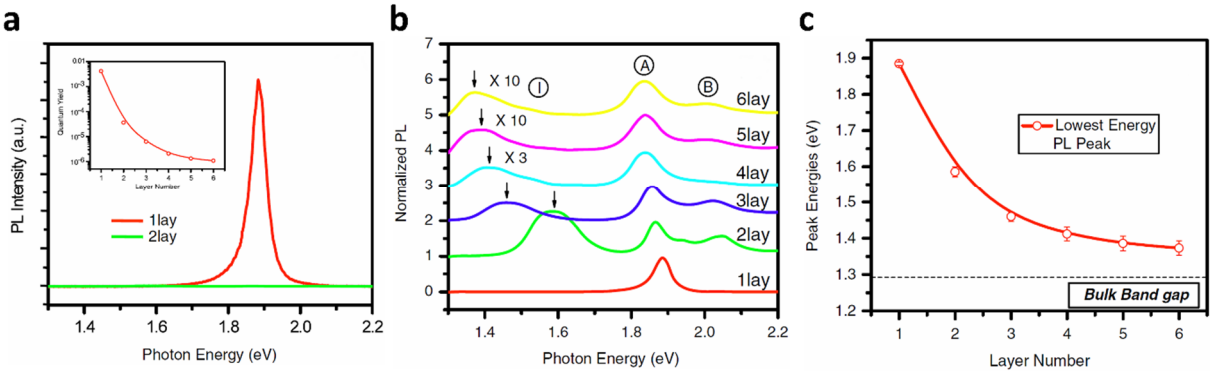


Figure 2.4 *(a) PL spectra for single- and two-layered MoS_2 in the photon energy range 1.3-2.2eV. The inset shows the PL quantum efficiency of N-layered MoS_2 with N=1-6. (b) PL spectra of N-layered MoS_2 normalized by the intensity of peak A (the feature I for N=4-6 is magnified). (c) Band-gap energy of N-layered MoS_2 calculated from the energy of the PL peak A for N=1 and from the feature I for N=2-6. The dashed line represents the indirect band-gap energy of bulk MoS_2. Adapted from Ref. [2].*

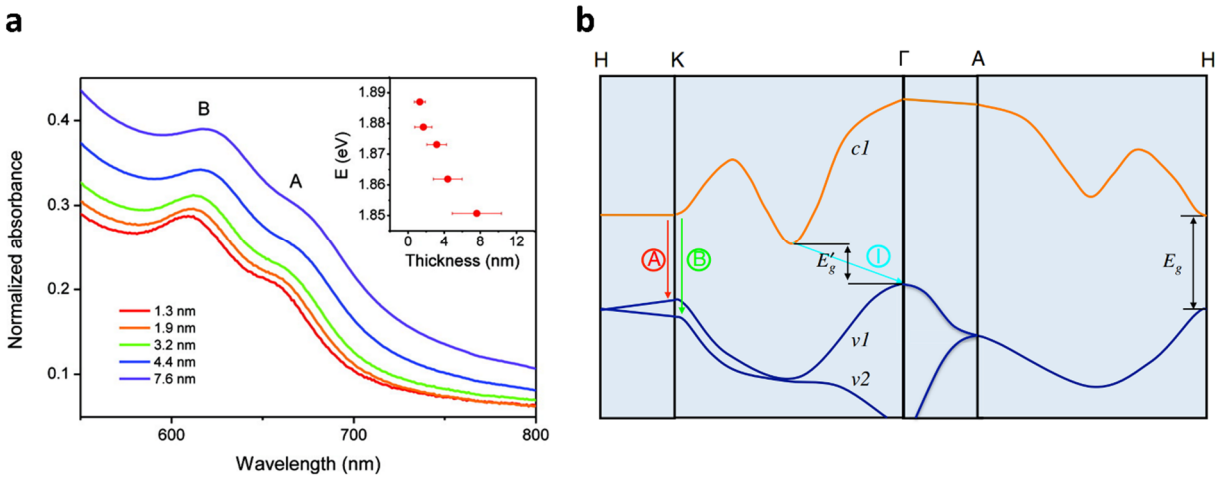


***Figure 2.5**: (a) Absorption spectrum of MoS_2 thin films. The inset shows the energy of the A exciton peak as a function of the average film thickness. Adapted from Ref. [31]. (b) Simplified schematic of the band structure of bulk MoS_2 showing the lowest conduction band c1 and the highest split valence bands v1 and v2, where: A and B are the direct band-gap transitions, I is the indirect transition, E'_g is the indirect gap for the bulk and E_g is the direct gap for the monolayer. Adapted from Ref. [2].*

Finally, since different 2D TMDs have different band-gaps, the vertical stacking of various 2D materials (including conducting graphene and insulating boron nitride) has also been explored to engineer hybrid materials with different emission and absorption properties [19]. However, efforts in this research direction are so far contradictory, either showing quenching of the PL emission while stacking together MoS_2 and WS_2 [34] or the emerging of a band-gap emission at ~850nm due to exciton recombination at the interface between the two materials [35].

2.3.3. PHONON DISPERSION

The phonon dispersion of TMDs has been calculated via ab-initio computational methods [36] and correlated with experimental data. The crystal structure of bulk 2H-MX_2 belongs to the D_{6h} point group where there are eighteen lattice dynamical modes at the centre of the Brillouin zone (Γ point) [37]. The irreducible representations of zone centre phonons are [37]:

$$\Gamma = A_{1g} + 2A_{2u} + B_{1u} + 2B_{2g} + E_{1g} + 2E_{1u} + E_{2u} + 2E_{2g}$$

where the atomic displacement of the four Raman active modes A_{1g}, E_{1g}, E^1_{2g} and E^2_{2g} is schematized in Figure 2.6. Specifically, the A_{1g} mode corresponds to out-of-plane vibrations involving only chalcogen atoms whereas the E^1_{2g} mode corresponds to in-plane displacements of both metal and chalcogen atoms [37]. Further, the E^2_{2g} mode is a shear mode representing the vibration of two rigid layers against each other and appears at low frequencies (<50cm^{-1}) while the E^1_g mode corresponds to in-plane vibrations of only chalcogen atoms and is forbidden in the backscattering Raman configuration [37].

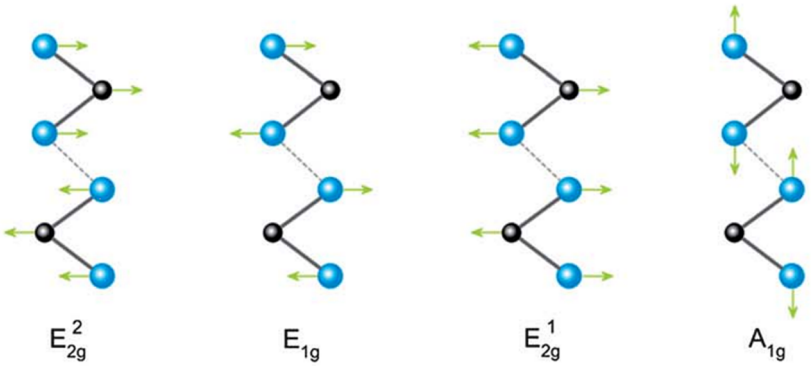


Figure 2.6 *(a) Schematics showing the atomic displacements for the four Raman active modes in MX_2 (metal atoms in black and chalcogen atoms in blue). Adapted from Ref. [37].*

Monolayered MX_2 belongs to the D_{3h} point group and has 9 modes at the Brillouin zone centre [37]. In particular, the shear mode E^2_{2g} is absent, thus providing a rapid identification for monolayered flakes. Further, although the thickness dependent shift of the Raman peaks for WX_2 is considerably smaller than for MoX_2 (due to larger atomic masses), the Raman spectra for WS_2 flakes with different thickness (Fig. 2.7*a*) show clear differences thus allowing for a precise identification of the number of layers [38]. The peak at low Raman shifts (~350cm^{-1}) (Fig. 2.7*a*) originates from a convolution of two Lorentzian functions whose positions depend on the layer number. The first Lorentzian is a resonant second-order Raman mode (2LA(M)) due to longitudinal acoustic phonons at the M point of the Brillouin zone and corresponds to collective oscillations of W and S atoms in the plane. Whereas the second Lorentzian is due to the optical phonon mode E^1_{2g} (Γ) representing the in-plane opposite oscillations of W and S atoms. Finally, the peak at high Raman shift (~416.6cm^{-1}) originates from the optical phonon mode A_{1g}(Γ) which corresponds to the out-of-plane displacements of W and S atoms [38][39].

Figure 2.7*b* shows that, upon increasing the number of layers, the 2LA(M) and $E^1_{2g}(\Gamma)$ peaks red-shift monotonously whereas the $A_{1g}(\Gamma)$ peak blue-shifts. These shifts are attributed to both the effect of inter-layer interactions on the effective restoring forces on atoms and to the increase of dielectric screening of long-range Coulomb interactions [19][40]. Further, the wavenumber shift between the 2LA(M) and $A_{1g}(\Gamma)$ peaks changes in a discrete way depending on the number of layers [38]. To conclude this section it is worth to note that the Raman features of TMDs depend on the excitation conditions due to the energy dependent Raman cross section of the phonons [37].

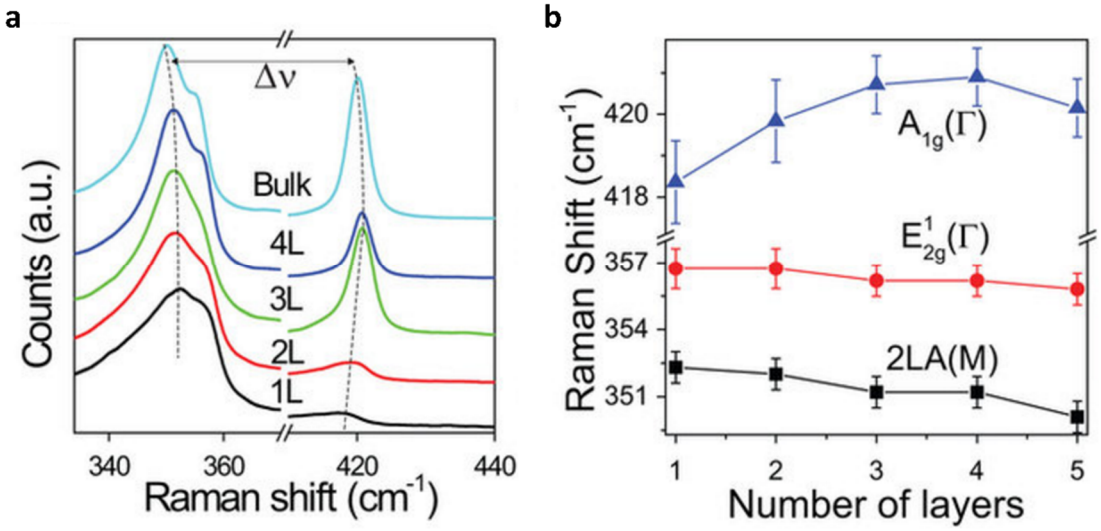


Figure 2.7 *(a) Evolution of the shape and position of the Raman peaks for bulk and N-layered WS_2 (with N=1-4). The Raman spectra were collected using a 532nm laser wavelength. (c) Measured Raman shifts for 2LA(M), $E^1_{2g}(\Gamma)$ and $A_{1g}(\Gamma)$ as a function of the layer number. Adapted from Ref. [38].*

2.4. SYNTHESIS METHODS

The currently available synthesis methods of atomically thin TMDs can be classified in either top down or bottom up approaches. Top-down methods are based on exfoliations from bulk crystals while bottom-up methods are synthesis from molecular precursors, either in vapour or liquid phase [19].

Bottom-up methods, which are the object of this thesis, can allow for a systematic control over the layer thickness and lateral size of TMDs [17][19][41]. In particular, the chemical vapour deposition (CVD) may offer strategies to synthesize high-quality atomically-thin continuous films over wafer-scale areas as previously demonstrated for graphene [42]. As discussed in Chapter 3, reported CVD methods

to synthesize atomically thin TMDs typically involve the vaporization of transition metal and chalcogen precursors and their co-deposition onto the substrate [24][43][44]. However, a systematic and reproducible control over the number of layers and lateral size of CVD-grown TMDs (especially W-based TMDs) has not yet been achieved [24][43][44].

2.5. APPLICATIONS OF TMDs

The layer-dependent properties of group VI-TMDs have recently attracted enormous attention for applications in electronics and optoelectronics. The large bandgap and adequate electron/hole mobility observed in several members of the TMDs family make them promising channel materials in transistors, while their direct bandgap in the monolayered form paves the way for next-generation ultrathin photovoltaic devices.

In particular, the tremendous interest in the group VI of transition metals (W, Mo) sulfides and selenides relies on their similitudes with silicon, but with advantages that can enable electronics at smaller scales, integration with photonics systems and new quantum electronics, such as valleytronics [7][24]. They present a direct band-gap in the visible-near IR range [24], carrier mobilities up to $1020 cm^2 V^{-1} s^{-1}$ [24][45], on/off ratios of $>10^7$ [24][46] and subthreshold swing values below 100mV per decade [24][46]. Further, single- and few-layered flakes exhibit elastic behavior up to strains of ~25-30% induced through flexible/stretchable supports while preserving photoluminescence and electrical properties [47][48][49]. In addition, unlike their bulk parent crystals, monolayered flakes are piezoelectric and DFT calculation have revealed that they can exhibit stronger piezoelectric coupling than traditionally employed bulk wurtzite structures [50]. Furthermore, due to their different polymorphisms [24][31][46][51], room-temperature semiconducting-to-metallic phase transitions can be induced by intercalated alkali metals [46], compressive strain [14], high pressures [52][53] or electric fields [54], which can enable unparalleled low contact resistance and open new electronic device concepts [46]. Therefore, these solid state materials can lead to the development of new nanoelectronics “beyond silicon” onto flexible lightweight substrates [48]. Finally, due to their intrinsically high surface-to-volume ratio, TMDs are particularly sensitive to changes occurring in their surroundings, thus also suggesting opportunities in molecular sensing applications

[19]. However, the development of CVD synthesis methods for the production of high-quality atomically-thin TMDs over large areas is a crucial aspect to achieve wafer-scale fabrication of TMDs-based devices.

2.5.1. TMDs-BASED ELECTRONICS

One of the most important applications of semiconducting materials is for digital transistors. In the basic field effect transistor (FET) structure, the source and drain electrodes are connected to a semi-conducting channel separated by a dielectric layer from the gate electrode (Fig. 2.8*a*). The function of the gate is to control the electrical current flowing through the channel, modulating its conductivity. Requirements for digital transistors include: high charge-carrier mobility ($\geq 10 cm^2V^{-1}s^{-1}$ [48]) to achieve fast operation, high conductivity (product between charge density and mobility), high on/off ratio (ratio of on-state conductance to off-state conductance) ($\geq 10^6$ [48]) for effective switching and low off-state conductance for low power consumption [19].

The electronic industry is currently based on silicon. State-of-the-art processors have silicon-based metal-oxide-semiconductor FETs with feature lengths of 22nm [19]. Further reduction in scale would require new materials which can overcome the current limitations of Si-based FET performance due to quantum effects (such as short-channel effects) and heat dissipation issues [19]. In recent years, graphene has been extensively investigated for electronic applications due to its atomically thin nature, exceptionally high carrier mobility and fast modulation of its current flow through an external gate voltage [19][48]. These properties led to high-performance graphene-based transistors for radio high-frequency (hundreds of gigahertz) applications [55]. However, the intrinsic lack of band-gap in graphene results in a high off-state current, limiting its use in digital logic transistors. On the contrary, semiconducting TMDs possess a sizable and tunable band-gap which can support high on/off ratios while maintaining sufficiently high carrier mobilities (comparable to Silicon) [19][48]. Further, it has been shown that their subnanometre thickness can allow for a more efficient control over switching and a reduction of short-channel effects and power dissipation [19], which are the limiting factors to 3D material-based transistor miniaturization.

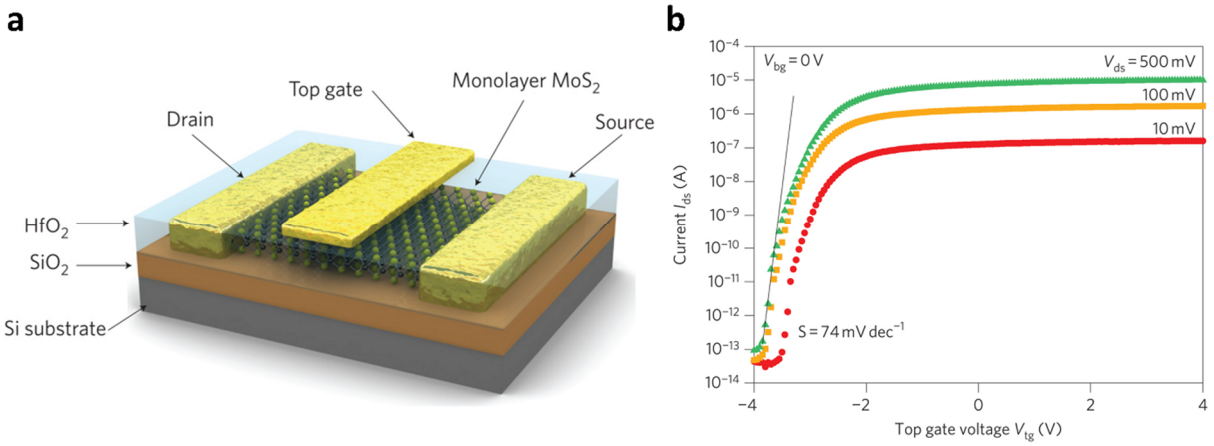


Figure 2.8 *(a) Schematic of a MoS_2-based FET with a top gate width and length of 4μm and 500nm, respectively. (b) Source-drain current (I_{ds}) versus top-gate voltage (V_{tg}) for a bias voltage ranging from 10mV to 500mV. The measurements were performed at room temperature with the back gate grounded. The device can be completely turned off by changing the top gate bias from -2 to -4V. The I_{on}/I_{off} ratio is $>1\times10^6$ for V_{ds}=10mV and $>1\times10^8$ for V_{ds}=500mV, while the subthreshold swing S is 74mVdec^{-1}. Adapted from Ref. [56].*

The first use of 2D TMDs as channel components in FETs was reported in 2004 by Podzorov et al. [57]. Bulk WSe_2-based FETs exhibited carrier mobility up to 500cm^{2}V^{-1}s^{-1} at room temperature (comparable to single-crystal Si-based FETs), on/off ratio of 10^4 at 60K and ambipolar behaviour [57]. While the first demonstration of a FET based on monolayered TMDs was reported in 2011 by Radisavljevic et al. [56]. Monolayered MoS_2-based FETs showed room-temperature mobility of >120cm^{2}V^{-1}s^{-1}, on/off ratio of ~10^8, subthreshold swing of 74mV per decade and n-type conductivity (Fig. 2.8*b*) [56]. Recently, monolayered WS_2 [58][59], WSe_2 [60][61] and $MoSe_2$ [62][63]-based FETs have also been demonstrated, showing average room-temperature carrier mobility of ~50cm^{2}V^{-1}s^{-1}, ~250cm^{2}V^{-1}s^{-1} and ~50cm^{2}V^{-1}s^{-1}, respectively, with on/off current ratios exceeding 10^6.

Mechanical characterizations on single-layered MoS_2 have shown that it is 30 times stronger than steel [64] and its atomic lattice can withstand strains of ~20%, at which point brittle fracture occurs at the ultimate strain limit of the constituent covalent bonds [48]. Therefore, the extraordinary degree of electrostatic control, good electrical characteristics and mechanical flexibility make atomically thin TMDs promising materials for applications in high-performance flexible electronics [19]. Integrated

electronic circuits based on multiple single-layered and two-layered TMDs FETs capable of performing digital logic operations have also recently been demonstrated [65][66].

2.5.2. TMDs-BASED OPTOELECTRONICS – P-N JUNCTIONS

The direct band-gap in the visible-near IR range of group VI-TMDs single-layers can enable a number of applications in flexible photovoltaic and photodetection [19]. Indeed, theoretical calculations have revealed that subnanometre thick-TMDs can absorb photon fluxes equivalent to short-circuit currents of 2-4.5mA/cm^2, whereas 1nm-thick Si, GaAs and P3HT (three of the most commonly used absorber materials in solar cells) generate currents in the 0.1-0.3mA/cm^2 range [33][67]. Therefore, ~50nm-thick Si and GaAs are needed to absorb the same fraction of sunlight absorbable by monolayered TMDs [33]. Accordingly, it has been recently demonstrated that a solar cell based on ~1nm-thick MoS_2/WS_2 bilayer can attain power conversion efficiencies ~1-3 orders of magnitude higher than the best existing ultrathin solar cells [33]. In addition, since atomically thin TMDs present carrier mobilities in the order of tens of $cm^2V^{-1}s^{-1}$, they are also suitable for light emitting applications (LEDs) [19]. Finally, monolayered MoS_2 and WS_2-based phototransistors have shown their potential as photodetectors [68] and, by using MoS_2 layers with different thicknesses, it has been demonstrated that single- and double-layered MoS_2 (with band-gap energies of 1.8eV and 1.65eV respectively) are effective for detecting green light, while triple-layered MoS_2 (with a band-gap of 1.35eV) detects red light [69].

The p-n diode represents the fundamental building block for diverse optoelectronic functions including photodiodes and light emitting diodes [70][71]. As Mo and W sulphides and selenides efficiently interact with light in the visible-near IR range in the monolayered form, TMDs-based p-n diodes can potentially lead to the development of flexible and transparent optoelectronic devices such as wearable electronics and transparent displays. However, p-n junctions are difficult to achieve using atomically thin TMDs due to challenges in the selective and uniform doping into n- or p-type semiconductors [70] which can be attributed to their intrinsic defects-driven propensity for unipolar transport [72]. Up until now, p-n junctions based on atomically thin TMDs have been demonstrated using different strategies, such as electrostatic doping and stacking of p- and n-type TMDs. In particular, a lateral p-n junction

based on electrostatically doped-monolayered WSe_2 has been reported and its applications as photovoltaic solar cell, photodiode and light emitting diode have been demonstrated, giving light-power conversion and electroluminescence efficiencies of ~0.5% and ~0.1%, respectively (Fig. 2.9) [71]. The p-n junction has been realized using a split gate electrode and by biasing one gate with a negative voltage (to draw holes into the channel) and the other with a positive voltage (to draw electrons) [71]. By using palladium (high-work-function metal) as anode and titanium (low-work-function metal) as cathode it has been possible to align the Fermi level with the valence (for hole injection) and conduction (for electron injection) band edges of WSe_2, respectively [71].

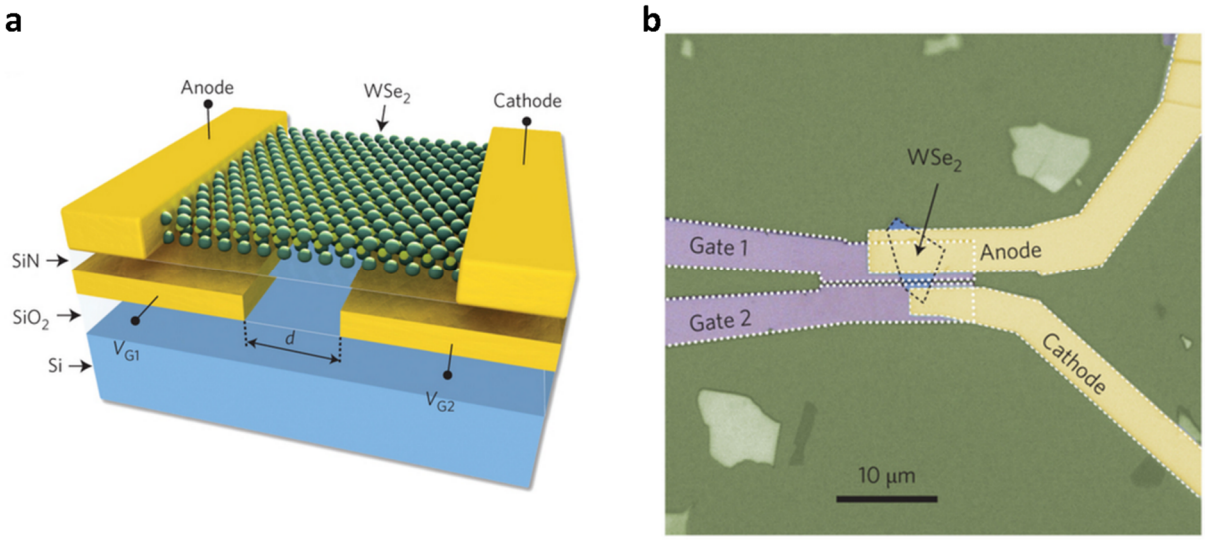


***Figure 2.9**: (a) Schematic of the lateral p-n junction-based device structure. (b) Coloured micrograph of the device. The anode and cathode electrodes are made of Pd/Au and Ti/Au, respectively. The gap between the gates is 460nm-wide. A 100nm-thick gate dielectric is inserted between the gate electrodes and the WSe_2 flake. Adapted from Ref. [71].*

Vertical p-n heterojunctions have been also obtained. An example is the vertical stacking of p-doped monolayered WSe_2 and n-type few-layered MoS_2 (Fig. 2.10) [73]. Unlike the planar p-n junction described above, where the active area was confined to the lateral interface zone [71], photocurrent mapping of the WSe_2/MoS_2 stacking showed that the p-n junction is now achieved throughout the entire overlapping area [73]. Thin Au and Ni/Au films were used as electrodes for WSe_2 and MoS_2, respectively, to form Ohmic contacts with minimized contact resistance and potential barrier. The external quantum efficiency

showed by the vertical WSe_2/MoS_2 heterostructure-based diode is much higher (up to 12%) than what obtained for lateral electrostatically doped-WSe_2 homojunctions (0.1-3%) [71][73]. This improved device performance is attributed to a more efficient charge separation at the atomically sharp vertical interface [73], in contrast to the electrostatically-induced junction which typically exhibits a spatial doping gradient [71].

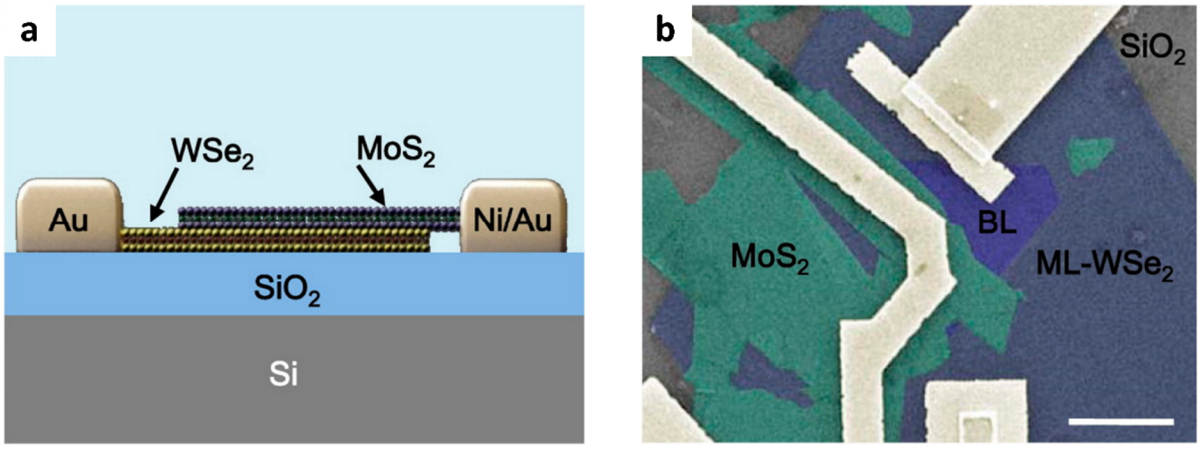


Figure 2.10 *(a) Schematic of the cross-sectional view of the WSe_2/MoS_2 vertical heterojunction-based diode. (b) False colour-SEM image of the device, in which multi-layered WSe_2 (ML-WSe_2) is highlighted by blue colour, bi-layered WSe_2 (BL) by violet colour, mono-layered MoS_2 by green colour and the metal electrodes by golden colour. The scale bar is 3μm. Adapted from Ref. [73].*

2.6. TRANSITION METAL-DOPED TMDs

The modification of TMDs through transition metal doping can extend their potential applications [16]. In semiconducting materials, atomic doping can cause a modulation of the Fermi level and/or band gap and thus it can be useful for controlling the p- or n-type semiconducting behaviour [16]. In addition, appropriate dopant selection can yield to magnetic properties [16][74]. Finally, metal doping can offer strategies to control the TMDs morphology for catalytic and tribological applications [16]. Atomic doping can be substitutional of atoms in the lattice, if the dopant is well matched in terms of size, valence and coordination (substitutional doping), interstitial in sites between existing lattice atoms (interstitial doping) or intercalating in between layers (intercalation doping) [16]. It is worth to note that metal doping levels

up to 50at.% have been reported for TMDs since in some cases it is desirable to induce vacancies, defects and even alter the host structure to create a new phase [16].

Compared to wet chemical preparation methods of TMDs (such as hydrothermal synthesis and heating or hot injection of precursor solutions), which can require the solubility compatibilities of the reaction components and where high temperatures cannot always being reached due to the limits imposed by the boiling points of the solvents, vapour phase processes (such as chemical vapour deposition and physical vapour transport) are more versatile and can be more easily adapted for the inclusion of dopant species in the TMDs synthesis itself [16]. Sputtering and pulsed laser evaporation, that use targets of the same material to be deposited as a thin film can also be adapted for the incorporation of dopants in TMDs by using additional targets of the doping materials [16][75][76][77][78][79].

Due to the first applications of bulk TMDs as solid lubricants, early works focused on the influence of transition metal inclusions on the tribological properties. In particular, MoS_2 thin films incorporating various d-block metals have been obtained by co-sputtering using targets of MoS_2 and dopant metals at 190°C under Ar flow [80]. The inclusion of Cr, Co, Ni, Au and Ta resulted in films with stable frictional response and reduced wear rate compared to pure MoS_2 films. Due to the current numerous applications of 2D TMDs, the influence of transition metal inclusions is nowadays also investigated for electronic, optoelectronic and catalytic applications. In addition, first-principles calculations have recently been performed to investigate the electronic and magnetic properties of monolayer MoS_2 substitutionally doped with Mn, Fe and Co (one dopant atom per 8×8×1 supercell) [81]. The predicted magnetic properties suggested possible applications of doped MoS_2 as dilute magnetic semiconductors for the preparation of contrast agents in magnetic resonance imaging of cancer tumours [81]. Further, WS_2 nanoflakes doped with a range of different transition metals (Fe, Co, Ni, Mn, Gd) and with polyethylene glycol (PEG) modification have recently been synthesized using a high-temperature solution method by reacting tungsten chloride and the relevant metal chloride with elemental sulphur dissolved in a mixed solvent of oleylamine and 1-octadecene at 300°C under a N_2 atmosphere [82]. It has been demonstrated that the doped-PEGylated WS_2 nanoflakes can be applied as imaging agents and can be used for photothermal therapy by conversion of near-infrared light into heat.

In the following, we review the predicted properties, potential applications and synthesis strategies of TMDs doped with transition metals from the groups IV-XI.

2.6.1. GROUP IV: Ti AND Zr

Density functional theory calculations on the MX_2 compounds (where M=Mo or W and X=S, Se or Te) have suggested that WSe_2 and WTe_2 are expected to display the lowest bulk contribution to the friction coefficient between sliding layers [16][83]. Nevertheless, MoS_2 substitutionally doped with Ti has been identified as an ideal material with enhanced tribological characteristics than undoped MoS_2 and similar frictional properties of WSe_2 and WTe_2. Therefore, doping of TMDs with group IV-transition metals (Ti, Zr) has mainly been investigated for tribological applications, and it has typically been achieved by co-sputtering synthesis techniques [16][84][85][86][87][88][89][90]. Since group IV-metals exhibit a stable oxidation state of IV, the metal ions can isovalently substitute Mo(IV) and W(IV) in their respective disulphides. However, high Ti and Zr dopant levels are likely to lead to a structural distortion of the trigonal prismatic TMDs structure as TiS_2 and ZrS_2 adopt an octahedral configuration around the metal ions in the layered CdI_2 crystal structure [91].

Ti-doped MoS_2 multiwalled nanotubes have been synthesized from a thermally oxidized Mo:Ti alloy (4:1 by weight) and H_2S at 950°C under N_2 atmosphere [84]. Ti incorporation was found to be in the form of both encapsulated TiO_2 crystallites and as a dopant into the 2H-MoS_2 lattice. Further, the same oxidation state and similar ionic radii of Ti and Mo, combined with the lack of significant lattice expansion along the c axis of the tubes, indicated that substitutional doping of Mo atoms by Ti into the MoS_2 lattice was achieved.

Aerosol-assisted CVD has been used to deposit nanoparticulated MoS_2 films onto ferrous substrates with 4-38% Ti inclusion by using tetrakis(diethyl-dithiocarbamato)molybdenum(IV) and tetrakis(tert-butylthiolato)titanium(IV) dissolved in tetrahydrofuran solutions [85]. The formation of a highly crystalline layer of FeS between the substrate and the MoS_2 films led to low coefficients of friction due to the combined performance of the FeS layer and burnishing of the MoS_2 film. However, Ti incorporation was found

to be in the form of TiO_2 byproduct and no significant improvement in the tribological performance of the MoS_2 films upon Ti incorporation was detected.

The doping of WS_2 with Ti at ~5-14 at.% through magnetron co-sputtering has resulted in films with slightly higher coefficients of friction than undoped WS_2 films but with significantly increased wear lifetimes [86]. Whereas higher dopant levels induced a dramatic change in the microstructure due to Ti preventing the formation of crystalline WS_2, and resulted in amorphous films with well-dispersed nano-crystalline (1-3nm) precipitates and compromised friction reduction properties.

The humidity of the atmosphere in which tribological MoS_2 and WS_2 coatings are applied can reduce their effectiveness as lubricants [87]. It has been found that by incorporating Ti or Cr into MoS_2 with an optimum dopant level around 15 at.% for preserving low friction properties, the films became denser and harder, and the wear rates were not affected by humidity.

Biased- and pulsed-DC sputtering of three MoS_2 and one Ti targets have produced MoS_2 films with 4-47 at.% Ti [88]. It has been shown that pulsed-DC sputtering can generate denser films than the biased-DC method and that the S/Mo ratio of all the films increased with increasing working pressure during deposition. Ti addition strengthened the films but caused an increase of the friction coefficient in pin-on-disc tribological testing due to abrasive effect. Nevertheless, the denser pulsed-dc sputtered films with low levels of Ti-doping exhibited the lowest friction coefficient increase.

Co-sputtering of MoS_2 and Ti targets in a closed-field unbalanced magnetron sputtering process yielded to MoS_2 films doped with approximately 16 at.% Ti. These were slightly substoichiometric with respect to sulphur, amorphous and exhibited a dense featureless morphology [89]. In general, experiments showed that the friction and wear performance of the Ti-doped MoS_2 films was influenced by humidity and temperature. Further, results of rolling contact tests performed in vacuum indicated that the doped MoS_2 films could function extremely well as a solid lubricant for ball bearings operating in vacuum.

Zr-doped WS_2 has been formed by medium-frequency magnetron sputtering, multi-arc ion plating and ion-beam-assisted deposition technique and displayed higher hardness, smaller coefficient of friction and lower wear rate than undoped WS_2 [90].

2.6.2. GROUP V: V AND Nb

Traditionally, extrinsic p-type doping in natively n-type TMDs such as MoS_2 has been approached with surface adsorption or intercalation of electron-accepting molecules [93]. However, this strategy did not lead to a stable and controllable p-type doping of TMDs, which hampered the development of charge-splitting p-n junctions [93]. Therefore, the stable doping of TMDs through substitution of host atoms with dopant atoms secured with covalent bonds is highly desirable. Doping of TMDs with group V-transition metals (V, Nb) has mainly been investigated for electronic applications, and it has typically been achieved by vapour or solid phase reaction of precursors [92][93][94][95].

Sulfurization of e-beam evaporated Mo (2.5nm)/Nb (0-0.3nm)/Mo (2.5nm) layered stacks onto sapphire (0001) surfaces by S vapours at 900°C in a CVD chamber has led to few-layered Nb-doped MoS_2 thin films stacked in the (0001) direction [92]. Spectroscopic characterization and diffraction measurements indicated that the host structure remained unaltered upon Nb-doping, thus suggesting a direct substitution of Nb into the MoS_2 lattice at Mo sites. As predicted by density functional theory calculations [92], Nb was found to act as an efficient acceptor in MoS_2 up to a relatively high density, leading to a relatively high hole density ($3.1 \cdot 10^{20} cm^{-3}$) and Hall mobility ($8.5 cm^2 V^{-1} s^{-1}$) at room temperature. The use of substitutional Nb to achieve p-type doping can thus expand the potential of semiconducting MoS_2 for optoelectronic applications which require p-n junctions such as LEDs.

Stable p-type conduction in multilayered MoS_2 with a degenerate hole density of $\sim 3 \cdot 10^{19} cm^{-3}$ has also been achieved by substitutional Nb doping in MoS_2 single crystals grown using high-temperature (935-1050°C) chemical vapour transport (CVT) from elemental precursors of Mo, S and Nb (with a Mo:S:Nb molar ratio equal to 1:2:0.005 for a nominal 0.5% Nb doping) and using iodine as the transport medium [93]. Van der Waals p-n homojunctions based on vertically stacked doped MoS_2 (p-type) and undoped MoS_2 (n-type) layers were fabricated, which enabled gate-tuneable current rectification. The CVD of Nb-doped WS_2 monolayers with additional PL peaks ascribable to the emission from impurity states generated by the substitution of W atoms with Nb has recently been reported and it will be discussed in Section 3.4 [95].

Ultrathin 2H-MoS_2 nanosheets with less than five atomic layers intercalated with V have been prepared by exfoliation into N-methyl pyrrolidone of bulk V-doped MoS_2. This was obtained by solid state reaction of Mo, V and S powders at 900°C for 12h in a sealed fused silica tube evacuated to 10^{-3}Torr [94]. The inclusion of intralayer V atoms significantly enhanced the electrical conductivity ($1.7 \cdot 10^3 Sm^{-1}$ at 280K) and the carrier concentration ($7 \cdot 10^{17} cm^{-3}$), which are about 40 and 20 times larger than those for undoped MoS_2 ($40 Sm^{-1}$ and $3.5 \cdot 10^{16} cm^{-3}$), respectively. Further, benefiting from these enhanced electrical properties, the semi-metal-like V-doped MoS_2 nanosheets exhibited enhanced catalytic activity for hydrogen evolution compared with pure MoS_2.

2.6.3. GROUP VI: Cr

The doping of TMDs with group VI-transition metals (Cr, Mo, W) has mainly been studied for tribological, magnetic and optoelectronic applications, and it has been achieved by vapour or solid phase synthesis [96][97][98][99][100][101][102][103][104][105][106][107][108][109]. Although Cr belongs to the same group of Mo and W, it has a tendency to adopt lower oxidation states (II or III) than the heavier elements in the group (IV or VI). Further, chromium sulphides typically show trigonal, monoclinic or rhombohedral crystal structures in the range $CrS_{0.95}$-$CrS_{1.5}$ rather than a TMDs-like hexagonal CrS_2 phase [16][110]. Therefore, the incorporation of Cr into the TMDs lattice cannot be easily achieved without inducing changes in the host structure. Whereas, $Mo_{1-x}W_xS_2$ alloys for $0 \leq x \leq 1$ can be easily formed since MoS_2 and WS_2 adopt the same hexagonal structure and Mo^{4+} and W^{4+} show similar Shannon-Prewitt crystal radii (0.790Å and 0.800Å respectively).

Cr-doped MoS_2 thin films have been obtained through liquid-phase exfoliation in N-methyl-2-pyrrolidinone (NMP) of thicker films grown by aerosol assisted-CVD from diethyldithiocarbamate complexes of Mo and Cr [96][97]. It has been shown that the inclusion of Cr into the MoS_2 lattice induces a number of morphological, crystallographic and nanomechanical changes. MoS_2 films with 5-10 mol% Cr exhibited relatively larger moduli of elasticity compared to undoped MoS_2 films and a more granular morphology which can potentially increase their persistence as antiwear materials. Further, the compressive

yield strength increased with increasing Cr content and the failure mode became brittle without undergoing plastic deformation as seen in pure MoS_2.

Cr has also been incorporated into layered $TiSe_2$ through solid state reaction of Ti, Cr and Se powders at 700°C for 120hr [98]. It has been shown that Cr atoms occupy the interstitial octahedral sites between $TiSe_2$ layers at dopant levels below ~20at%, whereas they are also found in higher concentration at the interlayer Ti sites, inducing significant disorder in the crystal lattice.

$Mo_{0.91}W_{0.09}S_2$ has recently been synthesized in the form of both ultrathin flakes and amorphous carbon-supported composites, and exhibited a higher specific capacitance than pure MoS_2 for the same active weight [111]. A previous work has demonstrated that the transition energies in $Mo_{1-x}W_xS_2$ compounds vary smoothly with the W composition x [112].

2.6.4. GROUP VII: Mn AND Re

Theoretical calculations have predicted that Mn inclusion into MoS_2 with S vacancy defects induce anti-ferromagnetism in several of the Mo atoms in the immediate vicinity of the Mn atom, and that the total magnetic moment can be increased with increasing S vacancies, suggesting the application of Mn-doped MoS_2 as a dilute magnetic semiconductor [113]. On the contrary to the trigonal prismatic coordination of Mo or W in their sulphides, ReS_2 adopts a layered structure with octahedral coordination around the Re atoms and formation of Re-Re bonds in the a-b plane [114]. Therefore, while the alloying between MoS_2 and ReS_2 appears feasible based on thermodynamic considerations and according to the similar Shannon-Prewitt radii of the cations, the in-plane bonding demanded by the Re atoms only allows for small Re dopant levels into MoS_2 (<10 mol%) and leads to negligible Mo incorporation into ReS_2 [115]. Further, the inclusion of Re into the MoS_2 or WS_2 lattice can induce a phase change from the hexagonal symmetry 2H to the tetragonal 1T or rhombohedral 3R symmetry, which was known formerly only for MoS_2 and WS_2 intercalated by alkali metals [116][117]. Doping of TMDs with group VII-transition metals (Mn, Re) has mainly been investigated for tribological and electrochemical applications, and it has typically been achieved by vapour phase methods [116][118][119][120][121][122][123].

It has been shown that inert substrates such as graphene permit the inclusion of Mn into mono-layered MoS_2 up to 2 atom% via physical vapour deposition from MoO_3, S and $Mn_2(CO)_{10}$ powders evaporated at 725°C, 300°C and 70°C, respectively, whereas substrates with reactive surface terminations, such as SiO_2 and sapphire, led to defective MoS_2 with no detectable Mn incorporation [118].

The treatment of multiwalled WS_2 nanotubes with ReO_3 vapours using I_2 transport gas in an evacuated quartz ampule subjected to a temperature gradient (800°C-950°C) has led to substitutional Re doping (~2at%) into the lattice of the outer layers, which induced a partial 2H→1T phase transition [119]. DFT calculations have suggested that this phase transition may be induced by the electron donation from Re impurity atoms, which can destabilize the 2H phase and stabilize the 1T phase. Further, Re-doped WS_2 nanotubes exhibited a higher strain than 2H-WS_2 nanotubes and are expected to exfoliate more readily into tribologically active sheets for the lubrication of sliding counter-faces subjected to mechanical wear [120].

Substitutional Re doping of MoS_2 single crystals has also been achieved via chemical vapour transport of the elements with Br as transport agent in an evacuated quartz ampoule subjected to a temperature gradient (960°C→930°C) for ~10 days [116]. It has been shown that Re doping stabilizes the formation of 3R-MoS_2 and alters the electronic states of MoS_2, causing a redshift of the direct band-edge A and B excitonic transitions while significantly reducing their energy splitting (150meV) in relation to undoped 2H-MoS_2 (200meV).

The beneficial effect of Re doping in MoS_2 fullerenes for electrochemical hydrogen evolution reaction and electrodes in sodium-ion batteries has also been demonstrated, due to the Re-induced higher density of catalytically active edge sites and n-type doping with enhanced electrical conductivity and increased number of diffusion defect sites, respectively [121][122].

Polycrystalline thin films of $Mo_{1-x}Re_xS_2$ ($0 \leq x \leq 0.06$) have recently been deposited onto glass substrates through aerosol-assisted CVD by using different molar ratios of rhenium iso-propylthiolate and tetrakis (diethylaminodithiocarbomato)molybdate(IV) single source precursors in tetrahydrofuran at 475°C for ~3h [123]. It has been shown that the morphology of the films changes from lamellar for pure MoS_2 to cluster at 6mol% alloying with Re. Further, due to crystal radii and thermodynamic similarities between Re(IV) and Tc(IV), it has been suggested that the as-grown $Mo_{1-x}Re_xS_2$ films could be used as

model system for the incorporation of radioactive ^{99}Tc into host MoS_2 crystals as a means of immobilisation in nuclear waste processing.

2.6.5. GROUPS VIII-X: Fe, Co AND Ni.

First-principles calculations have predicted that the electronic and magnetic properties of non-magnetic armchair and zigzag MoS_2 nanoribbons can be tuned via doping with transition metal impurities which tend to substitute the outermost cations of the nanoribbons [124]. In particular, Fe-doped and Co-doped armchair MoS_2 exhibited ferromagnetic and anti-ferromagnetic semiconducting characteristics, respectively, whereas Fe-doped and Co-doped zigzag MoS_2 ribbons showed weak semiconducting and strong metallic ferromagnetic behaviour, respectively. It has been predicted that Fe inclusions into mono-layered MoS_2 can also increase the catalytic activity of the basal plane for CO oxidation reaction due to charge transfer and orbital hybridization between the adsorbates and the embedded Fe atoms strongly constrained at S vacancy sites with an high diffusion barrier, which ensures stability of Fe-doped MoS_2 at room temperature [125]. Theoretical calculations on the Fe-doped MoS_2 system have recently shown that the layer number is crucial in determining its magnetic properties, with monolayered Fe-doped MoS_2 adopting ferromagnetic coupling and bi- and tri-layered Fe-doped MoS_2 becoming antiferromagnetic, due to a competition mechanism between the double- and super-exchange interactions [126]. Further, the model predicted that substitutional Fe dopant atoms at the Mo sites are energetically favoured in mono-layered MoS_2 synthesized in S-rich environment, while the formation of intercalation and substitutional Fe complexes are preferred in bi- and multi-layered MoS_2. It has been predicted that biaxial tensile strain also affect the magnetic properties of Fe-doped single-layered MoS_2 which undergoes a spin reorientation transition from out-of-plane to in-plane magnetization at critical 3% strain [127]. Further, it was found that small amounts of strain (0-6%) can significantly enhance the magnetic moment of Fe-doped MoS_2 and introduce electronic features such as spin-gapless and bipolar magnetic semiconducting behaviour.

First-principles calculations of binding energies and magnetic properties of monolayered MoS_2 doped with a number of transition metals (Mn, Fe, Co, Zn, Cd, Hg) have shown that Co (6.25%)-doped MoS_2 exhibit the highest magnetic moment (3.0μB) and have predicted antiferromagnetic coupling between

Co atoms for the ground state of the material, suggesting its potential as a dilute magnetic semiconductor [128]. Doping of TMDs with the iron triad (Fe, Co, Ni) has mainly been studied for magnetic, spintronic and catalytic applications, and it has typically been achieved by vapour and liquid phase methods [129] [130][131] [132][133][134][135][136].

Fe-doped MoS_2 single crystals with a Fe concentration of 0.5% have been grown by chemical vapour transport from the elements in an evacuated and sealed quartz tube subjected to a temperature gradient (1050°C→935°C) for 720h using I_2 as transport agent [129]. Compared to undoped MoS_2, Fe-doped MoS_2 exhibited an additional feature in the absorption spectrum at 1.2eV, longer carrier lifetime, higher n-type carrier concentration and lower mobility due to the effect of Fe dopants.

Co-doped MoS_2 and WS_2 nanowires supported onto Al_2O_3 substrates for improved hydro-desulphurization processes have been produced through atmospheric pressure sulfurization of ammonium heptamolybdate and cobalt nitrate with a H_2S/H_2 gas mixture at 400°C for 10h [130]. Co-doped MoS_2 nanoparticles for photo-electrocatalytic reduction of CO_2 to methanol have been prepared by a hydrothermal method at <100°C involving reactions of salts in aqueous media [131]. Compared to undoped MoS_2, Co (33at.%)-doped MoS_2 showed enhanced catalytic performance due to a band-gap of 1.41eV, which better matches the reduction potential of CO_2, and higher conductivity. MoS_2 nanosheets with varying concentration of dopant Co atoms (≤7%) incorporated at the edge sites have also been synthesized via hydrothermal method from sodium molybdate, thioacetamide and cobalt acetate [132]. The doped MoS_2 nanosheets exhibited room temperature ferromagnetism with total magnetic moment values decreasing with higher Co concentrations, probably due to the Co-induced increased thickness and flatness of the sheets and consequent reduced concentration of edge sites responsible for the observed magnetism.

Hollow structures of M-MoS_3 (M=Co, Ni) have been obatined via a template-engaged precipitation process by reacting water-soluble precursors with various morphologies and compositions (M acetate hydroxide prism, Co-glycerate sphere and ZIF-67 polyhedron) with ammonium tetrathio-molybdate in aqueous media, followed by a post-annealing treatment in nitrogen [133]. Benefiting from high-curvature surfaces with an increased density of exposed edge sites, the resultant M-MoS_3 catalysts, especially $CoMoS_3$ hollow prisms, exhibited enhanced electrocatalytic performance in terms of a large cathodic current density, small Tafel slope and good cycling stability.

Ni-doped WS_2 supported on silica with a Ni/(Ni+W) ratio of 7-22% has been prepared by calcining $WO_3 \cdot nH_2O/SiO_2$ impregnated with nickel(II) formate in air at 400°C for 3h, followed by annealing in H_2S at 300°C for 2h [134]. It has been shown that Ni incorporation into WS_2 increased the dark catalytic hydrogen evolution activity of WS_2. MoS_2 nanoparticles doped with small amounts of Ni have also shown improved hydrogen evolution reaction activity with a small Tafel slope of $47 mV dec^{-1}$, resulting from a higher density of electrochemical active sites, higher turnover frequency over each active site and better conductivity [135]. It is worth to note that the catalytic activation of basal-plane S atoms for hydrogen absorption has also been achieved by platinum-doping of MoS_2 [137]. However, the use of Ni or Co as dopant atoms represents an equally promising yet more realistic alternative in terms of cost per mole.

Ni-doped MoS_2 nanoparticles with different morphologies have been obtained by adding an ionic liquid (1-butyl-3-methylimidazolium bis(trifluoromethanesulfonyl)imide) to the main reactants (nickel nitrate and ammonium tetrathiomolybdate) in formamide [136]. It has been shown that the addition of the ionic liquid during the synthesis process led to shorter and more readily dismantled MoS_2 slabs, while also promoting the incorporation of Ni into MoS_2 with an optimal Ni/(Mo+Ni) atomic ratio of 0.3, which are potential benefits in hydrodesulphurisation catalysts.

2.6.6. GROUPS XI: Cu

Computational studies have suggested that substitutional copper can influence the magnetic properties of monolayered MoS_2. Although Cu is nonmagnetic in its bulk state, a total magnetic moment of 5.00-5.08μ_B per supercell is predicted which is higher than what calculated for any of the other first row transition metals [138]. The driving force was identified to be a strong hybridization between the 3d states of Cu and the 3p states of neighbouring S atoms, which results in an extreme unbalanced spin-population in the spin-split impurity bands near the Fermi level. The development of ferromagnetic properties has also been predicted for Cu-doped $MoSe_2$ and attributed to double-exchange interaction [139]. Further, DFT calculations have shown that monolayered WS_2 with a single substitutional Cu dopant atom is non-magnetic while two nearest-neighbour Cu-doped monolayered WS_2 is ferromagnetic with

a total magnetic moment of 1.089μ_B due to p-d hybridization between Cu dopant and its neighbouring S atoms with consequent splitting of the energy levels near the Fermi energy [140].

Despite these theoretical studies have suggested Cu-doped TMDs as promising candidates for thin dilute magnetic semiconductors, they have been experimentally investigated only for tribological application to the best of our knowledge. It has been shown that the incorporation of a suitable content of Cu dopant (~5.8-11.5at.%) into WS_2 films prepared by radio frequency co-sputtering with WS_2 and Cu targets can significantly improve their toughness, whereas excess amounts of Cu (≥16.2at.%) led to high brittleness [141]. The WS_2-Cu composite films generally exhibited a lower friction coefficient and wear rate than pure WS_2 films and 3- to 5-fold longer wear life both in vacuum and in humid air conditions.

2.7. CHEMICAL FUNCTIONALIZATION OF TMDs

In addition to the substitutional, interstitial and intercalation doping reviewed above, surface chemical functionalization of TMDs has also been investigated to tailor their carrier types and Fermi levels for Schottky barrier modulation at TMDs/metal interfaces, realization of p-n junctions, electronic band gap opening, charge storage and chemical or biological sensing [142]. Analogously to graphene [143][144][145], a number of different chemical functionalization approaches have been investigated, which include physisorption of molecules [60][146], metal nanoparticles functionalization [147][148], organometallic [149][150] and organic compounds functionalization [151][152][153], solution-based functionalization [151][154][155][156] and plasma-assisted doping [157][158].

It has been shown that the light emission efficiency in MoS_2, $MoSe_2$ and WSe_2 is largely modulated by charge transfer with physically adsorbed electronegative gaseous molecules. In particular, O_2 and H_2O electronically depleted intrinsically n-type doped TMDs such as MoS_2 and $MoSe_2$, which exhibited a drastic PL enhancement, whereas the opposite effect was observed in p-type WSe_2 [146]. Further, upon exposing WSe_2 to NO_2 environment in N_2 gas, NO_2 can physically and chemically adsorb onto the WSe_2 surface and withdraw electrons from WSe_2 due to its strong oxidizing property [60]. Cl was also used to degenerately n-dope few-layered WS_2 and MoS_2 by soaking the exfoliated TMDs flakes in undiluted

1,2 dichloroethane (DCE) at room temperature for more than 12h, which may lead to the replacement of S vacancies with Cl atoms [154].

The electronic beam deposition of noble metals (Au, Ag, Pd, Pt) nanoparticles onto MoS_2 has led to p-type doping, which showed an increasing trend with increasing work function of the metal particles and their concentration and with decreasing MoS_2 thickness [147].

The n-doping of monolayered MoS_2 and p-doping of few-layered and bulk WSe_2 has been achieved via surface functionalization using the organometallic compounds: cesium carbonate (Cs_2CO_3) and octadecyltrichlorosilane (OTS), respectively [149][150][159]. The p-doping effect in WSe_2 induced by OTS originates from the methyl ($-CH_3$) functional groups, which exhibit a positive dipole and can thus reduce the electron density at the WSe_2 interface.

It has been shown that organic compounds can dope TMDs via surface charge transfer mechanism. The solution-based chemical doping of MoS_2 using 2,3,5,6-tetrafluoro-7,7,8,8-tetracyanoquinodimethane (F4TCNQ) or 7,7,8,8-tetracyanoquinodimethane (TCNQ) resulted in p-type doping and enhanced PL intensity due to the switching of the dominant PL process from the recombination of negative trions to that of excitons through extraction of extra electrons [151]. Whereas nicotinamide adenine dinucleotide (NADH) led to n-type doping and reduced PL intensity due to the suppression of exciton recombination through injection of excess electrons. It has been reported that benzyl viologen (BV), which has one of the highest reduction potentials of all electron-donor organic compounds, can act as a surface electron transfer donor for few-layered MoS_2 [152]. BV-doped MoS_2 exhibited good stability in both ambient air and vacuum and high electron sheet density of $\sim 1.2 \cdot 10^{13} cm^{-2}$, which corresponds to the degenerate doping limit for MoS_2. Further, the BV dopant molecules can be reversibly removed by immersion in toluene, providing the ability to control the carrier sheet density and allowing the selective removal of surface dopants for patterned doping. N-doping in multilayered MoS_2 has also been achieved through exposure to p-toluene sulfonic acid (p-TSA), which is extensively used for tailoring the charge density of conducting polymers [153].

The electronic and optical properties of MoS_2 nanoflakes deposited onto SiO_2 substrates have also been modified by tuning the charge transfer between the flakes and the substrate through functional self-assembled monolayers (SAMs) with different dipole moments [156]. Fluoroalkyltrichlorosilane-

SAMs (with large positive dipole moment) acted as hole donors and significantly mitigated the intrinsic n-type characteristic of MoS_2 (p-type doping), whereas 3-(trimethoxysilyl)-1-propanamine-SAMs (with negative dipole moment) acted as electron donors and enhanced the MoS_2 n-type characteristic (n-type doping).

The charge transfer method has been employed to form a MoS_2-based van der Waals p-n junction where BV and $AuCl_3$ were used as n- and p-type dopants, respectively, to make few-layered MoS_2 behaving as n- and p-type semiconductor [160]. In particular, the p-doping was achieved by spin coating a $AuCl_3$ solution which is commonly used in graphene doping due to its large positive reduction potential where $AuCl_4^-$ receives electrons from MoS_2 forming Au aggregates [161][162]. The chemical functionalization of TMDs has also been used as a strategy to reduce both sheet and contact resistances of TMDs-based FETs [142]. An amine-rich polyethylenimine (PEI) solution was used as n-type dopant for multilayered MoS_2-based FETs leading to a 2.6 and 1.2 times reduction in sheet and contact resistance, respectively [155]. Further, K atoms were used to degenerately n-dope the source and drain contact regions of few-layered MoS_2- and WSe_2-based FETs under vacuum, thus achieving low contact resistances [148]. In particular, the K-doped n-type WSe_2 FETs exhibited higher mobility than previously reported p-type WSe_2 FETs.

2.8. CONCLUSIONS

Despite layered transition metal dichalcogenides (TMDs) compounds have been known and studied for decades, the properties and applications of 2D atomically thin TMDs are a relatively new, exciting and rapidly expanding research area. Monolayered TMDs are three-atom thick materials with extraordinaire physical properties arising from their reduced dimensionality, and they have attracted great attention as emerging post-graphene materials. In particular, individual layers of group VI-transition metals (Mo and W) sulfides and selenides present direct band-gap in the visible-near IR range, carrier mobilities up to 1020$cm^2V^{-1}s^{-1}$, on/off ratios of $>10^7$ and exhibit elastic behaviour up to strains of ~20% while preserving electrical and photoluminescence properties. Therefore, they are promising channel materials for FETs, while atomically thin TMDs-based p-n diodes can potentially lead to the development of flexible and transparent optoelectronic devices for light harvesting, emission and detection.

Careful selection of dopant atoms, their concentration and doping strategy can significantly modify the properties of TMDs, altering the intrinsic n-type semiconducting behaviour to p-type (Nb), introducing magnetic characteristics (Mn, Fe, Co, Cu), stabilizing octahedral symmetry or fullerene-like structures (Re), improving the wear resistance of thin films (Ti, Zr) and enhancing catalytic activities for hydrogen evolution (V, Re), hydrodesulfurization (Co) and reduction of carbon dioxide to methanol (Co) [16]. Chemical functionalization of TMDs typically conducted with metal nanoparticles or organic molecules has also been explored as a simple and efficient route to achieve electronic and optical modulation and practical p-n junctions [142].

3) VAPOUR PHASE SYNTHESIS OF WS_2: LITERATURE REVIEW

3.1. INTRODUCTION

While mono- and few-layered MoS_2 have been intensively studied in recent years due to the availability of MoS_2 as natural crystal, research on atomically thin tungsten-based TMDs (WS_2, WSe_2 and WTe_2) started relatively more recently due to the lack of natural crystals. Thus the synthesis of these materials is becoming more demanding in the light of their numerous potential applications. Bulk WS_2 is an indirect band-gap (~1.3eV) semiconductor which can present the 2H, 3R and 1T type structure [18] [163][164], 2H being the thermodynamically stable polytype. WS_2 nanomaterials (such as nanowires) are known to be efficient dry lubricants and they have been investigated in the past decades for catalytic applications, lithium ion batteries, scanning probe microscopy, as shock absorbers and solar cell active materials [164]. Atomically-thin WS_2 is found as n-type semiconductor (due to the numerous S vacancies) with a direct band-gap [4][165][166] and it has revealed superior optoelectronic properties compared to MoS_2 and higher chemical stability than WSe_2 and $MoSe_2$. In particular, WS_2 presents light emission in the monolayered form at ~2eV and it has shown intensities up to 50 times higher than MoS_2 [167]. Further, suspended monolayered WS_2, as well as monolayers deposited onto hexagonal boron nitride (h-BN), show significantly higher PL intensity [2][168]. This because suspended samples are not affected by charge trapping by the substrate and h-BN is a layered compound without dangling bonds. Therefore, as also observed for graphene/h-BN systems [169], h-BN does not affect the charge carrier distribution at its interface. However, the PL quantum yield measured so far in 2D TMDs is still limited to less than 10% [6]. The cause is not yet clear and it could be due to the presence of intrinsic defects [170] such as S vacancies which may suppress exciton formation and/or its radiative recombination, the atomically thin

nature of these materials [171] and their electronic band structure [172]. PL enhancement of MoS_2 has recently been demonstrated through defect engineering and oxygen bonding, exploiting the Purcell effect with photonic crystals and plasmonic nanostructures [173]. PL maps have revealed that the enhancement occurs at the defect sites and it is attributed to the oxygen bonding inducing heavy p doping and to a high quantum efficiency of the excitons due to the suppression of non-radiative recombination at defect sites. In particular, monolayered WS_2 shows photoluminescence efficiency limited to ~2-6% [167][174] [175] as due to defect-mediated non-radiative recombination centres [176] while light emitting devices have been demonstrated [177][178] with external quantum efficiency up to 10% [179].

Another important difference between WS_2 and MoS_2 is the larger amplitude of the spin-orbit-induced electronic band splitting in WS_2 (up to 0.45eV) due to the different size of the transition metal elements [6][12]. Further, the valley index is another property of charge carriers that can be exploited in TMDs and it refers to the confinement of electrons or holes in distinct conduction-band minima or valence band maxima with same energies and different positions in the momentum space [19]. Remarkably, it has been shown that the split spins at the time-reversed K and K' valleys in monolayered WS_2 have opposite signs and such spin-valley coupling can offer an extra degree of freedom to the charge carriers [173]. Therefore, the distinctively larger spin-orbit splitting and spin-valley coupling in WS_2, along with the lack of inversion symmetry in the monolayered form, allow for optical access to the valley degrees of freedom. Room temperature valley-selective circular dichroism has been recently observed in mono-layered WS_2 through circularly polarized PL (where the incident light was fixed as left-handed circularly polarized, whereas the emitting light was selectively collected from left- and right-handed circularly polarized) revealing a remarkable non-equilibrium charge carrier imbalance at the two valleys [173] [180]. These spin-orbit and valley properties, which are not observed in other two-dimensional materials such as graphene which is centrosymmetric and possesses a very weak spin-orbit interaction due to the low mass of carbon, offer a promising future for WS_2 in next-generation nanoelectronics, optoelectronics, spintronics and valleytronics. Finally, WS_2 has also become increasingly interesting for its catalytic properties in its metallic polymorphic phase [181] and piezoelectricity in the single-layered form [50].

The bottleneck of any envisioned application is the scalable synthesis of materials with high crystal and optical quality over wafer-size areas. Therefore, traditional synthesis methods of bulk semi-

conductors developed during the 1970s and 1980s have recently undergone a resurgence of research interest [24]. Physical vapour deposition (PVD), chemical vapour deposition (CVD) and metal organic chemical vapour deposition (MOCVD) have been rediscovered to achieve atomically thin TMDs. As previously shown from graphene, the CVD synthesis has emerged as a scalable method for the synthesis of high-quality and large-area material and it is widely employed for TMDs [182]. However, the CVD of WS_2 is still at the early stages of development, generally leading to sparse flakes of lateral size between 5-40μm [4][173][183][184][185][186][187]. The synthesis of a continuous WS_2 layer over centimeter-sized areas has been reported only in a very few cases [188][189] and at the expenses of the material quality. The CVD synthesis of WS_2 is typically carried out by co-evaporating a W precursor and sulphur powders in a horizontal tubular furnace in presence of a carrier gas and it has been achieved predominantly using tungsten oxide (WO_3) as metal precursor. Therefore, the CVD synthesis of high-quality and large-area monolayered WS_2 crystals still remains an experimental challenge and it is even more challenging than the CVD synthesis of MoS_2 because of the higher melting points of the W precursors compared to the Mo precursor counterparts.

In this chapter we review the tremendous progress that has been achieved in the synthesis of WS_2 and metal-doped WS_2 from bulk crystals to single layered form. Further, we demonstrate how the growth of bulk crystals developed during the 1970s and 1980s has led to the identification of physical-chemical mechanisms underlying the formation of TMDs which are still currently exploited to achieve synthesis of high quality atomically thin material [24]. The chapter is structured in five sections:

(1) Bulk single crystal growth by chemical vapour transport;

(2) Chemical vapour deposition of thin films from metal-organic precursors;

(3) Chalcogenization of pre-deposited transition metal-containing thin films (metal, metal oxide);

(4) Vapour phase reaction of transition metals and chalcogen precursors (in powder form and gas form);

(5) Vapour phase synthesis of metal-doped WS_2.

3.2. BULK SINGLE CRYSTAL GROWTH BY CHEMICAL VAPOUR TRANSPORT

The first syntheses of bulk crystals of Sn- and Ge-based chalcogenides have been achieved from molten compounds by using the Czochralski, Kyropoulos and Bridgman methods [24][190]. Nevertheless, this synthetic approach is not suitable for growing W and Mo sulphides and selenides due to the very high melting temperatures of W and Mo [24]. Therefore, alternative methods involving the evaporation of elemental precursors started to be investigated. They are known as chemical vapour transport (CVT) methods [24][191]. The CVT synthesis of TMDs has been studied in both open and closed systems [24]. In the open-configuration, the precursors in powder form are loaded in a tube made of quartz or ceramic with both ends unsealed and a temperature gradient is applied between the two ends of the tube [24]. The precursors are then evaporated at high temperatures under a continuous flux of a carrier gas or transport agent at one end and they deposit in the lower temperature-zone at the opposite end of the tube [24]. This open system-method has been soon abandoned in favour of closed system-methods as a high level of contamination was introduced [24]. The use of a closed-configuration has offered higher crystal quality, better control over the synthesis conditions and it allowed for the use of much smaller amounts of carrier gas [24][191]. A typical closed CVT system consists in a sealed and evacuated quartz ampoule (enclosure) containing transition metal powders and chalcogen pellets [24][192] (Fig. 3.1). A temperature gradient is then applied at the extremities of the enclosure, leading to the evaporation of the precursors at one end and to the deposition of the chalcogenide crystal at the opposite end [24][193][194]. The growth is carried out over different time lengths ranging from a few days to two weeks [24]. According to Le Chaterlier's principle, exothermic transport reactions lead to the transfer of the solid to the zone of higher temperature while endothermic reactions transport the material to the cooler zone [24]. A considerable advantage of this closed-system method is that small amounts of transport agent (generally I_2) can transport large amounts of precursors, because it can diffuse back in the enclosure to pick up more material [24].

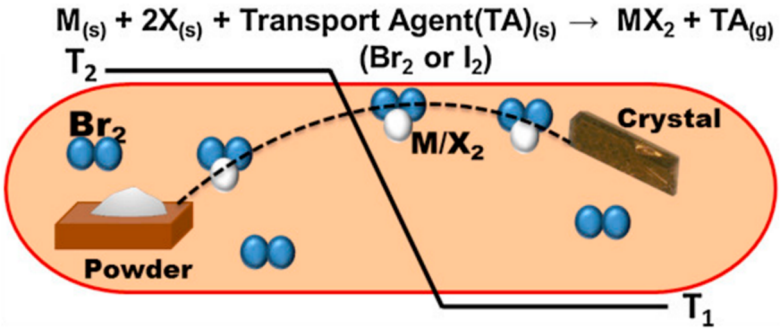


Figure 3.1 *Schematic showing bulk single crystal synthesis by CVT, where powders of the metal M and chalcogen X precursors are mixed with a transport agent (I_2 or Br_2) which assists the vaporization of the elements at the source zone and the material crystallization at the sink zone. The extremities of the enclosure are subjected to a temperature gradient throughout the process. Adapted from Ref. [24].*

In the attempt to build a growth model capable of guiding the choice of the synthesis parameters, the CVT synthesis of bulk single crystals in an enclosure has been investigated analytically [24]. The model assumes that the yield of a transport reaction is identified by the mass of material transported per unit time ($\dot{m}=dm/dt$) from the vaporization zone (source) to the crystallization zone (sink) [24][195]. The so-defined $\dot{m}$ can be expressed as a product of two quantities: the chemical potential difference between the two extremities of the enclosure (Δp) and the conductance of the system (L), which is described as the rate of vapour transport between the two ends [24][195]. Δp is a function of the chemical parameters of the system and it is proportional to the difference in vapour pressure of the transporter at the two ends of the ampoule [24][195]. While L is a function of both the geometrical parameters of the system and the physical nature of the vapour-transport mechanism: diffusion, convection or laminar flow [24][195]. Since these three transport mechanisms can coexist, L (and thus $\dot{m}$) cannot easily be represented by an analytical expression [24][195]. However, since the geometrical parameters of the system are fixed, L does not vary much if related reactions are compared and thus qualitative estimations of the parameter $\dot{m}$ have been obtained by calculating only Δp [24][195]. It has then been concluded that $\dot{m}$ must not exceed a certain maximum value otherwise the crystal growing seeds cannot digest excess precursors arriving at the sink [24][195]. Also, $\dot{m}$ must increase in a controlled manner during the process as a growing crystal requires a rising intake of new atoms while expanding its surface area [24][195]. To achieve this, the transport agent plays a major role and it has been experimentally observed that a strong transport effect

is brought by halogen gases and in particular I_2. While Br_2 gives much smaller $\dot{m}$ values and Cl_2 showed no transport at all [24][195].

This phenomenological model of single crystal growth has guided the optimization of growth conditions such as the dimensions of the enclosure, the temperature gradient, and the nature and amount of the transport agent [24][196]. This has led to the synthesis of WS_2, WSe_2, WTe_2, MoS_2, $MoSe_2$, $MoTe_2$ single crystals using their respective polycrystalline compounds as precursors and different chalcogens, halogens and other compounds as transport agents [24][191][196][197][198][199][200][201][202][203][204][205].

The CVT enclosure method is still used nowadays to synthesize TMDs bulk single crystals (Fig. 3.2) which are then mechanically exfoliated to access single-layered flakes [24][27][206][207]. CVTs methods have been recently applied to grow single crystals of $MoTe_2$, $MoSe_2$ and ReS_2 (which belongs to the group VII of TMDs) [24][208][209][210] and Mo and Ta dichalcogenides MX_2 (M=Mo, Ta and X=S, Se, Te) [24][211]. The latter have been achieved using an alternative chloride-driven CVT method which involves the addition of metal chlorides ($MoCl_5$, $TaCl_5$) in the enclosure [211]. These compounds have high vapour pressure and thus they can provide a high partial pressure of metallic molecular species in the reaction atmosphere [24][211]. Further, hydroxide species of tungsten and molybdenum (H_2WO_4, H_2MoO_4) have shown to be volatile and to facilitate the transport of the metal precursors [24][212][213].

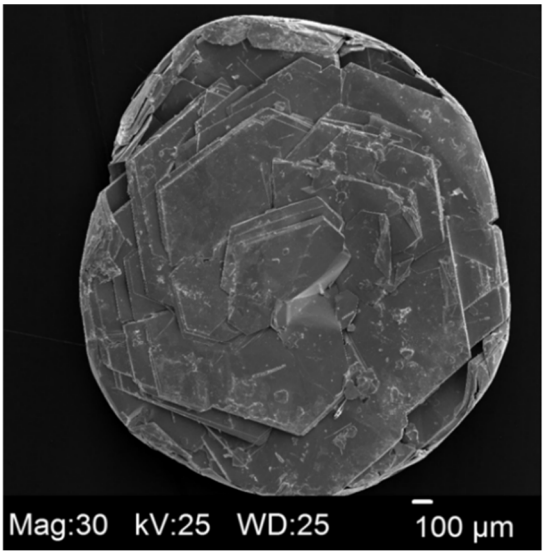


Figure 3.2 *SEM image of a single crystal of WS_2 synthesized via CVT for mechanical exfoliation. The crystal measures ~3mm x 3mm in lateral dimensions. Adapted from http://www.2spi.com.*

3.3. VAPOUR PHASE SYNTHESIS OF ATOMICALLY THIN WS_2

Any CVD process relies on the choice of the most suitable chemical precursors. Thus, before discussing the CVD synthesis of atomically thin WS_2, we first present a short discussion on the different precursors available, comparing their characteristics. CVD is currently the most widely used method to achieve atomically thin TMDs and it was first developed for the synthesis of thin films of pure W and Mo metals [24]. The two classes of precursors most extensively used were hexacarbonyls and halides due to their low decomposition temperatures [24]. W and Mo hexacarbonyls are known to stabilize a zero oxidation state of the metals and their stability increases descending the triad of the transition metals [W>Mo>Cr] [24][214]. This implies that to be able to form WS_2, where W is in the oxidation state (IV), the metal has to be oxidized [24][214]. In particular, $W(CO)_6$ and $Mo(CO)_6$ are stable in air and decompose at 230°C (with vapour pressure of 1Torr at 65°C) and 180°C, respectively [24][215]. However, it has been shown that carbon and oxygen contamination can be found in CVD-grown W thin films deposited at temperatures above 700°C, with a concentration critically depending on the CO decomposition reaction ($2CO \rightarrow CO_2+C$) and the interplay between CO and CO_2 [24][215]. It is worth noting that several other organometallic compounds of W (Mo) have been developed during the '70-'90 (such as Bis(arene) tungsten compounds, Tris(butadiene) tungsten, Tetraallyltungsten) presenting even lower decomposition temperature than hexacarbonyl precursors (typically below 190°C) and higher volatility (vapour pressure typically around 1Torr at 100°C) [24][215]. However, these compounds often lead to a larger amount of C and O impurities incorporated into the W films compared to hexacarbonyls and they have not been explored yet as W precursors for the CVD synthesis of WS_2 [24]. Halides compounds such as WF_6, WCl_6, WBr_6 (MoF_6, $MoCl_6$, $MoBr_6$) have been used in the microelectronic industry since more than four decades and present adequately high vapour pressure to be used as metal precursors in the CVD of WS_2 (MoS_2) [24][215]. However, the oxidation state of the metal atoms is VI in these compounds, and thus it has to be reduced to IV in order to form the disulphide [24]. Further, their decomposition typically requires high temperatures and the presence of a reducing agent such H_2 of H_2S [24]. In particular, WF_6 is a gas which decomposes above 750°C or at lower temperatures in the presence of a reducing agent (H_2, Si, SiH_4)

[24][215]. However, WF_6 releases HF upon decomposing, which is highly corrosive for the CVD system and growth substrate [24]:

$WF_{6\,(g)} + 3H_{2\,(g)} \rightarrow 6HF_{\,(g)} + W_{\,(s)}$

While WCl_6 is a solid which vaporizes at 346°C under atmospheric pressure, easily sublimes at 150°C under vacuum and decomposes at temperatures between 600-900°C in presence of H_2, releasing HCl as reaction product, which is much less corrosive than HF [24][215].

$WCl_{6\,(s)} + 3H_{2\,(g)} \rightarrow 6HCl_{\,(g)} + W_{\,(s)}$

However, WCl_6 is a solid at room temperature (typically in powder form) and its vapour pressure is much lower than WF_6, which makes more difficult to control its evaporation and decomposition rate [24][215]. It is worth noting that WCl_6 (with H_2 as carrier gas) has been the first W precursor used to deposit W films back in 1855 [24][215]. Finally, WBr_6 has also been used in a very few cases for the CVD growth of highly pure, dense and uniform W films [24][215].

The sulfurization/selenization of WO_3 and MoO_3 thin films established during the '80 has led to a recent wide use of the oxide powders as metal precursors for the CVD of WS_2/WSe_2 and MoS_2/$MoSe_2$, due to easy handling, effective replacement of O by S and low toxicity compared to organometallic/halides precursors [24][184][216]. However, WO_3 sublimes at temperatures above 750°C and its vapour pressure is very low, requiring the use of high growth temperatures to synthesize WS_2 [24]. Further, the oxidation state of W in WO_3 is VI and therefore a reducing agents is often needed for its reduction to IV [24]. The suggested reaction mechanism for the synthesis of WS_2 from WO_3 is [24][217]:

$2WO_{3\,(s)} + (7/2)\ S_{2\,(g)} \rightarrow 2WS_{2\,(s)} + 3SO_{2\,(g)}$

It is worth noting that MoO_3 is more volatile than WO_3 and it has higher vapour pressure (it evaporates at 500°C in vacuum). These characteristics have enabled the synthesis of MoS_2 at much lower temperatures than those required for WS_2, allowing for increasing work on the synthesis of this material as compared to W-based compounds (WS_2 and WSe_2) [24].

To summarize, tungsten hexacarbonyl has higher volatility than tungsten-halides (except for WF_6), presents low thermal stability, decomposes at low temperatures and releases non-corrosive byproducts, allowing for the synthesis of WS_2 at temperatures lower than 300°C [24]. However, it can lead to C and O incorporation in the final growth product [24]. On the other hand, tungsten-halides precursors lead to

highly pure WS_2 films but they release highly corrosive byproducts [24]. Finally, sulfurization of tungsten trioxide requires high temperatures and it can potentially lead to a complete conversion to WS_2 with least concentration of impurities. Currently, it is the most widely investigated synthesis route for atomically thin WS_2 [24].

3.3.1. CVD OF WS_2 THIN FILMS FROM METAL-ORGANIC PRECURSORS

The MOCVD of WS_2 films has been obtained by the reaction of solid $W(CO)_6$ with gaseous H_2S [24] [218]:

$$W(CO)_{6\,(s)} + 2H_2S_{\,(g)} \rightarrow WS_{2\,(s)} + 6CO_{\,(g)} + 2H_{2\,(g)}$$

where $W(CO)_6$ was chosen as metal precursor due to its easy handling and pyrolysis into molecules at low temperatures [24][218]. A vertical cylindrical reactor equipped with a gas-inlet funnel and a substrate holder and heater was used to generate asymmetric three-dimensional flow patterns with no azimuthal gradients, resulting in WS_2 films with good surface uniformity [24][218]. $W(CO)_6$ was evaporated in a heated-bubbler while H_2S gas was inlet at pressures between 7×10^3Pa and 4.2×10^4Pa [24][218]. It has been demonstrated that heating $W(CO)_6$ and the substrate at 70°C and 420°C, respectively, under a growth pressure of 100Torr, lead to the best growth results [24][218]. Figure 3.3*a* shows a bright-field TEM image of an as-grown free-standing WS_2 thin film with a thickness of ~65nm, revealing the presence of vertically oriented platelets (darker areas) which has been also confirmed by SEM imaging (Fig. 3.3*b*) [24][218].

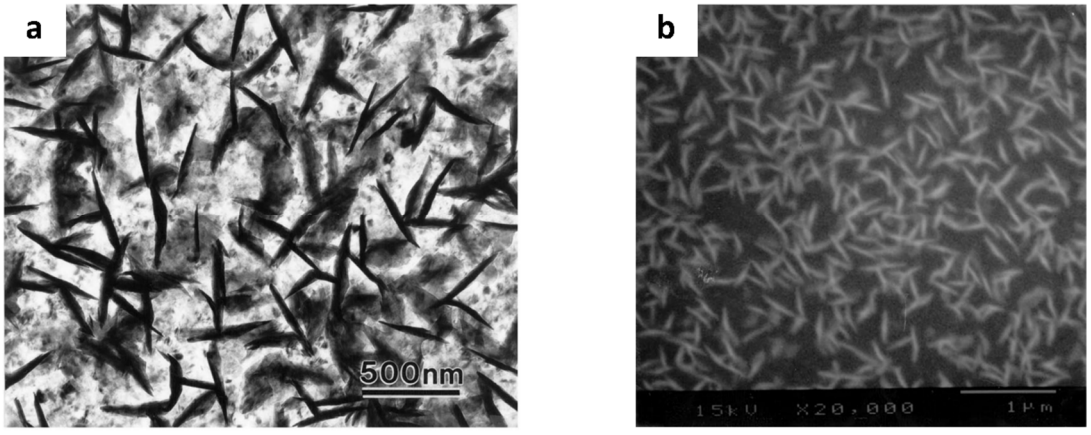


Figure 3.3 *(a) Plan-view bright-field TEM image and (b) SEM surface analysis of a WS_2 thin film with average thickness of 65nm. Adapted from Ref. [218].*

3.3.2. CHALCOGENIZATION OF PRE-DEPOSITED METAL-CONTAINING THIN FILMS

3.3.2.1. CHALCOGENIZATION OF A PRE-DEPOSITED METAL THIN FILM

A simple way to synthesize atomically thin TMDs films is a two step-CVD process in which an ultrathin transition metal film is first deposited onto a substrate and then converted into the corresponding TMD compound by exposure to chalcogen vapours (Fig. 3.4) [24]. Films of tungsten and molybdenum have been deposited onto dielectric (SiO_2/Si, MgO) or epitaxial substrates (sapphire) by different techniques, such as electron beam evaporation and magnetron sputtering [24][25][219][220][221][222]. Typically, the coated substrate is then loaded in a tubular furnace together with chalcogen powders and heated up to 550-800°C under a chalcogen-rich atmosphere [24][25][219][220][221][222][223].

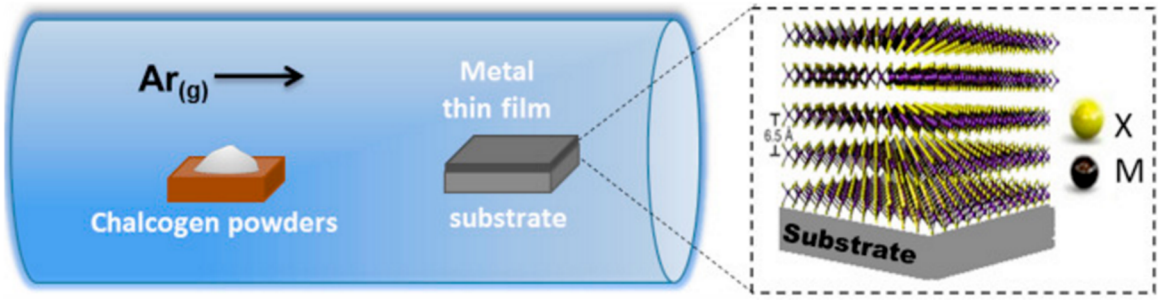


Figure 3.4 *Schematic showing the vapour phase synthesis of atomically thin TMDs by chalcogenization (via S/Se/Te) of pre-deposited transition metal-containing (metal or metal oxide) thin films. Adapted from Ref. [24].*

In particular, mono- to few-layered polycrystalline WS_2 films with grain size ranging from 50 to 200nm have been obtained by sulfurization of ultrathin (~1-5nm) tungsten films which were pre-deposited via magnetron sputtering onto MgO (Fig. 3.5) [24][220]. Remarkably, ~1nm thick-W films did not lead to significant clustering after sulfurization, suggesting that they are directly converted into WS_2 films via chemical reaction and that their surface energy is not high enough for the metal atoms to aggregate into islands (as observed in the case of MoS_2) [24][220]. This is attributed to the high melting temperature of W, which is much higher than the sulfurization temperature (800°C), preventing the self-diffusion of W atoms [24][220]. Further, although the crystalline MgO substrates display atomically thin terraces, the resulting WS_2 domains appear to grow continuously across the steps (Fig. 3.5*a*), similarly to

the growth of graphene across the grain boundaries of a polycrystalline substrate [224] and of monolayered MoS_2 on a stepped sapphire substrate [220][225]. Finally, some WS_2 domains show a triangular and butterfly-like shape, indicating that upon sulfurization of ultrathin W films, the WS_2 species arrange in triangular shapes to minimize the surface free energy (Fig. 3.5*b*) [220].

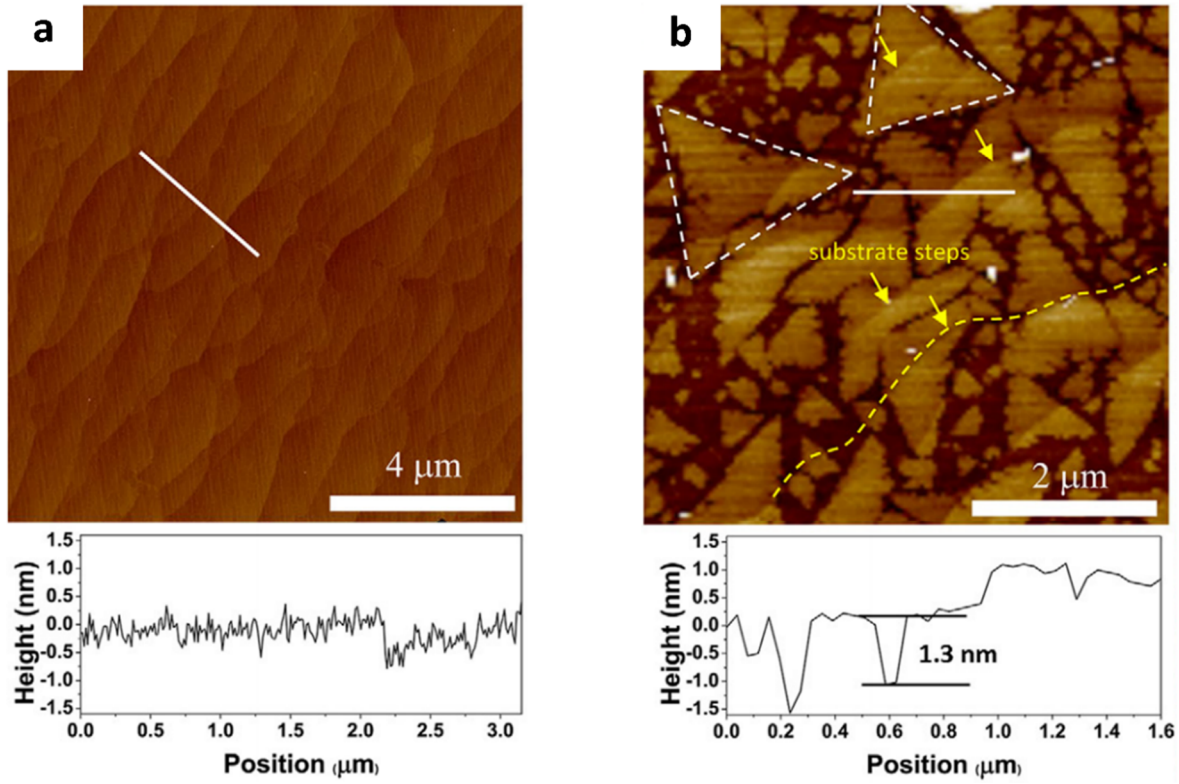


Figure 3.5 *(a) AFM image of a ~1nm-thick W film sputtered onto an MgO substrate. The morphology of the sputtered W film conforms very well to the substrate and reflects its atomic steps. The surface of the film is very smooth and the step height ranges from less than a nanometre to a few nanometres. (b) AFM image showing WS_2 islands with a triangular and butterfly shape grown across the step edges of the MgO substrate. Yellow arrows and dotted line indicate the steps. Adapted from Ref. [220].*

3.3.2.2. CHALCOGENIZATION OF A PRE-DEPOSITED METAL OXIDE THIN FILM

Metal oxide thin films have been extensively used as alternative metal precursors for the synthesis of atomically thin TMDs due to their lower decomposition temperature as compared to their metal counter-parts [4][24][173][226][227][228]. WO_3 and MoO_3 thin films have been deposited through evaporation

or sputtering of the corresponding metals, followed by thermal oxidation [4][24][173][226][227][228]. Overall, the synthesis process is very similar to the chalcogenization of pure metal films described in the previous section: the MO_3-coated substrate is converted into MX_2-coated substrate (M=W, Mo and X=S, Se, Te) in a tubular furnace under a chalcogen-rich atmosphere generated from evaporation of S, Se and Te powders or H_2S [4][24][173][226][227][228].

In particular, synthesis of single- and few-layered WS_2 microplatelets with triangular morphologies has been achieved by means of sulfurization of ultrathin WO_3 films (Fig. 3.6*a*) [4][24]. 5-20Å-thick WO_3 films were thermally deposited on SiO_2/Si substrates in a high-vacuum chamber (10^{-5}-10^{-6}Torr) [4]. The sulfurization process was carried out at atmospheric pressure under Ar gas flowing at 100-500sccm in a quartz tubular furnace [4]. The WO_3-coated substrates were kept at 800°C for 30min and S vapours were generated from S powders placed in the upstream zone of the reactor which was kept at a lower temperature (~250°C) [4]. The thinnest WO_3 films (5-10Å) led to the formation of WS_2 triangular islands with lateral size ranging from hundreds of nanometers to a few micrometers (Fig. 3.6*a*) [4]. It has been proposed that the WS_2 islands may nucleate upon sulfurization of WO_3 clusters and then grow laterally as W and S species diffuse on the substrate [4]. Further, the lateral growth could eventually result from coalescence of neighbouring islands with different orientation, thus yielding to the observed morphologic variety of WS_2 domains (Fig. 3.6a) [4]. The synthesis of large-area (~cm^2) single-, bi- and few-layered WS_2 films using the two-step thermal reduction-sulfurization method has also been reported (Fig. 3.6*b*) [24][173]. Tungsten oxide was thermally evaporated and deposited on Si/SiO_2 substrates at low pressures (10^{-5}-10^{-6}Torr) in the form of WO_x 1-18nm-thick films [173]. The so-coated substrates were then loaded into a tubular furnace and sulfurized at 750-950°C for 30min under vacuum (450mTorr) and Ar gas [173]. The S powders-containing crucible was loaded in the upstream zone of the quartz tube outside the furnace, which was wrapped around with a heating belt and heated to 200°C [173].

To summarize, the chalcogenization of metal and metal oxide thin films deposited onto a substrate by evaporation or sputtering has led to TMDs thin films across wafer-scale areas [24]. However, the main limitation of this two-step process is the lack of a precise control over the thickness of the metal or metal oxide films and difficulties in reaching an atomically thin thickness, which is a pre-requisite for the atomically thin growth of TMDs [24].

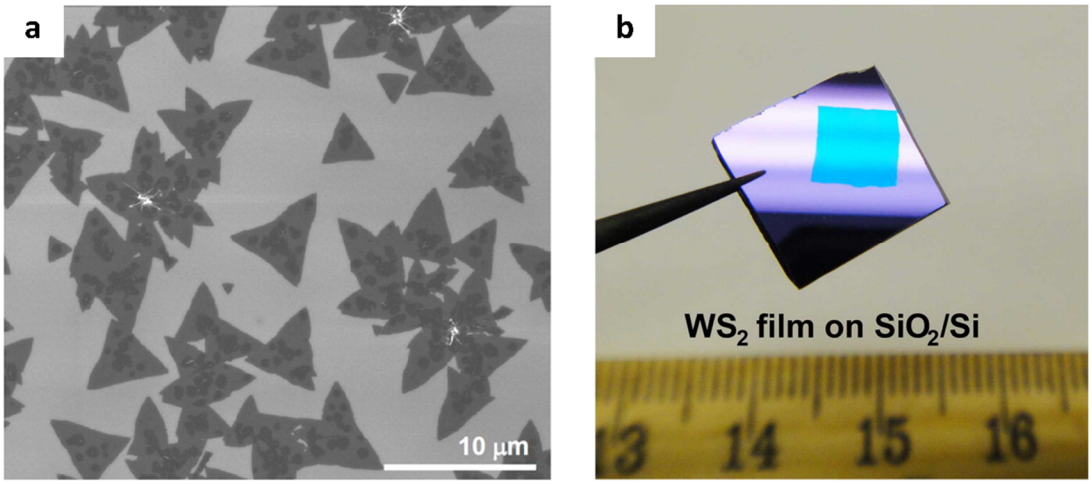


Figure 3.6 *(a) SEM image of small triangular and star-like shaped WS_2 monolayers onto SiO_2/Si. The dark contrast-spots on top of the flakes are WS_2 second-layers in an early stage of growth. Adapted from Ref. [4]. (b) Photograph of a transferred WS_2 thin film onto a SiO_2/Si substrate (the film appears in a cyan colour upon contrast with the SiO_2). Adapted from Ref. [173].*

A significant progress in this direction has recently been achieved by depositing metal oxide layers via atomic layer deposition (ALD) [24][229][230][231][232][233][234]. In the ALD process the precursors are delivered separately into the growth chamber and, if the substrate surface is sufficiently reactive to the precursors and does not bind itself, the thickness of the deposited layers can be tailored by defining the number of precursor's injection cycles [24]. Thin films of WO_3 with controlled layer number over mm-size areas have been deposited by ALD using $W(CO)_6$ and WF_6 as W precursors [24] [230][231] [232][233]. Further, a newly synthesized W precursor $WH_2(iPrCp)_2$ has recently led to the deposition of single-layered WO_3 films and consequent formation of monolayered WS_2 nanosheets with high crystal quality and field effect electron mobility (~3.9$cm^2\,V^{-1}s^{-1}$) comparable to reported values for CVD-grown WS_2 [24][234]. However, the limited availability of this precursor and its non-wettability to hydrophobic substrates may limit a widespread use [24][234]. To conclude, the synthesis of atomically thin WS_2 via chalcogenization of pre-deposited W-containing ultrathin films (W, WO_3) is an effective approach for preparing large-areas few-layered WS_2 films [24] [43][44]. Nevertheless, the synthesis of monolayered WS_2 films with wafer-level uniformity has not yet been achieved due to the non-uniform conversion of W or WO_3 layers into WS_2 [24][43][44]. Furthermore, the WS_2 films are polycrystalline with small single crystal domain size (from tens of nanometres to sub microns) [24][43][44].

3.3.3. VAPOUR PHASE REACION OF METAL AND CHALCOGEN PRECURSORS

3.3.3.1. METAL AND CHALCOGEN PRECURSORS POWDERS

In the last few years the most extensively used method to synthesize atomically thin TMDs consisted in the simultaneous evaporation of transition metal oxide and chalcogen powders (Fig. 3.7) [24][43][167][180][183][216][225][235][236][237][238][239][240][241][242][243]. On the contrary to the two-step CVD techniques described in the previous sections, this single-step route allowed for the synthesis of high-quality monolayered WS_2 with grain sizes up to millimeters [24][183]. However, since the W and S precursors have significantly different vapour pressures, one of the main challenges of this approach is the controlled evaporation and deposition of both precursors onto the growth substrates, often limited by the quick exhaustion of sulphur which readily evaporates at low temperatures (100-150°C) [24][235]. Therefore, overall this method presents poor reproducibility and has led to WS_2 films which are continuous across mm-size areas in a very few cases and at the expenses of the material quality [24][188][189].

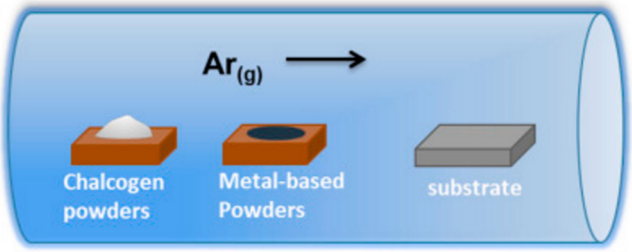


Figure 3.7 *Schematic showing the CVD synthesis of atomically thin TMDs by vapour phase reaction of transition metal and chalcogen precursors supplied from powders. Adapted from Ref. [24].*

Typically, WO_3 powders (~0.5-1g) and S powders (~0.5-1g) are placed in two distinct crucibles loaded in the correspondence of the low- and high-temperature zones of a CVD tubular furnace, respectively [24][43][44]. As the S evaporation temperature is significantly lower (100-150°C) than the W precursors vaporization temperature and growth temperature, two independently controlled heaters are typically used [24][43][44]. Compared to MoO_3, which is usually heated up to 500-750°C for the synthesis of MoS_2, WO_3 is evaporated at significantly higher temperatures in the range of 800-1070°C [24][43][44]. At these temperatures WO_3 forms suboxide species (WO_{3-x}) which then reacts with S vapours to form WS_2 [184]:

$$2WO_{3\,(s)} + 7S_{\,(s)} \rightarrow 2WS_{2\,(s)} + 3SO_{2\,(g)}$$

In contrast to the synthesis of selenides where H_2 gas is commonly used as reducing agent to reduce the metal oxides to suboxides species [244], WS_2 is normally grown under inert Ar or N_2 atmosphere due to the higher reactivity of S in reducing WO_3 as compared to Se [24][43][44]. Nevertheless, it has been shown that the addition of H_2 in the reaction chamber can still tailor the shape of WS_2 monolayers from jagged to straight edged-triangles [184]. It has been suggested that H_2 can promote the reduction of WO_3 either directly or through the formation of H_2S, thus creating a WO_{3-x}-rich environment for the synthesis of WS_2 [24][184]:

$WO_{3\ (s)} + 3S_{\ (s)} + H_{2\ (g)} \rightarrow WS_{2\ (s)} + SO_{2\ (g)} + H_2O_{\ (g)}$

Overall, the CVD of WS_2 is particularly challenging due to the high sublimation temperature of the WO_3 powders [24][43][44] [245]. Synthesis at both atmospheric and low pressures (1-500Torr) have been reported [24][43][44], where the low-pressure (~1Torr) growth condition is expected to aid the volatilization and diffusion of suboxide species and prevent the deposition of particulate material, thus leading to uniform nucleation [24][245]. However, the synthesis of high-quality WS_2 at atmospheric pressure has recently been demonstrated by using alkali metal halides (MX, M=Na, K; X=Cl, Br, I) as growth promoters [24][245]. The presence of the metal halides allowed for the atmospheric pressure-growth of monolayered WS_2 at temperatures as low as 825-850°C due to chemical reactions between tungsten oxide and the halide species with formation of volatile tungsten-oxyhalide species [24][245]. As discussed in Section 3.2, halogen molecules such as Cl_2, I_2 and Br_2 have been extensively used as transport agents in the growth of WS_2 bulk crystals via chemical vapour transport due to their reactivity with metal oxides to form oxyhalide species with much lower melting point than the oxides [24][191]. Finally, the synthesis of small (~3μm) WS_2 domains has also been demonstrated by using volatile W precursors such as WCl_6 along with S powders [24][246]. In the following we review the recent advances in the CVD synthesis of atomically thin WS_2 from W precursors (WO_3, WCl_6) and sulphur powders. We summarize the main advances in terms of:

- Strategies to enable controlled nucleation of WS_2;

- Strategies to optimize crystal quality;

- Strategies to enable large-area deposition of monolayered WS_2 films;

- Strategies to optimize the materials chemical purity and facilitate nucleation and lateral size of monolayered WS_2.

Strategies to enable controlled nucleation of WS_2

Lee et al. have demonstrated the ambient-pressure CVD synthesis of mono- and few-layered WS_2 onto various surfaces with the seeding of perylene-3,4,9,10-tetracarboxylic acid tetrapotassium salt (PTAS) which has good thermal stability and slow decomposition rate at temperatures below 820°C [187]. The growth of WS_2 triangular crystals was achieved onto crystalline and amorphous substrates (sapphire, quartz, silicon) and on surfaces with different morphologies (micron-sized Si particles, cleaved side-wall of Si substrates, aggregation of TiO_2 nanoparticles). WO_3 (1g) and S (0.015g) powders were loaded at the centre and upstream zones of a quartz tubular furnace (Fig. 3.8*a*). Prior to the growth, a droplet of aqueous PTAS solution was spun onto the surfaces of the various substrates and a gentle gas blow enabled the droplet to uniformly precipitate into tiny PTAS seeds. The WS_2 layers were synthesized at 800°C for 5min with a heating rate of 15°C/min and at atmospheric pressure under Ar flow (5sccm). It has been demonstrated that the presence of the PTAS seeds significantly enhances the growth of WS_2 possibly via assisting the adsorption of precursors molecules onto the growth surfaces facing down the WO_3-containing crucible and the initiation of heterogeneous nucleation. This seed-initiated synthesis process has shown significant flexibility to surface corrugations and led to WS_2 crystals with electronic transport and optical performances comparable to exfoliated WS_2 flakes [187]. However, the as-grown WS_2 crystals exhibit a variety of layer number and lateral size smaller than 20μm (Fig. 3.8*b*). Further, the facing-down configuration of the substrates does not allow a uniform and large-area deposition of monolayered WS_2 (Fig. 3.8*c*).

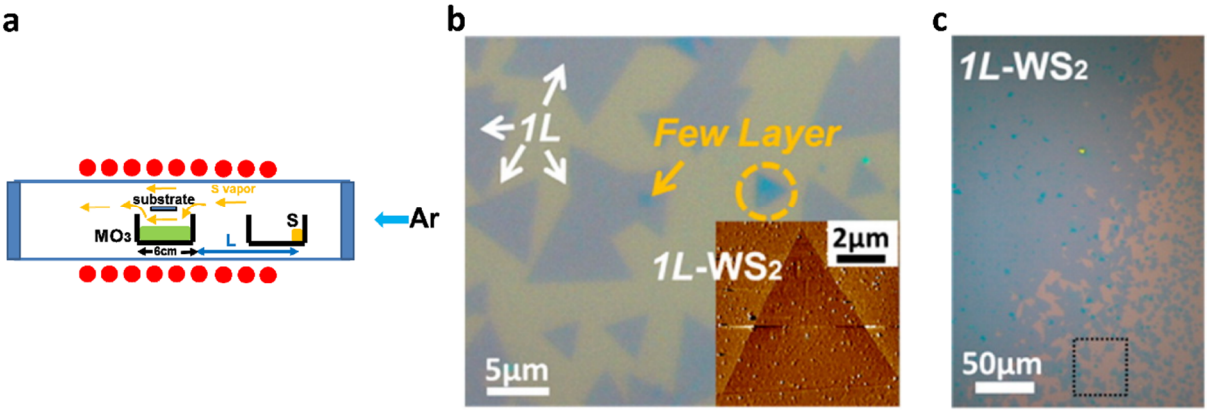


Figure 3.8 *(a) Schematic of the atmospheric pressure-CVD setup used to grow WS_2 flakes onto various surfaces with PTAS seeds. (b) Optical and AFM images of the as-grown mono (1L)- and few-layered WS_2 triangles onto SiO_2/Si. (c) OM image of the edge region of the substrate which shows the highest nucleation density of WS_2 flakes. Adapted from Ref. [187].*

A different approach has been introduced by Zhang et al. who have utilized a crystalline substrate with the aim to obtain controlled orientation of the WS_2 flakes [184]. They have demonstrated the synthesis of mono- and few-layered WS_2 flakes onto sapphire (Al_2O_3) substrates by low-pressure CVD from WO_3 and S. WO_3 powders and Al_2O_3 substrates (<0001>-oriented single crystals) were loaded in the centre of a quartz tubular furnace, whereas S powders were placed outside the hot zone and mildly sublimated at ~100°C using a heating belt (Fig. 3.9*a*). The growth temperature, pressure and time were set to be 900°C, 0.3mbar and 60min, respectively. The lateral size and thickness of the as-grown WS_2 flakes were controlled by adjusting the growth temperature and the substrate-precursors distance. In particular, it has been found that upon increasing the temperature from 880°C to 900°C, the lateral size of the WS_2 flakes increases from ~5μm to ~50μm, while few- vs mono-layered domains are formed onto Al_2O_3 at ~9cm and ~10cm from the initial WO_3 location, respectively. Further, by using a mixture of Ar (80sccm) and H_2 (10sccm) as carrier gas, it has been possible to tailor the shape of the WS_2 crystals from jagged- to straight-edged triangles (Fig. 3.9*b*). Since H_2 is a more effective reducing agent reagent than S, it may promote the reduction of WO_3 either directly or through formation of H_2S, thus generating a WO_{3-x}-rich environment for the formation of WS_2 [184]. However, despite these growth conditions have shown a greater level of control than the previously discussed synthesis of WS_2 from W precursors and S powders [167][180][246], they involve the use of H_2 gas and Al_2O_3 substrates. As Al_2O_3 needs to be dissolved

in order to transfer the grown material onto the desired target substrate, the direct synthesis of WS_2 onto inexpensive and easily dissolvable substrates is preferable for scalability of the CVD process.

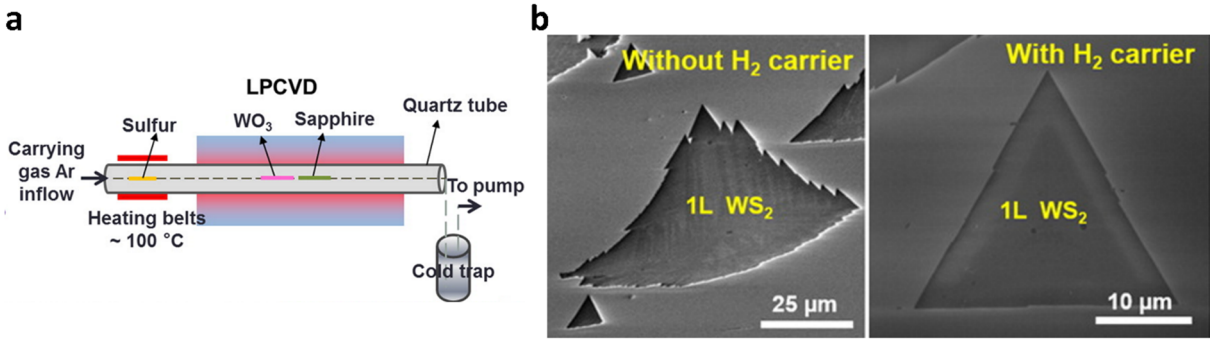


Figure 3.9 *(a) Schematic of the low-pressure CVD setup used for the growth of mono- and few-layered WS_2 onto Al_2O_3 substrates. (b) SEM images of the as-grown WS_2 flakes using Ar and Ar/H_2 as carrier gas. Adapted from Ref. [184].*

Strategies to optimize crystal quality

Peimyoo et al. have reported two CVD growth strategies to obtain monolayered WS_2 flakes from WO_3 and S powders [167]. The first synthesis was obtained by loading 1mg of WO_3 and 200mg of S powders at the centre and upstream zones of a quartz tubular furnace, respectively (Fig. 3.10*a*). The furnace was heated up at a rate of 18°C/min up to 550°C. At this temperature the S powders started to melt due to the heating from the furnace itself. The temperature was then raised up to 800°C with a ramp rate of 5°C/min and held for 10min. Finally, the furnace was naturally cooled down to room temperature under Ar gas (flowing at 200sccm throughout the whole growth process). The second strategy differs from the first in respect to the heating of S powders, which has been carried out independently from the heating of WO_3 by using a heating belt (Fig. 3.10*a*). The first synthesis strategy has led to the formation of WS_2 triangular nuclei with anisotropic PL intensity across an individual nuclei area, while the second strategy has led to flakes with uniform PL intensity across the triangular flakes (Fig. 3.10*b*). The non-uniform PL features observed in the first group of samples, such as PL quenching and blue-shift of the PL peak position in certain areas, is attributed to structural defects due to the unstable supply of sulphur, resulting from the variation of its heating temperature, and to n-doping induced by S vacancies.

Although this work has provided important insight into the PL emission of CVD-grown mono-layered WS_2, the employed synthesis method has led to WS_2 flakes with later size not exceeding 10µm.

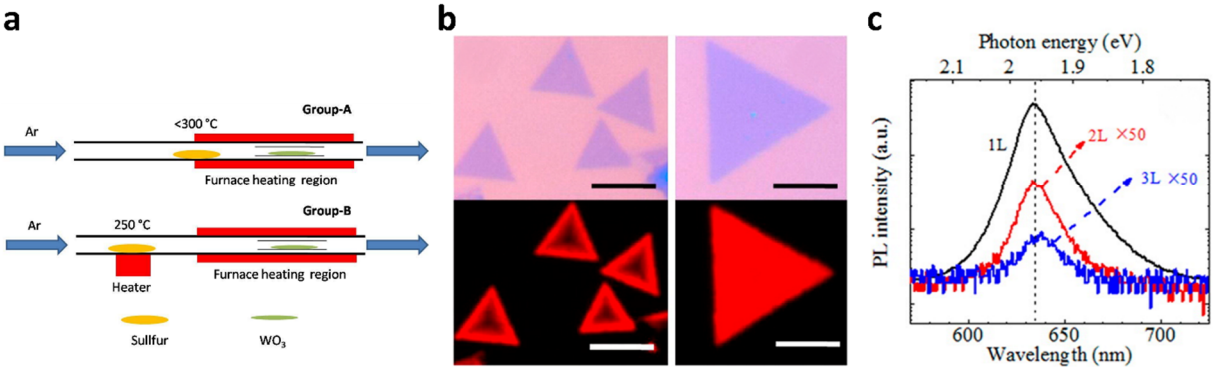


Figure 3.10 *(a) Schematic of the CVD setups used to grow the two groups of WS_2 samples. The indicated temperatures at the S location place were reached when the furnace heating region reached 550°C. (b) Optical images and corresponding fluoresce maps of WS_2 triangles onto Si/SiO_2 from the first (left) and second (right) group (scale bars represent 5µm). (c) PL spectra for single (1L)-, double (2L)- and triple (3L)-layered WS_2. Adapted from Ref. [167].*

Cong et al. have synthetized triangular WS_2 monolayers with lateral size up to hundreds of micro-metres via a one-step sulfurization of WO_3 powders directly spread onto the substrate [180]. This strategy does not involve the pre-deposition of WO_3 thin films in a high-vacuum chamber as per the two-step process described in Section 3.3.2. A well cleaned Si/SiO_2 substrate was sequentially covered with 1mg of WO_3 powders and then with a second piece of blank Si/SiO_2 placed face-down above the bottom substrate. In the attempt to effectively increase the concentration and pressure of S vapours for the growth of WS_2, the sandwiched WO_3 powders were placed together with 100mg of S powders into a small-diameter one-ended sealed quartz tube, which was then loaded into a standard big-diameter quartz tubular furnace (Fig. 3.11*a*). The furnace was heated at first to 550°C and then up to 750°C for 5min with ramping rates of 20°C/min and 3°C/min, respectively, under Ar gas flowing at 100sccm, while the temperature at the S location place was kept at 200-250°C.

This synthesis approach has led to the formation of high-quality triangular WS_2 monolayers (Fig. 3.11*b*). However, due to the sensitivity to the local environment of the CVD growth, the distribution of dimensions of the as-grown WS_2 crystals is significantly broad, ranging from a few to hundreds of micro-

metres (Fig. 3.11*b*). Moreover, due to the abundant precursors sources, large and thick multiple domain flakes are formed and unreacted WO_3 agglomerates are still found onto the growth substrate at the end of the growth process.

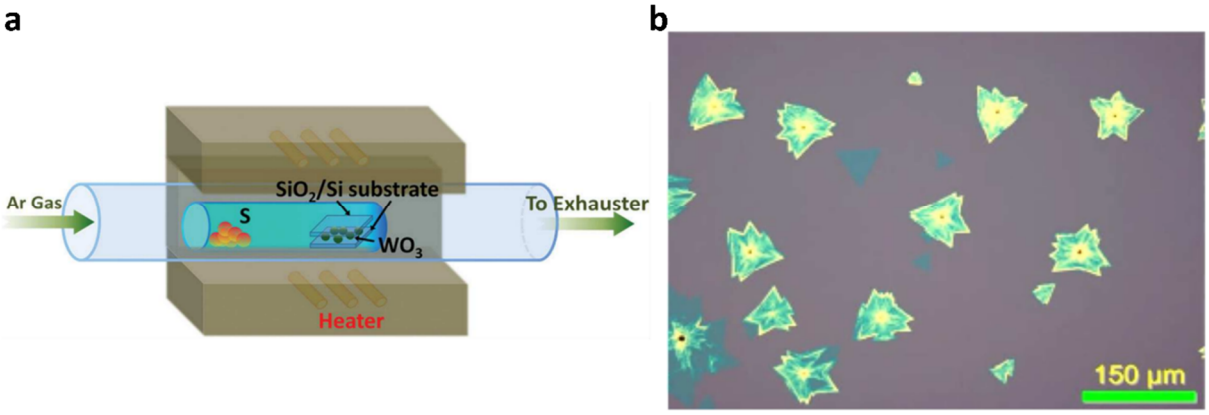


Figure 3.11 *(a) Schematic of the two-quartz tubes CVD setup used for the growth of WS_2 onto Si/SiO_2. (b) Optical image of the as-grown material where the dark dots at the centre of the flakes correspond to the initial locations of WO_3 particles. Adapted from Ref. [180].*

Okada et al. have reported the synthesis of atomically thin WS_2 onto high-quality exfoliated hexagonal boron nitride (h-BN) flakes by using WCl_6 and S powders [246]. Single crystals of h-BN were applied to an adhesive tape and they were mechanically exfoliated into small thin flakes by a repeated folding and peeling apart process. The prepared h-BN flakes were then deposited onto Si/SiO_2 substrates and loaded together with 40mg of WCl_6 and 240mg of S powders at the upstream, centre and downstream zones of a three-zone quartz tubular furnace, respectively (Fig. 3.12*a*). The synthesis of WS_2 was carried out at atmospheric pressure under Ar gas flowing at 400sccm by heating the WCl_6-, S- and substrates-containing furnaces at 185°C, 80°C and 900°C, respectively, for 10min. The as-grown triangular WS_2 flakes on h-BN (Fig. 3.12*b*) show PL emission centred at 2.01eV, which is comparable to the emitted energy from mechanically exfoliated single crystals. The emission intensity is comparable to previously reported values for exfoliated flakes [6] (Fig. 3.12*c*). The full width at half-maximum of the PL emission peak is narrower (26meV) than previously reported values for both CVD-grown (50-55meV [4]) and exfoliated (75meV [6]) WS_2 on SiO_2. Since the FWHM of the PL emission peak is related to the exciton lifetime and interfacial quality [246], the observed small value can be attributed to the high crystallinity of the material and to the clean interface between WS_2 and h-BN. Further, in contrast to previous studies

on the CVD growth of TMDs, a distinct crystallographic orientation between the grown WS_2 crystals and h-BN is observed, which may arise from interlayer Coulomb interactions.

Despite the high crystal quality and interfaces, the lateral size of the as-grown triangular WS_2 monolayers is limited to less than 3µm (Fig. 3.12*b*). Thus, this synthesis strategy would need further developments to make the material of useful dimensions for any applications.

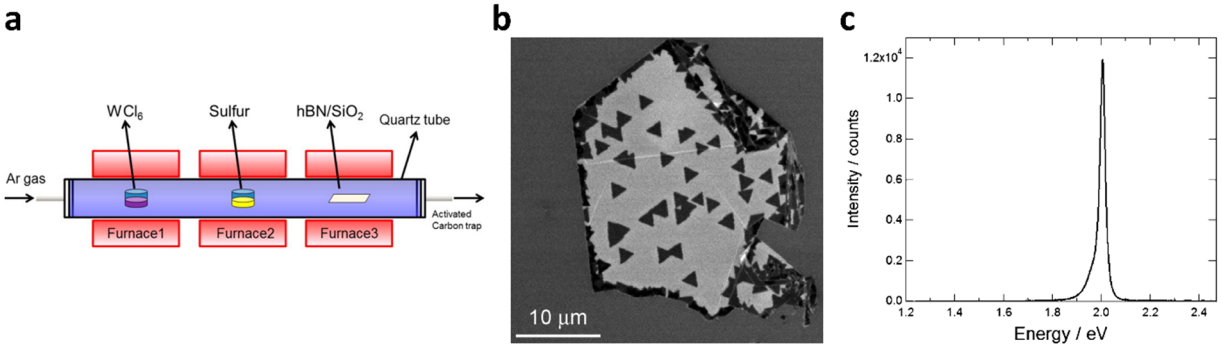


Figure 3.12 *(a) Schematics of the three-zone CVD setup used to grow WS_2 from WCl_6 and S powders. (b) SEM image of triangular-shaped WS_2 flakes grown onto an h-BN flake. (c) PL spectrum of mono-layered WS_2 grown onto h-BN. Adapted from Ref. [246].*

Strategies to enable large-area deposition of monolayered WS_2 films

Rong et al. have shown that controlling the introduction time and the amount of S vapours during the CVD synthesis of WS_2 is a critical parameter to achieve large WS_2 crystals onto Si/SiO_2 substrates [183]. WO_3 powders (1g) were loaded in the high-temperature zone of a two-zone quartz tubular furnace and heated to 1070°C at 40°C/min, whereas S powders (1g) were placed in the low-temperature zone and independently heated to 180°C at 30°C/min. The Si/SiO_2 substrates were loaded downstream and the WS_2 synthesis took place at 860°C for 60min at atmospheric pressure under Ar flow (100sccm) (Fig. 3.13*a*). Monolayered WS_2 with lateral size up to a few hundreds of micrometres were achieved at 1070°C by pre-sulphurized WO_3 powders. These were partially converted in WS_2 by sublimating S powders 10min before the high-temperature furnace was reaching 1070°C.

While this synthesis approach has provided important insights into the factors that influence the synthesis of WS_2, it presents two main limitations for any potential scaling up. The as-grown WS_2 domains are scattered across the growth substrate with a very low nucleation density (Fig. 3.13*b*) which hinder the achievement of large-area coverage. Further, the growth conditions involve the use of very high temperatures (up to 1070°C) which approach the decomposition temperature of WS_2. These involve high costs for the process and may lead to the partial decomposition of WS_2.

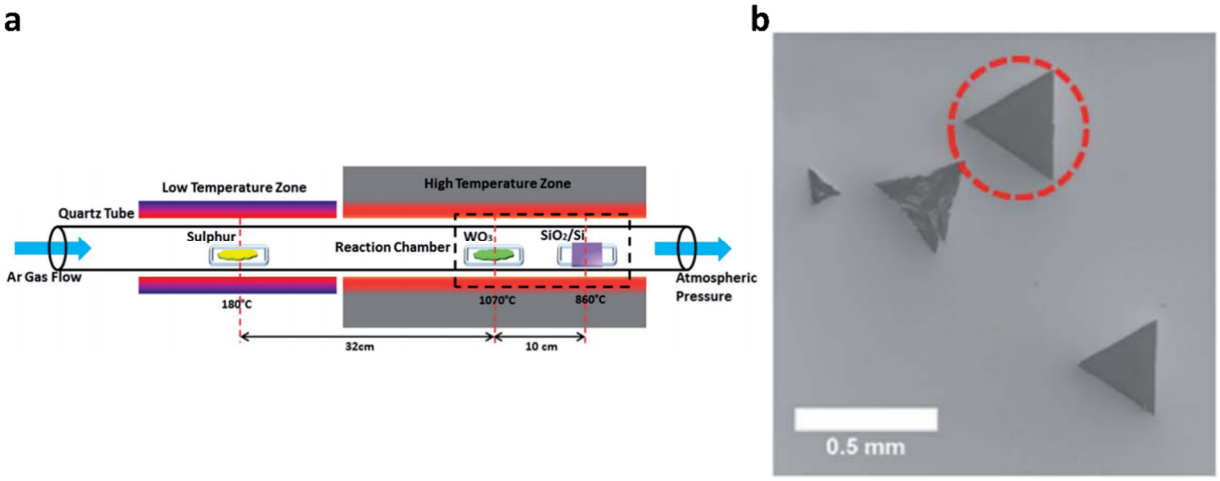


Figure 3.13 *(a) Schematic of the atmospheric pressure-CVD setup used to deposit large monolayered WS_2 flakes onto SiO_2/Si substrates. (b) SEM image of the as-grown triangular WS_2 crystals onto Si/SiO_2. Adapted from Ref. [183].*

Fu et al. have investigated the effect of different growth conditions on the atmospheric pressure CVD synthesis of WS_2 from WO_3 and S powders, showing how the growth temperature and flow rate of the carrier gas play key roles on the nucleation and growth of WS_2 domains [186]. WO_3 (0.5g) and S (0.015g) powders were loaded in a two-zone quartz tubular furnace, whereas SiO_2/Si substrates were placed upside down at 5mm above the WO_3-containing holder (Fig. 3.14*a*). The WO_3-controlling furnace was heated up to 880°C with a rate of 15°C/min and then slowly cooled down to 780°C over 40min once the S-controlling furnace reached 250°C. While reaching high temperatures ensure reaction between WO_3/WO_{3-x} and S vapours, the slow cooling down stage was found to enhance both growth quality and coverage of the WS_2 domains (Fig. 3.14*b*) [186].

In order to have a better understanding of the growth mechanism, the set temperature of the WO_3- and substrate-containing furnace was varied to 750°C, 850°C, 900°C and 950°C, while keeping

all the other growth parameters fixed. At 750°C, the growth of monolayered WS_2 was not achieved and only thick and stacked WS_2 particles were observed onto the substrate (Fig. 3.15*a*) likely due to the low diffusion rate of the precursor species at this temperature, which can lead to their trapping at the early nucleation sites. By increasing the growth temperature to 850°C (Fig. 3.15*b*) and 900°C (Fig. 3.15*c*), monolayered WS_2 with similar triangular morphology and lateral size of ~30μm were obtained. By further increasing the set temperature to 950°C, no WS_2 domains were observed onto the substrate (Fig. 3.15*d*) due to the low thermo-stability of the as-grown atomically thin WS_2 at high temperatures in vacuum.

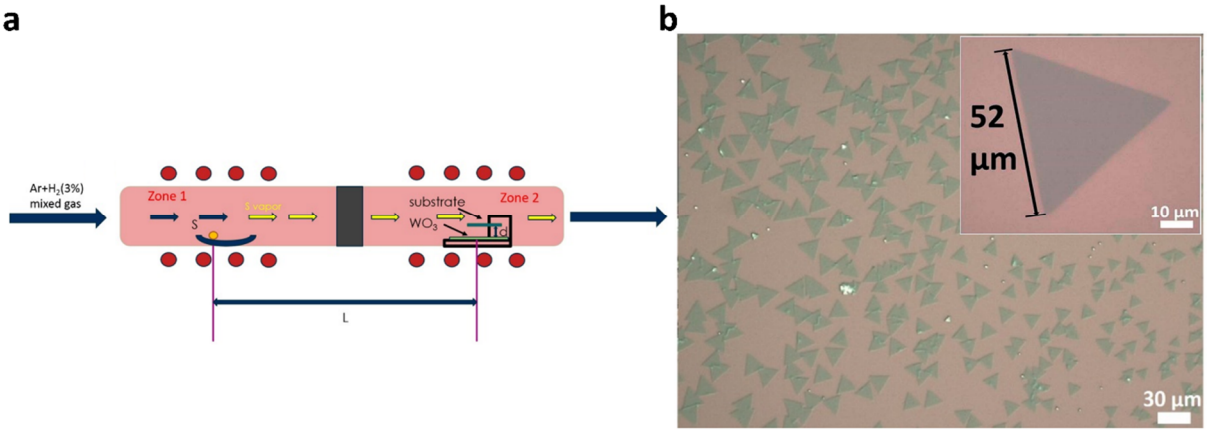


Figure 3.14 *(a) Schematic of the two-zone atmospheric pressure-CVD setup used to grow WS_2 domains onto SiO_2/Si. (b) Optical image of as-grown triangular WS_2 monolayers with lateral size up to ~52μm. Adapted from Ref. [186].*

The carrier gas flow rate is another important growth parameter which controls the exposure time and amount of S vapours participating in the reaction with WO_3/WO_{3-x} species to form WS_2. At flow rates lower than 5sccm, no WS_2 formation was observed due to the coagulation of S at the upstream zone of the furnace and insufficient transport of its vapours to the growth substrate. By gradually increasing the flow rate, more S vapours can be carried downstream, resulting in a widespread WS_2 nucleation at 10sccm (Fig. 3.15*e*) and growth of hexagonal WS_2 domains at 15sccm (Fig. 3.15*f*) which are believed to be an early stage-configuration in the growth of triangular WS_2 crystals. By further increasing the flow rate to 20sccm and 50sccm, enough S source can be transferred on the substrate and the hexagonal WS_2 domains turns into triangular crystals with an average domain size of ~25μm and ~45μm, respectively (Fig. 3.14*b*). As shown in Figure 3.15*g*, the WS_2 domain size started to decrease as the gas flow rate is raised

above 50sccm and no WS_2 formation is achieved at 150sccm. This is due to the transfer of the precursors to the downstream zone of the furnace rather than onto the growth substrate.

Overall, this work has provided important insights into the factors that affect the nucleation and growth of WS_2. However, the achievement of monolayered WS_2 with lateral size of ~50μm is limited to the use of forming gas containing a substantial hydrogen gas percentage which may limit manufacturability.

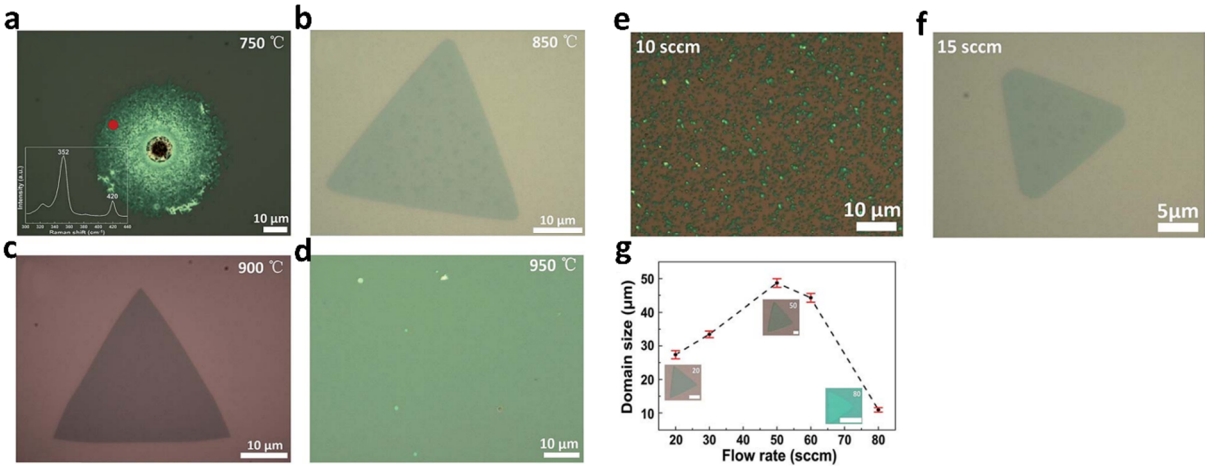


Figure 3.15 *Optical images of the SiO_2/Si growth substrates after synthesis carried out at (a) 750°C, (b) 850°C, (c) 900°C and (d) 950°C, under the same gas flow rate of 50sccm. The Raman spectrum in the inset of (a) (collected from the area highlighted with a red dot) indicates multilayered growth of WS_2. Triangular WS_2 monolayers are achieved at temperatures in the range 850°C- 900°C. Optical images of WS_2 domains grown by using Ar/H_2 gas flowing at (e) 10sccm and (f) 15sccm, under the same growth temperature of 880°C. Three side lengths of the WS_2 hexagon are longer than the others, which may be due to different growth velocities originating from the same nucleus. (g) Statistical analysis of the WS_2 domain size versus gas flow rate in the range 20sccm-80sccm (error bars are shown in red). The optical images in the insets show triangular WS_2 monolayers grown at 20sccm, 50sccm and 80sccm. Scale bar is 10μm. Adapted from Ref. [186].*

Lan et al. have demonstrated the synthesis of large-area continuous monolayered WS_2 films onto (0001)-oriented Al_2O_3 substrate by a seed-assisted CVD method [314]. The seeds consisted of WO_3 nano-powders with an average size of 100nm and were spread onto the growth surface by dipping the Al_2O_3 substrate into a WO_3-isopropanol solution. The seed-coated Al_2O_3 substrate, WO_3 (50mg) and S (200mg) powders were then placed at the downstream, centre and upstream zones of a tubular furnace, respectively,

which was flushed with Ar gas several times and purged to 0.1Pa with a mechanical pump. The temperature was then raised to 950°C for 40min under Ar flow (30sccm) maintaining a growth pressure of 15Pa, whereas S powders were evaporated through a heating belt heated to 110°C.

This seed-assisted CVD growth has led to centimetre-scale monolayered WS_2 films with sparse multi-layered regions (Fig. 3.16*a*). However, the FET electron mobility of the as-grown WS_2 film was limited to 0.91$cm^2V^{-1}s^{-1}$. Further, only sparse WS_2 flakes were observed without seeding of the growth substrate even by using larger amounts of WO_3 and longer growth times (Fig. 3.16*b*).

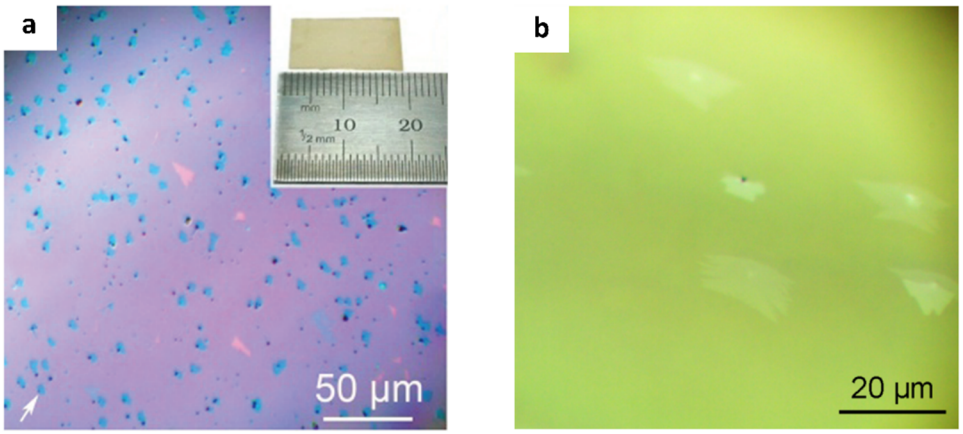


Figure 3.16 *(a) Optical image of a transferred monolayered WS_2 film onto SiO_2/Si substrate. The blue dots (indicated by a white arrow) are multilayered WS_2 domains. The inset shows the as-grown large-area WS_2 film onto Al_2O_3 substrate. (b) Optical image of isolated WS_2 flakes grown without seeding of the sapphire substrate. Adapted from Ref. [314].*

Xu et al. have reported the atmospheric pressure CVD growth of large-area (~135µm) mono-layered WS_2 onto sapphire substrates and they have demonstrated a polystyrene (PS)-mediated delamination process to transfer the as-synthesized WS_2 flakes onto arbitrary substrates without cracks or wrinkles [185]. Due to the hydrophobicity of the PS transfer layer and the capillary forces at the air/water interface, the WS_2-attached PS film can be readily peeled off from the substrate in water. WO_3 powders (50mg) and Al_2O_3 substrates were loaded at the centre and downstream (18cm from the centre) zones of a quartz tubular furnace, respectively, and heated to 900°C for 60min. Whereas S powders (500mg) were placed at the upstream zone and heated independently to 180°C. The growth of WS_2 was performed at atmospheric pressure under Ar (250sccm) and Ar (250sccm)/H_2 (5sccm) once the growth temperature reached 900°C (Fig. 3.17*a*). Three successive growth-delamination-transfer cycles on the same Al_2O_3 substrate have

been demonstrated. Compared to the poly(methyl methacrylate) (PMMA)-based transfer method, in which a highly concentrated acid (HF) or base solution (KOH, NaOH) is used to deep-etch the growth substrates (SiO_2/Si or sapphire) at high temperature (80-100°C) for 30-60 min, the PS-mediated transfer allows to peel the WS_2 flakes from Al_2O_3 within 30s after pre-etching in NaOH solution for 5-10min at 90°C, thus significantly reducing the etching time in hot base solution and bubble generation which can cause non-recoverable damage to both samples and substrates [185]. In addition, the high solubility of PS in organic solvents enables quick and complete removal of the protecting layer. The transferred WS_2 flakes exhibit comparable domain size and electron mobility after several growth cycles on the recycled sapphire substrate. Further, the photoluminescence emission from monolayered WS_2 grown on the reused sapphire is higher than what recorded for WS_2 grown on fresh substrates, possibly due to p-type doping induced by a thin layer of water intercalated at the atomic steps of the recycled sapphire (Fig. 3.17*b*).

Therefore, the PS-mediated delamination process has proved to be a non-destructive transfer technique which can offer the possibility to recycle Al_2O_3 substrates. However, the synthesis conditions involve the use of H_2 gas and result in WS_2 flakes with limited lateral size of ~10μm and less intense PL emission if SiO_2 substrates are used instead of costly sapphire crystals (Fig. 3.17*c*).

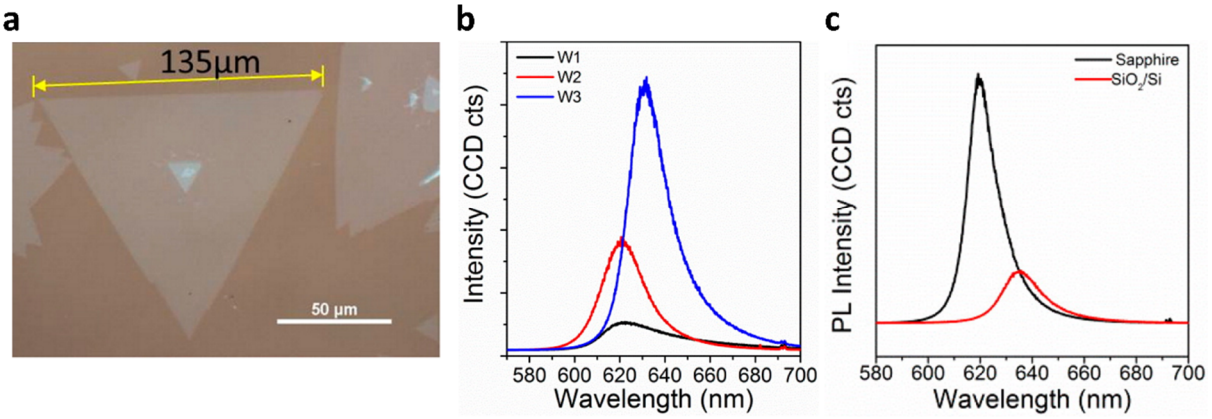


Figure 3.17 *(a) Optical image of a large monolayered WS_2 triangle synthesized onto sapphire substrate by atmospheric pressure CVD, being among the largest TMDs crystals grown on c-sapphire (0001) via CVD [185]. (b) PL spectra obtained from the centre of WS_2 monolayers from the first (W1), second (W2) and the third (W3) cycle of successive growth-delamination-transfer cycles on the same Al_2O_3 substrate. (c) Comparison of PL spectra of WS_2 flakes onto sapphire and SiO_2/Si grown by using the same growth conditions. Adapted from Ref. [185].*

Kang et al. have shown that controlling the H_2 concentration in the CVD synthesis of WS_2 from WO_3 and S powders is crucial to achieve large-area deposition of monolayered WS_2 domains and continuous polycrystalline films up to mm^2 coverage [247]. A 5 nm-thick WO_3 film was deposited through electron beam evaporation from pellets onto a Si substrate, placed face down above a second clean SiO_2 substrate in a sandwich configuration and loaded together with S powders at the centre and upstream zones of a tubular furnace, respectively (Fig. 3.18*a*). The furnace was heated up to 900°C for 30min at 15°C/min and the growths were carried out by low pressure-CVD under S vapours, Ar and/or H_2 gases. The best results were obtained at 4.5Torr deposition pressure under 60sccm H_2 flow rate (Fig. 3.18*b*).

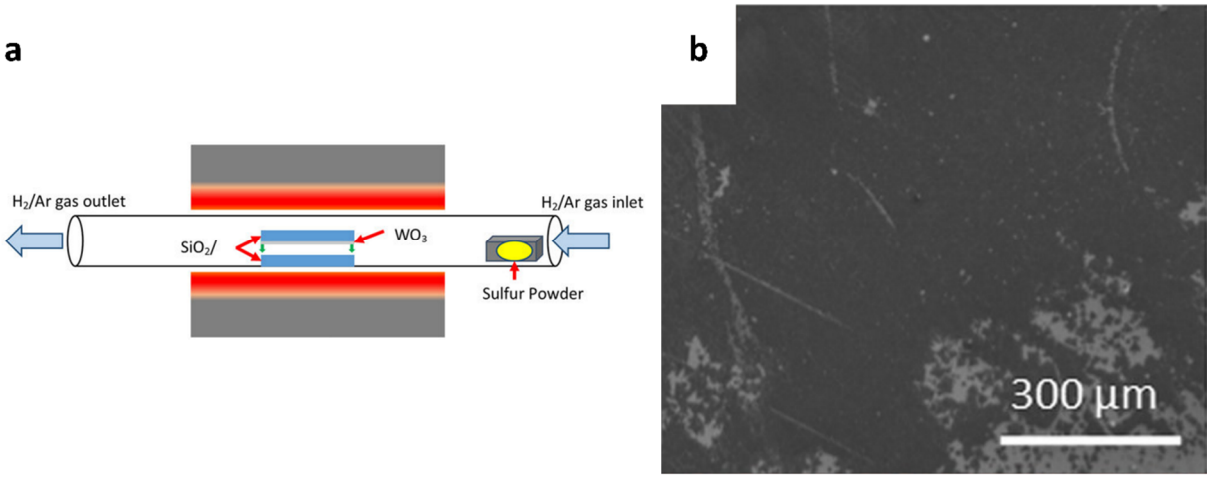


Figure 3.18 *(a) Schematic of the low-pressure CVD setup for WS_2 deposition under H_2/Ar mixture gas. (b) SEM image of a polycrystalline WS_2 coverage over ~1mm^2-sized area grown by using H_2 gas flowing at 60sccm. Adapted from Ref. [247].*

SEM images (Fig. 3.19*a-d*) of monolayered WS_2 flakes grown under 30, 40, 50 and 60sccm of forming gas flowing at 100sccm, reveal that both size and density of the WS_2 flakes slightly increase with increasing H_2 flow rate. Whereas SEM images (Fig. 3.19*e-g*) of monolayered WS_2 flakes grown by supplying 45, 50 and 60sccm of H_2 gas, show a significant increase in the domain size (up to ~30µm) and nucleation density compared to the same experimental conditions but with the presence of Ar. This can be attributed to the improved H_2-driven WO_3 reduction. In addition, a quasi-continuous polycrystalline WS_2 film with surface coverage up to ~1mm^2 was observed by using 60sccm of H_2 (Fig. 3.19*h*, Fig. 3.18*b*). However, while no WS_2 formation was achieved by using only Ar, high H_2 flow rates (above

60sccm) resulted in the after-growth lateral etching of the WS_2 domains. Thus, this growth strategy, although it shows high area coverage, it is limited by the exclusive use of H_2 gas as carrier gas, which poses safety and costs limitations.

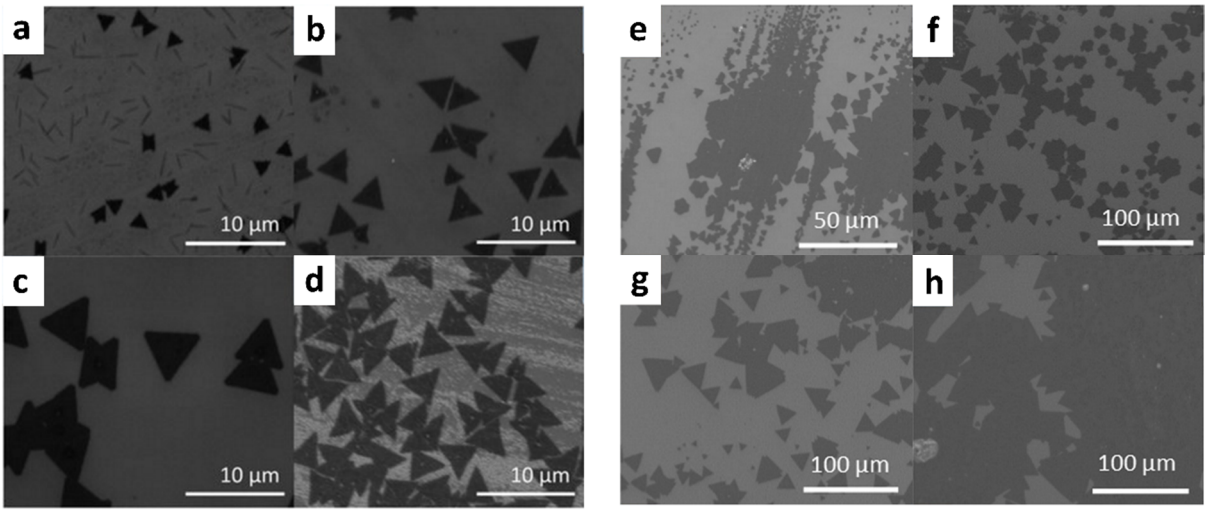


Figure 3.19 *SEM images of monolayered WS_2 flakes grown under Ar flowing at 100sccm and H_2 flowing at (a) 30sccm, (b) 40sccm, (c) 50sccm and (d) 60sccm. SEM images of monolayered WS_2 flakes grown under only H_2 flowing at (e) 45sccm, (f) 50sccm, (g-h) 60sccm. Adapted from Ref. [247].*

Yun at al. have reported the CVD synthesis of centimetre-scale monolayered WS_2 films on gold foils by using ammonium metatungstate (AMT, $(NH_4)_6H_2W_{12}O_{40}{\cdot}x(H_2O)$) and H_2S as W and S precursors, respectively [257]. Since AMT is water soluble, it can be easily deposited on gold and it can be efficiently converted to a W source by catalytic decomposition onto Au substrates. It has been suggested that the combination AMT/Au is advantageous for improving the distribution and adhesion of the precursors onto the growth surface. Further, the limited solubility of tungsten and sulphur in gold at high temperatures and the lack of compound formation between W or S and Au, make Au foil a promising metal substrate for the surface-mediated growth of monolayered WS_2 [257].

Before synthesis, AMT was dissolved in deionized water, dropped onto an Al_2O_3 plate and dried in an oven, while the Au foil was annealed at 1035°C for 2h and polished with a diluted Au etchant to smooth the gold surface. The AMT-coated Al_2O_3 plate and Au foil were then placed in parallel and loaded into a one zone-CVD furnace (Fig 3.20*a*). The furnace was first heated to 500°C at 50°C/min for 20min in a N_2 atmosphere (300sccm) to evaporate the water in AMT, and then further heated to 935°C for

15min under H_2S gas (20sccm). Triangular WS_2 islands were formed across the grain boundaries of the gold polycrystalline foil within the first 5min of growth (Fig. 3.20*b*) indicating Au surface-mediated growth of WS_2. Upon increasing the growth time to 15min, the growing WS_2 domains (Fig. 3.20*c*) merge forming a uniform monolayered WS_2 film (Fig. 3.20*d*). After 30 min of growth, multi-layered WS_2 flakes were grown over some regions of the first layer (Fig. 3.20*e*).

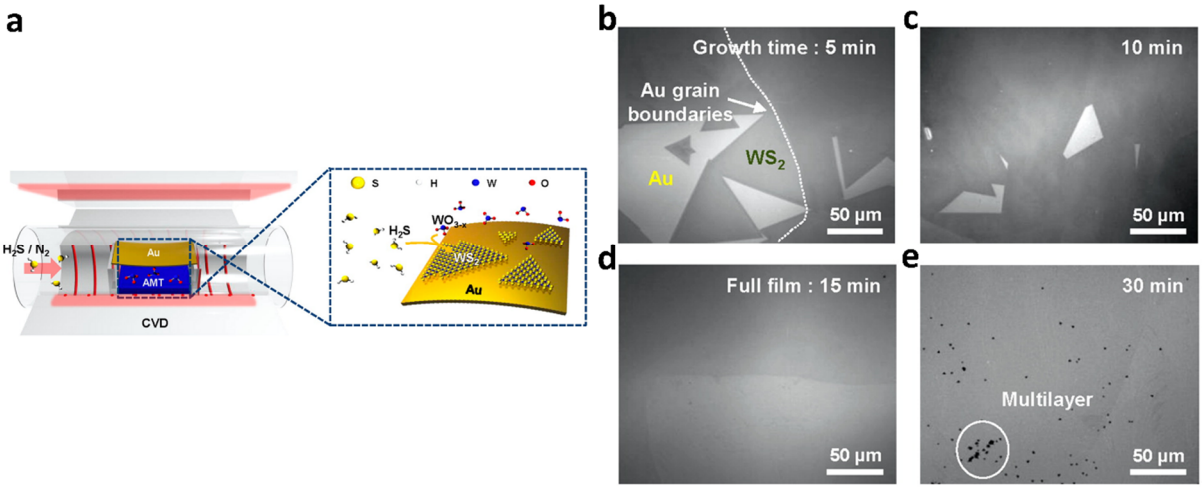


Figure 3.20 *(a) Schematic of CVD setup used to growth centimetre-scale monolayered WS_2 films onto gold foils and illustration of the synthesis reaction. (b-e) SEM images of WS_2 domains as a function of growth time. The maximum size of WS_2 domains in this study was ~420μm at 935°C. The white dotted line in (b) indicates the grain boundary of Au while the white circle in (f) highlights some multilayered flakes. Adapted from Ref. [257].*

The as-grown WS_2 was transferred onto SiO_2/Si substrates using both wet-etching and bubbling transfer methods. In order to prevent damage to the WS_2 films during the transfer process, a PMMA supporting layer was spin-coated onto the WS_2/Au foil. To achieve the wet-etching transfer, the Au foil was etched away by an Au etchant (GE-8148, Transene) and the PMMA/WS_2 film floating on deionized water was transferred to the target substrate. While in the "bubbling" method, the WS_2 was transferred by building an electrochemical cell. A negative voltage was applied to the WS_2/Au system immersed in a NaCl solution. Hydrogen bubbles were generated between the WS_2 film and the Au surface according to the reaction:

$$2H_2O_{(l)} + 2e^- \rightarrow H_{2(g)} + 2OH^-_{(aq)}$$

They eventually cause the delaminating of the PMMA-coated WS_2 film from Au. The bubbling method lead to superior material quality with room temperature FET electron mobility of $20cm^2V^{-1}s^{-1}$ and on/off ratio of $\sim10^8$ while the wet-transfer method provided material with electron mobility of $\sim0.1cm^2V^{-1}s^{-1}$. Further, compared to the wet-etching method, the bubbling transfer has a cost advantage because the Au foil can be reused for repeatable growths. However, the WS_2 films transferred through the bubbling method exhibited cracks and were significantly less uniform than those transferred via the wet-etching. Further, a degradation of the PL intensity in some areas of the WS_2 domains was observed and attributed to n-doping caused by chlorine during the NaCl-based bubbling transfer process. Thus, while this synthesis methods looks advantageous in terms of material quality and large-area scalability, the transfer methods associated need further development to an exclusive superior strategy.

Soon after, a second work has been published about the synthesis of WS_2 on Au substrates. Gao et al. have reported the self-limited surface-catalytic growth of uniform monolayered WS_2 single crystals and large-area films onto reusable Au foils by ambient-pressure CVD from WO_3 and S powders [189]. A 25-100μm-thick piece of Au foil was polished and annealed at 1040°C for over 10h before the first use, and loaded into a quartz tubular furnace placed face-down above a WO_3 (200mg)-containing crucible. Whereas another S (100mg)-containing crucible was placed at the upstream zone of the tube, where the temperature was independently controlled (Fig. 3.21*a*). The Au foil (and WO_3 powders) was first annealed at 800°C in Ar atmosphere (200sccm) for 10 min to remove organics adsorbed onto its surface. The S powders were then heated to 200-240°C to initiate the synthesis of WS_2 (which lasted up to 4h for large WS_2 single crystals) under Ar flow (10-500sccm).

The solubility of W in gold is extremely low (below 0.1atomic% at 800°C), preventing the segregation and precipitation processes for the growth of multilayered domains and thus ensuring a self-limited growth of monolayered WS_2 [189]. Au can also lower the energy barrier for the sulphurization of WO_3 since it has been found that the S_2 dimer can be easily dissociated into S atoms on the Au(111) surface and the obtained S atoms can also easily diffuse, due to the low barriers for these two processes (0.22eV for S_2 dissociation and 0.58eV for S atoms diffusion) (Fig. 3.21*b*) [189].

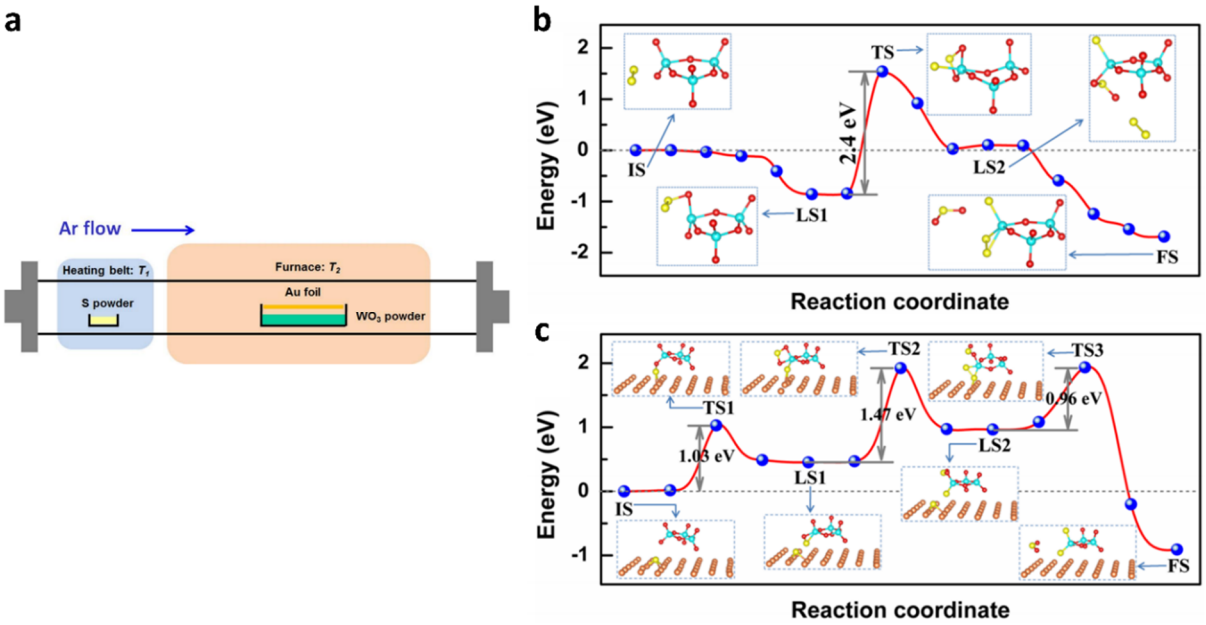


Figure 3.21 *(a) Schematic for the self-limited surface-catalytic growth of large-area monolayered WS_2 single crystals and continuous films onto Au foils by ambient-pressure CVD. (b-c) Calculated minimum energy paths for the possible first step of W_3O_9 reduction by (b) S_2 molecules in a sulphur atmosphere and (c) S atoms onto the Au(111) surface. Schematic structures of the initial (IS), local (LS) and final (FS) states are also presented, where W, O, S and Au atoms are represented by cyan, red, yellow and brown balls, respectively. A second S_2 molecule is introduced from LS2 in (b) while a second and third S atoms are introduced from LS1 and LS2 in (c), respectively. It is concluded that S atoms on Au(111) can reduce W_3O_9 clusters into $W_3O_7S_2$ under an energy barrier of 1.47eV, which is significantly lower than that for the direct sulfurization of W_3O_9 clusters by S_2 dimers in a sulphur atmosphere without the presence of Au (2.39eV). Adapted from Ref. [189].*

Finally, the weak interaction between monolayered WS_2 grown by ambient-pressure CVD and the Au substrate enabled the transfer of WS_2 onto arbitrary substrates by using the electrochemical bubbling method, allowing reuse of the Au foil. This has been attributed to the presence of gases trapped between WS_2 and the Au substrate in ambient-pressure CVD [187]. On the contrary, these gas molecules are not present in the WS_2 grown by low-pressure CVD, rendering the use of the bubbling method unsuccessful [189].

As shown in Figure 3.22*a-d*, the domain size of the individual WS_2 triangles grown by ambient-pressure CVD is increased by increasing the growth time, lowering the heating temperature of the S source

and increasing the Ar flow rate. Ultimately, this can lead to the formation of millimetre-size monolayered WS_2 single crystals. As shown in Figure 3.22*g-h*, upon increasing the growth time, adjacent WS_2 domains expand, join and eventually form a continuous monolayered WS_2 film. Similarly to the CVD synthesis of graphene on Cu, where an increase of the concentration of methane in the reaction system can lead to the formation of bi-, tri- and tetra-layered graphene despite the very low solubility of Cu for carbon [189], multilayered WS_2 domains were formed on the Au foil when the concentration of sulphur in the reaction chamber was significantly increased.

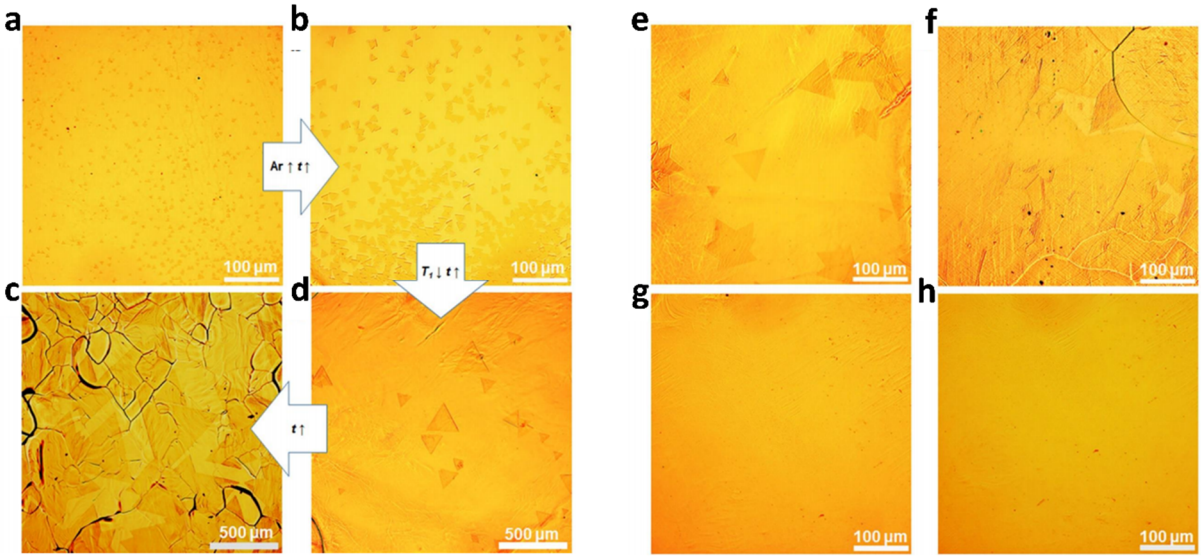


Figure 3.22 *(a-d) Optical images of monolayered WS_2 domains synthesized using different conditions, where T_1 and t refers to the heating temperature of the sulphur powders and growth time, respectively: (a) T_1=240°C, Ar=10sccm, t=10min; (b) T_1=240°C, Ar=200sccm, t=0.5h; (c) T_1=200°C, Ar=200sccm, t=4h; (d) T_1=200°C, Ar=200sccm, t=1h. (e-h) Optical images of monolayered WS_2 domains prepared at T_1=220°C, Ar=10sccm and with growth times of (e) 0.5h, (f) 1h, (g) 1.5h and (h) 4h. Upon increasing the growth time, adjacent WS_2 domains (e) expanded, (f) joined up and (g) finally formed a continuous film. By further increasing the growth time, no additional WS_2 layers were formed onto the surface of the monolayered film (h). Adapted from Ref. [189].*

As discussed above, Yun et al. have also reported the growth of WS_2 on Au at higher temperatures (935°C) by using ammonium metatungstate and H_2S [257]. However, the self-limited growth of exclusively monolayered WS_2 was not achieved and additional multilayered WS_2 domains nucleated and grew upon

extending the growth time. As it has been shown that the concentration of W and S precursors plays an important role in the self-limited growth of monolayered WS_2, these contradictory results are probably due to the different precursors and experimental parameters (such as growth temperature) used [189].

After the CVD synthesis, the electrochemical bubbling method was used to transfer WS_2 from the Au foils to SiO_2/Si. Remarkably, the WS_2 domains grown on reused Au foils showed a similar structure to those grown on the original ones. Further, using the good flexibility of Au foils and the electrochemical bubbling method, the roll-to-roll/bubbling production of large-area mono- and double-layered WS_2 films onto transparent and flexible substrates such as polyethylene terephthalate and polyethylene naphthalate has also been achieved. Nevertheless, the FET electron mobility of the transferred monolayered WS_2 did not exceed 1.7$cm^2V^{-1}s^{-1}$, which is lower than the electron mobility often reported for WS_2 domains grown on SiO_2/Si [188][245] which is in the order of ~10$cm^2V^{-1}s^{-1}$. This suggests that materials quality need further understating and development.

Overall, the CVD of atomically thin WS_2 using Au as growth substrate, opens up the possibility for the large-scale production of WS_2 and integration in integrated circuits, FETs and photovoltaic devices for transparent flexible electronics/optoelectronics. However, material quality needs further optimization for practical applications.

Strategies to optimize the materials chemical purity and facilitate nucleation and lateral size of monolayered WS_2

Li et al. have demonstrated the atmospheric pressure CVD synthesis of monolayered WS_2 at moderate temperatures (700-850°C) by using alkali metal halides MX (NaCl, KI) as growth promoters [245]. $WO_{2.9}$/MX mixed powders (100mg) with an optimal mass ratio of 7:3 were placed at the centre of a quartz tubular furnace, while sulphur powders (10-50mg) were loaded in the upstream zone, which reached a temperature of ~200°C during the growth process (Fig. 3.23*a*). As $WO_{2.9}$ has proved to work better than WO_3 for the synthesis of monolayered WSe_2 [245], it was also used as tungsten precursor for growing WS_2. SiO_2/Si substrates were placed face down ~8mm above the $WO_{2.9}$ powders. After the furnace was pumped down to ~1Pa to remove air and moisture, Ar/H_2 (80/20sccm) gases were introduced

into the tube until atmospheric pressure was achieved. The furnace was then heated to 700-850°C with a ramp rate of 35°C/min and held at these temperatures for 5min before cooling down. The as-grown monolayered WS_2 crystals were found to be highly crystalline, free of unintentional doping with alkali metal or halogen atoms and they exhibited good FET performance (electron mobility of ~14$cm^2V^{-1}s^{-1}$ and current on/off ratio of ~10^6).

This facilitated growth has been attributed to the chemical reaction between tungsten oxide and alkali metal halides during the CVD process, resulting in the formation of volatile tungsten oxyhalide species (i.e., $WOCl_4$, WO_2Cl_2) which facilitate the transport of W precursors onto the growth substrate [245]. In the absence of metal halides, no sublimation of $WO_{2.9}$ occurred under typical growth conditions at 850°C, and no deposition of WS_2 was observed onto the growth substrate. On the contrary, $WO_{2.9}$ mixed with NaCl was found to undergo significant weight loss and colour change under the same conditions, and formation of triangular WS_2 crystals was observed onto the substrate. Figure 3.23*b* shows that the optimal growth temperature depends on the alkali metal halides used and roughly corresponds to their melting points. It has been found that the synthesis of WS_2 is more efficient (in terms of yield and crystal quality) when NaCl (T_m=801°C) is used and the growth temperature is between 825°C and 850°C (Fig. 3.23*b*, *c*). Nevertheless, small WS_2 domains have also been obtained at 700-750°C using KI (T_m=681°C) (Fig. 3.23*d*). Finally, it has been demonstrated that the yield, shape, size and quality of the WS_2 domains depends not only on the choice of the growth temperature and metal halide but also on the amount of chalcogen precursor. Upon reducing the S source from ~50mg to ~10mg, the shape of the WS_2 crystals changed from triangular to hexagonal while their average size increased from ~80μm to ~200μm (Fig. 3.23*e*). However, these quasi-hexagonal monolayered WS_2 domains are expected to exhibit much lower crystal quality than triangular WS_2 monolayers and thus poorer optical and electrical properties.

Therefore, despite this halide-assisted synthesis approach has led to the synthesis of monolayered WS_2 crystals at temperatures in the range 825-850°C, WS_2 domains with lateral size >100μm were only obtained at the expenses of the material quality.

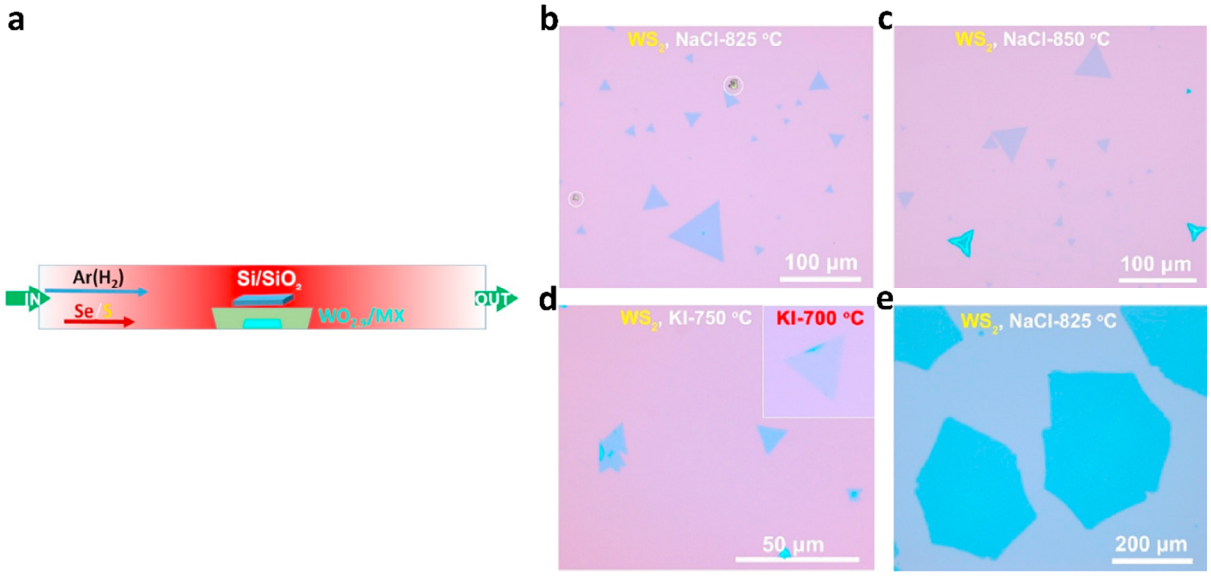


Figure 3.23 *(a) Schematic of the atmospheric pressure-CVD setup used for the halide-assisted synthesis of WS_2 onto SiO_2/Si. Optical images of monolayered WS_2 grown with NaCl as the growth promoter at (b) 825°C and (c) 850°C using ~50mg of S powders. (d) Optical image of small WS_2 domains grown by KI-assisted synthesis at 750°C. The inset shows an optical image of a WS_2 flake grown at 700°C. (e) Optical image of hexagonal WS_2 monolayers grown with NaCl at 825°C using ~10mg of S powders. Adapted from Ref. [245].*

Gong et al. have developed a Te-assisted CVD strategy to synthesize monolayered WS_2 domains from W metal powders at temperatures as low as 500°C and with crystal and optical quality comparable to WS_2 grown at higher temperatures [248]. Bulk W and Te powders were physically ground with a mortar, mixed and scattered onto a SiO_2/Si substrate, which was loaded together with S powders at the centre and upstream zones of a quartz tubular furnace, respectively (Fig. 3.24*a*). The W- and Te-coated growth substrate was then heated to 500°C at a rate of 50°C/min under atmospheric pressure and with Ar gas flowing at 100sccm, whereas the S powders were evaporated at ~200°C. These synthesis conditions led to the formation of monolayered WS_2 triangles with lateral size up to 30μm, W:S atomic ratio of 1:2.05 and free of unwanted Te phases due to the thermal instability of WTe_xS_{2-x} ternary alloys [248] (Fig. 3.24*b*). It is worth to note that the sulfurization of micrometre-sized W powders at 500°C without the addition of Te resulted in micrometre-sized WS_2 powders instead of monolayered WS_2 domains, due the high melting point of W.

The use of Te to control the growth of WS_2 was introduced in a previous work on the synthesis of MoS_2/WS_2 heterostructures, were Te powders were added to slow down the deposition of WS_2 and thus obtain phase-segregated MoS_2/WS_2 heterostructures rather than $Mo_xW_{1-x}S_2$ ternary alloys [34]. It has been suggested that upon mixing Te powders with W powders, Te melts at a relatively low temperature (~450°C) and a small fraction of W powders dissolves into the molten Te (shaded region in Fig. 3.24*b*). In a S-rich atmosphere, W can react in solution rather than in a vapour form and WS_2 crystals precipitate from Te agglomerates and grow onto the SiO_2/Si substrate [248].

Overall, although this Te-assisted CVD strategy has led to the synthesis of monolayered WS_2 at temperatures as low as 500°C, the lateral size of the flakes does not exceed 30µm (Fig. 3.24*c*).

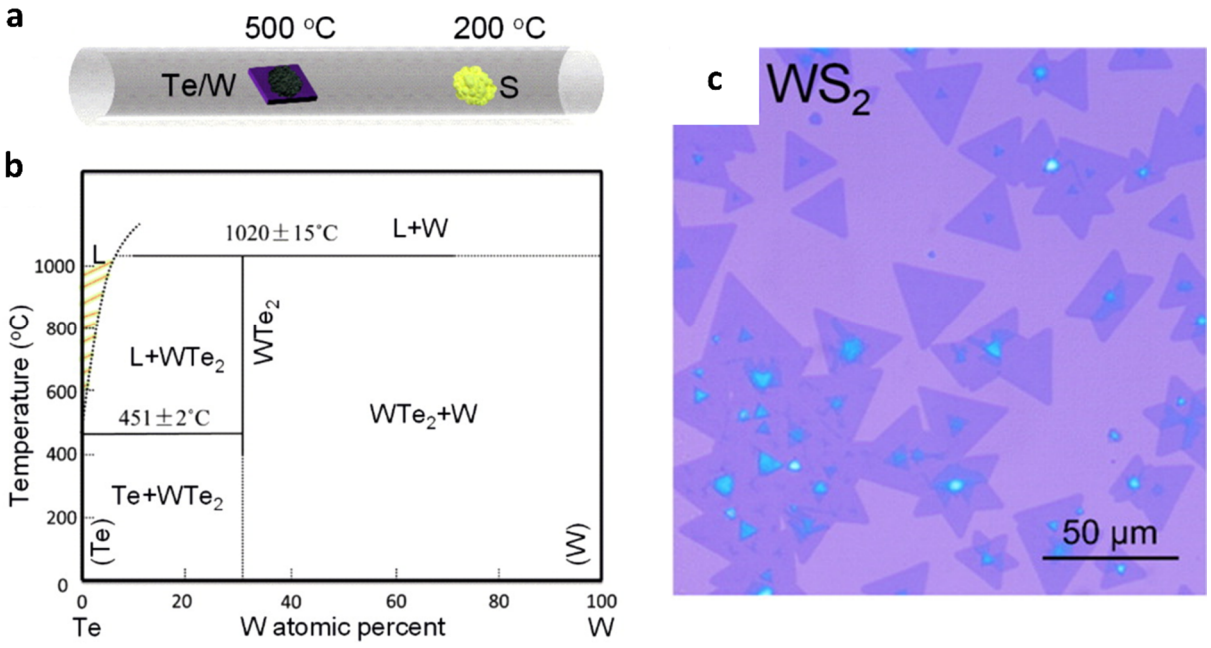


Figure 3.24 *(a) Schematic of the Te-assisted CVD synthesis of monolayered WS_2. (b) Binary Te-W phase diagram in which the reaction conditions are indicated by the shaded area. Te exhibits a melting point around 451°C and at this temperature W can slightly dissolve into Te. L stands for liquid. (c) Optical image of WS_2 triangles onto a SiO_2/Si substrate. Adapted from Ref. [248].*

3.3.3.2. METAL AND CHALCOGEN PRECURSORS IN GASEOUS PHASE

Since the evaporation rate of precursors in powder form can be only controlled by the temperature and it can be largely affected by the powders distribution in the crucible and their grain size, an alternative CVD route to achieve a controllable supply of the precursors is the use of gaseous metal and chalcogen compounds (Fig. 3.25) [24][188][249][250][251][252][253][254][255][256][257]. The inlet of gases to the growth chamber can be regulated through mass flow controllers, thus potentially allowing for higher reproducibility and scalability of the synthesis process than what achievable with CVD routes based on the evaporation of powders [24][43][44].

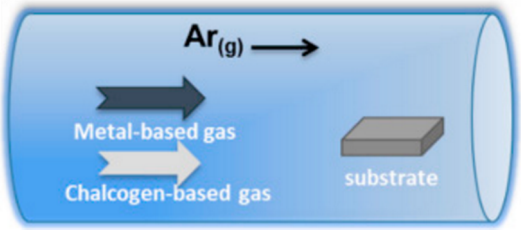


Figure 3.25 *Schematic showing the CVD synthesis of atomically thin TMDs by vapour phase reaction of transition metal and chalcogen precursors supplied from gases. Adapted from Ref. [24].*

Carmalt et al. [254] have reported the atmospheric pressure-CVD synthesis of WS_2 thin films on glass substrates by using a number of W precursors ($W(CO)_6$, WCl_6, $WOCl_4$) and thiols ($HSC(CH_3)_3$, $HS(CH_2)_2SH$) as sulphur source. The W and S precursors were placed into two separate stainless steel bubblers and heated through heating jackets to 165-245°C and 55-63°C, respectively, depending on the precursors choice. The so-produced vapours of W and S sources were first mixed together by using N_2 carrier gas, which was preheated to 157°C and passed through the bubblers, and then introduced into a horizontal CVD reactor where the flow rates were adjusted by using flow controllers. Remarkably, the atmospheric pressure-deposition of WS_2 films was achieved with all the precursors and at temperatures between 350°C and 600°C. Further, it has been shown that pure WS_2 with no evidence for carbon, oxygen or chlorine contamination is formed over a wide variety of precursors concentrations, provided the reagents are combined at sufficiently high temperatures. In particular, $WOCl_4$ did not form tungsten oxysulfide coatings despite having a built-in strong tungsten-oxygen double bond, proving to be an effective metal precursor for the synthesis of WS_2.

The as-grown WS_2 films exhibited a thickness in the order of a few hundred of nanometres and consisted of randomly arranged plate-like WS_2 crystallites of sizes of ~200nm (Fig. 3.26*a*). The film deposited from WCl_6 and $HS(CH_2)_2SH$ at 350°C and then annealed at 600°C for 30min under a flow of $HS(CH_2)_2SH$ exhibited the highest crystal quality. However, even under these circumstances the crystallite size was limited to 25nm probably due to the fast growth kinetics employed in this CVD approach where multiple nucleation sites are generated on the growth substrate. Further, even though thiols do not have the same level of extreme toxicity as the most used H_2S and lead to WS_2 free from pin-hole defects associated with gas phase reactions involving H_2S, the resulting WS_2 films are less crystalline and ordered than those grown using H_2S which exhibit preferential growth parallel to the substrate surface [254].

Park et al. have described the CVD synthesis of mono-, bi-, and tetralayered WS_2 nanosheets on SiO_2/Si substrates with good stoichiometry, uniformity and thickness control by regulating the reaction time between gas-phase WCl_6 and H_2S precursors [255]. SiO_2/Si substrates were placed in the centre of a tubular furnace and heated to 700°C for 30min under Ar gas (20sccm) to remove organic contaminants on the surface. The WCl_6-containing bubbler was kept at 100°C to maintain an adequate vapour pressure and gas-phase WCl_6 with bubbling Ar and H_2S were then injected into the reaction chamber at the same time by Ar carrier gas (20sccm) under a growth pressure of 0.27Torr.

It has been shown that the growth of WS_2 nanosheets starts with the nucleation of small triangular WS_2 domains of ~100nm in size randomly located onto the substrate surface (Fig. 3.26*b*). Upon increasing the growth time, the nucleation sites continue to grow, leading to the formation of boundaries when two or more domains meet (Fig. 3.26*c*) and resulting in a semicontinuous WS_2 film over $1\times7cm^2$ (Fig. 3.26*d*). When the growth time is sufficiently long, this process eventually leads to a uniform large-area WS_2 nanosheet (Fig. 3.26*e*). Figure 3.26*e* shows the nucleation of WS_2 second layers onto the monolayered WS_2 film, which suggests a layer-by-layer growth mode. Bi- and tetra-layered WS_2 nanosheets have been obtained by increasing the growth time to 15min and 25min, respectively.

Overall, this gas-phase CVD process has proved to offer a systematic control over the number of layers of WS_2 nanosheets by tailoring the growth time. However, the as-grown polycrystalline films consist of randomly merged WS_2 crystallites with size in the order of a few hundreds of nanometres.

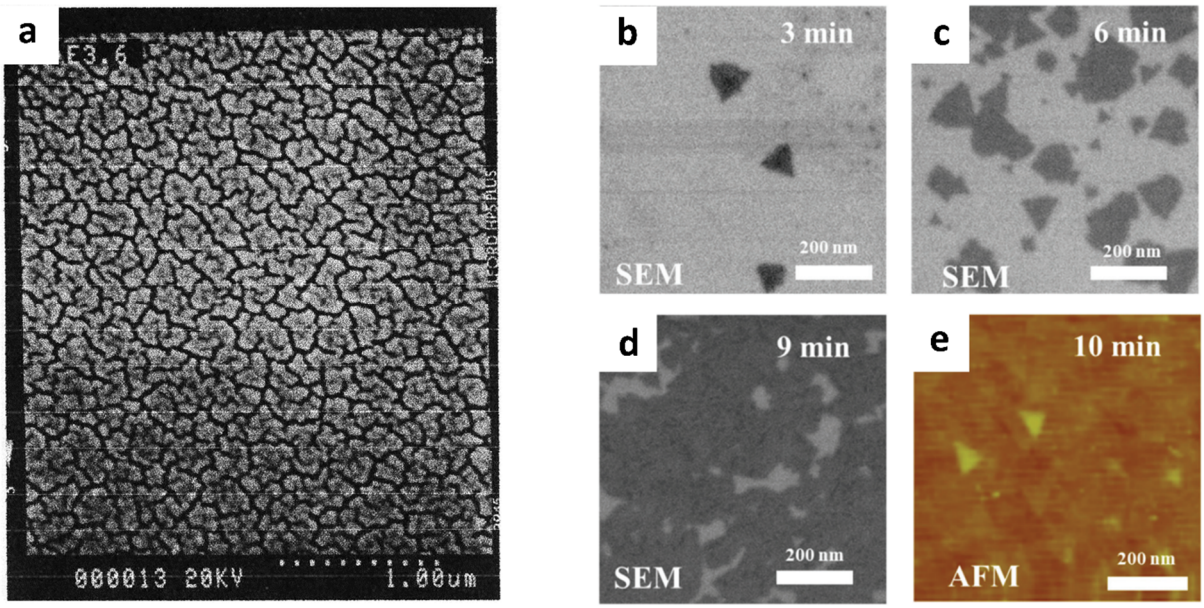


Figure 3.26 *(a) Scanning electron microscopy image of a WS_2 film prepared by atmospheric pressure-CVD of $WOCl_4$ and $HS(CH_2)_2SH$ at 275°C. Adapted from Ref. [254]. (b-d) SEM images as function of the synthesis time showing the growth process of WS_2 nanosheets from small triangles to a continuous film. (e) AFM image showing second layer growth. Adapted from Ref. [255].*

Kang et al. have demonstrated the metal-organic CVD synthesis of wafer-sized monolayered WS_2 films onto SiO_2/Si with spatial homogeneity over the entire films by using tungsten hexacarbonyl ($W(CO)_6$) and diethyl sulphide ($(C_2H_5)_2S$) as W and S sources, respectively, which have high equilibrium vapour pressure near room temperature [188]. A 4-inch fused silica wafer or Si wafer with 285nm-thick thermal SiO_2 was loaded at the centre of a hot-wall quartz tubular furnace while NaCl was placed at the upstream zone of the furnace as a desiccant to dehydrate the growth chamber, which can significantly increases the grain size. Gas-phase $W(CO)_6$ (0.01sccm), $(C_2H_5)_2S$ (0.4sccm), H_2 (5sccm) and Ar (150sccm) were then introduced into the furnace through separate lines regulated by individual mass flow controllers and the synthesis were carried out at 550°C for 26 hours under a total pressure of 7.5Torr (Fig. 3.27*a*).

To achieve a uniform layer control over large scales, the WS_2 films were grown in the layer-by-layer growth mode. Figure 3.27*b* plots the areal coverage of mono- (θ_{1L}) and multi-layered ($\theta_{\geq 2L}$) regions as a function of the growth time t, where t_0 represents the optimal growth time for full monolayer coverage. Photoluminescence and electron microscopy characterizations have suggested that the edge attachment was the main mechanism for the monolayer growth after nucleation: the growth proceeds

by enlarging the already-nucleated grains and additional nucleation on the existing first layer does not occur for $t<t_0$. Upon completion of the first layer growth ($t=t_0$), neighbouring grains are uniformly connected laterally by tilt grain boundaries before further nucleation for the second layer occurs on top of the mono-layered film. It has been shown that this layer-by-layer growth mode is effective below a certain deposition rate of the growth species, above which a different mode leads to the formation of thicker islands. Indeed, spatially homogeneous monolayer nucleation was only obtained using a low partial pressure (~10^{-4}Torr) of W vapour (produced by thermal decomposition of $W(CO)_6$) in the presence of excess $(C_2H_5)_2S$, while a mixture of mono-, multi-layered and no-growth regions was observed at higher W partial pressures.

Further, it has been demonstrated that the grain structure of the WS_2 film, including the average grain size and the intergrain connection, depends sensitively on the concentration of H_2 and residual water. Even though the presence of H_2 is necessary for removing carbonaceous species generated during the metal-organic CVD growth, the average grain size increased from hundreds of nanometres to more than 10μm with decreasing H_2 flow. Further, the grains grown under higher H_2 flow did not merge into each other. The dependence on the water concentration was observed under the presence of salt desiccants (NaCl, KCl and NaBr). As a consequence of the addition of these salts, the grain size increased up to 100-fold. These observations are consistent with the H_2- and H_2O-induced decomposition of $(C_2H_5)_2S$ through hydrogenolysis and hydrolysis, respectively, which enhance the concentration of sulphur vapour, and with the etching of WS_2, which prevents intergrain connections [188]. Also, the concentration of sulphur vapour linearly depends on the concentration of $(C_2H_5)_2S$. Since the concentration of W is kept low to achieve layer-by layer growth, the concentration of S affects the nucleation kinetics and grain size [188]. Indeed, when a W atom (produced by thermal decomposition of $W(CO)_6$) arrives at the growth surface, it diffuses until it reacts with S (produced by decomposition of $(C_2H_5)_2S$), preferentially being adsorbed at a WS_2 edge [188]. However, if the rate of $(C_2H_5)_2S$ decomposition is fast, W atoms do not have a chance to find energetically favourable positions and the nucleation occurs at a non-edge region [188]. Therefore, the nucleation density and size of the WS_2 grains increases and decreases, respectively, when the concentration of H_2, H_2O and $(C_2H_5)_2S$ are high, leading to a fast decomposition kinetics of $(C_2H_5)_2S$ [188].

Figure 3.27*c* shows a photograph of a WS_2 film grown under optimized conditions on a transparent 4-inch fused silica wafer, revealing that the WS_2 region (right half) is uniform over the whole wafer and clearly distinguishable from the bare silica (left half). FET devices fabricated at random locations on the as-grown polycrystalline WS_2 films exhibited good electrical properties with high spatial homogeneity at length scales ranging from micrometres to millimetres, on/off ratio of 10^6 and mobility of $18 cm^2V^{-1}s^{-1}$ at room temperature, which is higher than previously reported values for CVD-grown single-grain WS_2 samples [188].

Overall, this metal-organic CVD method has offered the possibility to precisely control the nucleation density and intergrain stitching to achieve large coverage of monolayered WS_2 films. However, the safety ratings for $W(CO)_6$ and $(C_2H_5)_2S$ require them to be handled inside of a fume hood. Further, a long growth time (26hrs) was necessary to achieve uniform monolayer growth and the addition of H_2 was found to be indispensable for removing carbonaceous species generated during the growth.

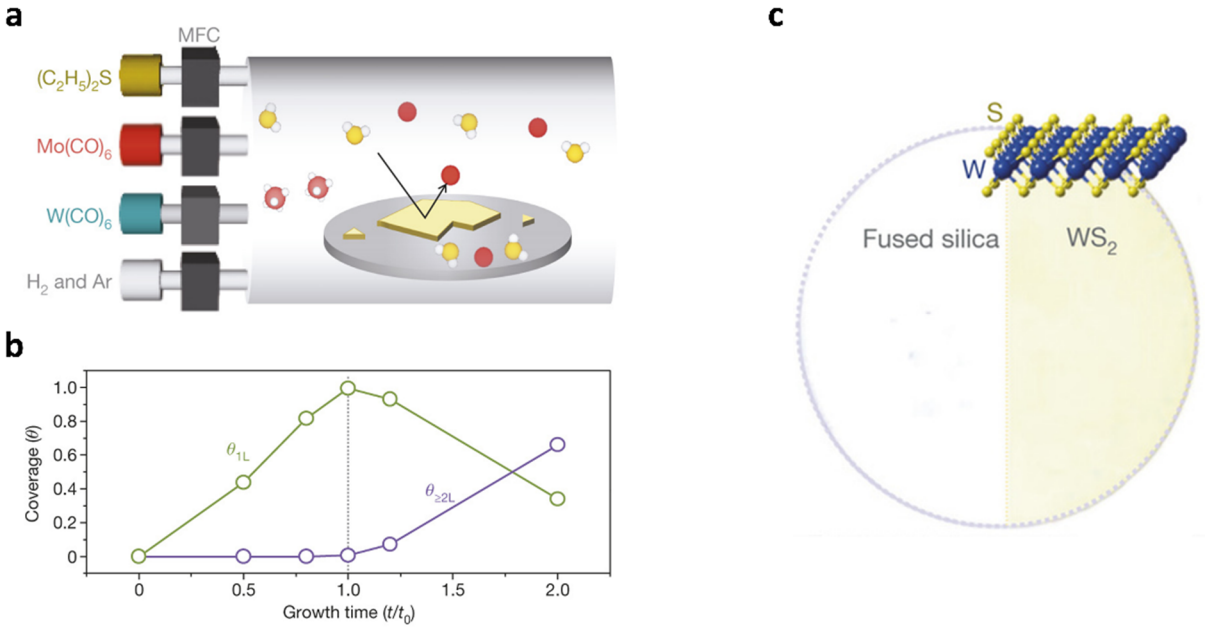


Figure 3.27 *(a) Schematic of the metal-organic CVD setup, where the precursors are introduced to the growth chamber with individual mass flow controllers (MFC). W, S and carbonyl or ethyl ligand atoms are highlighted in red, yellow and white, respectively. (b) Coverage ratio for mono- (θ_{1L}, green) and multi-layered ($\theta_{\geq 2L}$, purple) regions as a function of growth time t, where t_0 was the optimal growth time for full monolayer coverage. (c) Photograph of a monolayered WS_2 films grown on 4-inch fused silica wafer, where the left halve shows the bare substrate for comparison. Adapted from Ref. [188].*

To conclude this session, Table 3.1 summarizes recent advances in the CVD growth of atomically thin WS_2 (listed in publication order) which we have discussed in this chapter [4][167][180][183][184][185][186][187][188][245][246][247][248][255][257][314]. It can be seen that the synthesis of mono- to few-layered WS_2 flakes has mainly been achieved by co-evaporating tungsten oxide and sulphur powders as metal and chalcogen precursors, respectively. Nevertheless, the growth of high-quality monolayered WS_2 crystals still remains an experimental challenge, typically leading to sparse flakes which are a few tens of microns in lateral size. While the formation of a continuous WS_2 layer over centimeter-sized areas has been reported only in a very few cases but at the expenses of the material quality.

Authors; Publication date	**Precursors; Substrates**	**Furnace temperature; Pressure; Carrier gas**	**WS_2 thickness; WS_2 domain size**	**FET device; On/off ratio; Mobility**
Gutierrez *et al.* [4]; November 29, 2012	WO_3 films, S powders; SiO_2/Si+WO_3	800°C; Atmospheric pressure; Ar	Mono-, bi-, tri-, many-layers; <10μm	N.A.
Lee *et al.* [187]; March 18, 2013	WO_3 powders, S powders; SiO_2/Si + PTAS seeds	800°C; Atmospheric pressure; Ar	Mono-, few-layers; <20μm	Back-gated monolayer device; ~10^5; e: ~0.01cm^2/Vs
Zhang *et al.* [184]; September 18, 2013	WO_3 powders, S powders; Sapphire	900°C; 30Pa; Ar/H_2	Mono-, bi-, tri-layers; <50μm	Ion-gel gated monolayer device; ~10^2; h: 0.28cm^2/Vs e: 0.46cm^2/Vs
Peimyoo *et al.* [167]; November 22, 2013	WO_3 powders, S powders; SiO_2/Si	800°C; Atmospheric pressure; Ar	Mono-, bi-, tri-layers; <20μm	N.A.
Cong *et al.* [180]; December 11, 2013	WO_3 powders, S powders; SiO_2/Si + WO_3	750°C; Atmospheric pressure; Ar	Monolayers; ~180μm	N.A.
Okada *et al.* [246]; August 5, 2014	WCl_6 powders, S powders; h-BN	900°C; Atmospheric pressure; Ar	Monolayers; <5μm	N.A.
Rong *et al.* [183]; September 8, 2014	WO_3 powders, S powders; SiO_2/Si	1070°C; Atmospheric pressure; Ar	Monolayers; ~370μm	N.A.
Park *et al.* [255]; October 14, 2014	WCl_6 gas, H_2S gas; SiO_2/Si	700°C; 0.27Torr; Ar	Mono-, bi-, tetra-layers; Nanosheets	N.A.

Fu *et al.* [186]; January 28, 2015	WO_3 powders, S powders; SiO_2/Si	850-900°C; Atmospheric pressure; Ar + H_2	Monolayers; ~50μm	N.A.
Lan *et al.* [314]; March 9, 2015	WO_3 powders, S powders; Al_2O_3 + WO_3 seeds	950°C; 15Pa; Ar	Mono-, multilayers; Films	Back-gated monolayer device; 10^6; e: 0.91cm^2/Vs
Yun *et al.* [257]; April 14, 2015	Ammonium metatungstate powders, H_2S gas; Gold	935°C; Atmospheric pressure; H_2S	Monolayers; ~420μm	Back-gated monolayer device; ~10^8; e: ~20cm^2/Vs
Kang *et al.* [188] April 30, 2015	$W(CO)_6$ gas, $(C_2H_5)_2S$ gas; SiO_2/Si, Fused silica	550°C; 7.5Torr; Ar + H_2	Monolayers; Films	Back-gated monolayer device; 10^6; e: 18cm^2/Vs
Xu *et al.* [185]; May 11, 2015	WO_3 powders, S powders; Sapphire, SiO_2/Si	900°C; Atmospheric pressure; Ar + H_2	Monolayers; ~135μm	Back-gated monolayer device; ~10^5; e: ~4cm^2/Vs
Kang et al. [247]; August 17, 2015	WO_3 film, S powders; SiO_2/Si	900°C; 4.5Torr; Ar + H_2, H_2	Monolayers; ~30μm, films	N.A.
Li *et al.* [245]; September 23, 2015	$WO_{2.9}$ powders + halides, S powders; SiO_2/Si	700-850°C; Atmospheric pressure; Ar + H_2	Monolayers; Triangles ~80μm, Hexagons ~200μm	Back-gated monolayer device; >10^6; e: 14.2cm^2/Vs
Gao *et al.* [189]; October 9, 2015	WO_3 powders, S powders; Gold	800°C; Atmospheric pressure; Ar	Monolayers; ~400μm, films	Back-gated monolayer device; ~10^7; e: 1.7cm^2/Vs
Gong *et al.* [248]; October 26, 2015	W powders + Te powders, S powders; SiO_2/Si	500°C; Atmospheric pressure; Ar	Monolayers; <30μm	N.A.

Table 3.1 *Recent advances in the CVD synthesis of atomically-thin WS_2 (N.A.: not available; e and h: electron and hole mobility, respectively).*

3.4. VAPOUR PHASE SYNTHESIS OF METAL-DOPED WS_2

As discussed in Chapter 2, the electronic, optical, magnetic, catalytic and tribological characteristics of TMDs can eventually be altered by compositional variation through metal doping. In particular, defect-derived excitonic states have recently received much attention for their applications in single-photon emitters [95]. It has been reported that TMDs atomic layers exhibit PL from optically active defects at low temperature (~4-90K) and that such two-dimensional single-quantum emission may have practical advantages in efficient photon extraction and high integration capability [95]. Therefore, the controlled fabrication of defect states in atomically thin TMDs represents an important challenge to be addressed for their application as quantum light sources.

This section reviews the vapour-phase synthesis strategies that have been used to incorporate transition and post-transition metals into WS_2 and the predicted properties and applications of the resultant ternary compounds. It has been reported that In_xWS_2 intercalation compounds show higher electrical conductivity and photocurrents than pure WS_2 [258] whereas impurity Mo atoms cause band gap narrowing through the substitution of W sites in monolayered WS_2 [105][259][260][261]. Finally, Nb doping has also been investigated since its atomic size is comparable to Mo and it is reported to generate acceptor states in MoS_2 [93][95][262].

Srivastava et al. have reported the formation of indium-intercalated compounds In_xWS_2 ($0 \leq x \leq 1$) synthesized directly from the elements [263][264]. W, S and In powders were mixed in stoichiometric proportions to give the desired composition and were loaded into a quartz tube which was subsequently evacuated to 10^{-3}Torr and sealed. The tube was then slowly heated to 750°C through a muffle furnace, maintained at this temperature for 40h and cooled down to room temperature. The as-obtained reaction product was mechanically mixed for ~30min without opening the quartz ampoule, reheated again at 1000°C for 48h, and finally slowly cooled down first to 500°C and then to room temperature with the furnace switched off.

X-ray analysis showed that, like the host 2H-WS_2, all the In_xWS_2 compounds consists of single-phase materials with hexagonal structure and free of any binary phases. It was observed that the a-parameter remained more or less constant upon In intercalation, whereas a small but continuous increase in the c-

parameter with increasing In concentration was detected and attributed to the In intercalation-induced expansion of the interlayer spacing. SEM images for WS_2 and In_xWS_2 are shown in Figure 3.28, which reveals the presence of hexagonal flakes in all the compounds.

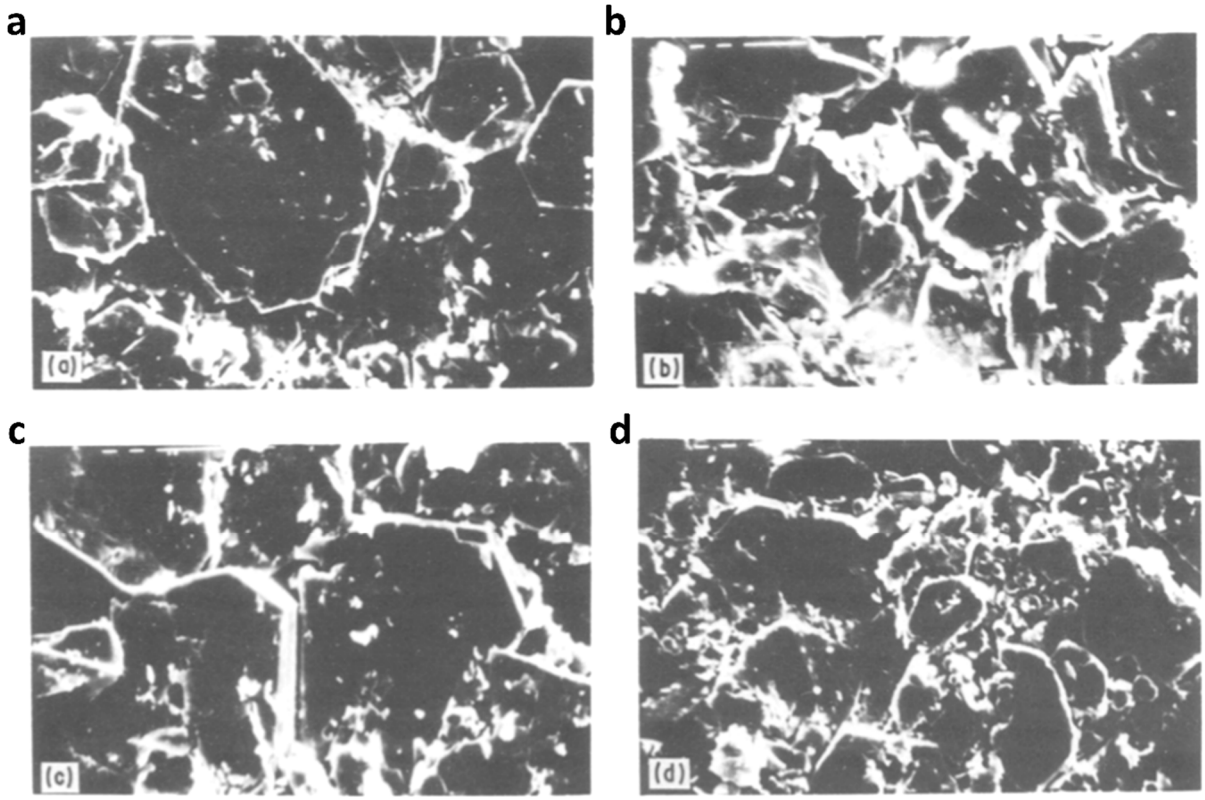


Figure 3.28 *Scanning electron micrographs of bulk In_xWS_2 intercalation compounds ($0 \leq x \leq 1$): (a) WS_2, (b) $In_{1/3}WS_2$, (c) $In_{2/3}WS_2$, (d) $InWS_2$. Adapted from Ref. [264].*

Remarkably, room-temperature magnetic susceptibility and thermoelectric effect, together with low-temperature (150-300K) conductivity measurements on compressed pellets, indicated that all In_xWS_2 compounds are diamagnetic semiconductors with p-type conductivity similar to that of the base 2H-WS_2 (Fig. 3.29*a*, Table 3.2). Figure 3.29*b* shows the variations in room-temperature conductivity and activation energy of In_xWS_2 with the composition x, where it is shown that the conductivity first increases with increasing indium content and then becomes almost constant beyond x=2/3, whereas the activation energy follows a reverse trend. The increase in the conductivity at low In contents has been attributed to the increased carrier concentration due to the presence of In atoms which donates their extra electrons to WS_2 [264]. However, since the conductivity is proportional to both carrier concentration and carrier mobility, the saturation behaviour beyond x=2/3 suggests a decrease in the mobility [264].

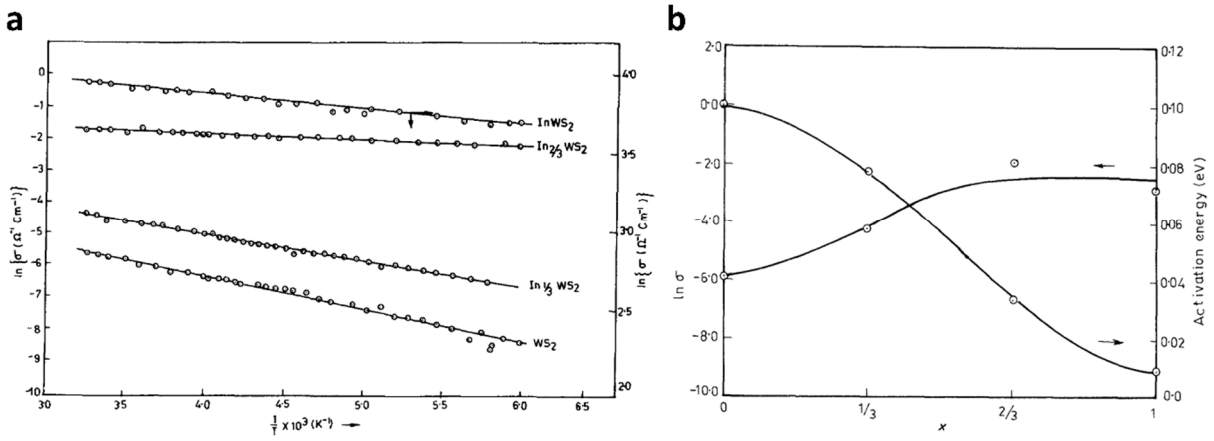


Figure 3.29 *(a) Temperature dependence of the electrical conductivity for In_xWS_2 ($0 \leq x \leq 1$) intercalation compounds. Adapted from Ref. [263]. (b) Variation in the room-temperature electrical conductivity and activation energy for In_xWS_2 with the composition x, where the activation energy was determined from the conductivity data. Adapted from Ref. [264].*

Compound	Lattice parameter (Å)		Type of conductivity	Room temp. conductivity (Ω^{-1} cm^{-1})	Activation energy (eV)	Magnetic susceptibility $-\chi_g$ ((cgs emu) × 10^{-6})
	a	*c*				
WS_2	3.645	12.350	p	1.79×10^{-3}	0.0961	0.350
$In_{1/3}WS$	3.642	12.356	p	1.5×10^{-2}	0.0776	0.110
$In_{2/3}WS_2$	3.6413	12.360	p	0.1655	0.0326	0.135
$InWS_2$	3.6406	12.366	p	51.49	0.0091	0.378

Table 3.2 *Crystallographic and electrical data in In_xWS_2 intercalation compounds. Adapted from Ref. [263].*

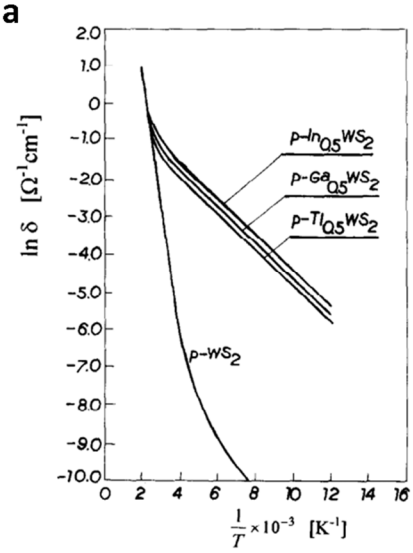
Hryniewicz et al. have reported the preparation of non-stoichiometric polycrystalline thin films of WS_2 intercalated with In (Ga, Tl). This was based on the chemical reaction of oxidation and reduction between W, S and In_2S_3 ($4W+In_2S_3+5S=4In_{0.5}WS_2$) [258]. Substrates of W, S and In_2S_3 in stoichiometric amount were powdered, triturated, mixed, pressed into ~5mm-thick and ~10mm-large tablets and introduced into a quartz ampoule. The ampoule was then evacuated to 10^{-4}Torr, gradually heated to 1050°C through a muffle furnace, kept at this temperature for 168h and finally naturally cooled down to room temperature over ~24h. This process led to 0.01-0.05mm-thik plates with an area of ~0.02cm^2 and of composition $In_{0.5}WS_2$ as confirmed by wet chemical analysis. It has been reported that the as-obtained intercalates

contain the maximum amounts of guest atoms that can be introduced into the interlayer spaces of WS_2, and that attempts to produce intercalates with contents of guest atoms higher than 0.5g atom mol^{-1} were not successful and led to the occurrence of a new phase.

Similarly to what reported by Srivastava, the crystallographic group of the as-obtained $In_{0.5}WS_2$ thin films was found to be hexagonal as for pure WS_2. However, the space group undergoes a change from $P6_3/mmc$ for WS_2 to P622 for its intercalates, where the interlayer spacing c increases while the lattice constant a does not vary. Electrical conductivity measurements were carried out at temperatures ranging from -190°C to 227°C by using a modified four-probe Van der Pauw method and liquid N_2 as cooling medium. Figure 3.30*a* shows that the specific conductivity increases with increasing temperature for all the materials, indicating a semiconducting character. Further, this behaviour is more pronounced for pure WS_2 than for its intercalates, suggesting that the doping of WS_2 led to an increase in the specific conductivity. In particular, In doped-WS_2 films exhibited the highest increase in specific conductivity compared to Ga-and Tl-doped WS_2 (Fig. 3.30*b*). Thermoelectric power experiments using the Seebeck method and Hall effect measurements revealed the occurrence of p-type conductivity in all the compounds, indicating that the intercalation process did not affect the type of conductance. Further, in spite of introducing a significant amount of guest atoms (0.5g atom g mol^{-1}), intercalated WS_2 only exhibited a slight decrease in the width of the energy gap (1.03-1.12eV) compared to that of pure WS_2 (1.19eV). However, doped WS_2 showed acceptor energy levels of energy 0.15eV in the forbidden band (Fig. 3.30), which were confirmed by optical absorption measurements. Finally, photoelectrical measurements revealed that the intercalated WS_2 films generate higher photocurrents than pure WS_2 due to the intercalation-induced introduction of additional acceptor doping levels in the forbidden band, with the highest photocurrents exhibited by $In_{05}WS_2$**.**

Dumcenco et al. have reported the synthesis of $Mo_{1-x}W_xS_2$ (with x=0, 0.2, 0.5, 0.8 and 1) bulk single crystals by chemical vapour transport of the corresponding powdered compounds previously prepared from their elements [105]. The $Mo_{1-x}W_xS_2$ compounds and Br_2 transport agent were placed in a quartz ampoule, which was chilled in liquid nitrogen, evacuated to ~$5\cdot10^{-6}$mbar and sealed. Optimum growth was achieved by maintaining the charge and growth zones at 1030°C and 980°C, respectively, for 20 days, using a two-zone furnace.

a



b

Chemical compound	Specific conductivity at room temperature (Ω^{-1} cm^{-1})	Energy gap E_g (eV)	Activation energy of acceptor levels E_d (eV)
WS_2	0.016	1.19	–
p-$Ga_{0.5}WS_2$	0.181	1.04	0.15
p-$In_{0.5}WS_2$	0.247	1.03	0.15
p-$Tl_{0.5}WS_2$	0.146	1.12	0.15

Figure 3.30 *(a) Semi logarithmic plot of the conductivity as a function of reciprocal temperature and (b) specific conductivity at room temperature and energy gap for WS_2 and its intercalates in the form of polycrystalline thin films. Adapted from Ref. [258].*

The as-grown $Mo_{1-x}W_xS_2$ crystallized in a layered structure with hexagonal symmetry similarly to MoS_2 or WS_2 in the shape of thin plates with thicknesses and surface areas ranging from 20 to 1000μm and from 20 to 100mm^2, respectively. Atomically resolved annular dark field (ADF) scanning transmission electron microscope revealed a random alloying throughout all the mixture compositions (x=0 to 1) where the W and Mo atoms share the metal sites of the hexagonal lattice without any evidence of ordered structures and phase separation or segregation (Fig. 3.31).

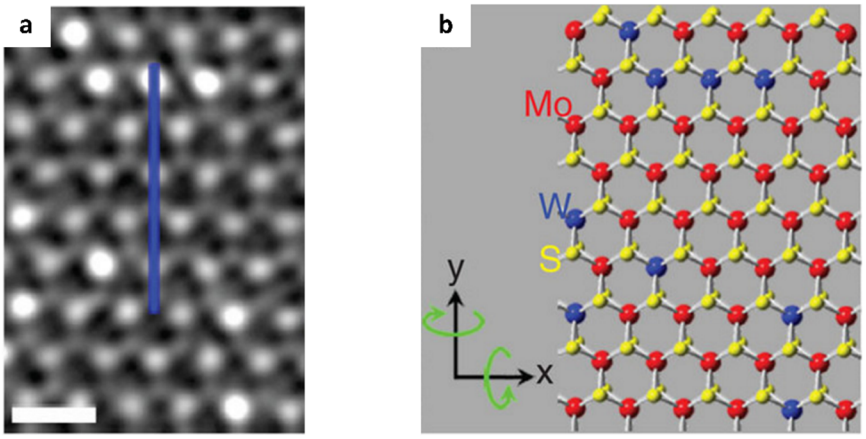


Figure 3.31 *(a) ADF image of monolayered $Mo_{1-x}W_xS_2$ with x=0.2, in which the brighter and less bright spots correspond to W and Mo atoms, respectively, and the S atomic positions are also visible. Scale bar is 0.5nm. (b) Modelled structure of $Mo_{1-x}W_xS_2$ (red: Mo, blue: W, yellow: S). Adapted from Ref. [105].*

Chen et al. have studied monolayered $Mo_{1-x}W_xS_2$ (with x between 0 and 1) alloys cleaved from bulk crystals grown with the chemical vapour transport method described above [105]. They found a random arrangement of Mo and W atoms, composition-dependent photoluminescence emission energy and band gap bowing [261]. The PL emission energy vs. W composition (Fig. 3.32*c*) shows that the A emission can be controllably tuned from 1.82eV (for x=0, i.e. MoS_2) to 1.99eV (for x=1, i.e. WS_2). While the B emission changes from 1.98eV (for x=0) to 2.36eV (for x=1). Moreover, it can be noticed that, upon increasing the W composition x, the A exciton emission first red shifts and then blue shifts (Fig. 3.32*a*) whereas the B exciton emission continuously blue shifts (Fig. 3.32*b*). Finally, it is worth to note that the band-gap emission energy of monolayered $Mo_{1-x}W_xS_2$ is smaller than the linear combination of that of MoS_2 and WS_2, which is the so-called bowing effect previously observed in other bulk semiconductor alloys and attributed to different LUMO (lowest unoccupied molecular orbital) compositions of MoS_2, WS_2 and $Mo_{1-x}W_xS_2$ [261].

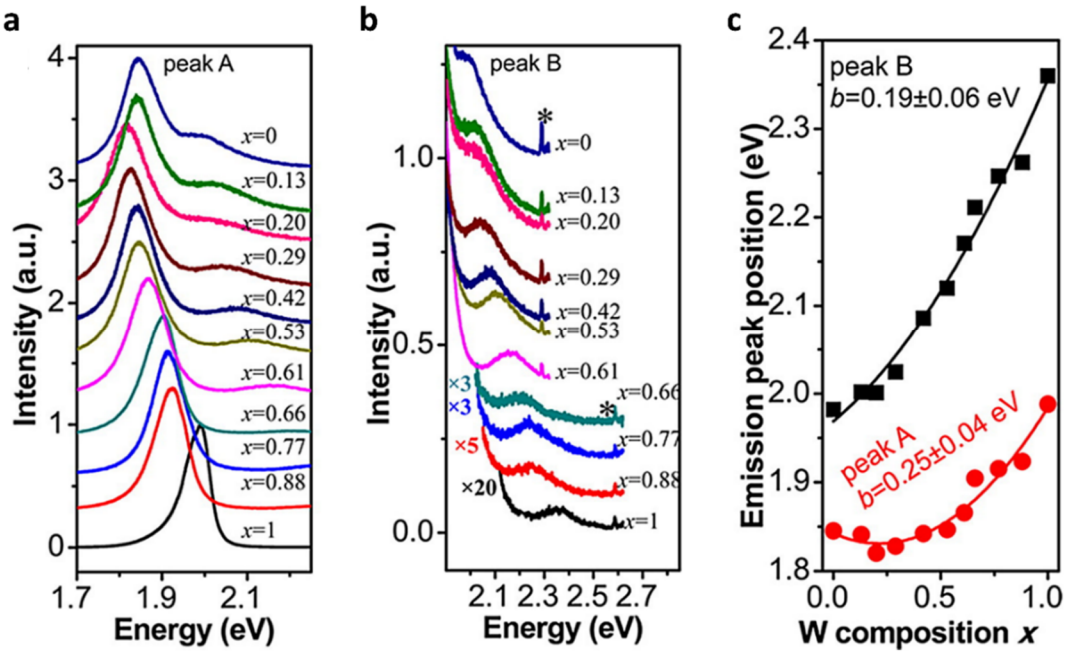


Figure 3.32 *(a) A exciton and (b) B exciton emissions of monolayered $Mo_{1-x}W_xS_2$ as a function of the W composition x. The PL intensity is normalized by the maximum A intensity at 1.82eV. The spectra were collected using 514.5nm (for x=0-0.61) and 457.9nm (for x=0.66-1) lasers. The peaks marked by * are Raman peaks of the Si substrates. (c) Composition-dependent emission energies for A and B excitons. The red and black lines are parabola fittings for A and B giving a bowing parameter b of 0.25±0.04eV and 0.19±0.06eV, respectively. Adapted from Ref. [261].*

Sasaki et al. have reported the CVD synthesis of monolayered WS_2 domains substitutionally doped with Nb at the W sites at rate of approximately 0.5% [95]. Unlike Mo doping of WS_2, Nb doping led to the appearance of new PL peaks with energies in the range 1.4-1.6eV at room temperature, which are lower than the optical bandgap (1.8eV), and intensities exhibiting a clear saturation behaviour with increasing excitation power. These results suggest that the observed PL peaks can be assigned to the emission from impurity states generated by the substitution of Nb [95].

Nb-doped WS_2 monolayers with a crystal size of ~30μm have been grown onto SiO_2/Si and quartz substrates by using the halide-assisted atmospheric pressure CVD method reported by Li et al. [245]. The growth substrates and a mixture of WO_3 (35mg), Nb (5mg) and NaCl (15mg) powders were loaded into the centre of a quartz tubular furnace, while S flakes were placed at the upstream zone of the furnace at 35cm from the centre. The furnace was filled with Ar flowing at 200sccm under atmospheric pressure and gradually heated to 830°C over a period of 45min. When the substrate temperature reached the set point, the S source was heated at 200°C for 15min through a second heater and the quartz tube was then readily cooled down by using an electric fan.

The Nb-doping level in the as-grown monolayered WS_2 flakes (Fig. 3.33*a*) was estimated to be ~0.55% via a statistical analysis of annular dark-field STEM images (Fig. 3.33*b-d*) and its substitutional nature was studied by Raman and PL spectroscopy. In addition to the major 2LA, E^1_{2g} and A_{1g} Raman modes for WS_2 [38], Nb-doped WS_2 exhibited two novel peaks located at 379cm^{-1} and 401cm^{-1} in spite of the very low Nb concentration (0.55%) probably due to a resonance Raman effect (Fig. 3.34*a*) [95][265]. In a previous study on $Nb_{1-x}W_xS_2$, only a single peak at 383.4cm^{-1} was observed for x=0.92 and it was assigned to the 2H-type NbS_2-like A_{1g} mode [262]. Further, similar novel Raman peaks at 374cm^{-1} and 394cm^{-1} have been also observed in CVD-grown W-rich monolayered $Mo_{1-x}W_xS_2$ alloys (x=0.5-0.9), where the low frequency peak at 374cm^{-1} was interpreted as a MoS_2-like E^1_{2g} mode from the polarization properties of Raman intensity [95][259][266]. Within this interpretation, the observed shift (of ~5-7cm^{-1}) in Raman frequencies has been attributed to the difference in binding energy between the Nb-S and W-S bonds [95].

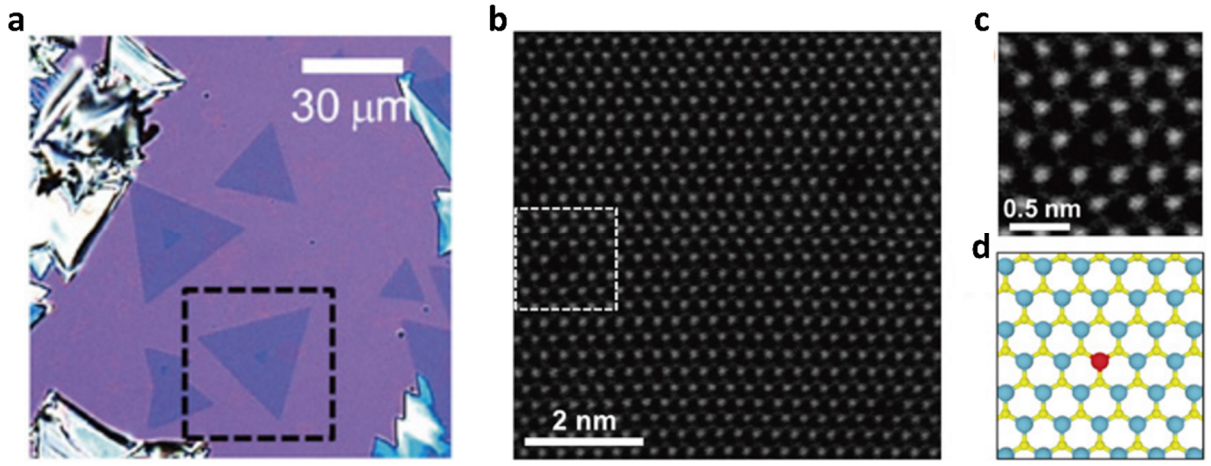


Figure 3.33 *(a) Optical image of typical Nb-doped WS_2 crystals grown onto SiO_2/Si by halide-assisted atmospheric pressure CVD. The white crystals are multilayered domains. (b) Annular dark field (ADF)-STEM image of monolayered Nb-doped WS_2. Because of their large atomic weight, W atoms exhibit a brighter ADF contrast than Nb and S atoms. (c) Enlarged ADF-STEM image of the area indicated by a white box in (b), showing a dark spot at a W site, which can be assigned to the substitution of W atoms with Nb. The overall ratio of dark spots was estimated to be 0.55±0.03% through statistical analysis of ADF-STEM images obtained at six different positions of the same flake. (d) Structure model of the same area of (c) where the blue, red and yellow spheres indicate W, Nb and S atoms, respectively. Adapted from Ref. [95].*

In contrast to Mo-doped WS_2 [259][261][267], Nb-doped WS_2 exhibited new PL peaks at 1.4-1.6eV in addition to the emission at ~1.9eV of monolayered WS_2 (Fig. 3.34*b*). The observed low-energy peaks have been assigned to emissions from localized excitons trapped in the potential induced by Nb atoms, whereas the peak at ~1.9eV has been attributed to the emission of free neutral and charged excitons. Further, the doping-induced PL emission at 1.39eV is enhanced near the edge of the triangular domain, whereas the emission at 1.92eV becomes more intense in the interior of the triangle (Fig. 3.34*c-f*). These results indicate that individual domains have a composition gradient of Nb with increasing Nb concentration towards the edges [95].

Because individual Nb-doped WS_2 crystals exhibit compositional gradients, the synthesis process reported in this work could be used to fabricate TMDs atomic layers with controlled defect sites. This would be useful to investigate the effects of the impurity concentration on various chemical and physical

properties, such as chemical and catalytic reactivity, charge transfer, quantum yield, valley polarization and single photon emission. It is worth noting that the resultant Nb concentration of 0.55% is significantly smaller than the initial Nb:W atomic ratio of 26:74 for the precursors, indicating a very low supply rate of Nb probably due to its fast oxidation and formation of Nb_2O_5 crystals [95]. Therefore, the suppression of Nb oxidation would be desirable and may be achieved using an alternative W precursor.

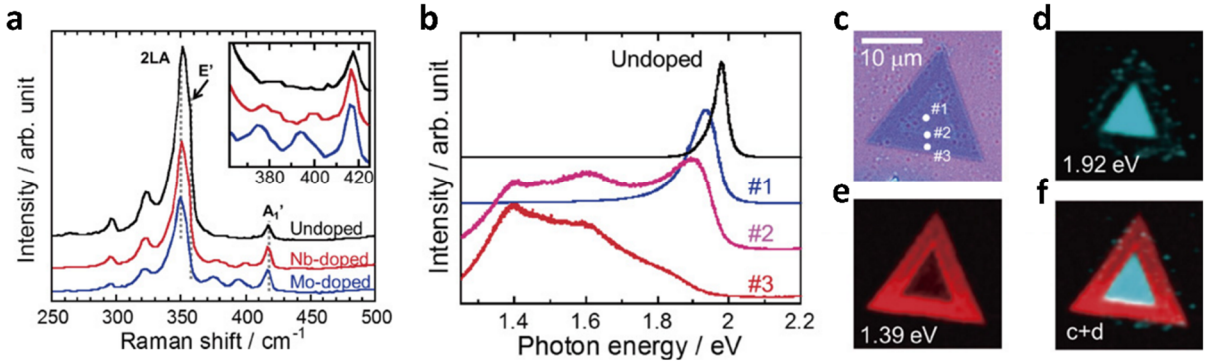


Figure 3.34 *(a) Normalized Raman spectra of undoped, Nb-doped and Mo-doped WS_2 monolayers. (b) Normalized PL spectra of undoped and Nb-doped WS_2 monolayers at the three positions indicated in (c). (c) Optical image of a typical monolayered Nb-doped WS_2 flake and (d-f) PL intensity maps of the same flake where cyan and red colours indicate the PL emissions at 1.92eV and 1.39eV, respectively. Adapted from Ref. [95].*

3.5. CONCLUSIONS

Within the family of group VI-TMDs, atomically thin WS_2 has emerged as a unique candidate for future nanotechnologies due to its high electrical mobility, intense photoluminescence emission, large valence band splitting and good thermal stability. Nevertheless, practical device applications of atomically thin WS_2 rely on breakthroughs in the controllable and reproducible synthesis of high-quality and large-area material. While several research groups have reported a successful CVD growth of WS_2 atomic layers, the experimental conditions (Table 3.1) and the quality of the deposited material vary significantly. As a matter of fact, to date the large-scale synthesis of high-quality and large-area monolayered WS_2 with spatial homogeneity and good electrical performance remains an unsolved challenge and it is yet to see its full realization. Typically, tungsten oxide and sulphur powders are used as metal and chalcogen precursors, respectively, due to their low toxicity compared to halides and organometallic compounds, and effective substitution of O by S. However, as they have significantly different vapour pressures, the delivery of both precursors to the growth substrate at a controlled flux requires a careful optimization of the growth temperature, pressure and carrier gas flow. In particular, recent reports have shown that high temperatures (>925°C) and low pressures (~1Torr) are required to achieve a sufficient vapour-phase flux of W precursor to the substrates, yet yielding to sparsely distributed flakes with lateral size not exceeding several tens of microns. These growth requirements are partly relaxed when WO_3 is placed in direct contact with the substrates. However, this approach prevents a controllable deposition of uniform large-area WS_2 domains. Further, while the use of more volatile or gaseous W-containing precursors such as WCl_6, $W(CO)_6$ and $WOCl_4$ has been reported, the quality of the material and growth rate had to be compromised. Therefore, since structural defects in CVD-grown TMDs (such as sulphur vacancies, adatoms, antisite defects and dislocations) introduce localized states in the bandgap leading to hopping transport behaviour and to a decrease in the carrier mobility, a systematic study on the factors which affect the synthesis of high-quality WS_2 has still to be developed and alternative W precursors which effectively decompose and undergo a complete sulfurization at molecular level must be identified. Finally, the vapour-phase synthesis of atomically thin WS_2 incorporating different transition and post-transition metals still remains a largely unexplored territory.

4) CHARACTERIZATION TECHNIQUES

4.1. INTRODUCTION

A number of different state-of-art characterization techniques are required to obtain information on the chemistry, morphology, crystallinity, optical and electrical properties of TMDs atomic layers. In this chapter, we explain the basics of the experimental techniques which have been used to characterize the CVD-grown WS_2 materials, which include microscopies (SEM, AFM, TEM), spectroscopies (Raman, PL, XPS), XRD and electronic devices.

4.2. SCANNING ELECTRON MICROSCOPY (SEM)

High-resolution scanning electron microscopy (SEM) has been employed to probe the morphology of the WS_2 materials. Thus, lateral size, distribution and density of WS_2 flakes have been characterized (Chapters 5-7). SEM imaging is carried out by rastering a high-energy (1-30keV) focused electron beam under high vacuum ($<10^{-5}$mbar) onto a sample and detecting the scattered electrons in the vicinity of the surface (Fig. 4.1*a*) [268][269][270]. The incident electron beam interacts with the sample generating backscattered electrons, secondary electrons, Auger electrons, characteristic X-rays, fluorescent X-ray and continuum X-ray (Fig. 4.1*b*). In this thesis, we have exploited backscattered electrons and secondary electrons to gain information about the CVD grown-WS_2. Backscattered electrons are a small fraction of the beam electrons which undergo elastic scattering with the atoms of the sample, while secondary electrons are the result of the inelastic scattering between the beam electrons and the sample atoms. In backscattered electron (BSE) imaging mode, where a specialized detector can select predominantly BS electron to form an image of the sample, the spatial resolution is limited to ~100nm due to a large beam-

sample sampling volume. While using a specialized detector to selectively collect secondary electron (SE), the spatial resolution that can be achieved is ~2-10nm due to the much smaller sampling volume of the secondary electrons as compared to the backscattered electrons (Fig. 4.1*b*) [270].

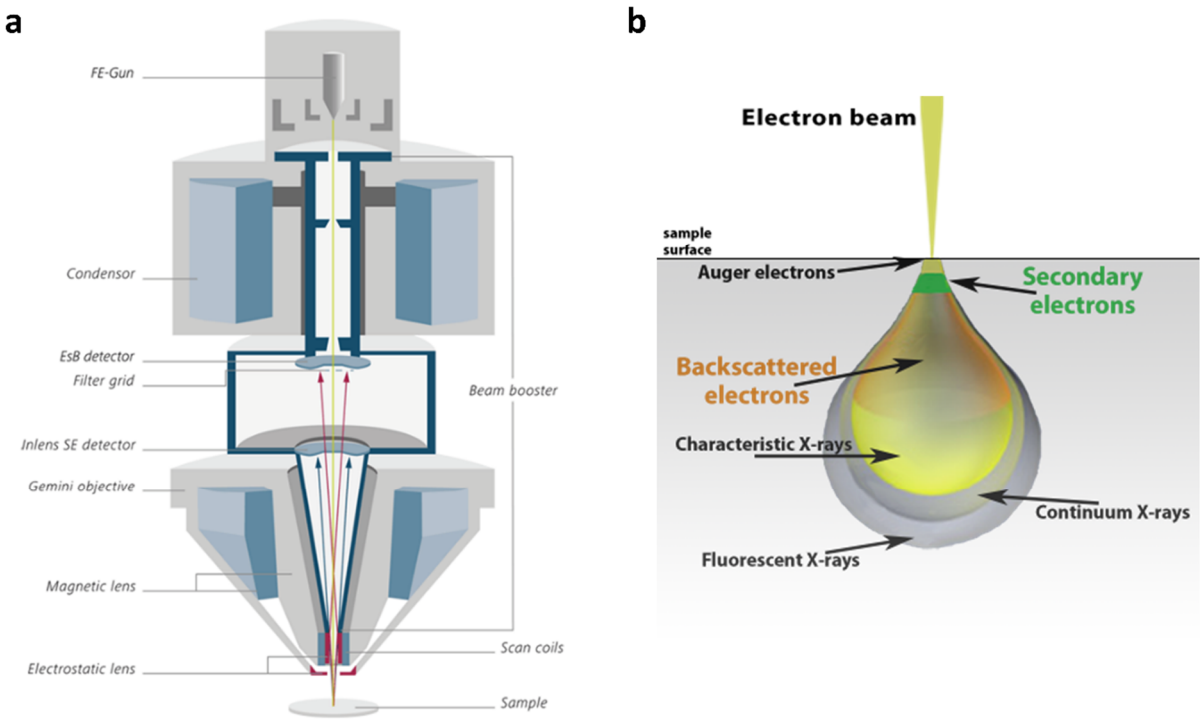


Figure 4.1 *(a) Schematic cross section of a SEM optical column. Adapted from www.zeiss.com. (b) Schematic of the electron beam-sample interactions. Adapted from www.nanoscience.com.*

High-resolution SEM characterization of the WS_2 samples was conducted using a high-resolution field emission gun SEM (FEG-SEM, Gemini 1525) equipped with an In-Lens secondary electron detector. In FEG-SEMs, a field emission gun is used to generate an electron beam with incident spot size much narrower (<5nm on a flat surface) and with significantly higher current density than what achievable in conventional thermionic emitters-based SEMs, resulting in improved spatial resolution and signal-to-noise ratio [271]. As WS_2 is atomically thin, the samples were imaged in the secondary electron imaging mode using an in-Lens SE detector. Contrarily to conventional SE detectors, which are located at a certain angle with respect to the sample surface, the in-Lens SE detector is placed inside the electron column of the microscope and is arranged rotationally symmetric around the optical axis (Fig. 4.1*a*). Due to its proximity to the sample surface and high sensitivity to low-energy secondary electrons (<few tens of

eV), the in-Lens detector allows for high-contrast imaging of atomically thin materials such as graphene and TMDs, in particular at low voltages (~1-5kV) and small working distances [269]. Further, it has been shown that under these working conditions thinner layers of graphene appear much brighter than thicker layers as a result of the attenuation of the secondary electrons from the underlying insulating substrate by multilayered graphene, thus allowing for the identification of the number of layers [269]. Although very low accelerating voltages of the incident electron beam (1kV) result in high-contrast imaging and low damaging/charging of the sample surface at high magnification (>20000X), they also reduce the number of secondary electrons produced. Thus, in our case the voltage was set to be in the range 5-10kV in order to obtain sharp images due to a poor signal to noise ratio under 5kV [269][272]. Finally, since elements with a greater atomic number Z yield more backscattered electrons than lower Z-elements, resulting in brighter image areas, the BSE imaging mode has also been employed to obtain compositional information for In-doped WS_2 (Chapter 7).

Energy dispersive x-ray spectroscopy (EDS) is a complementary characterization technique which can be carried out within the same experimental setup of the SEM by using the electron beam to excite core shell electrons to the valence band. The decay of electrons from the valence band back to the core bands releases x-rays which can be picked up by a detector and whose energy is uniquely associated with the transition energy of each elements. EDS was employed to investigate the elemental composition of bulk crystals sometimes observed on the growth substrate after the CVD of In-doped WS_2 (Chapter 7).

4.3. ATOMIC FORCE MICROSCOPY (AFM)

Atomic force microscopy (AFM) is a type of scanning probe microscopy used for manipulation, force measurement and imaging of surfaces morphology with demonstrated resolution of the order of fractions of a nanometre. In this work, AFM has been used to obtain three-dimensional topologies of the as-grown and transferred-WS_2 flakes, and to measure their thickness and surface roughness (Chapters 5-7). Figure 4.2 shows the basic operating principle of a typical AFM where the information is acquired by “feeling” or “touching” the surface of the sample with a mechanical probe. The probe consists of a cantilever ending with a micro-fabricated ultra-sharp tip typically made of silicon or silicon nitride and

with a tip radius of curvature of the order of nanometres. The movement of the tip is controlled by piezo-electric actuators which are regulated through a feedback mechanism based on a proportional-integral differential (PID) system. The PID controller uses the signal from a photodiode which detects the reflection of a laser beam from the upper surface of the cantilever tip. When the tip is brought into proximity of a sample surface, forces between the tip and the sample (such as mechanical contact force, van der Waals forces, capillary forces, chemical bonding forces, electrostatic forces, magnetic forces, Casimir forces, solvation forces) lead to a deflection of the cantilever according to the Hooke's law [273].

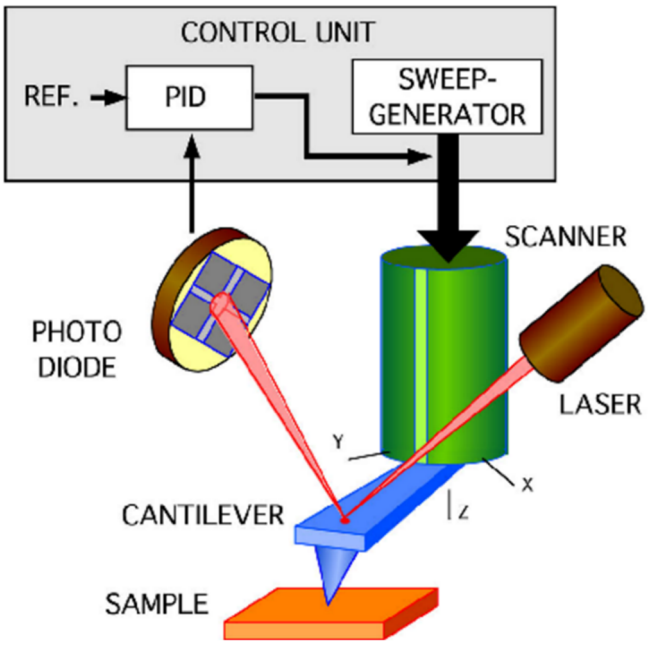


Figure 4.2 *Schematic diagram of the AFM working principle. Adapted from www.cds.caltech.edu.*

In contact imaging mode, the cantilever tip is “dragged” across the surface of the sample and the surface contours are imaged either by monitoring the deflection of the cantilever or, more frequently, by analyzing the feedback signal required to maintain the tip at a constant height [274]. While in tapping mode, the cantilever is driven to oscillate up and down at a constant frequency (at or near its resonance frequency) and amplitude (typically from several nanometers to 200nm) [274]. The forces acting on the cantilever as the tip gets closer to the sample (such as Van der Waals forces, dipole-dipole interactions and electro-static forces) change its oscillation amplitude. Thus, a tapping AFM image is obtained by monitoring the adjustments on the cantilever height above the sample to maintain a set amplitude [275]. The tapping mode is useful for characterizing two-dimensional materials as the damage and distortion

of the sample surface are minimized compared to the contact mode where the tip can "snap-in" the surface. However, the tapping imaging mode requires a longer acquisition time than the contact mode and the tip oscillation can induce surface deformations and artefacts [276].

A maximum lateral resolution of ~5nm can be achieved under ambient conditions by using a pristine Si or Si_3N_4 tip with a <5nm radius of curvature [277]. While the vertical resolution is expected to be in the order of a few Angstroms. However, due to contaminations of the tip and surface adsorbates, the lateral resolutions is typically reduced and the measured thickness of two-dimensional materials can be higher than the actual value [278]. Therefore, thickness measurements via AFM may overestimate the number of layers of atomically thin TMDs as reported in other studies as well [4][245] and thus be less reliable than Raman and PL characterization.

In this work, the thickness and surface topology of the WS_2 flakes have been examined using an AFM (Asylum MFP 3D) in tapping mode. The AFM probe consisted of a silicon nitride tip with a radius of curvature of ~8nm mounted onto a PPP-NCHR 20 Nanosensors cantilever.

4.4. TRANSMISSION ELECTRON MICROSCOPY (TEM)

Transmission electron microscopy (TEM) is a microscopy methodology in which a beam of electrons accelerated at voltages in the range of 60-300kV is transmitted through an ultrathin specimen (less than 100nm-thick) to form an image of the sample at significantly higher lateral resolution than what achievable with light microscopes (Fig. 4.3). The higher resolution is due to the smaller de Broglie wave-length of electrons which acquire significantly higher kinetic energies as compared to in SEM. The electron beam is usually generated by thermionic emission from a tungsten filament or by field electron emission and it is then accelerated under vacuum (~10^{-4}Pa) through an electric potential and focused on the sample using electrostatic and electromagnetic lenses (condenser and objective lenses). The transmitted electron beam through the sample contains information about the electron density, phase and periodicity of the sample and it is expanded using projector lenses to form a magnified and focused image onto a fluorescent screen or other imaging devices. In the typical bright-field imaging mode, the contrast formation at lower magnifications is due to the different absorption of electrons by the sample due to composition or thickness

variations. The lateral resolutions typically achieved are in the order of nanometres. Whereas at higher magnifications the image contrast intensities are modulated by complex wave interactions, displaying lateral resolution at the atomic level.

As the wavelength of high-energy electrons (100-400keV) is a few thousandths of a nanometer whereas the spacing between atoms in a solid is about a hundred times larger, the atoms of the TEM sample act as a diffraction grating for the incident electron beam. By adjusting the magnetic lenses such that the back focal plane rather than the image plane is in correspondence with the imaging screen, a diffraction pattern can be obtained. By inserting a selected area aperture (thin strip of metal containing holes with different sizes) into the beam path below the sample holder, the diffraction pattern from the selected area (SADP) can be obtained. The SADP can be used to identify crystal structures and defects within areas significantly smaller (several hundred nanometers in size) than what achievable through X-ray diffraction (several centimeters in size).

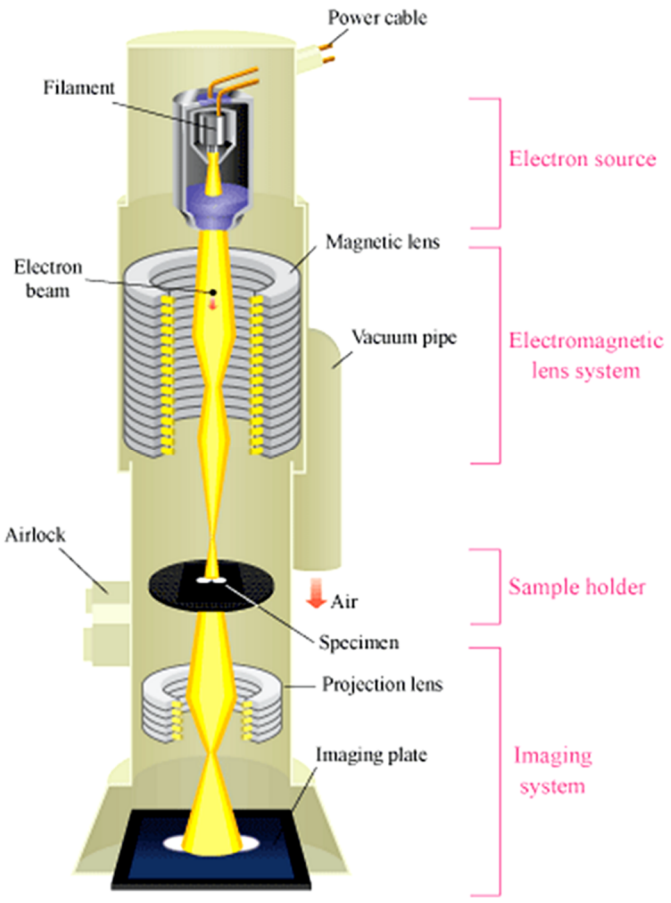


Figure 4.3 *Schematic cross section of a typical TEM column. Adapted from www.hk-phy.org.*

In this work, TEM has been used to visualize the crystal structure of CVD-grown WS_2 and to determine the lattice parameters (Chapter 6). TEM analysis was carried out on a FEI Titan 80-300 S/TEM operated at 80kV and equipped with a monochromator and a Cs aberration image corrector. Focal series images of a representative WS_2 flake were acquired at different objective lens focus values (using a spherical aberration coefficient Cs ~ -4μm). Exit-wave reconstruction was performed using TrueImage software (FEI).

4.5. RAMAN AND PHOTOLUMINESCENCE (PL) SPECTROSCOPY

Raman spectroscopy is a versatile, non-destructive and high-throughput spectroscopic methodology for characterizing atomically thin materials. In this work, micro-Raman spectroscopy has been extensively used to identify the chemical nature, structure and layer number of CVD-grown materials (Chapters 5-7). The Raman process relies on the inelastic scattering of incident monochromatic light in the visible, near infrared and near ultraviolet range by the sample due to interactions between the incident light and lattice vibrations (phonons) [279]. These interactions can involve either emission (Stokes scattering) or absorption (anti-Stokes scattering) of phonons and result in an energy shift of the scattered photons (measured in cm^{-1}) which depends on the specimen electronic structure and phonon dispersion. Therefore, by analysing the photons scattered by the sample it is possible to acquire information about the vibrational modes in the material [279].

In a typical Raman spectrometer, the sample is irradiated with a laser beam and the elastically scattered radiation with the same wavelength of the excitation source (Rayleigh radiation) is filtered out by using a filter, whereas the inelastically scattered photons (Raman radiation) are dispersed onto a CCD detector and analysed (Fig. 4.4). The same experimental setup can also be used to detect light emitted (photoluminescence) from semiconducting materials excited through a light-source with larger energies than the materials band-gap. Since, as discussed in Section 2.3.2, the PL intensity of group VI-TMDs significantly increases from the multi- to the mono-layered form due to the indirect-to-direct band-gap transition, and since the PL energy and line shape values are used to assess the material structural quality,

PL spectroscopy has been often used in this work to identify the layers number, structural and optical quality of CVD-grown materials (Chapters 5-7).

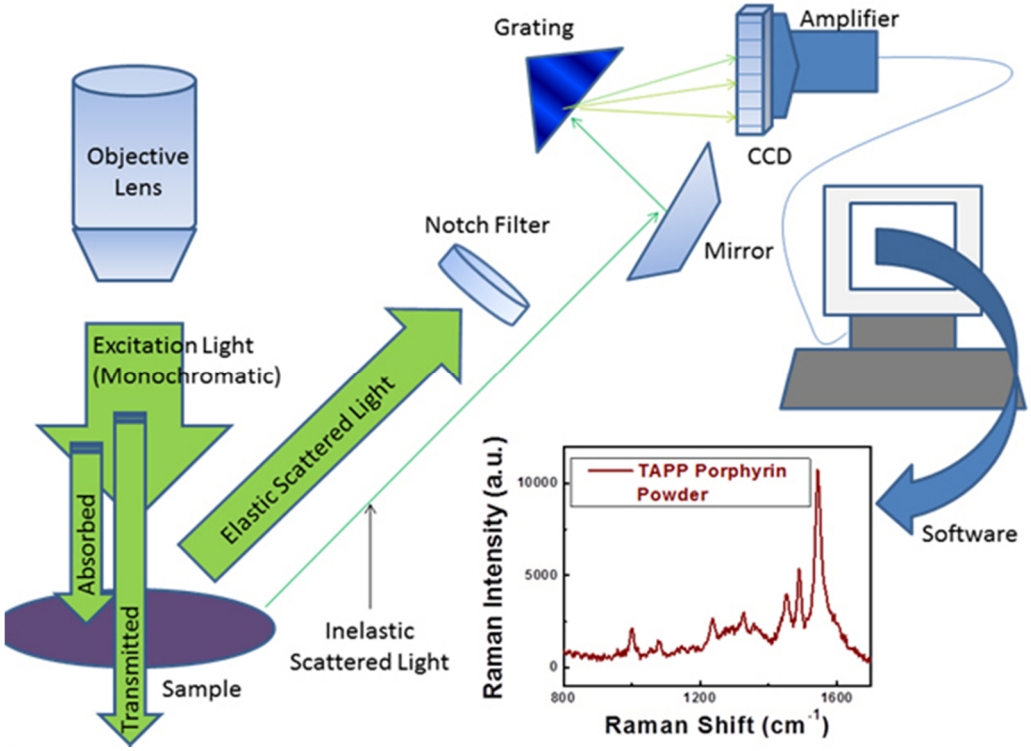


Figure 4.4 *Schematic for the acquisition process of Raman spectra. Adapted from www3.nd.edu.*

Raman and PL spectra and spatial maps were collected using a WITec confocal Raman system and a Renishaw inVia spectrometer (Chapters 5-7, Appendix). All the measurements were carried out at room temperature in atmospheric conditions. The data were recorded in the back-scattering geometry using a 532nm (2.33eV) laser excitation. A 100x objective lens with a numerical aperture of 0.9 was used to focus the laser light on the samples. The laser power and exposure time were set to be 1.6mW and 0.1s for Raman maps, 0.32mW and 0.1s for PL maps, $3.2 \cdot 10^{-4}$mW and 10s for extended PL single spectra. A grating of 1800line/mm was used to achieve spectral resolution of ~1.5cm^{-1}. The silicon Raman mode at 520cm^{-1} was used for calibration prior to measurements. Data analysis was done by using Origin and MATLAB software.

4.6. X-RAY DIFFRACTION (XRD)

The diffraction of X-rays by a periodic atomic structure of a material allows the study of its crystallinity. This occurs via analysis of the specific directions of the crystal atoms-induced diffraction of an incident x-ray radiation along the lattice planes on the bases of the Bragg's law, which states that the diffraction angle is related to the distance between the reflecting planes. Due to variations in the lattice parameters for different chemical compounds, the diffraction angle is thus characteristic for a given material. Further, the rotation of the stage upon which the sample is mounted allows for the analysis of multiple different planes, thus providing lattice structural information (Fig. 4.5).

In this work, XRD has been used to determine the chemical composition of residual reaction powders to gain insights into the reaction mechanism (Chapter 6) and to study the crystal structure of In-doped WS_2 crystals (Chapter 7). The XRD patters were collected via a Panalytical X'Pert Pro diffractometer using a Cu x-rays. Scans were performed in the 2θ range 5-80° with a typical step size of 0.033°. X'Pert Highscore plus software was used to match the database.

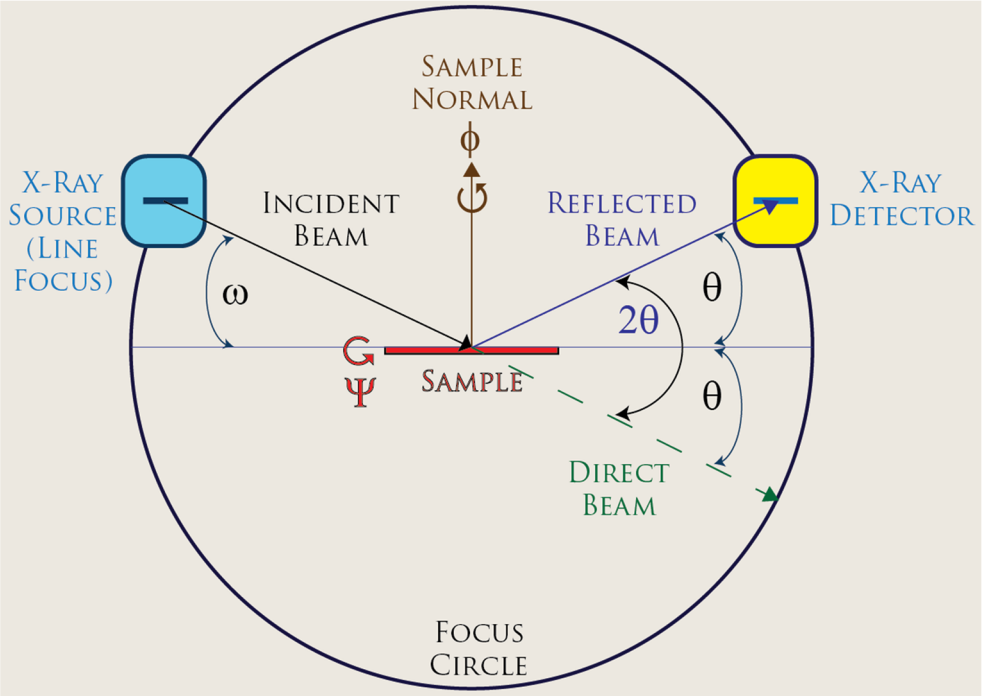


Figure 4.5 *Schematic of a typical XRD diffractometer. Adapted from http://biophysics.fsu.edu/soma/projects/powder-xrd-csl/.*

4.7. X-RAY PHOTOELECTRON SPECTROSCOPY (XPS)

X-ray photoelectron spectroscopy (XPS) is a non-destructive surface sensitive spectroscopic technique that allows the determination of the chemical composition of materials surfaces. By irradiating a material with a beam of X-rays and by dispersing the photoelectrons emitted as a function of their kinetic energy it is possible to gain information about the chemical bonding present in the first ~10-50nm of the material surface (Fig. 4.6). As the energy of X-rays with a particular wavelength is known (1253.6eV for Mg K_α X-rays), the binding energy of each emitted electron can be determined by using the following energy conservation equation:

$$E_{binding} = E_{photon} - (E_{kinetic} + \Phi)$$

where $E_{binding}$ is the binding energy of the electron, E_{photon} is the energy of the incident photons, $E_{kinetic}$ is the kinetic energy of the emitted electron measured by the detector and Φ is an adjustable instrumental correction factor which depends on both the spectrometer and the specimen being analysed. A typical XPS spectrum results as a plot of the number of electrons detected versus their binding energy. As each element produces a characteristic set of spectral peaks at characteristic binding energy values, which correspond to the electron configuration of the specific atoms (e.g., 1s, 2s, 2p, 3s etc.), the elemental composition of the sample surface can be determined. Further, as the number of detected electrons for each spectral peak is directly related to the concentration of the elements within the XPS sampling volume, atomic percentage values can also be calculated.

In this work, XPS has been used to corroborate the chemical purity and the absence of unintentional doping with alkali metals and halogen atoms of CVD-grown WS_2 samples (Chapter 6) and to estimate the stoichiometry of CVD-grown In-doped WS_2 samples (Chapter 7). XPS spectra (Chapter 6) were acquired on a custom made ultra-high vacuum ($<10^{-9}$ mbar) XPS system equipped with a VG Escalab Mk-II electron analyzer and a twin anode (Al/Mg) non-monochromatized x-ray source (Omicron DAR 400). All the measurements were taken in quasi-normal emission (5° off) at room temperature using a pass-energy of 20eV, an energy step of 0.1eV and the Mg K_α emission line as exciting radiation. XPS spectra (Chapter 7) were also acquired on a different XPS system (Thermo Scientific K-Alpha) using

similar conditions (room temperature, pass-energy of 20eV, energy step of 0.1eV, Al K_α X-ray source). The data were analyzed using the Avantage software package.

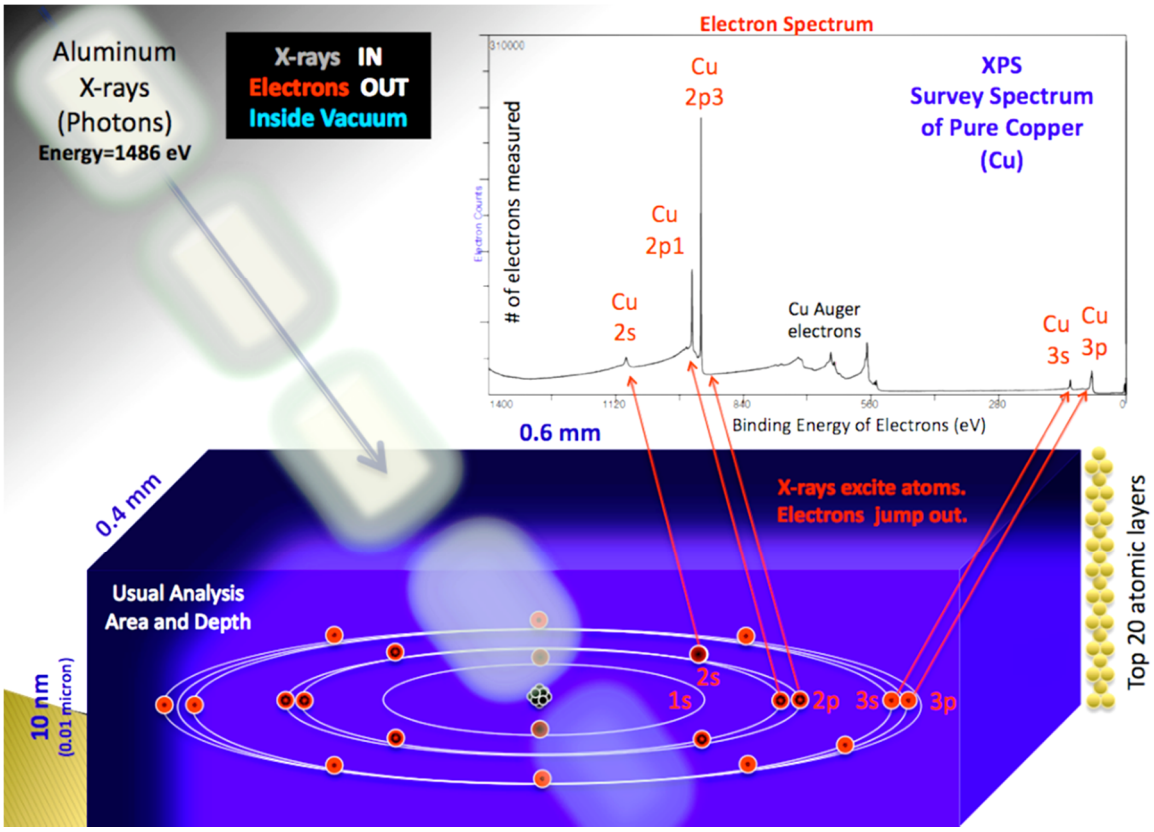


Figure 4.6 *Schematic of the basic XPS physics. Adapted from https://upload.wikimedia.org.*

4.8. TRANSFER PROCEDURE

For TEM analysis and field-effect mobility measurements (Chapter 6) the CVD-grown WS_2 flakes were transferred from the growth substrate to carbon-coated TEM grids and fresh SiO_2/Si substrates, respectively. The transfer was achieved by depositing a 350nm-thick PMMA film onto the target sample, which was then immersed in a KOH solution (0.1M) until detachment of the PMMA from the SiO_2/Si substrate. The PMMA/WS_2 film was subsequently scooped out with a new SiO_2/Si substrate, repeatedly washed with deionized water and finally immerged in an acetone bath at 45°C for 20min to dissolve the PMMA film.

4.9. DEVICE FABRICATION AND ELECTRICAL MEASUREMENTS

For field-effect mobility measurements (Chapter 6), mono- and bi-layered WS_2 flakes-based FETs were fabricated after transferring the WS_2 flakes from the growth substrate to a fresh Si substrate with a thermally deposited 285nm-thick SiO_2 layer, where Si is highly p-doped and acts as a global gate electrode while SiO_2 serves as gate dielectric. The FETs were fabricated on dried $WS_2/SiO_2/Si$ samples. In addition to the current bearing contacts (source and drain), two additional voltage probes were added to each FETs in order to eliminate the contribution of the contacts and thus allowing for an accurate determination of the channel conductance. Both the current bearing leads and voltage probes were patterned simultaneously by using a standard electron beam lithographic process. The source, drain and voltage probes consisted of 50nm-thick Au while the electronics leads consisted of 5nm-thick Ti and 50nm-thick Au. A two-step annealing process followed the FETs fabrication, where the devices were first annealed at 200°C for 2 hours under H_2/Ar (10/90) flowing at atmospheric pressure to etch residues of PMMA (used as electron resist for the lithography step) and then baked at 115°C for 60 hours under high vacuum (~10^{-6} mbar) to promote the desorption of water molecules from the channel surface.

The FETs were characterized after the second annealing step inside the vacuum chamber at a constant pressure of ~10^{-6}mbar. The drain electrode was biased with a low noise source-meter while the source electrode was grounded throughout the measurements. Further, an additional source-meter was used to bias the global gate electrode with respect to the source. The transistor current I_{ds} was measured using an ammeter while the potential difference across the voltage probes $V_{A\text{-}B}$ was measured using a voltmeter. The measurement set-up is shown schematically (not to scale) in Figure 6.16*a*. The gate bias range was extended up to the point where the channel current reaches a linear regime, described by the equation [280][281][282]:

$$I_d=\mu_n C_{ox}(W/L)((V_{gs}-V_{th})V_{ds})$$

μ_n being the electron field-effect mobility, C_{ox} the SiO_2 capacitance, W and L the channel's width and length, V_{th} the threshold voltage, V_{ds} and V_{gs} the source-drain and source-gate voltages respectively. The field-effect mobility of mono- and bi-layered WS_2 was thus calculated from the linear region of the FET transfer curve (marked with a red-dashed line in Fig. 6.16*c*) by using the equation [280][281][282]:

$\mu_n = C_{ox}^{-1}(d\sigma/dV_{gs})$

σ being the channel conductivity, obtained from the formula $\sigma = (L\, I_{ds})/(W\, V_{A\text{-}B})$ [280][281][282], while the oxide capacitance C_{ox} was estimated to be 115μFm^{-2} from $C_{ox} = \varepsilon_0\, \varepsilon_r / d_{ox}$, where d_{ox} is the oxide thickness and ε_0 and ε_r are the vacuum permittivity and relative permittivity of SiO_2, respectively [280][281][282].

For resistance vs temperature measurements of In-doped WS_2 samples (Chapter 7), individual flakes were contacted in a two-wire configuration through a standard photolithographic technique by masking the photo resist (AZ 5214E) and subsequently evaporating Ti (5nm) and Au (30nm) contacts through thermal evaporation and sputtering, respectively. The devices were then mounted on a micro-manipulated six-arm cryogenic probe station to perform electrical characterization. The main chamber was operated at a pressure of 10^{-5}mbar and cooled down by purging liquid N_2 through the cold head and cryogenic inlet. The conductivity σ of the flakes was estimated by using the formula $\sigma = L/(R\, A)$, where L is the length between the contacts (~3μm), R is the measured resistance and A is the cross-sectional area of the flake (0.9nm · ~40μm). As discussed in Chapter 7, the conductivity values as a function of temperature depicts a semi-metallic like behaviour. Kiethley 2410 source measure unit and Lakeshore temperature controller were used to measure the transport properties.

4.10. CONCLUSIONS

In this chapter, the basic physical theory, instrumental apparatus and operating conditions of the main characterization techniques required to obtain information on the chemistry, morphology, optical and electrical properties of WS_2 atomic layers were discussed. Different experimental techniques have been employed throughout this work to generate a structure-optical-electrical properties correlation of WS_2 crystals grown by using different precursors. To this aim we have presented the basics of: SEM, AFM, TEM, Raman spectroscopy, PL, XPS and XRD. Further we have described the fabrication of FET devices, which have been utilized to characterize the carrier mobility and on/off ratio of WS_2.

5) TUNGSTEN TRIOXIDE-BASED CVD SYNTHESIS OF WS_2

5.1. INTRODUCTION

As discussed in Chapter 3, the most extensively used CVD method to synthesize mono- and few-layered WS_2 crystals is a one-step process consisting in the co-evaporation of a W precursor and S powders in a horizontal tubular furnace in the presence of a carrier gas. In particular, the oxide precursors have seen a widespread use [4][173][183][184][185][186][187] mainly due to their low toxicity compared to halides/organic compounds, easy handling and effective replacement of the O by S [24]. However, due to their high sublimation temperature and low vapor pressure, the controlled evaporation and deposition of the precursors onto the growth substrate requires high temperatures (up to 1070°C) and low pressures (~1Torr) [43][183]. The synthesis of WS_2 from WO_3 involves a topotactic transformation [283] which generally yields to sparsely distributed domains onto amorphous [4][173][183][186][187] or crystalline [184][185] substrates.

In this chapter we investigate the WO_3-based CVD synthesis of WS_2 from the early stages of nucleation up to formation of film-like continuous domains over hundreds of micron-sized areas. To achieve this, a parametric study of the CVD reaction variables, such as the amount of precursors, reaction time, growth temperature, precursors-substrate distance, heating profile of S and carrier gas flux, has been developed. To provide important insights into the factors that affect the growth of WS_2 we used a CVD setup which allowed the control of each precursor temperature. In a typical growth, WO_3 powders were heated to high temperatures in a quartz tubular furnace, whereas S powders were evaporated either due to the heat coming from the furnace itself or by using a second heater module. Both the WO_3 and S vapours were carried downstream to the growth substrate by pure argon gas under vacuum. Further, the use of alternative CVD setups, such as the use of a second one-end sealed quartz tube containing WO_3

powders sandwiched between two substrates, has also been explored. As a result of this study, we have identified the basic principles that govern the growth mechanism of WS_2 atomic layers from WO_3 and S powders, understanding how different synthesis conditions lead to different layer numbers, size and density of the WS_2 nuclei. Further, we have identified the main limitations of the oxide precursors which prevent a controllable synthesis of high-quality and large-area monolayered WS_2, motivating the search for alternative W precursors (Chapter 6).

5.2. SULFUR TEMPERATURE: ≥250°C

The first set of samples was synthesizes using a single-zone CVD tubular furnace (Fig. 5.1). An alumina crucible containing WO_3 powders (0.3-1.5g, ≥ 99.5%, Sigma Aldrich) was loaded at the central zone of the furnace, whereas a second crucible containing S powders (0.6-1.5g, ≥ 99.5%, Sigma Aldrich) was loaded upstream outside the heating zone. A 500µm-thick Si substrate with 285nm of SiO_2 thermally deposited on top was sequentially cleaned in an ultrasonic bath with acetone, isopropanol and deionized water for 15min each step, followed by 2h in H_2SO_4/H_2O_2 (3:1). SiO_2/Si was then blow dried with high purity N_2 gas, exposed to O_2 plasma for 5min and finally loaded in the upstream zone of the furnace at a distance of 1-10cm from the WO_3-containing crucible. This CVD-approach allows for a more uniform deposition of WS_2 crystals than placing the growth substrate above the metal precursor crucible.

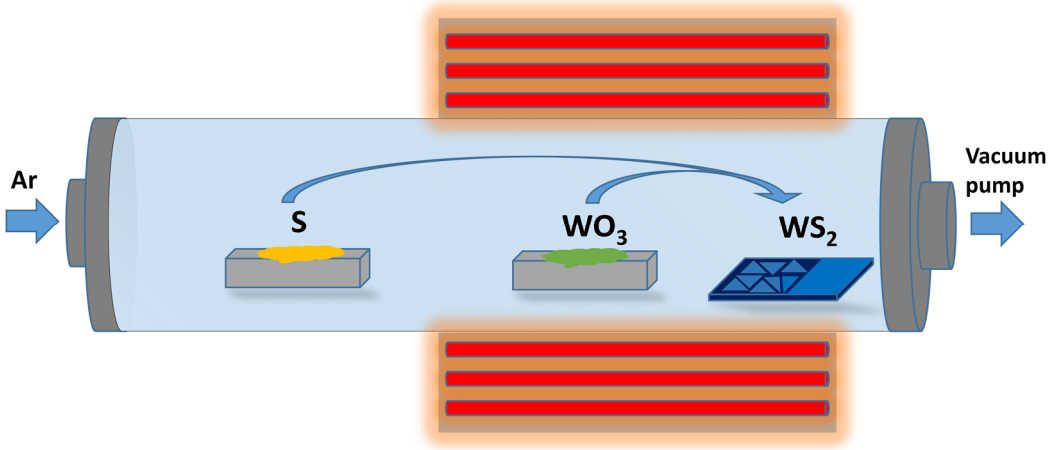


Figure 5.1 *Schematic of the single-zone CVD horizontal tubular furnace. The diameter of the quartz tube is 2inches.*

The syntheses were carried out at the moderately low pressure of 10^{-1}mbar under high purity argon gas flowing at 80sccm throughout the whole process. The furnace was heated up to 925-950°C at the rate of 15-25°C min^{-1}, held at these high temperatures for 6-45min and then naturally cooled down to room temperature. By monitoring the temperature with a thermocouple in air condition, we estimated that the zone in correspondence with the S-containing crucible position reaches ~250-350°C depending on its distance from the heating zone.

At the S evaporation temperature of ~250°C, a sparse distribution of WS_2 domains with lateral size of ~1-5μm and different thicknesses has been obtained (Fig. 5.2). However, the WS_2 flakes have irregular shapes in most cases (Fig. 5.2*b*-*c*) suggesting a low degree of crystallinity. They result to be embedded in a discontinuous matrix made of randomly arranged WS_2 nano-platelets (Fig. 5.2*e*). Since the edges of the platelets and any steps, stacking faults and near surface dislocations introduce electron states which act as preferential centres for the recombination of photo-generated charge carriers and flow of dark current [284], the obtained irregular WS_2 films are unsuitable for any device application. Raman spectroscopy has been used to identify the different phases and thickness of the flakes. Raman spectra collected on both WS_2 flakes and matrix (Fig. 5.2*f*) show the characteristic 2LA-E^1_{2g} and A_{1g} vibrational modes for WS_2 at ~350cm^{-1} and ~416cm^{-1}, respectively [38]. However, the peak shift between 2LA(M) and A_{1g} is >66cm^{-1} indicating bulk WS_2 [38].

By controllably shifting the S-containing crucible towards the high temperature-zone of the furnace, it has been possible to increase the temperature at the S powders from ~250°C to ~350°C when the furnace reaches 950°C. At the S evaporation temperature of ~350°C, particulate materials such as nano-wires (Fig. 5.3*a*) and dot-like structures (Fig. 5.3*b*) are formed. Raman characterizations has ascertained that these structures are not made of WS_2 as they do not show any WS_2 Raman features (Fig. 5.3*c*). As under SEM analysis these structures appear to charge more than a pure WS_2 phase, we believe that they consist of WO_3-rich phases [285][286](WO_3 is a semiconductor with a larger band-gap than WS_2) and they are likely to be intermediate products formed either due to an insufficient supply of S or due to condensation phenomena during the cooling stage.

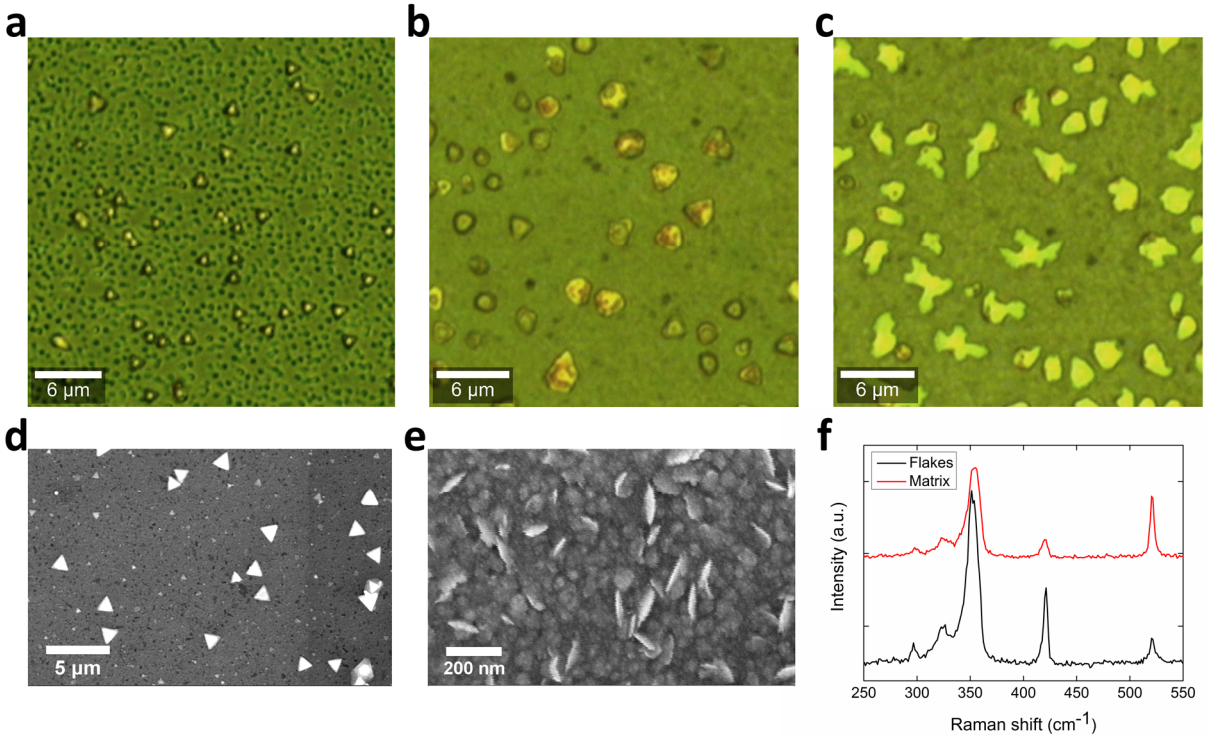


Figure 5.2 *(a-c) Optical images of ~1-5µm large-WS_2 flakes onto a SiO_2/Si substrate. (d) Low- and (e) high-magnification SEM images of the sample shown in (a), revealing the triangular shape of the flakes and the discontinuous morphology of the surrounding matrix, respectively. (f) Representative Raman spectra of both WS_2 flakes and matrix.*

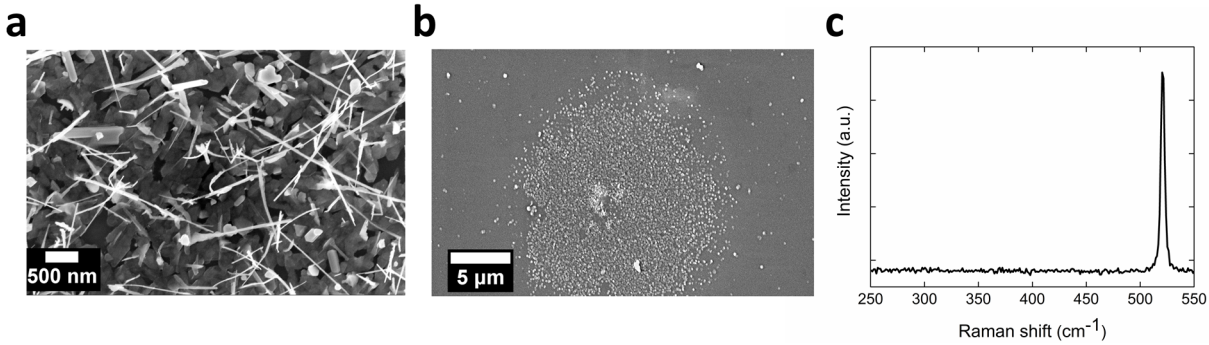


Figure 5.3 *SEM images of WO_3-rich (a) nano-wires and (b) dot-like structures onto SiO_2/Si. (c) Raman spectra of these structures not showing any WS_2 peaks.*

The fact that WS_2-phases (Fig. 5.2) versus WO_3-phases (Fig. 5.3) are formed by heating S powders at ~250°C and ~350°C, respectively, shows that the evaporation rate of S and therefore the duration of its supply are critical parameters in the CVD growth of WS_2, affecting its formation, crystal quality, shape and thickness. Decreasing the amount of precursors in the reaction chamber and/or the growth time in

order to decrease the amount of material deposited onto the substrate did not lead to reproducible results, likely due to instabilities in the S supply rate occurring for a very short time. The lack of a temperature control system for the S evaporation in the CVD setup used for this first set of samples did not allow us to decrease the S evaporation temperature below ~250°C, since this would mean shifting the S powders far away from the hot temperature zone and thus causing the condensation of S vapours in the upstream part of the quartz tube.

5.3. SULFUR TEMPERATURE: ~250°C

The second set of samples was synthesized using a single-zone CVD tubular furnace equipped with a heating belt wrapped around the low temperature zone of the tube and used as heating system for the S powders (Fig. 5.4). The cleaning of the SiO_2/Si substrates and their loading into the quartz tube together with the WS_2 precursors were performed in the same way as for the first set of samples. As before, the syntheses were carried out at low pressure (10^{-1}mbar with a base pressure of 10^{-2}mbar) under vacuum and Ar gas (flowing at 50-80sccm throughout the whole process). The furnace was heated up to 850-950°C at 25°C min^{-1}, held at these temperatures for 15-60min and then naturally cooled down to room temperature. The heating belt was switched on to 250°C when the furnace reached 700°C (temperature at which WO_3 begins to evaporate). Since the heating belt allows for a fast heating of the S powders, their evaporation rate is now much higher compared to the syntheses of the first set of samples (where the S powders were evaporated by using the heat coming from the WO_3-controlling furnace).

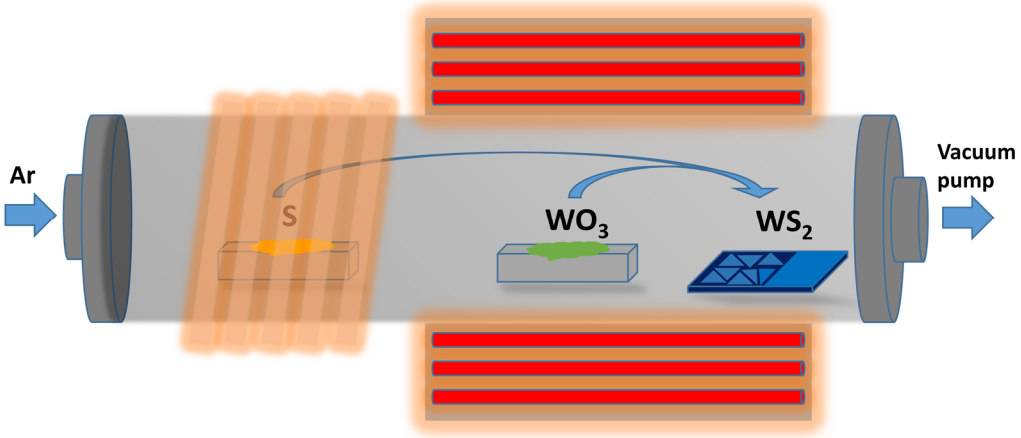


Figure 5.4 *Schematic of the single-zone CVD horizontal tubular furnace equipped with a heating belt.*

By evaporating 0.6g of S at ~250°C and 0.3g of WO_3 at 900°C for 30min, triangular WS_2 domains with lateral size up to 5μm were obtained (Fig. 5.5*a, b*). The representative Raman spectrum of the as-grown flakes is reported in Fig. 5.5*c*, exhibiting a peak separation between the E^1_{2g} and A_{1g} modes of ~66cm^{-1} which corresponds to the reported value for single-layered WS_2 onto SiO_2/Si (Section 2.3.2) [38]. It is worth noting that the formation of triangular-shaped flakes is due to the energetically preferred formation of zigzag sulphur edge terminated domains, which ultimately impart a triangular shape [246].

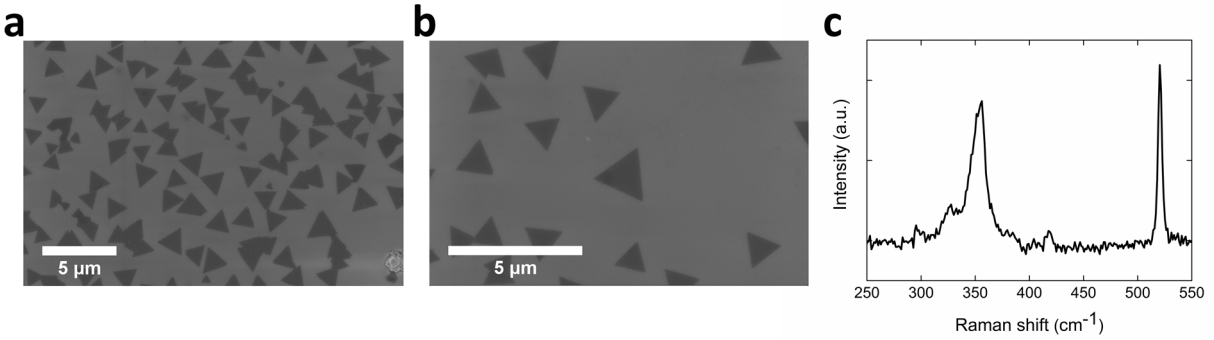


Figure 5.5 *(a) Low- and (b) high-magnification SEM images of triangular shaped WS_2 monolayers. (c) Representative Raman spectrum of the WS_2 triangles, revealing their monolayered nature.*

With the purpose of extending the WS_2 lateral extension, we have increased either the growth time or the amount of both WS_2 precursors. By increasing the growth time (from 30min to 1h), while keeping constant all the other growth parameters (amount of precursors, growth temperature, growth pressure, Ar flow and precursors-substrate distance), irregular WS_2 nuclei with higher density than what reported in Figure 5.5 were obtained (Fig. 5.6). Whereas, by increasing the amount of WS_2 precursors (S from 0.6g to 2.4g and WO_3 from 0.3g to 1.2g), while again keeping constant all the other growth parameters, discontinuous films formed by mixed phases of WS_2 platelets and WO_3 wires were obtained (Fig. 5.7).

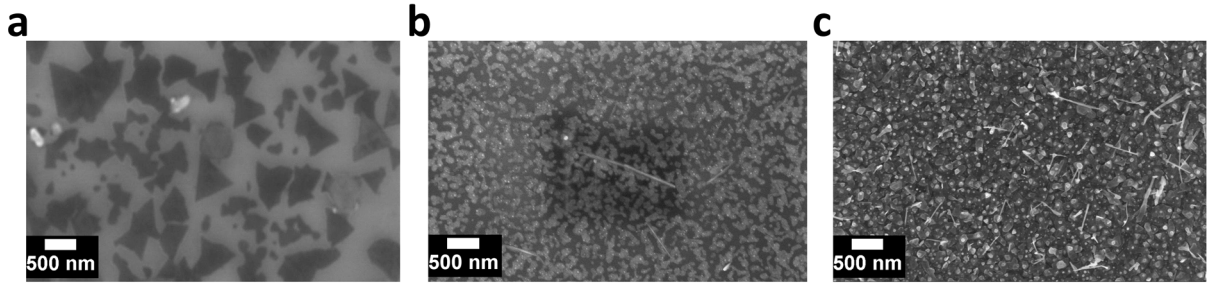


Figure 5.6 *SEM images of irregular WS_2 domains obtained by increasing the growth time from 30min (Fig. 5.5) to (a) 40min, (b) 50min and (c) 60min.*

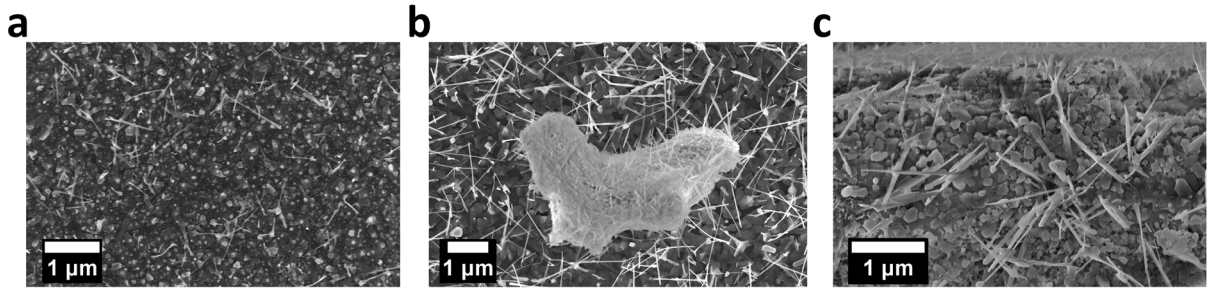


Figure 5.7 *SEM images of WS_2 platelets and WO_3 wires obtained by increasing the amount of WO_3 and S from 0.3g and 0.6g (Fig. 5.5) to (a) 0.6g and 1.2g, (b) 0.9g and 1.8g, (c) 1.2g and 2.4g, respectively.*

Overall, compared to the CVD setup used to prepare the first set of samples, the tube furnace equipped with a heating belt allowed for a more reproducible control over the S evaporation. However, the S vapours were supplied for a very short time due to the fast heating of the powders to high temperatures (~250°C), leading to WS_2 domains with lateral size not exceeding a few microns. In order to maintain the supply of S vapours constant during the reaction time with the purpose of increasing the lateral size of the WS_2 domains or the overall coverage, we doubled (~2g) and even tripled (~3g) the amount of S powders by loading three spate adjacent crucibles in the low temperature zone of the tube. The crucibles were systematically heated one after the other using both the heat coming from the furnace itself (as per the configuration of the first set of samples) and the heating belt. However, this strategy has not resulted in the formation of WS_2, thus suggesting that the constant supplying of S vapours is not the most critical parameter in these work conditions.

The third strategy that we used in the attempt to obtain a continuous layer of WS_2 over large areas was to sandwich the WO_3 powders between two SiO_2/Si substrates (with the second substrate placed face-down above the bottom one). The sandwiched powders were then loaded into the hot temperature zone of the quartz tube, while S powders were placed upstream outside the hot temperature zone. By heating the WO_3-coated substrates to 950°C for 30min at the ramp rate of 25°C min^{-1} and evaporating the S by means of the heat from the furnace itself and/or with the aid of the heating belt, millimetre-sized WS_2 films were obtained along the substrate edges (Fig. 5.8*a*). Raman characterization ascertained the monolayered nature of the material. However, the substrate coverage is not uniform at the nanometre scale (Fig. 5.8*b*) and cluster of unreacted WO_3 particles are still present at the end of the syntheses (Fig. 5.8*c*). It is worth noting that the continuous supplying of sulphur vapours throughout the entire growth

time by using the strategy described above (multiple S-powders containing crucibles) did not lead to an increase in the substrate coverage by WS_2 which again did not form.

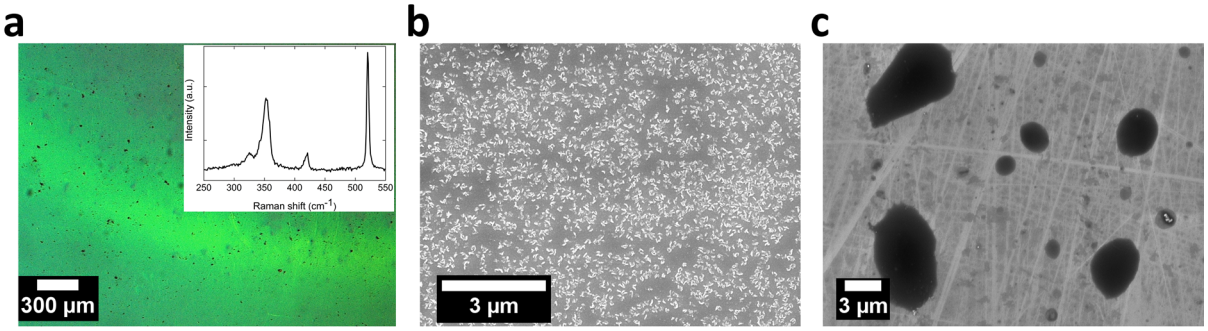


Figure 5.8 *(a) Low resolution optical micrograph of a circular crown-shaped WS_2 deposition. The inset shows a representative Raman spectrum of the area. (b) High resolution SEM image of the WS_2 area showed in (a). (c) Low resolution SEM image showing WO_3 clusters.*

5.4. SULFUR TEMPERATURE: ≤250°C

The third set of samples was prepared using a CVD setup with two adjacent furnaces, which allowed us to independently control the evaporation rates of both WS_2 precursors (Fig. 5.9). The cleaning procedure of the substrates and their loading into the quartz tube together with the WS_2 precursors were carried out in the same way as for the previous sets of samples. The CVD growths were performed at low pressure (10^{-1}-10^{-2}mbar) under vacuum and ultra-high purity Ar gas (flowing at 0-150sccm). Unlike before, the flow of the carrier gas was not kept constant throughout the whole CVD process in order to further control the supply rates of WO_3 and S. The main furnace, containing between 0.05-0.6g of WO_3 powders and SiO_2/Si substrates, was heated to 850-950°C at the rate of 25°C min^{-1}, held at the highest temperature for 6-30min and then naturally cooled down to room temperature. While the second furnace, containing 0.1-1g of S powders, was heated to 105-125°C at 5°C min^{-1}, held at the highest temperature for 6-30min and naturally cooled down. The use of a two-zone furnace, together with a systematic program for the Ar flow rate, was crucial to achieve a stable supply of each precursor source at the optimum rate to allow the formation of triangular-shaped monolayered WS_2 flakes which can merge into film-like domains with lateral size up to several tens of microns.

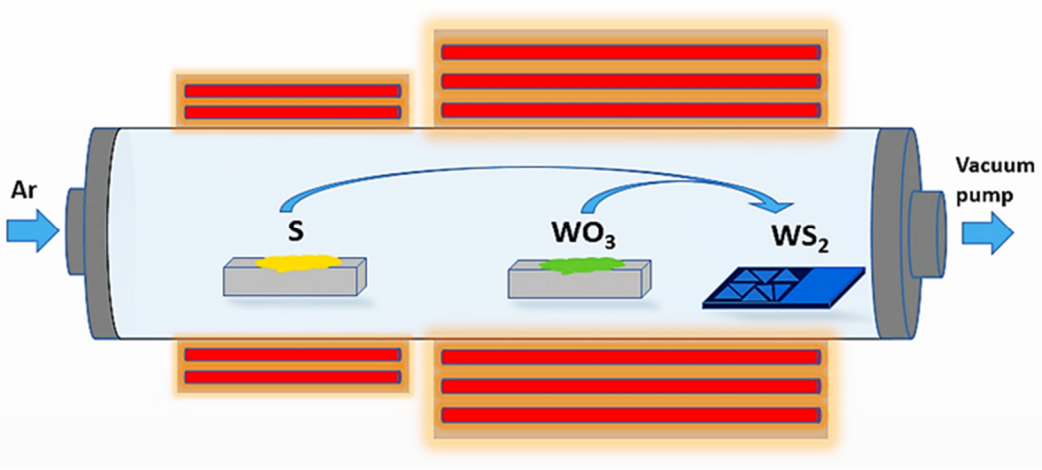


Figure 5.9 *Schematic of the two-zone CVD horizontal tubular furnace.*

The CVD setup used for this set of samples allowed us to optimize the heating profile of the S powders. In particular, a minimum S evaporation temperature of 125°C has been necessary to synthesize WS_2 as decreasing the maximum temperature of the S heating profile to 100-115°C, while keeping constant the temperature of the WO_3-controlling furnace at which the S powders reach these temperatures, did not result in the formation of WS_2. Once again this proved that the supply of S for a shorter time (by heating the powders at higher temperatures) favours the deposition of WS_2. On the other hand, increasing the temperature of the WO_3-furnace (from 700°C to 900-950°C) at which S reaches the highest evaporation rate (125°C), resulted in the formation of a pure WS_2 phase with high crystal quality (as suggested by the deposition of triangular-shaped monolayered domains with lateral size up to ~10μm). Therefore, by taking into account these two trends, the optimized heating profiles for both WS_2 precursors have been identified as the following: WO_3 is heated to 900°C (or 950°C) whereas S is heated to 125°C with both the precursors reaching these temperatures at the same time (Fig. 5.10*a*). As the set heating ramps for WO_3 and S are 25°C min^{-1} and 5°C min^{-1} (for technical reasons and other aspects related to the supply rates), respectively, and considering that the two furnaces start their respective programs at about room temperature, the optimized heating profiles (Fig. 510*a*) are achieved by switching on the S-controlling furnace ~15min (~17min in the case the growth temperature is 950°C) after the WO_3-controlling furnace starts its program or, equivalently, when the WO_3-furnace reaches 400°C (450°C).

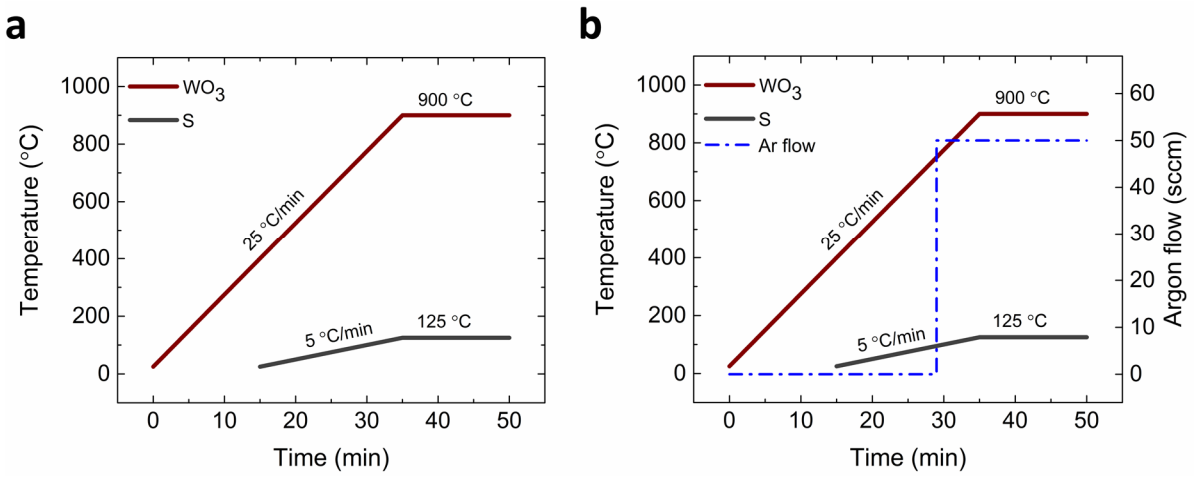


Figure 5.10 *Optimized heating and dwelling profiles for (a) WO_3, S and (b) Ar flow. Both the furnaces are naturally cooled down afterwards.*

While the S powders start to evaporate at relatively low temperatures (~100°C), the vaporization of the WO_3 powders occurs at much higher temperatures (starting from ~700°C under vacuum) and it is highly hindered by the Ar gas flow as the Ar significantly increases the chamber pressure. In order to maximize the supply of W precursor, a systematic study on the evaporation of WO_3 at different temperatures and Ar gas flow rates has been conducted (Table 5.1). We characterized the WO_3 evaporation in terms of coverage of the SiO_2/Si substrate placed downstream (via optical microscopy and SEM analysis) and by weighting the WO_3 powders-containing crucible before and after each evaporation. We found that the evaporation of WO_3 is maximized at temperatures in the range 900-950°C and in the absence of Ar (0sccm). This is understandable considering the very high temperatures and low pressure used. Finally, we also found that WO_3 already evaporates at 700-750°C in the absence of Ar (0 sccm) under a pressure of 10^{-2}mbar.

	750 °C	**850 °C**	**950 °C**
150 sccm (~1 mbar)	~ 0% coverage	~ 0-20% coverage	~ 20-40% coverage
50 sccm (10^{-1} mbar)	~ 0-20% coverage	~ 20-40% coverage	~ 40-60% coverage
10 sccm (10^{-1}-10^{-2} mbar)	~ 20-40% coverage	~ 40-60% coverage	~ 60-80% coverage
0 sccm (10^{-2} mbar)	~ 40-60% coverage	~ 60-80% coverage	~ 80-100% coverage

Table 5.1 *Evaporation of WO_3 under vacuum at different temperatures and Ar gas flow rates (chamber pressures) characterized in terms of coverage of the SiO_2/Si substrate.*

However, while the WO_3 evaporation is more efficient at very low pressures, the whole growing process of WS_2 cannot be conducted in the absence of a carrier gas since the sulphur vapours would condensate upstream on the tube inner wall. Figure 5.10*b* shows the optimized profile (in terms of sccm against time) for the Ar flow together with the heating profiles for WO_3 and S. It can be seen that Ar gas flowing at 50sccm is introduced into the reaction chamber when the WO_3- and S-controlling furnaces reach ~750°C and ~80°C, respectively. Introducing Ar from the beginning of the heating process would hinder the evaporation of WO_3 due to the higher pressure generated (Table 5.1). On the contrary, introducing Ar when the temperature of the WO_3-furnace is above 750°C would lead to the condensation of S vapours upstream. The value of 50sccm has been chosen to be the minimum carrier gas flow to efficiently carry the S vapours to the hot temperature zone and growth substrate.

In summary, a lower pressure (~10^{-2}mbar) in the initial growth stages favours the evaporation of WO_3 at relatively low temperatures (from ~700°C). Meanwhile, S starts to evaporate in the low temperature zone and it is then transported to the hot temperature zone with a WO_3-rich atmosphere by the Ar flow (which increases the pressure to ~10^{-1}mbar). If S vapours were introduced earlier, then there would be not sufficient WO_3 precursor onto the growth substrate to react with S and to lead to the formation of large WS_2 domains (Fig. 5.11*a*). On the other hand, if S vapours were introduced later, then there would be an abundance of WO_3 precursor onto the substrate, leading to thick multi-layered and wire-like WS_2 structures (Fig. 5.11*b*). In the following chapter (Chapter 6), tungsten precursors with a lower evaporation point than WO_3 will be employed to facilitate the supply of the metal source.

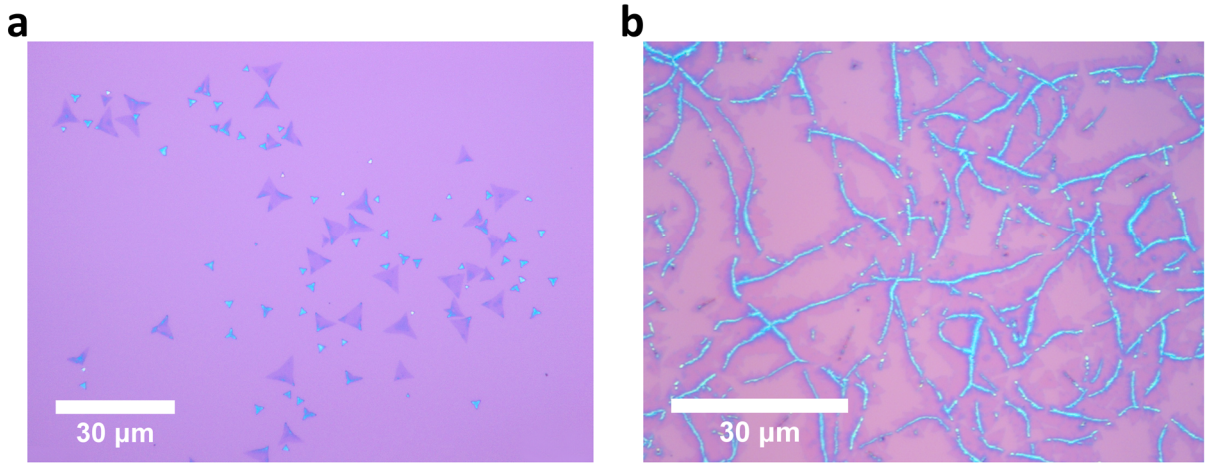


Figure 5.11 *Optical micrographs of (a) small WS_2 domains and (b) wire-like WS_2/WO_3 structures.*

Figure 5.12*a-c* shows optical and SEM images of WS_2 flakes grown using the optimized growth conditions (Fig. 5.10*b*), where it can be clearly seen that atomically thin WS_2 domains with a triangular shape and sharp edges are formed on SiO_2/Si substrates. The difference in frequency between the 2LA-E^1_{2g} and A_{1g} Raman modes is ~66cm^{-1} (Fig. 5.12*d*) in agreement with the reported wavenumber shift for CVD-grown single-layer-thick WS_2 onto SiO_2/Si [38]. Further, the E^1_{2g}/A_{1g} peaks intensity ratio is ~6 which matches the reported value for monolayered WS_2 (for double-layered WS_2 the reported E^1_{2g}/A_{1g} ratio is ~2) collected with a 532nm laser source [183]. Finally, Figure 5.13 shows Raman intensity maps for the E^1_{2g} peak revealing a good uniformity of the WS_2 triangles.

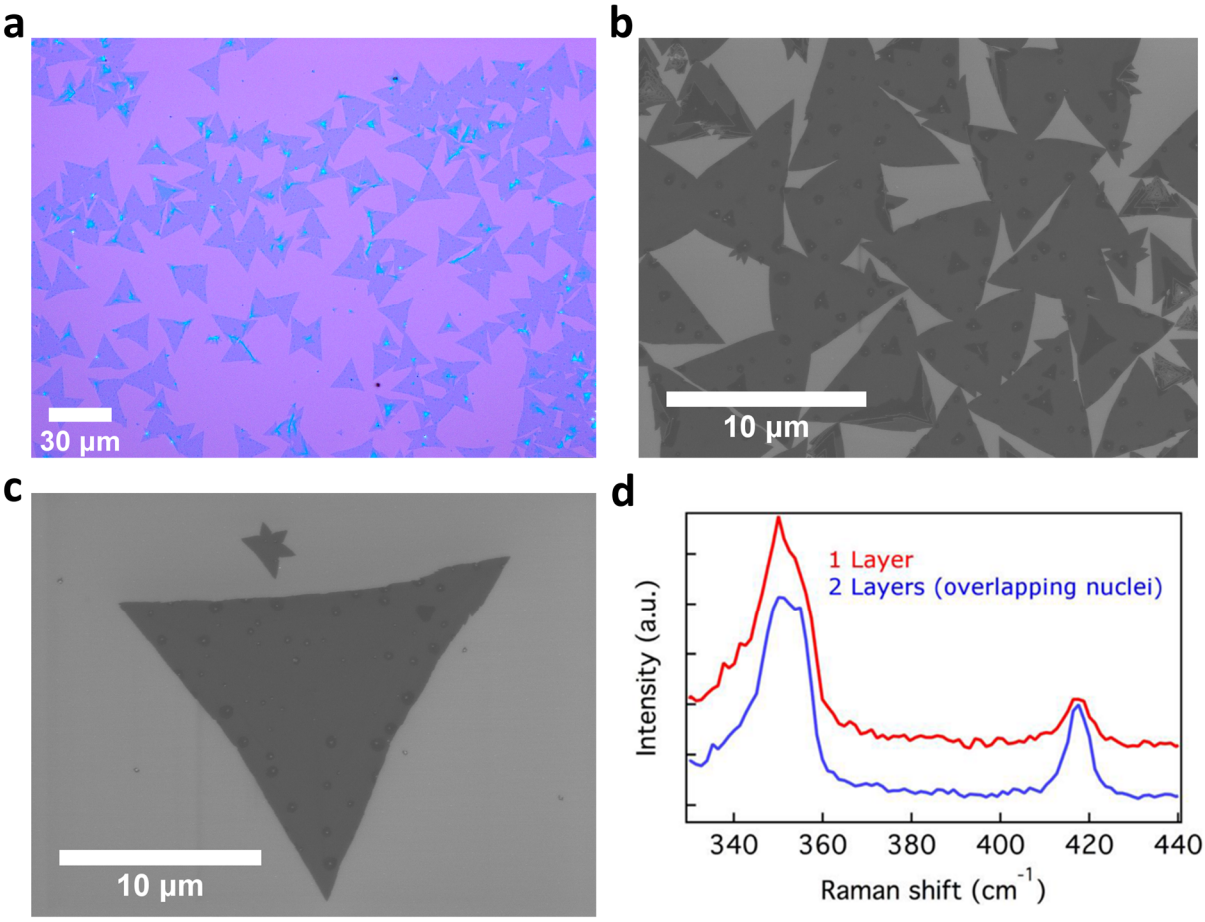


Figure 5.12 *(a) Optical micrograph and (b, c) high resolution SEM images of triangular WS_2 flakes. (d) Raman spectra of the WS_2 domains shown in (a-c). The spectrum of the overlapping area sometimes observed between two adjacent WS_2 triangles is also reported.*

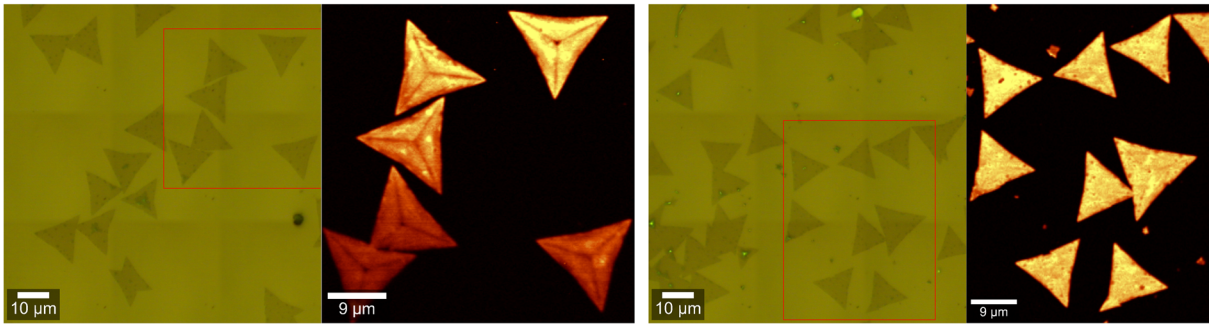


Figure 5.13 *Optical micrographs of monolayered WS_2 domains and Raman intensity maps for the WS_2 E^1_{2g} peak over the highlighted areas, revealing a good uniformity of WS_2 across the whole triangular area.*

Upon increasing the growth temperature from 900°C to 950°C, the nucleation density of the triangular WS_2 flakes decreases while their lateral size increases and they even merge forming a quasi-continuous domain over hundreds of μm^2 (Fig. 5.14*a, b*). In order to explain this temperature effect, it is reasonable to infer that higher growth temperatures restrain the nucleation of WS_2 crystals due to a higher desorption rate of the absorbed species (WO_x and S), thus resulting in a decreased nucleation density. On the other hand, higher temperatures favour the surface diffusion of WO_x species, as well as the reaction between WO_{3-x} and S, thus in line with a better crystallization of the WS_2 lattice and with the observed increased domain size [287]. However, the WS_2 domains grown at 950°C are often "etched" (Fig. 5.14*c*) possibly due to "absorption-desorption" phenomena during the first stages of the cooling stage when the temperature is still above 900°C which is higher than the formation temperature of WS_2.

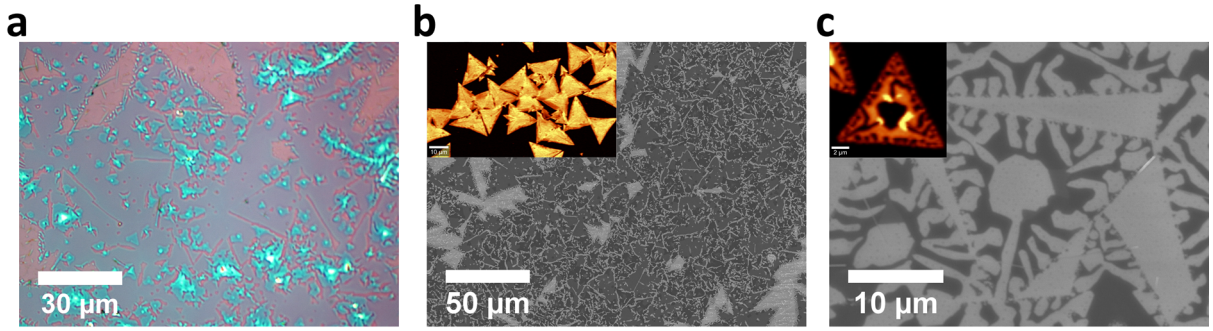


Figure 5.14 *(a) Optical micrograph of a film-like WS_2 domain grown at 950°C. (b) SEM image showing a high degree of substrate coverage by WS_2. (c) SEM image showing an extreme case of etched flakes. The insets in (b) and (c) report Raman intensity maps for the WS_2 E^1_{2g} peak over representative areas.*

The etching of the WS_2 flakes could be minimized by increasing the chamber pressure during the cooling stage by flowing Ar gas at 150sccm. However, this strategy induced the formation of WS_2 nano-wires (Fig. 5.15*a, b*). These are likely to be formed in the vapour phase and to precipitate on the growth substrate. On the other hand, fast cooling of the substrate by opening the furnace at high temperatures did also lead to formation of spurious phases (Fig. 5.15*c*).

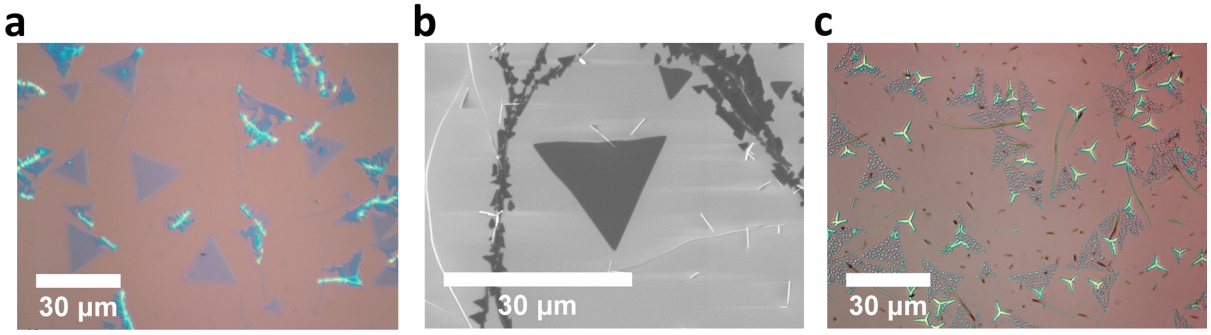


Figure 5.15 *(a) Optical and (b) SEM images of WS_2 domains grown by using Ar gas flowing at 150sccm during the cooling stage. (c) Optical micrograph showing the effects of fast cooling by furnace opening.*

It is also found that the distance between the WO_3 powders and the growth substrate D_{ps} (Fig. 5.16) is another crucial parameter in determining the nucleation density, lateral size and thickness of the WS_2 domains. Figure 5.17*a* shows that triangular-shaped WS_2 flakes are formed at D_{ps}~10-15cm, which are thicker, much smaller and with higher nucleation density compared to those formed at D_{ps}~5-10cm. Since at the growth temperature of 900°C the substrates at D_{ps}~5-10cm and D_{ps}~10-15cm reach ~800°C and ~700°C during the dwelling time, respectively, this trend is consistent with what reported for CVD grown-graphene [287]: low temperatures lead to high nucleation density, where the nuclei are small and multi-layered, whereas high temperatures lead to large monolayered nuclei sparsely distributed. It is worth noting that at D_{ps} less than ~5cm or more than ~15cm, no deposition of WS_2 was observed under our growth conditions.

Further, by systematically decreasing the amount of both WS_2 powdered precursors, we found that 0.3g of WO_3 and 0.6g of S lead to the larger WS_2 nuclei (Table 5.2). The necessity to use small quantities has to be correlated to the fact that high amounts of precursors increase the evaporation rate and therefore the growth pressure and precursors partial pressures.

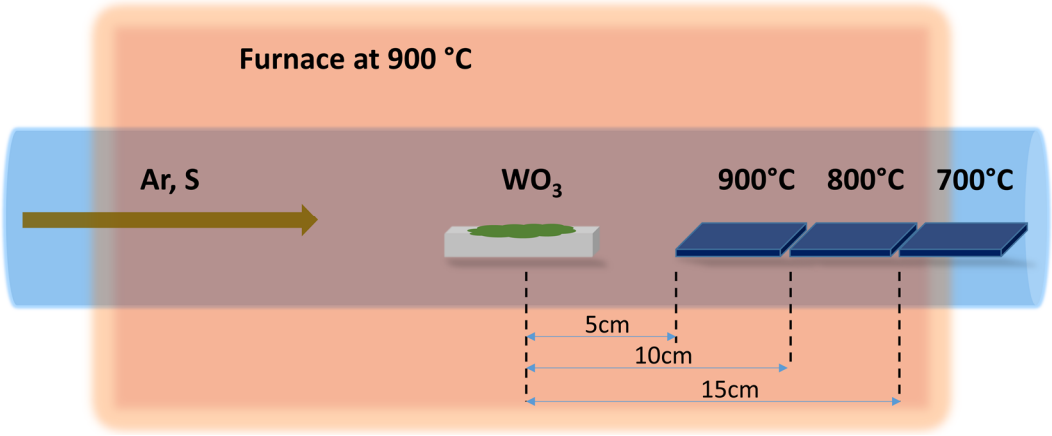


Figure 5.16 *Schematic of the WO_3-controlling furnace showing the correlation between the precursor-substrate distance and the substrate temperature.*

S \ WO_3	0.9 g	0.6 g	0.3 g
0.9 g	WS_2 triangles up to ~5 µm		WS_2 triangles up to ~10 µm
0.6 g		WS_2 triangles up to ~10 µm	WS_2 triangles up to ~20 µm
0.3 g			WS_2 irregular flakes

Table 5.2 *Effects of the concentration of precursors on the average lateral size of WS_2 domains. It is worth to note that a minimum S amount of 0.6g was necessary to growth high-quality WS_2 triangles.*

Finally, while increasing the growth time from 15min to 30min did not lead to significant variations in the WS_2 domains morphology, differences were clearly visible for growths lasting 5min (Fig. 5.17*b, c*). As reported by other authors [180][246], we observed a Frank-van der Merwe mechanism for the CVD growth of WS_2, in which small nuclei are formed and then expand into larger 2D crystals. Firstly, nuclei of WO_yS_{2-y} are formed which subsequently lead to triangular-shaped thick WS_{2+x} flakes as a result of further sulfurization. Since the apexes of the triangles are very active nucleation sites, a series of small triangles form and merge into a bigger triangle. Finally, due to the continuous heating, the thick WS_{2+x} flakes start expanding and thinning, eventually leading to WS_2 monolayers.

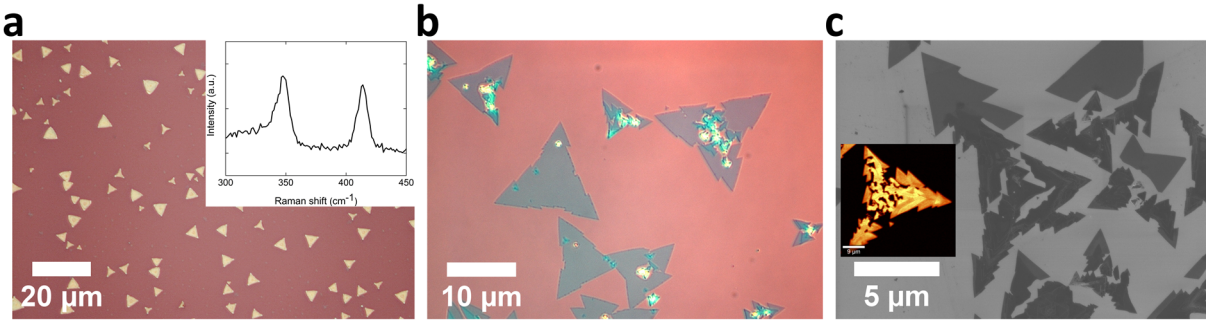


Figure 5.17 *(a) Optical micrograph of WS_2 crystals grown at D_{ps}=10-15cm (~700°C). From the inset, reporting a representative Raman spectrum, it can be seen that the E^1_{2g}/A_{1g} peak intensity ratio is much less than 6 (reported value for monolayered WS_2). (b) Optical and (c) SEM images of flakes at the initial growth stage. The inset in (c) shows the Raman intensity map for the WS_2 E^1_{2g} peak.*

To conclude this chapter it is worth noting that one of the main limitations of the discussed WO_3-based CVD synthesis of isolated domains of WS_2 is the uniform dispersion of precursors onto the substrates which is limited by the employed powdered WO_3. In order to improve the metal precursor dispersion uniformity and increase the substrate coverage by WS_2, we have loaded into the CVD quartz tubular furnace a small-diameter one-end sealed quartz tube containing WO_3 powders sandwiched between two SiO_2/Si substrates facing each other (Fig. 5.18). The one-end sealed tube was used to ensure adequate sulphur vapours concentration and pressure in between the bottom WO_3-containing substrate and the above growth substrate. All the other growth conditions were the same as for the previous set of samples (Fig. 5.10).

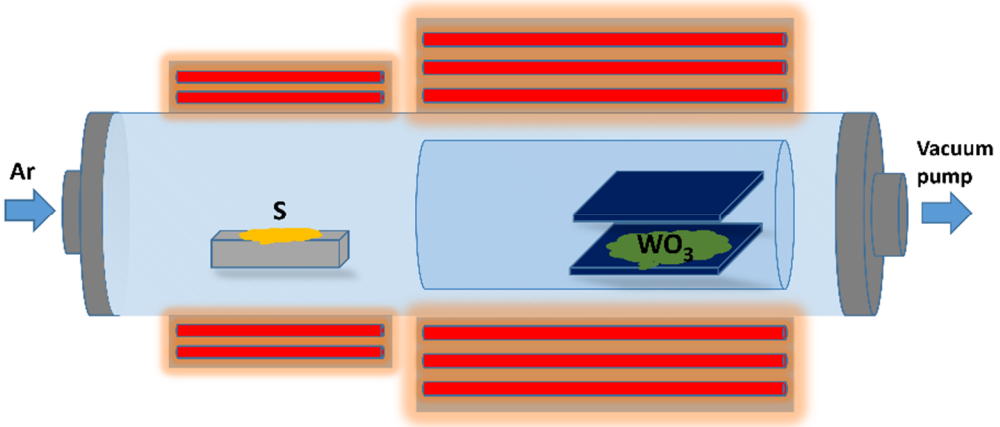


Figure 5.18 *CVD setup employed to improve the dispersion uniformity of the metal precursor onto the substrate.*

Figure 5.19 shows that while the bottom SiO_2/Si substrate is significantly contaminated with clusters of WO_3 particles (Fig. 5.19*a*), the top SiO_2/Si substrate is covered with ~5-10µm-large WS_2 flakes merging in a continuous WS_2 film over hundreds of micron sized-areas (Fig. 5.19*b-d*). However, the complexity of the CVD setup resulted in a low reproducibility of the synthesis products. Hexagonal-shaped domains, bulk flakes and WO_3 rich-wires were also obtained likely due to an insufficient supply of sulphur vapours (Fig. 5.20). The use of a longer one-end sealed quartz tube directly containing S powders in the upstream zone, a larger spacing between the two substrates and higher Ar flow rates did not lead to a higher degree of growth control, thus motivating the search for alternative W precursors more volatile than WO_3 and capable of improving the tungsten dispersion onto the growth substrate or enable more effective reaction mechanism at the molecular level and in vapour phase.

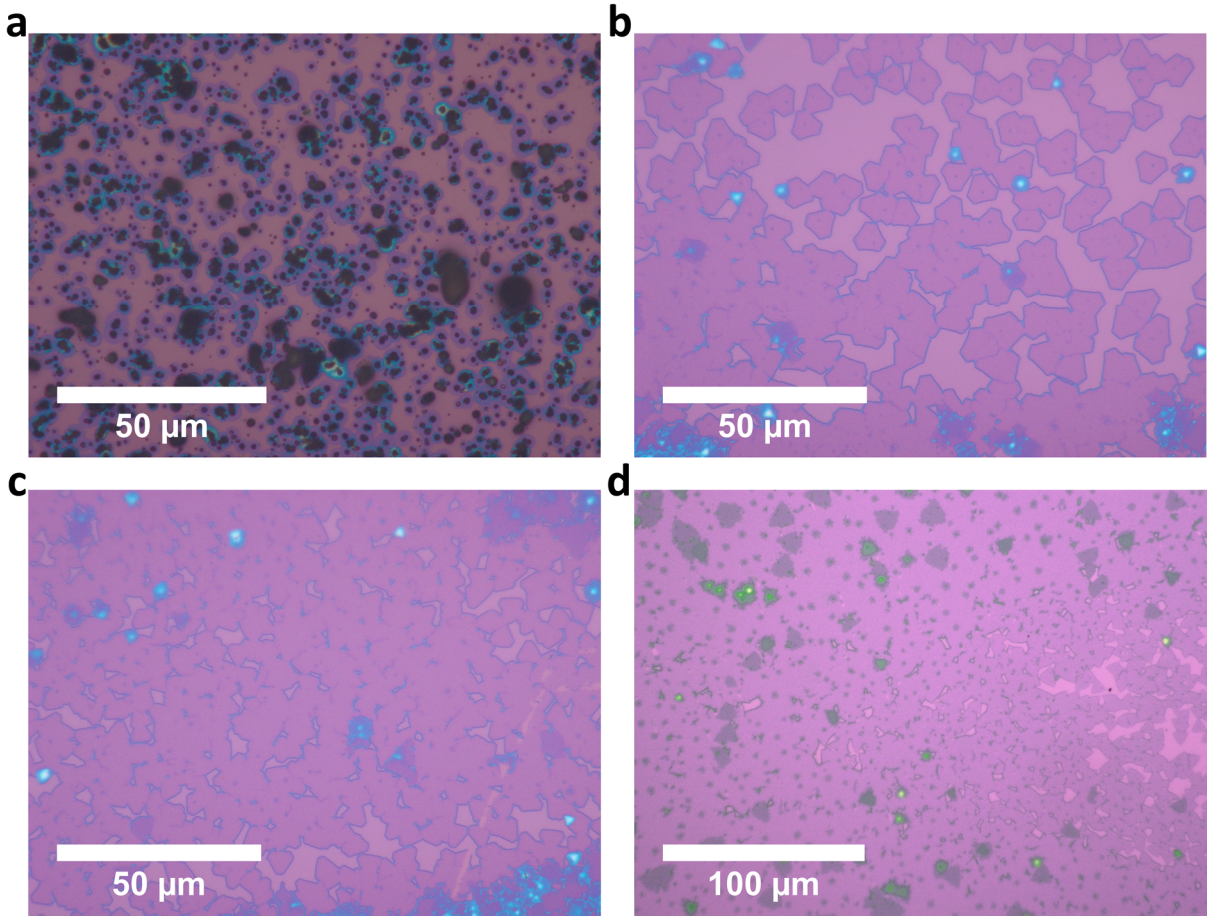


Figure 5.19 *Optical micrographs of the (a) bottom and (b-d) top SiO_2/Si substrates showing clusters of WO_3 particles and small WS_2 flakes merging into a quasi-continuous film over a few hundreds of micron sized-areas, respectively.*

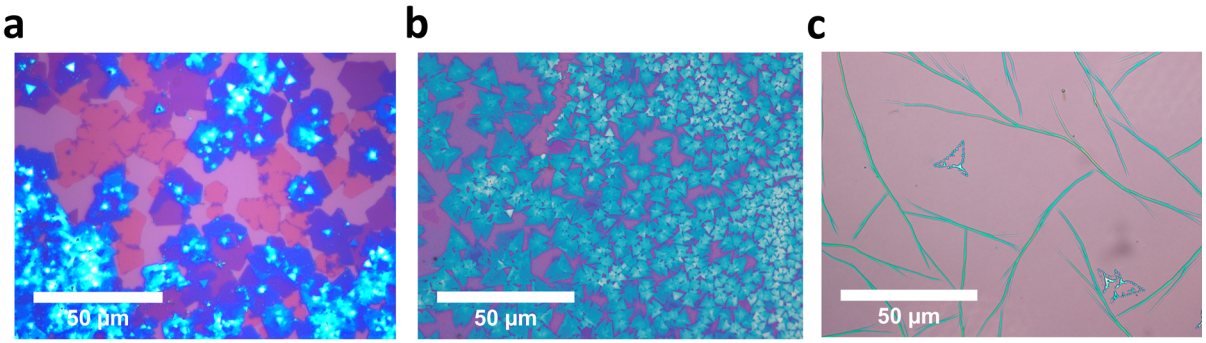


Figure 5.20 *Optical micrographs of (a) multi-layered and (b) balk WS_2 flakes with different geometries. (c) Optical micrograph of WO_3-rich wire-like structures.*

5.5. CONCLUSIONS

As discussed in Chapter 3, the most widely used vapour-phase method to synthesize atomically thin WS_2 is a one-step CVD process consisting in the co-evaporation of WO_3 and S powders in a horizontal tubular furnace in the presence of a carrier gas. In particular, WO_3 has seen a widespread use as metal precursor due to its low toxicity compared to halides or organic compounds, easy handling and effective replacement of O by S. However, even though WS_2 flakes have been successfully synthesized through this WO_3-based CVD approach by several research groups, the reported synthesis conditions and results are often contradictory and reveal reproducibility issues. In this chapter we have presented a parametric study on the CVD reaction variables such as reaction temperature and time, heating profile of sulphur, carrier gas flux, amount of precursors and precursors-substrate distance. As a result, we have provided insights into the key factors that govern the WO_3-based growth mechanism of WS_2 atomic layers from the early stages of nucleation up to the formation of polycrystalline films over hundreds of micron-sized areas, discussing how different growth conditions can lead to a different size, thickness and density of the WS_2 nuclei.

The evaporation and deposition of WO_3 onto the growth substrate requires high temperatures ($\geq$900°C) and low pressures, due to its high sublimation temperature and low vapour pressure. Further, due to the fact that both precursors are in powder form and have very different vapour pressures, the precursors flux cannot be monitored and thus the growth time is often not sufficiently long to enable individual WS_2 nuclei to grow and form a uniform layer. Continuous WS_2 films over larger areas have been sometimes obtained by placing the WO_3 powders in direct contact with the growth substrate, but at the expense of the controllability, reproducibility and scalability of the synthesis process. Therefore, these limitations of the WO_3-based CVD synthesis of WS_2 have motivated the search for alternative W precursors with higher volatility than WO_3 and which can be sulfurized at molecular level, thus eventually ensuring a reproducible deposition of high-quality and large-area WS_2 atomic layers.

6) WATER-ASSISTED CVD SYNTHESIS OF WS_2

6.1. INTRODUCTION

As discussed in Chapter 3 and Chapter 5, in the literature, the CVD synthesis of atomically thin WS_2 has been achieved predominately by co-evaporating WO_3 and S powders at temperatures >900°C in a tubular furnace and in the presence of a carrier gas [4][173][183][184][185][186][187]. This synthesis method involves a topotactic transformation which typically leads to sparse distributions of WS_2 flakes with lateral size not exceeding a few tens of microns onto both amorphous [4][173][183][186][187] and crystalline substrates [184][185][246]. In a very few cases, a continuous WS_2 film over centimeter-sized areas has been obtained by sacrificing the quality of the material which showed lower carrier mobility as compared to individual flakes [188][189][257]. These results can be attributed to three main factors: the low evaporation rate of WO_3, the crystallographic defects induced by the topotactic sulfurization of WO_3 clusters and the short growth time dictated by the readily exhaustion of sulphur powders. To bypass the growth challenges originating from the very different vapour pressures of WO_3 and S powders, the W precursors have been scattered in direct contact or close proximity of the growth substrate [34][167] [180][189][245][248][257]. Nevertheless, this strategy has given non-consistent growth results with poor reproducibility, leading to non-uniform WS_2 domains with variable thickness and stoichiometry, and significant residual of unreacted precursors onto the growth surface. Further, the use of volatile W precursors which can decompose at temperatures lower than 900°C, such as WCl_6 [254] and $W(CO)_6$ [188][256], often accompanied with the use of organic compounds as sulphur precursors, has enabled the synthesis of WS_2 over large areas at lower temperatures but at the expense of the crystal quality of the grown material.

In this chapter, we report the synthesis of monolayered WS_2 extended over 300 micron-sized areas at temperatures as low as 750°C by using monohydrated tungsten oxide (H_2WO_4) as W precursor in the presence of a chlorine source (NaCl). Continuous polycrystalline monolayered coverage has also been obtained over areas of 0.8x0.8mm^2 and selective growth of monolayers and bilayers was achieved by varying the growth pressure. The as-grown monolayered WS_2 shows light emission with intensity one order of magnitude higher than monolayered WS_2 grown using WO_3 and ultra-sharp full width at half maximum (FWHM) of 36meV at room temperature. Furthermore, we report record electron mobility reported so far of mono- and bi-layered WS_2 sheets onto SiO_2 of 28cm^2/Vs and 52cm^2/Vs, respectively.

6.2. RESULTS

The synthesis of all the WS_2 samples presented in this chapter were performed starting from commercial powders of WO_3 (0.3g, ≥99.5%, Sigma Aldrich), H_2WO_4 (0.3g, 99%, Sigma Aldrich), S (0.6g, ≥ 99.5%, Sigma Aldrich) and NaCl (0.3g, ≥99.5%, Sigma Aldrich). Similarly to the third set of samples described in Chapter 5, the W precursors and S powders were placed in two separate alumina crucibles well-spaced in a 2inch-diameter horizontal quartz tube CVD furnace and they were heated up independently using different controllers as reported in Figure 6.1*a*. The growth substrates were 500μm-thick Si wafers with 285nm of SiO_2 thermally deposited on top. They were sequentially cleaned in an ultrasonic bath with acetone, isopropanol and deionized water for 15min each step. The cleaned substrates were then loaded downstream in the furnace. This allows for a more controllable and reproducible large-area deposition of uniform WS_2 domains compared to placing them above the metal precursor-containing crucible. The WS_2 synthesis were performed at 10^{-1}mbar under vacuum and high purity Ar gas flowing at 100sccm. The W precursors-controlling furnace was heated up to 750-950°C at 25°Cmin^{-1}, kept at those temperatures for 15min and then naturally cooled down to room temperature. As discussed in Chapter 5, the heating profile of S has been optimized to ensure maximum supply when the W-precursors start evaporating. Thus, the S-controlling heater was heated up to 125°C at 5°Cmin^{-1}, kept at this temperature for 15 min and then naturally cooled down (Fig. 6.1*b*).

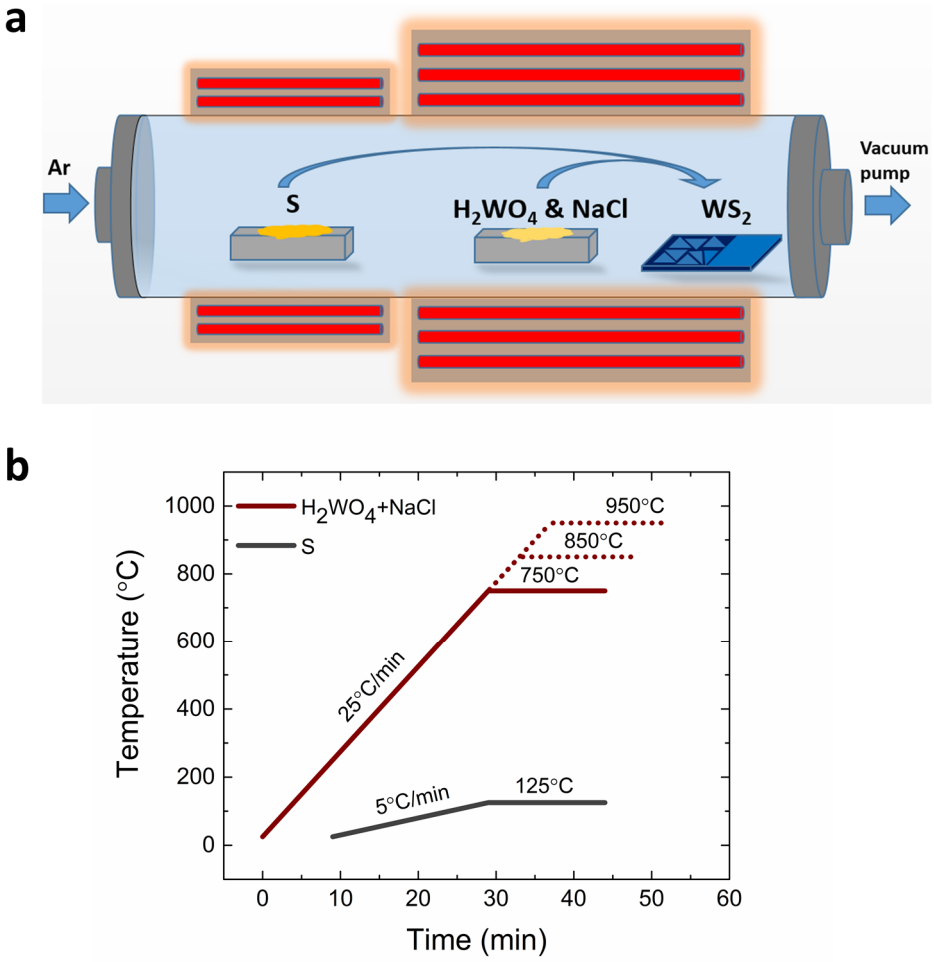


Figure 6.1 *Illustration of the (a) two-zone CVD tubular furnace set-up and (b) temperature profiles of the tungsten precursors- and sulphur-heating modules. The S reaches 125°C when the W precursor is at the maximum temperature. The SiO_2/Si substrate is loaded downstream at 1-8cm away from the W precursors-containing crucible and it is subjected to the same temperature.*

Figure 6.2 shows optical micrographs of WS_2 domains grown by using different W precursors (WO_3, WO_3-NaCl, H_2WO_4-NaCl) at different temperatures (950°C, 850°C, 750°C). The WS_2 triangles present sharp straight edges and uniform color contrast onto SiO_2 substrate for all growth conditions, suggesting the formation of pristine and highly crystalline monolayered WS_2 across the entire triangle area. These characteristics have been confirmed by Raman, PL and TEM characterizations discussed in the following. Interestingly, Figure 6.2 shows a dramatic increase in the lateral size of the triangles from the left to the right side of the figure and a favorable synthesis at lower temperatures by using H_2WO_4-NaCl rather than WO_3 and WO_3-NaCl as W precursor.

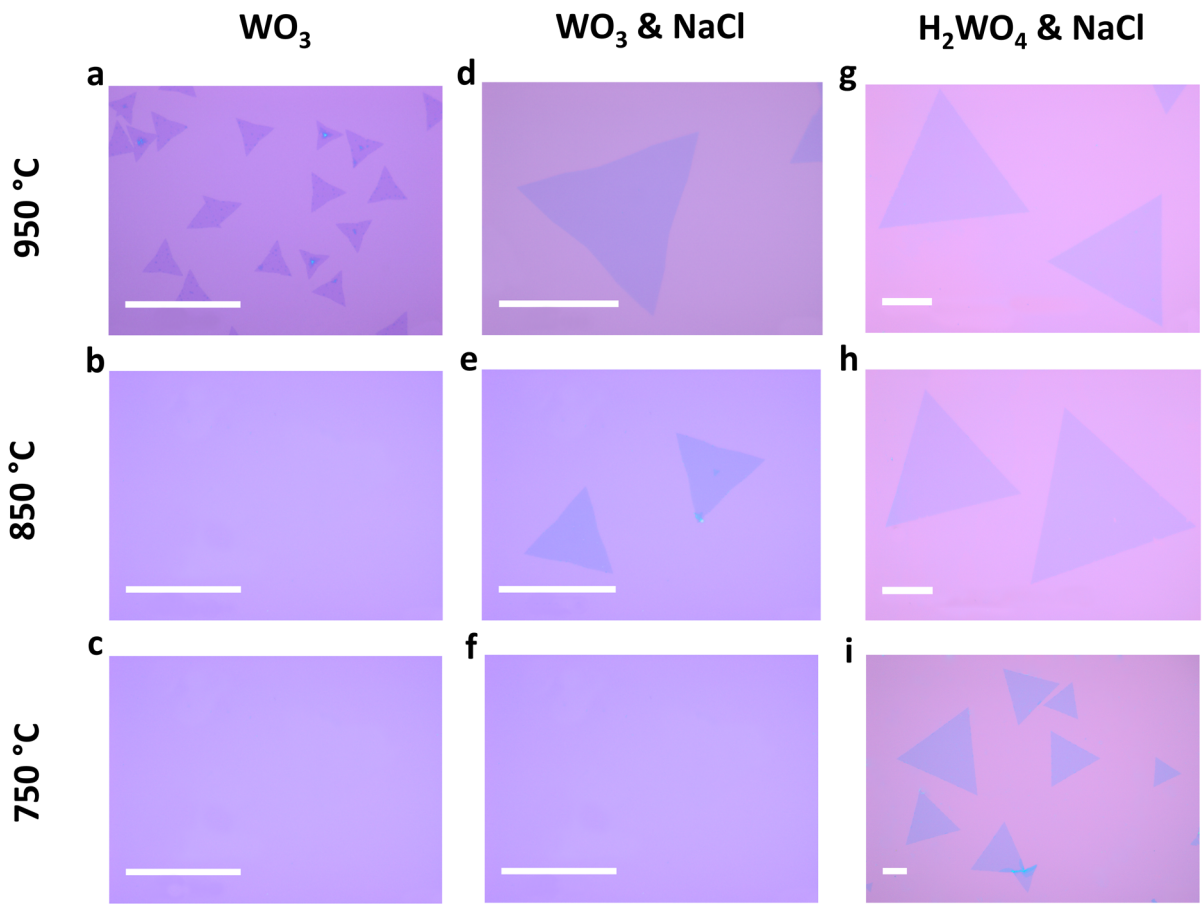


Figure 6.2 *Optical micrographs of the SiO_2/Si growth substrates after CVD synthesis carried out using different precursors at different temperatures: (a) WO_3 at 950°C and the OM shows ~10µm WS_2 flakes, (b) WO_3 at 850°C and the OM appears as a bare SiO_2 substrate, (c) WO_3 at 750°C (bare SiO_2 substrate), (d) WO_3 and NaCl at 950°C (~60µm WS_2 flakes), (e) WO_3 and NaCl at 850°C (~30µm WS_2 flakes), (f) WO_3 and NaCl at 750°C (bare SiO_2 substrate), (g) H_2WO_4 and NaCl at 950°C (~150µm WS_2 flakes), (h) H_2WO_4 and NaCl at 850°C (~150-200µm WS_2 flakes), (i) H_2WO_4 and NaCl at 750°C (~50-200µm WS_2 flakes). Scale bar is 50µm.*

As shown in Chapter 5, WO_3 leads to WS_2 triangles with lateral size of ~10µm at 950°C (Fig. 6.2*a*) while no formation of WS_2 is observed at 850°C (Fig. 6.2*b*) and 750°C (Fig. 6.2*c*). The fact that the synthesis of WS_2 occurs only at very high temperature is explained by the high sublimation temperature of WO_3. WO_3+NaCl precursors lead to a facilitated synthesis of ~60µm (Fig. 6.2*d*) and ~30µm (Fig. 6.2*e*) WS_2 triangles at 950°C and 850°C, respectively. The larger flakes obtained at higher temperatures can be explained in the light of the Robinson & Robin model [287]. At high temperature the diffusivity of the

adsorbed precursors on the growth surface is facilitated, leading to the lateral expansion of the existing nuclei. At the same time, desorption of absorbed species is higher than at lower temperatures, preventing the achievement of a supersaturation concentration and therefore reducing the nucleation density. No WS_2 deposition is observed at 750°C (Fig. 6.2*f*). By replacing WO_3 with H_2WO_4, the size of the WS_2 domains significantly increases (Fig. 6.2*g,h,i*). The triangles have edge lengths exceeding 200µm at 950°C (Fig. 6.2*g*) and 850°C (Fig. 6.2*h*) and between 50-200µm at 750°C (Fig. 6.2*i*).

By doubling the amount of tungsten precursors (from 0.15g to 0.3g) loaded in the CVD chamber, continuous polycrystalline monolayered WS_2 coverage over areas of ~0.8mm extension has been obtained at 850°C (Fig. 6.3). While upon increasing the growth pressure (from 1.6mbar to 13mbar), bilayered WS_2 domains are preferentially formed at 950°C (Fig. 6.4).

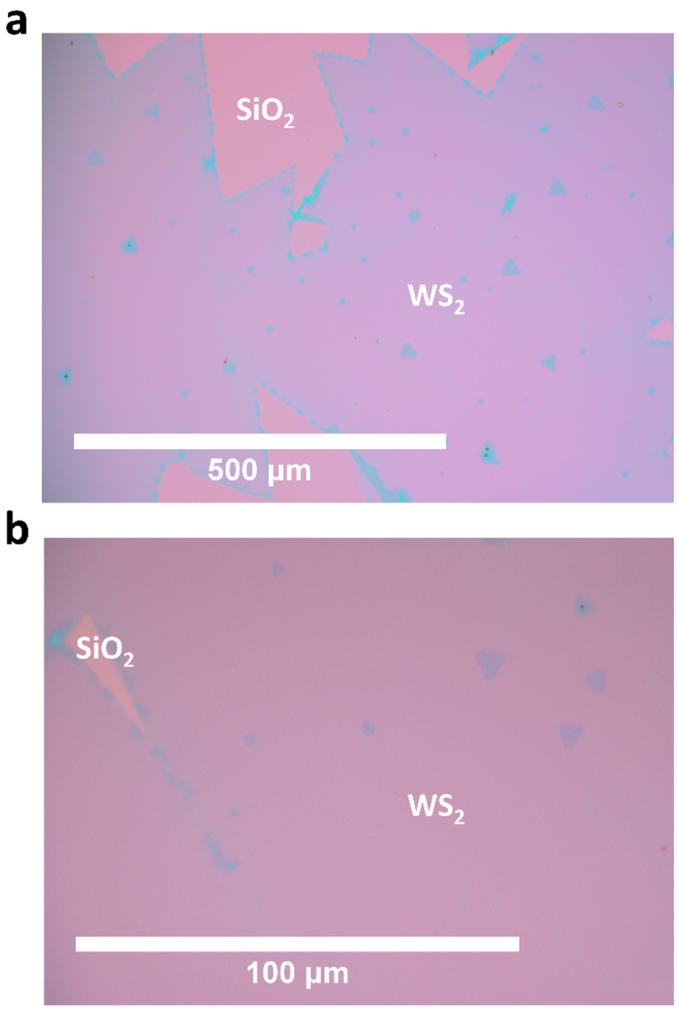


Figure 6.3 *(a) Low and (b) high magnification optical micrographs of continuous polycrystalline mono-layered WS_2 coverage.*

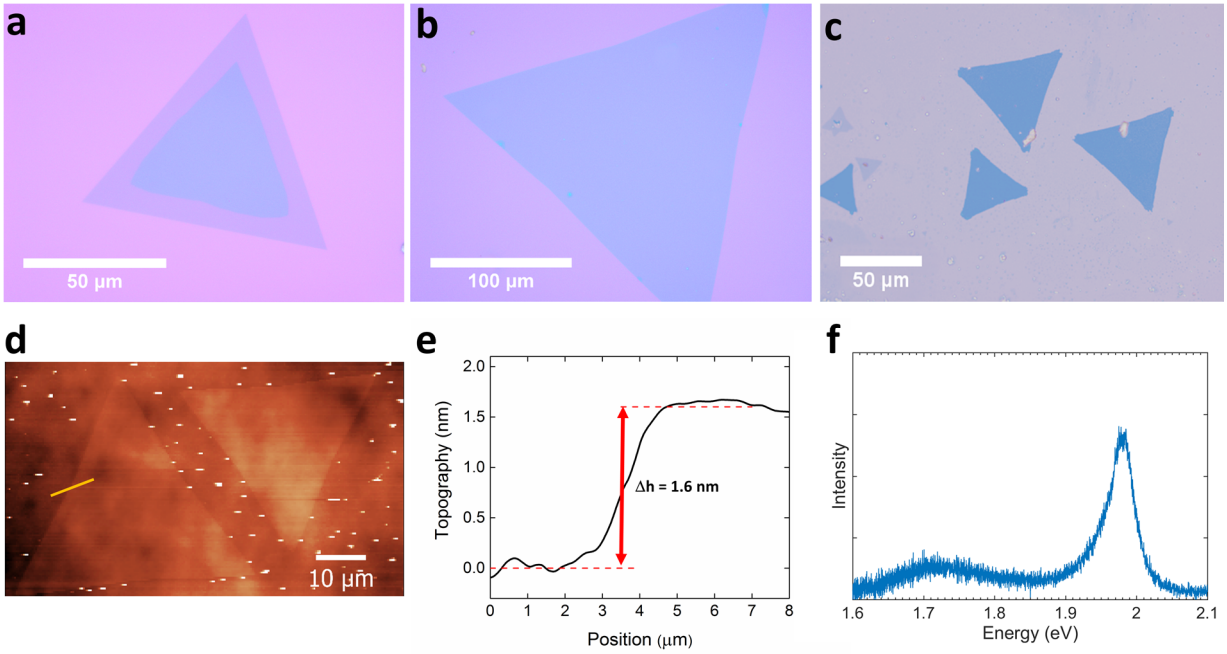


Figure 6.4 *Optical micrographs of (a) second WS_2 layer growing on top of a monolayered WS_2 triangle, (b) uniform bilayered WS_2 triangle, (c) bilayered WS_2 flakes with high nucleation density. AFM (d) image and (e) corresponding thickness profile of a bilayered WS_2 triangle. (d) PL spectrum of bilayered WS_2 showing both direct and indirect peaks.*

6.3. REACTION MECHANISM

To understand the facilitated synthesis of WS_2 using H_2WO_4 and NaCl, we conducted X-ray diffraction (XRD) analysis on the reaction products of H_2WO_4 and WO_3 with NaCl after CVD processes at different temperatures (500°C, 650°C and 750°C) and in the absence of S vapours (Fig. 6.5). We found that both H_2WO_4+NaCl (Fig. 6.5*a*) and WO_3+NaCl (Fig. 6.5*b*) systems lead to the formation of $Na_xW_yO_z$ compounds (i.e., $Na_2W_4O_{13}$, $Na_2W_6O_{19}$). However, the reaction occurs at lower temperatures (~650°C) for H_2WO_4 (Fig. 6.5*a*) compared to WO_3 (~750°C) (Fig. 6.5*b*). This means that the system H_2WO_4+NaCl releases chlorine at lower temperatures than WO_3+NaCl. Cl acts as transport agent by reacting with tungsten oxide to form volatile tungsten-based oxide halide species (i.e., WO_2Cl_2, $WOCl_4$) [288] for the transport of the metal precursor onto the growth substrate. The low-temperature dissociation of NaCl is promoted by H_2O molecules which are gradually released by H_2WO_4 upon heating. Indeed, the solid state structure of H_2WO_4 (Fig. 6.6) consists of vertex-sharing layers of octahedrally coordinated $WO_3(H_2O)$ units where

the layers are held together by hydrogen bonds between the terminal oxygens and by coordinated water molecules [289][290][291]. The weakly bonded H_2O molecules can be liberated at temperatures as low as 100-200°C and they can promote the low temperature-dissociation of NaCl which would otherwise occur at temperatures higher than 1000°C without water. The previously reported facilitated growth of WS_2 by using the system WO_3-NaCl (Fig. 6.2*d,e*) [245] can be explained with the inevitable presence of water impurities in the CVD reaction chamber, in particular when the synthesis is performed at atmospheric pressure.

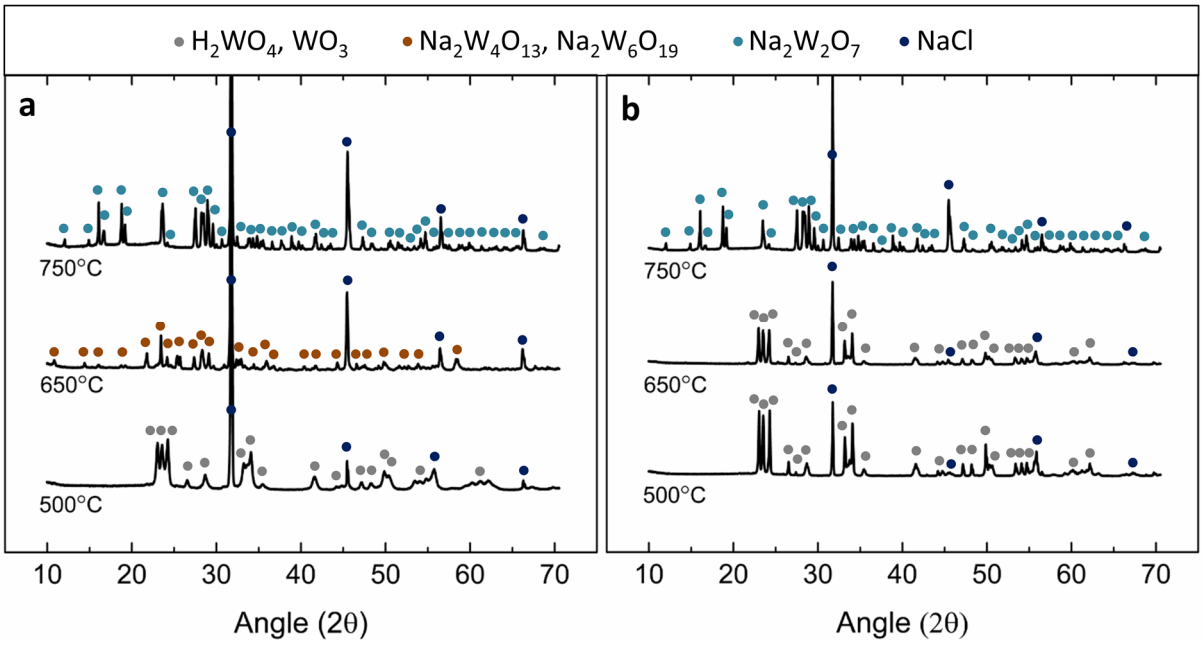


Figure 6.5 *XRD patterns of the residual powders of W-precursors after thermal treatment at 500°C, 650°C and 750°C using (a) H_2WO_4+NaCl and (b) WO_3+NaCl as precursor.*

Based on the XRD analysis (Fig. 6.5) and literature data [245][254][289][290][292][293][294][295][296] [297] four reaction steps have been identified as likely to occur in our water-assisted-halide-mediated synthesis of WS_2:

1) $H_2WO_4(s) \rightarrow WO_3(s) + H_2O(l)$

2) $NaCl(s) + H_2O(l) \rightarrow Na^+(aq) + Cl^-(aq) + H_2O(l)$

3) $6Na^+(aq) + 6Cl^-(aq) + 14WO_3(s) \rightarrow Na_2W_4O_{13}(s) + Na_2W_6O_{19}(s) + [Na_2W_2O_7(s)] + WOCl_4(g) + WO_2Cl_2(g)$

4) $WOCl_4(g) + WO_2Cl_2(g) + 3S(g) + 4H_2O(g) \rightarrow 2WS_2(s) + 2SO_2(g) + H_2SO_3(g) + 6HCl(g) + S(g)$

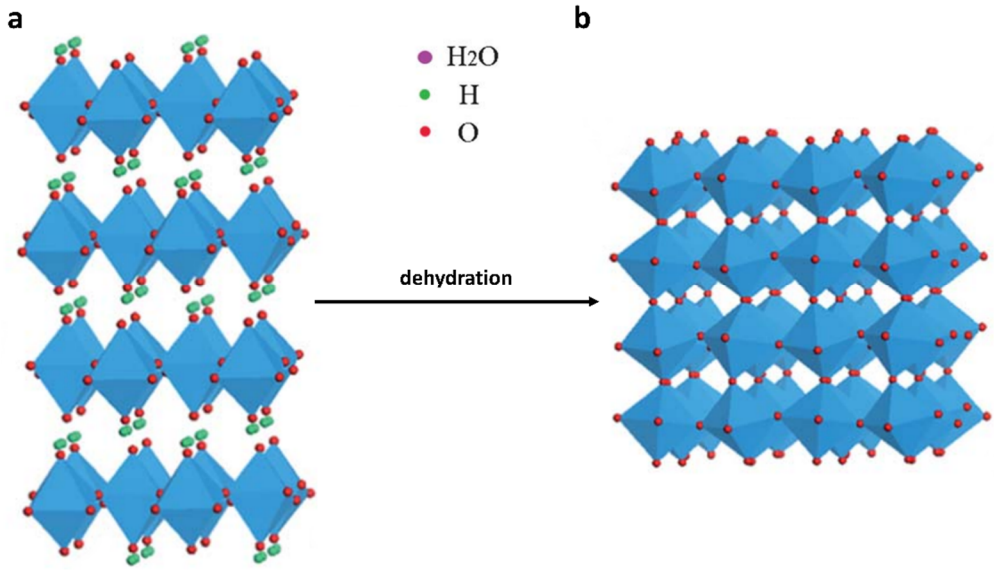


Figure 6.6 *Schematic illustrations of the crystal structures of (a) H_2WO_4 and (b) WO_3. Adapted from Ref. [286].*

The formation of volatile tungsten oxide halide species (WO_2X_2, WOX_4) has been previously reported for the synthesis of WS_2 bulk crystals via chemical vapor transport (CVT) [298][191] (Chapter 3) by reacting halogen molecules such as Cl_2, I_2 and Br_2 (used as transport agents) and tungsten oxides species. Further, thermodynamic studies on the transport of tungsten and sulphur compounds by chlorine for the growth of WS_2 have shown that the primary transport species are tungsten oxide halides rather than metal halides (e.g., WCl_6) [296][297]. The oxyhalides can decompose at lower temperatures compared to pure halides and show high volatility [288]. WO_2Cl_2 and $WOCl_4$ are volatile at temperatures as low as 200°C [288]. In particular, $WOCl_4$ has been previously used [254] as precursor for the CVD synthesis of WS_2 bulk films. Despite its strong tungsten-oxygen double bonds, $WOCl_4$ proved to be an effective precursor with a clean decomposition pathway in the CVD process without formation of tungsten oxysulfide [254]. Indeed, we have verified that it is possible to synthesize WS_2 domains at temperatures as low as 600°C by using commercial $WOCl_4$ powders (Fig. 6.7*a*). Additionally, the key role played by the WO_xCl_y species becomes apparent if we attempt to grow WS_2 by using only H_2WO_4 as W precursor. As this decomposes to WO_3, only small WS_2 domains are observed with similar PL characteristics to the WO_3 precursors-growth (Fig. 6.7*b*) (Chapter 5). Finally, by replacing NaCl with KCl we obtained comparable growth results (Fig. 6.7*c*) suggesting that other sources of Cl can also be used. Nevertheless, Cl_2 was reported to be the most effective halogen element for both single layer and bulk crystals growth [24][245].

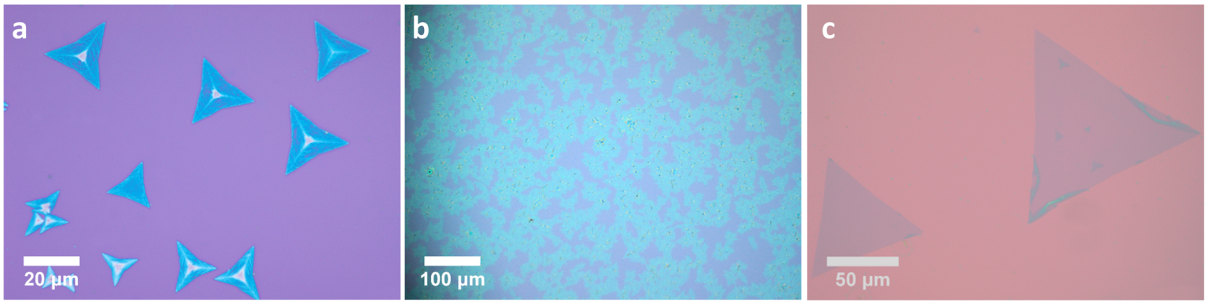


Figure 6.7 *Optical micrographs of WS_2 triangles and amorphous domains grown on SiO_2/Si substrates by using (a) $WOCl_4$ at 600°C, (b) only H_2WO_4 at 850°C, (c) H_2WO_4+KCl at 850°C.*

It is worth noting that the $Na_xW_yO_z$ compounds cannot be responsible for the synthesis of WS_2 as they present high evaporation temperatures. XRD characterization has confirmed that they remain in the crucible after the CVD process is completed (Fig. 6.8). Further, the attempt to use $Na_xW_yO_z$ residual powders as W precursors for a new growth at 950°C did not lead to the formation of any WS_2 flakes, confirming again that their high evaporation temperature hinders the synthesis. Finally, the superior volatility of the H_2WO_4+NaCl system has been confirmed by visual inspection of the amount of residual powders (Fig. 6.8). Growths performed by using only WO_3 and H_2WO_4 (Fig. 6.8*a, b*) lead to a large amount of WO_3 and substoichiometric WO_3 remaining in the crucible. On the contrary, WO_3 and H_2WO_4 mixed with NaCl undergo a significant weight loss and only a little amount of $Na_xW_yO_z$ compounds (and unreacted NaCl) is found in the crucible (Fig. 6.8*c, d*). In the case of H_2WO_4+NaCl, the residual is less compared to the WO_3+NaCl system.

Finally, it has been reported that the vapour phase transport of tungsten and its dioxide and sulphide using iodine as transport agent proceeds via the gaseous WO_2I_2 and $WO_2(H_2O)$ [213]. The latter is formed due to the presence of small amounts of water impurities liberated from the wall of the quartz ampoule. Thus we can conclude that the transport of the tungsten precursor in our system may also secondarily take place via the H_2O-driven formation of volatile W based-hydroxides species and that H_2O may act as transport agent itself.

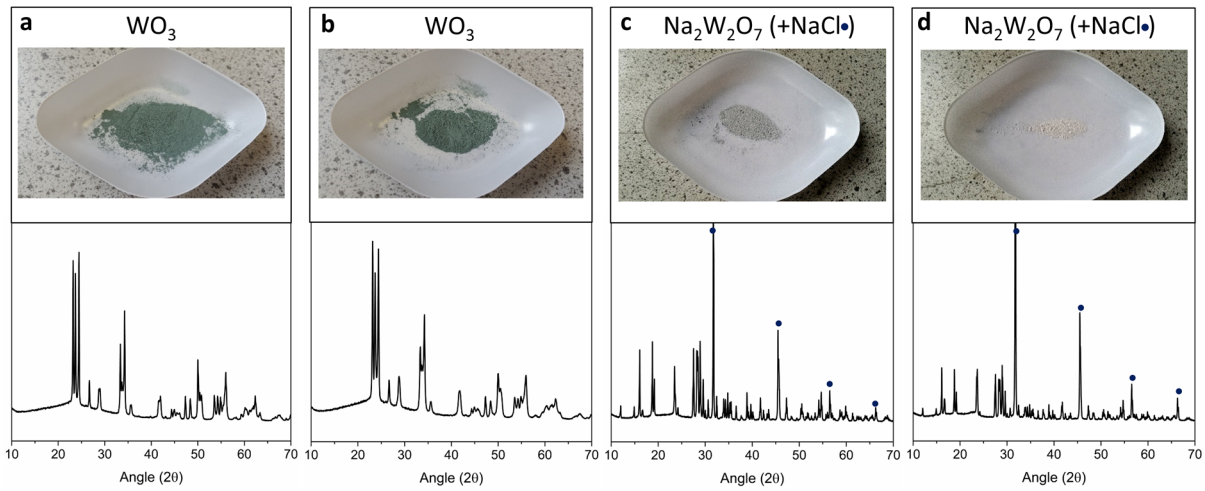


Figure 6.8 *Residual powders of the W-precursors and their XRD patterns after thermal treatment at 750°C using (a) WO_3, (b) H_2WO_4, (c) WO_3+NaCl and (d) H_2WO_4+NaCl.*

6.4. STRUCTURAL AND PHYSICAL CHARACTERIZATION

In the following, a comprehensive characterization of the WS_2 crystals grown by using WO_3, WO_3+NaCl and WH_2O_4+NaCl precursors is reported.

6.4.1. STRUCTURAL CHARACTERIZATION

High resolution TEM (Fig. 6.9*a*) and SEM (Fig. 6.9*b*) imaging reveal the pure crystalline nature of the materials and their high uniformity across the entire triangular area, respectively. The measured lattice constant is 0.3nm consistent with that of 2H-WS_2 (a=0.318nm). The AFM thickness profile analysis of WS_2 triangles confirms the monolayered (Fig. 6.9*c, d*) and bilayered (Fig. 6.9*e, f*) nature of the flakes, showing an edge step height of ~0.8nm (Fig. 6.9*d*) and ~1.6nm (Fig. 6.9*f*), respectively [299][300]. The Raman spectra of WS_2 grown using the three different W precursors are shown in Figure 6.10. All of the spectra exhibit two characteristic peaks located at ~(351±0.53)cm^{-1} and ~(417.6cm^{-1}±1)cm^{-1}, which correspond to the 2LA-E^1_{2g} and A_{1g} Raman modes of pristine monolayered WS_2 [38][265]. The distribution of the peak positions is increasingly narrower going from WO_3 precursor to WO_3+NaCl and to H_2WO_4+NaCl (Appendix, Fig. A1-A2). The Raman peak intensities are uniform across the entire triangle area (Fig. A3-A4) suggesting the absence of strains or unintentional doping in our materials.

The energy difference (Δν) between 2LA(M) and A_{1g} is ~(66.5±0.53)cm^{-1} (Fig. A5), which is in agreement with the Raman signatures of pristine CVD-grown monolayered WS_2 onto Si/SiO_2 previously reported in the literature [38].

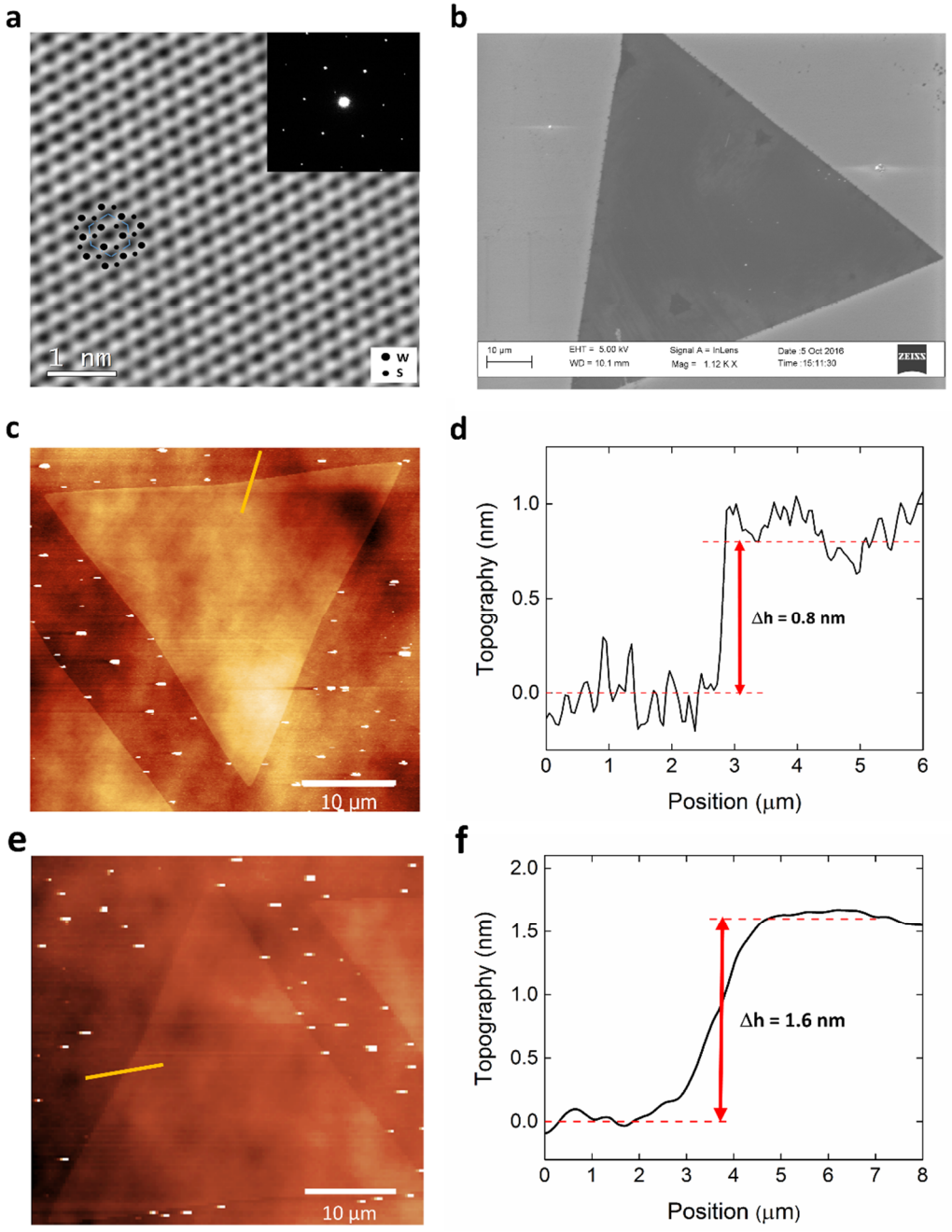


Figure 6.9 *Structural and physical characterization of WS_2 crystals grown by using H_2WO_4+NaCl. (a) Phase image of the reconstructed exit-plane wave function from a focal-series of HRTEM images of the WS_2 lattice. The inset reports a selected area diffraction pattern which shows hexagonal symmetry. (b) HRSEM image. (c) AFM images and (d) corresponding thickness profile of monolayered WS_2. (e) AFM images and (f) corresponding thickness profile of bilayered WS_2.*

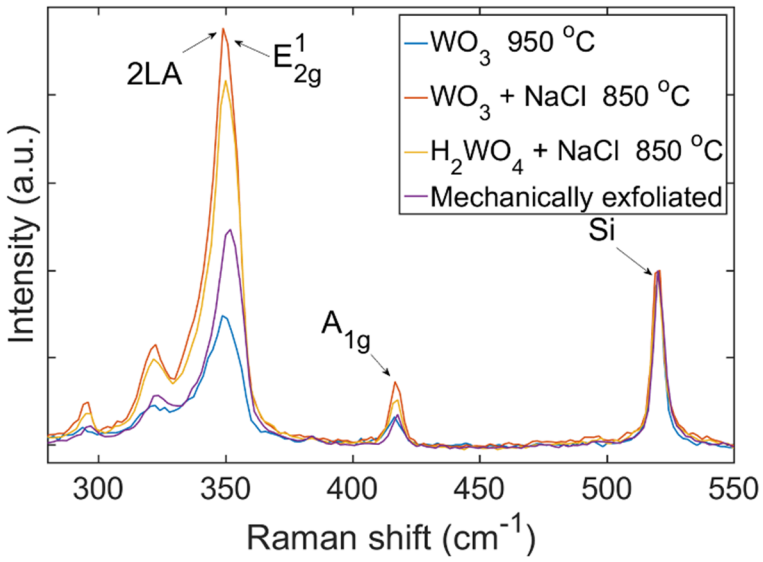


Figure 6.10 *Raman spectra of WS_2 grown using WO_3, WO_3+NaCl and H_2WO_4+NaCl at 950°C, 850°C and 850°C, respectively. The spectra show the characteristics active modes of WS_2 which allow for the identification of the layer number. The Raman spectrum of mechanically exfoliated WS_2 is also shown. All the spectra have been fitted with Voigt profiles for both 2LA-E^1_{2g} and A_{1g} modes.*

6.4.2. PHOTOLUMINESCENCE

A comparison of representative PL intensity maps of monolayered WS_2 triangles grown by the three metal precursors systems (WO_3, WO_3+NaCl, H_2WO_4+NaCl) at different temperatures (950°C, 850°C, 750°C) is reported in Figure 6.11. Remarkably, the intensity of the PL emission peak systematically increases from the left-hand side to the right-hand side of the figure, revealing the superior optical properties of WS_2 grown by using H_2WO_4-NaCl (Fig. 6.12).

The PL intensity map of monolayered WS_2 grown from WO_3 at 950°C (Fig. 6.11*a*) shows three lobes of high intensity. The PL peak position and FWHM maps of the same flake (Fig. A6, A7) reveal bimodal distributions centred at 1.94eV (position, Fig. 6.14*a*, Fig. A8*a*) and 75meV (FWHM, Fig. 6.14*b*, Fig. A8*b)* respectively in correspondence of the high PL intensity-three lobes versus 1.96eV (position) and 55meV (FWHM) in correspondence of the low PL intensity-remaining areas. Both PL peak position and FWHM values are comparable with the current state of the art of WS_2 monolayered synthesized from WO_3 [4][183][247][301]. The red shift of ~0.02eV of the peak position and the larger FWHM of the three-

lobe areas suggest the presence of structural defects [302][303] in the form of S-vacancies which increases the electron density and consequently the trion population [4][304]. This leads to the strengthening of the PL emission at lower energies than the optical band gap, causing a redshift and an increased FWHM of the peak. It has been shown that strain variations in the lattice can also affect the PL emission intensity and energy [47][303]. To verify whether any strain could be responsible for the observed PL patterns, we have relaxed the lattice by cutting the WS_2 flake using a high intensity 532nm laser. As reported in Figure 6.13, the PL peak intensity and energy position patterns remain unchanged along with the Raman peaks position after cutting the triangle. Thus, structural defects in variable concentration are likely to be the main responsible for the variable PL intensity and peak position [305].

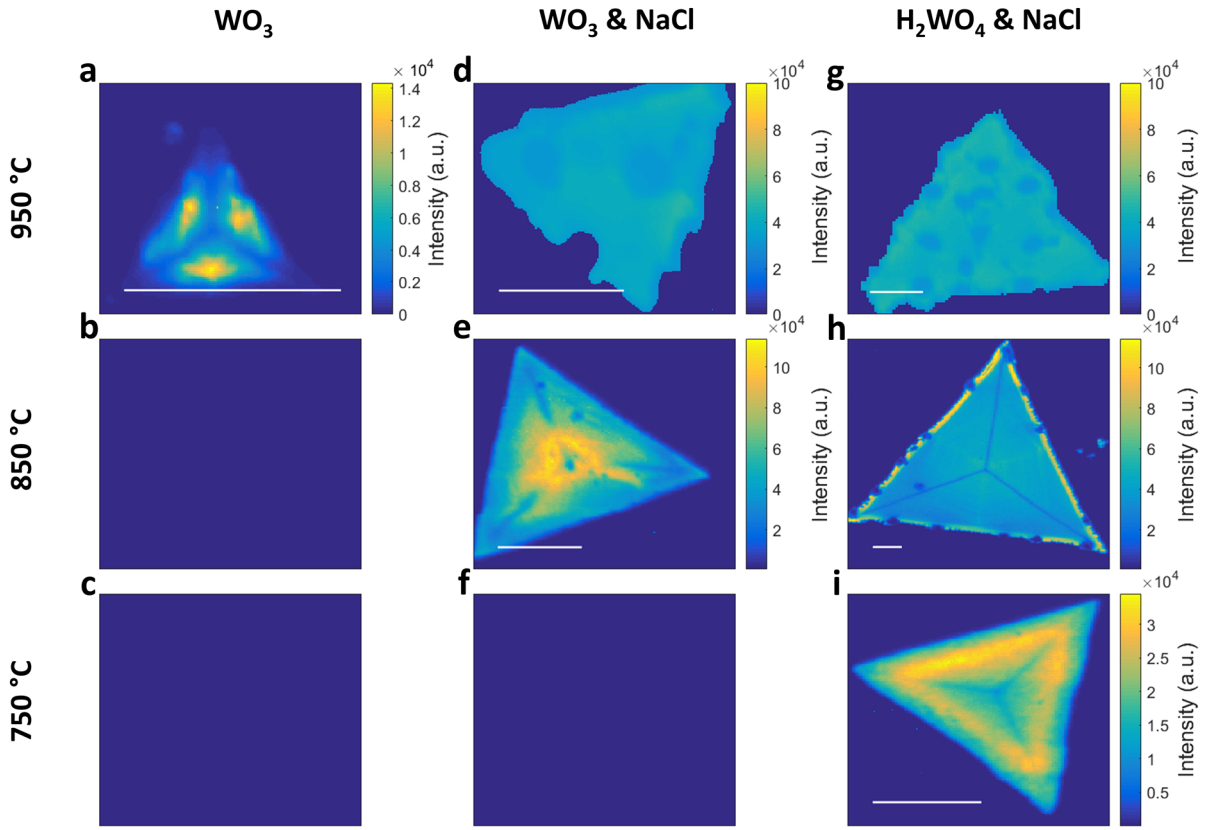


Figure 6.11 *PL intensity spatial maps of monolayered WS_2 triangles grown in the conditions exemplified in Fig. 6.2. Scale bar is 10µm.*

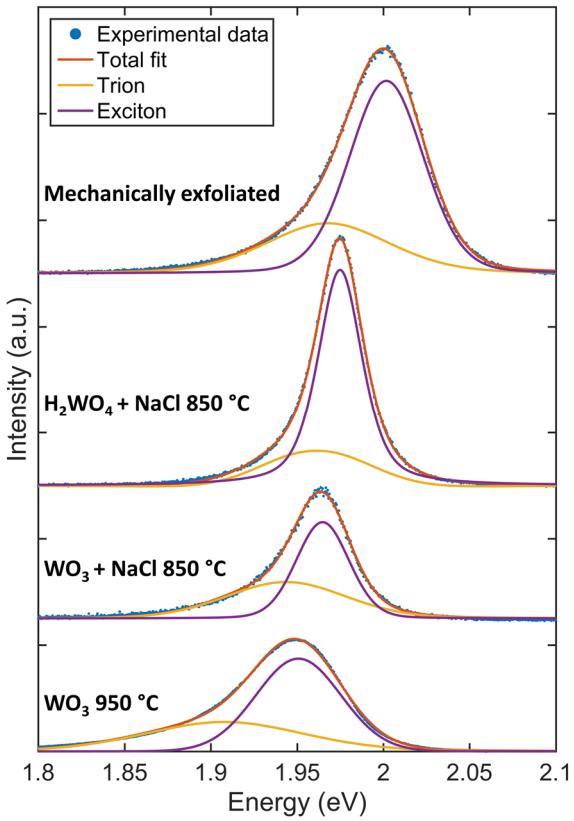


Figure 6.12 *Individual PL spectra of mechanically exfoliated and CVD-grown monolayered WS_2 using: WO_3 at 950°C, WO_3+NaCl at 850°C and H_2WO_4+NaCl at 850°C. The experimental spectra (dotted lines) appear asymmetric and they can thus be deconvolved in two distinct peaks which have been attributed to an exciton and a trion component [306]. All the spectra have been fitted with Voigt profiles for both exciton and trion components.*

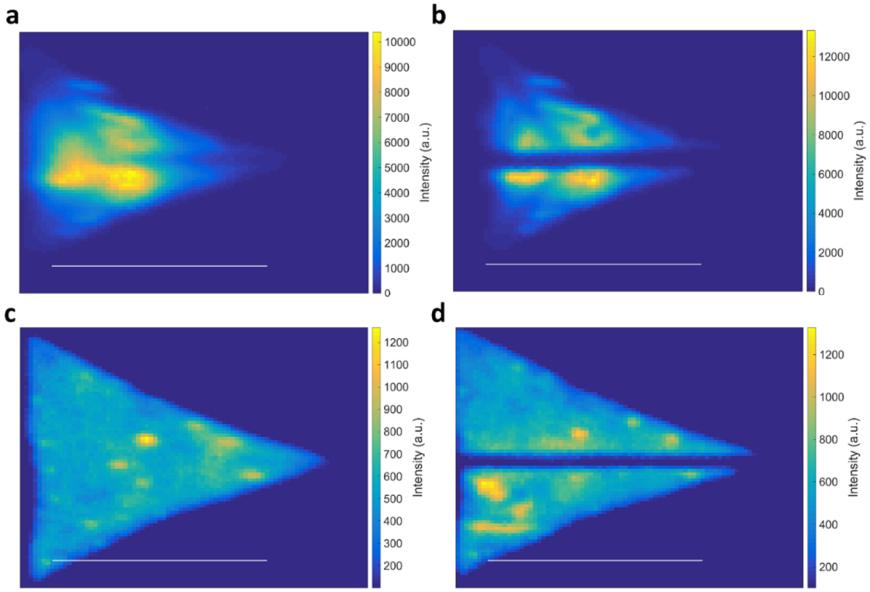


Figure 6.13 *PL intensity (a) before and (b) after the cutting. 2LA+E^1_{2g} Raman peak intensity (c) before and (d) after the cutting. Scale bar is 10μm.*

Monolayered WS_2 grown from WO_3+NaCl at 950°C (Fig. 6.11*b*) and 850°C (Fig. 6.11*c*) presents PL emission at higher energy (Fig. 6.12, Fig. A6, Fig. A9*a*) and a narrower FWHM (Fig. 6.12, Fig. A7, Fig. A9*b*) compared to the WS_2 flakes grown without the addition of NaCl. The distribution of the PL peak position and FWHM is again bimodal but with a smaller standard deviation as compared to the samples grown by using WO_3 (Fig. 6.14). The light is emitted at higher energy (~1.95±0.002eV and ~1.96±0.002eV) and the FWHM is narrower (~43±2.8meV and ~51±3meV) than what reported in most of the literature [4][183][247][301]. The latter is comparable to the H_2-assisted synthesis of WS_2 from WO_3 [307]. These results suggest that the trions component in the PL signal is reduced and it is much smaller than what exhibited by WS_2 samples grown from WO_3. We can conclude that WO_3+NaCl leads to monolayered WS_2 affected by less structural defects as compared to the WO_3-based growth. A different sulfurization mechanism and growth dynamics (molecular conversion *versus* topotactic conversion) may account for the structural differences observed and for the disappearance of the three-lobes-PL intensity distribution (Fig. 6.11*b-c*).

Finally, the PL peak position of monolayered WS_2 grown by using H_2WO_4+NaCl is at higher energy (~1.980±0.005eV) (Fig. 6.12, Fig. A6, Fig. A10*a*) and the FWHM is significantly narrower (~36±3meV) (Fig. 6.12, Fig. A7, Fig. A10*b*) than what observed for WS_2 grown from WO_3 and WO_3+NaCl. The PL intensity pattern across individual flakes presents small intensity variations and no appreciable differences are observed from flake to flake. Thus, the distribution of the PL peak position and FWHM are much narrower (5meV and 3meV respectively) compared to what registered for WO_3- and WO_3+NaCl-based synthesis results (Fig. A11, Fig. 6.14). These results suggest that monolayered WS_2 grown using H_2WO_4+NaCl as W precursors have much less structural defects (S vacancies) which lead to a negligible contribution from trions. Remarkably, the FWHM is narrower than previously reported values for CVD-grown [4][183][247][301] and exfoliated WS_2 [6][165] and it is comparable to CVD-grown WS_2 onto van der Waals substrates [246] and high quality exfoliated WS_2 [177].

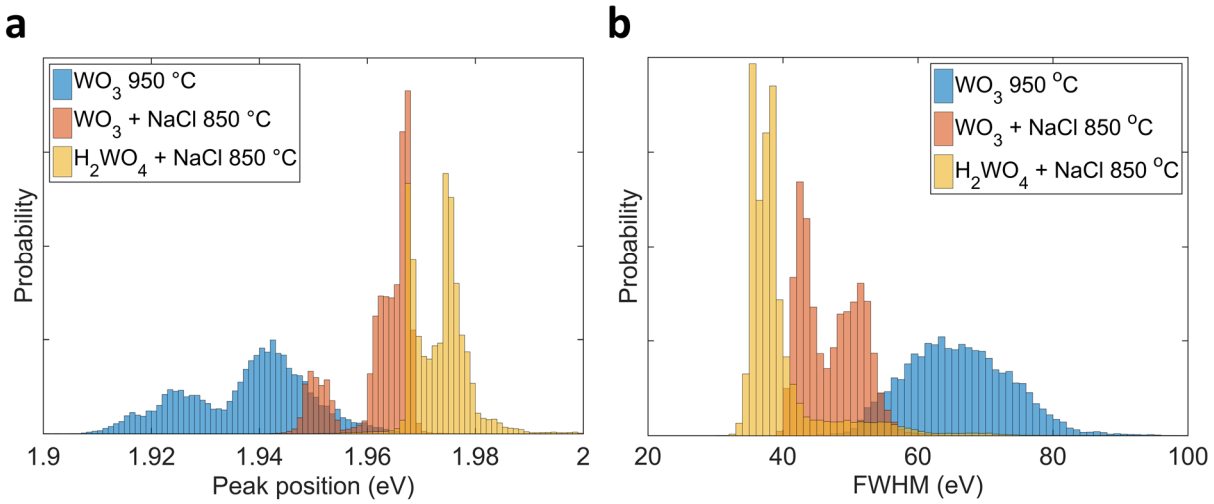


Figure 6.14 *Distribution of (a) PL peak position and (b) PL FWHM for several WS_2 flakes grown using: WO_3 at 950°C, WO_3+NaCl at 850°C and H_2WO_4+NaCl at 850°C.*

6.4.3. CHEMICAL PURITY AND STRUCTURAL DEFECTS

X-ray photoelectron spectroscopy (XPS) has also confirmed the greater efficiency of tungstic acid in inducing a complete sulfurization of the precursors and a smaller concentration of structural defects in the final WS_2 crystals compared to tungsten oxide. For WS_2 grown from H_2WO_4+NaCl, the W $4f_{5/2}$ and W $4f_{7/2}$ core levels (Fig. 6.15*a*) exhibit peak positions at 32.4eV and 34.7eV, respectively, which are characteristic of W^{4+} in WS_2 [308][309], and show the narrowest achievable FWHM (1eV) using a Mg source of X-ray. These results indicate high chemical purity and a nearly perfect stoichiometric ratio of W and S, which has also been confirmed by calculating the concentration of W and S from the integrated intensity of the W 4f and S 2p core levels. The S $2p_{1/2}$ and $2p_{3/2}$ core levels (Fig. 6.15*b*) also appear at the expected positions for pristine WS_2 of 162eV and 163.5eV [309], respectively, and again exhibit a very narrow FWHM (1eV). Further, the very small amount of WO_3 detected on the as-grown samples, which partially overlaps with the W 5p core level (Fig. 6.15*a*), disappears after transferring the flakes onto a fresh SiO_2/Si substrate (Fig. 6.15*c*), suggesting that it originates from residual precursors on the substrate (the XPS spot size is ~1mm). It is worth noting that the FWHM of the W 4f core level remains unchanged in the transferred flakes (Fig. 6.15*c*), thus suggesting that the transfer process preserves the crystallinity of the material and no additional defects are introduced.

Chemical purity and a W:S stoichiometric ratio of 1:2 have also been observed for the WS_2 flakes grown from WO_3+NaCl (Fig. 6.15*a*). However, a much larger WO_3 component has been detected in this case, suggesting that a significant amount of the oxide precursor is not sulfurized. Upon transferring the flakes onto a fresh SiO_2/Si substrate, the WO_3 component entirely disappears (Fig. 6.15*c*), indicating that the detected unsulfurized WO_3 is mostly distributed onto the growth substrate rather than lying onto the WS_2 crystals. The transferred flakes show an increase in the FWHM of the W 4f core level peak from 1.2eV of the as-grown samples (Fig. 6.15*a*) up to 1.3eV (Fig. 6.15*c*), which originates from the introduction of atomic defects as a consequence of WO_3 desorption-induced mechanical stresses.

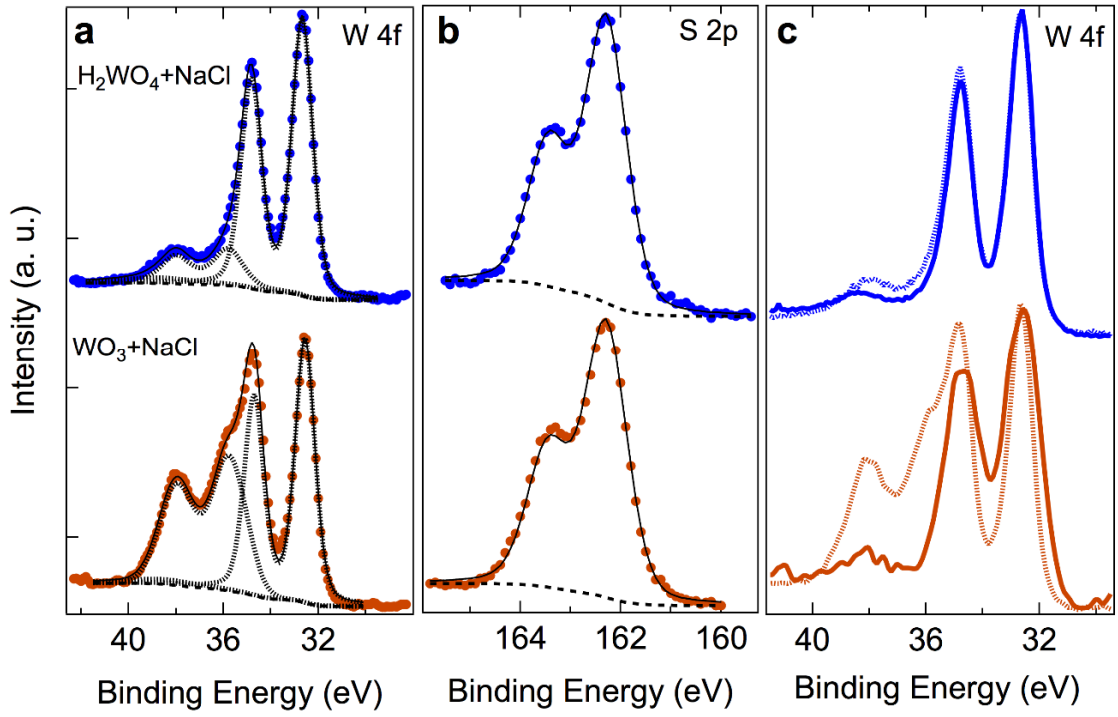


Figure 6.15 *XPS spectra of the W 4f and S 2p core level peak regions, confirming the effectiveness of H_2WO_4 as precursor versus WO_3. (a) W $4f_{5/2}$, W $4f_{7/2}$ and W 5p core levels for WS_2 grown using H_2WO_4+ NaCl (blue spectrum) at 950°C and WO_3+NaCl (red spectrum) at 950°C. The deconvolution of each W 4f core level peaks and the overall fit of the spectra are reported as black dashed and continuous lines, respectively. (b) S $2p_{1/2}$ and $2p_{3/2}$ core levels for each of the two growth conditions. (c) W 4f core levels before (dashed line) and after (continuous line) transfer on a fresh SiO_2/Si substrate, demonstrating the complete disappearance of residual WO_3 components. The spectra were fit by Doniach-Sunjic function after subtracting a Shirley background (black dashed line).*

6.4.4. ELECTRICAL CHARACTERIZATION

The effectiveness of H_2WO_4+NaCl versus WO_3 as metal precursor for the synthesis of mono-layered WS_2 with less structural defects has also been verified by characterization of WS_2-based bottom-gated field effect transistors (Fig. 6.16). The recorded FET transfer curve for a typical monolayered WS_2 flake grown by using H_2WO_4+NaCl at 950°C and transferred onto a fresh Si/SiO_2 substrate (Fig. 6.16*c*) is characteristic of an accumulation-type n-channel FET, in which the current flowing through the channel increases with increasing gate bias (above the threshold voltage). The response curves for the same WS_2 monolayer at different gate biases (Fig. 6.16*d*) exhibit asymmetry at V_{ds}~0V which originates from the different electrostatic potentials at the source and drain electrodes. While the Schottky barrier at the source electrode is pinned by the gate, the barrier at the drain electrode increases and decreases with positive and negative drain biases, respectively. Nevertheless, as the semi-conductor bands at the semiconductor/metal interface become more bent with increasing gate bias, the contribution of tunnelling currents through the barrier increases and thus the contacts become more Ohmic in nature.

Remarkably, monolayered WS_2 triangles grown from H_2WO_4+NaCl at 950°C exhibit electron mobility of $28 cm^2V^{-1}s^{-1}$ (Fig. 6.16*c, f*), which is comparable to what reported for mechanically exfoliated WS_2 [38][310][311][312] and higher than the mobility values reported so far for CVD grown-WS_2 onto SiO_2 (Fig. 6.17*a*) [184][185][187][188][189][223][245][257][313][314][315]. This result is in agreement with the fact that H_2WO_4+NaCl leads to WS_2 crystals with a low concentration of defects. Monolayered WS_2 grown from WO_3+NaCl at 950°C and 850°C show the second highest mobility of $22 cm^2V^{-1}s^{-1}$ and the lowest mobility of ~$2 cm^2$/Vs, respectively, suggesting that the growth temperature plays a key role in improving the crystallinity without promoting S desorption (Fig. 6.16*e, f*). Nevertheless, mobility values in the range 10-$20 cm^2V^{-1}s^{-1}$ have been obtained for WS_2 monolayers grown from H_2WO+NaCl at different temperatures (Fig. 6.16*f*), indicating that the role played by the chemical nature of these precursors in determining the crystallinity of the synthesis product prevails over the temperature effect observed in the case of WO_3+NaCl.

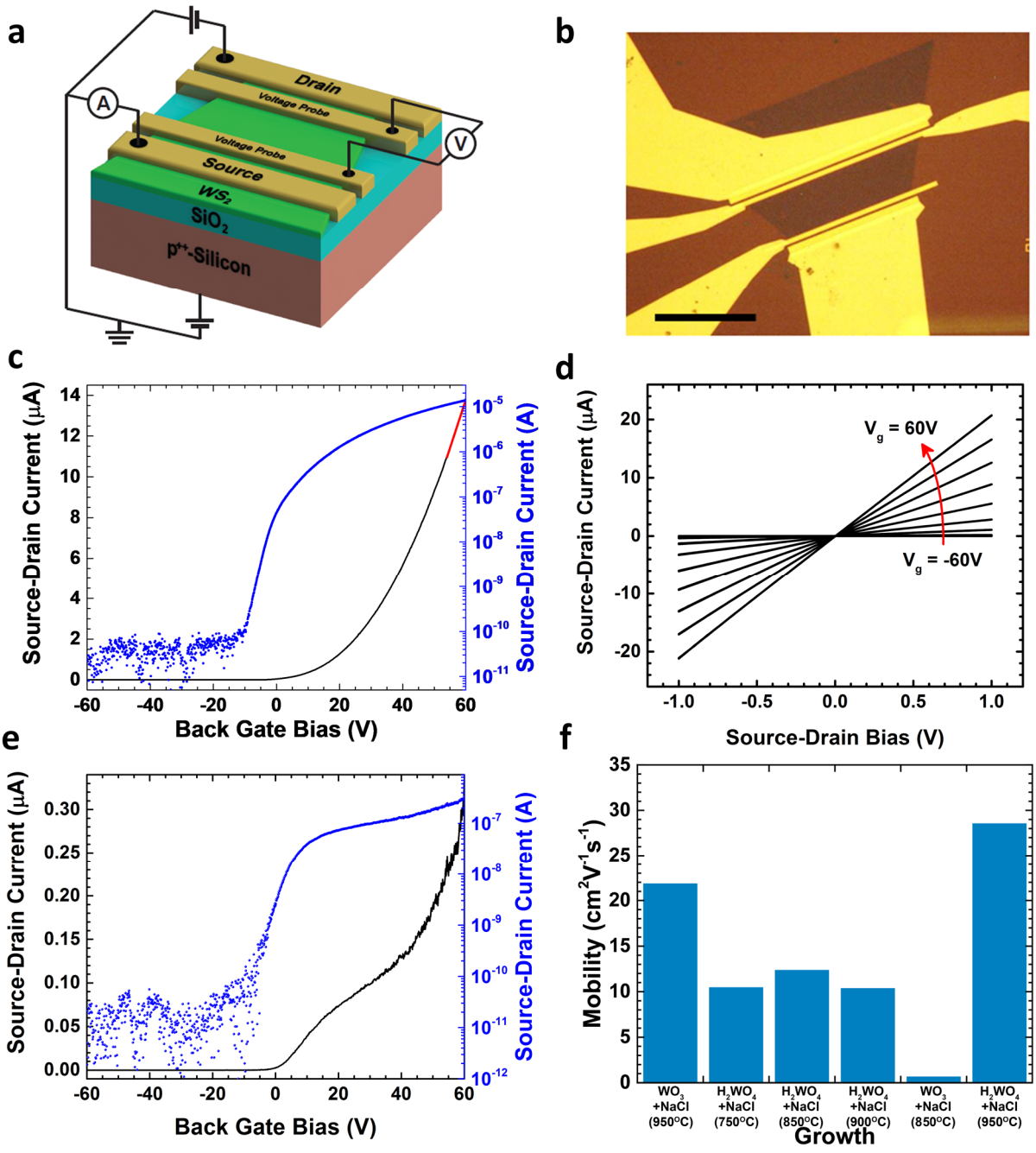


Figure 6.16 *Electrical characteristics of monolayered WS_2. (a) Schematic of the bottom-gated field effect transistors. (b) Optical micrograph of the device (scale bar is 20μm). (c) FET transfer curve for WS_2 grown using H_2WO_4+NaCl at 950°C showing the highest mobility of 28$cm^2V^{-1}s^{-1}$. The linear region of the transport graph is marked with a red dashed line. (d) Response curves at different gate biases for WS_2 grown using H_2WO_4+NaCl at 950°C. (e) FET transfer curve for WS_2 grown using WO_3+NaCl at 800°C showing the lowest mobility of* ~2$cm^2/V^{-1}s^{-1}$. *(f) Mobility values of WS_2 monolayers grown using different precursor systems and growth temperatures.*

Bilayered WS_2 triangles exhibit electron mobility systematically higher (~38cm^2/Vs) than monolayered flakes. This has been previously observed for mechanically exfoliated WS_2 [59][312]. Remarkably, WS_2 bilayers grown from WO_3+NaCl at 950°C exhibit the highest mobility of 52$cm^2V^{-1}s^{-1}$ (Fig. 6.18) which is higher than what reported so far for both CVD grown- and mechanically exfoliated-bilayered WS_2 flakes deposited onto SiO_2 (Fig. 6.17*b*) [59][166][312]. The fact that the highest mobility for bilayered WS_2 has been obtained using WO_3+NaCl rather than H_2WO_4+NaCl suggests that the bilayered system is less affected by the precursors choice and exhibits in general crystal quality superior to monolayers.

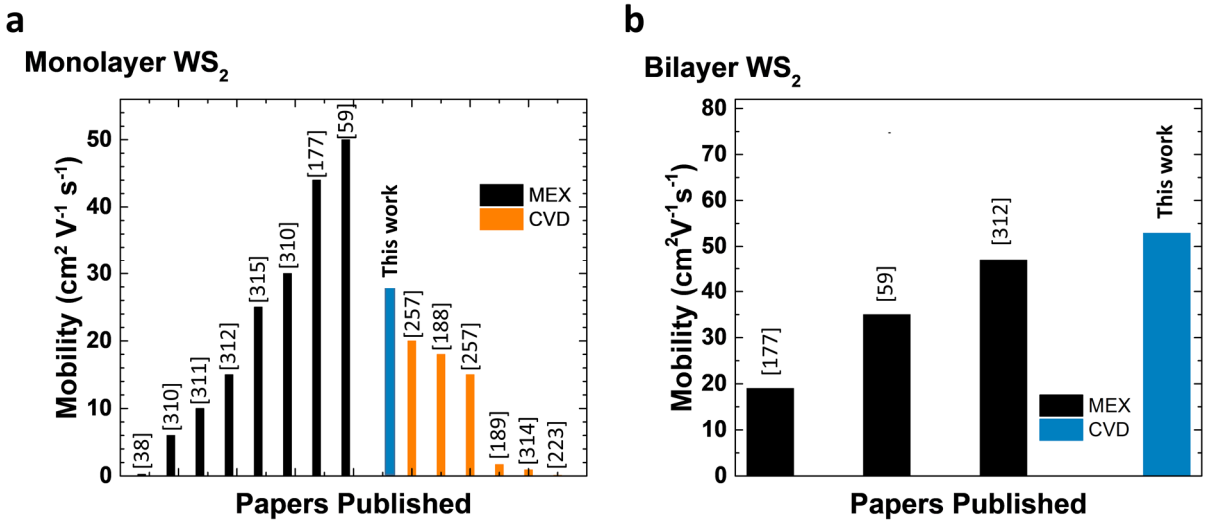


Figure 6.17 *Comparison of the results presented in this work with the literature on CVD grown- and mechanically exfoliated (MEX)-WS_2, showing electron mobility record values for both (a) monolayered and (b) bilayered WS_2 amongst the best values reported for CVD grown-WS_2.*

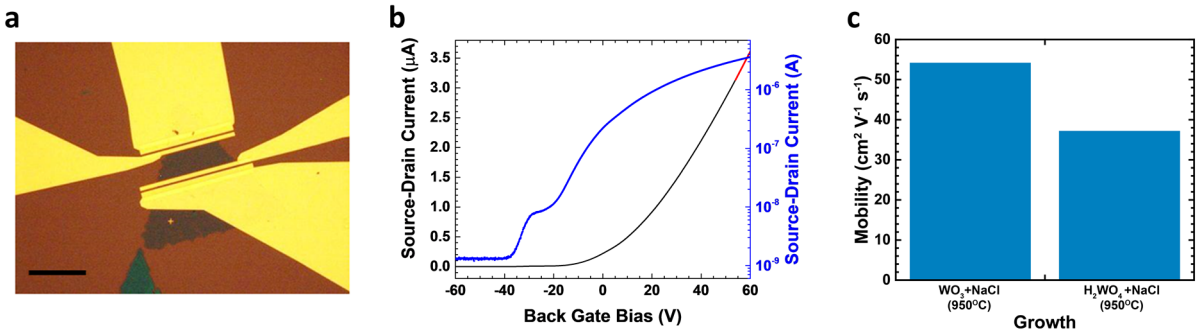


Figure 6.18 *Electrical characteristics of bilayered WS_2. (a) Optical micrograph of the device (scale bar is 30μm). (b) FET transfer curve for bilayered WS_2 grown using WO_3+NaCl at 950°C showing the highest mobility of 52$cm^2V^{-1}s^{-1}$. The linear region of the transport graph is marked with a red line. (c) Mobility values of WS_2 bilayers grown using different precursors and growth temperatures.*

6.5. CONCLUSIONS

In conclusion, we have developed a CVD strategy to synthesize large single- and double-layered WS_2 domains at temperatures as low as 750°C. The WS_2 crystals show a superior optical quality and higher carrier mobility values than what reported so far in the literature. Compared to the widely used metal oxide-based conversion synthesis of WS_2 (Chapter 5), the molecular approach adopted in this chapter, were tungsten oxyhalide molecules are sulfurized in vapour phase, leads to a more efficient sulfurization of W and thus to less defects in the resulting WS_2. These results can be applied to the synthesis of other TMDs and can pave the way towards the scalable synthesis of atomically thin WS_2 over large areas.

7) CVD SYNTHESIS OF INDIUM-DOPED WS_2

7.1. INTRODUCTION

As reported in Chapter 3, very few experiments have been done so far that attempted the doping of WS_2 with post-transition metals. Srivastava et al. have reported the synthesis of indium-intercalated MoS_2 (In_xMoS_2 with $0 \leq x \leq 1$) for the first time in the 80s and studied its properties [316]. X-ray analysis showed that In_xMoS_2, like the host 2H-MoS_2, also possess hexagonal symmetry exhibiting a small but continuous increase in the interlayer spacing with increasing x. Further, room-temperature thermoelectric power experiments and two-probe low temperature (150-300K) conductivity measurements indicated that the intercalated compounds also exhibit an n-type semiconducting behaviour similar to 2H-MoS_2. In_xWS_2, In_xMoSe_2 and In_xWSe_2 ($0 \leq x \leq 1$) intercalation compounds have also been synthesized and exhibited semiconducting characteristics with p-type (In_xWS_2, In_xMoSe_2) and n-type (In_xWSe_2) conductivity as the host materials (Section 3.5) [263][264][317][318], while in the case of In_xWSe_2 a shift form p- to n-type occurred [319][297].

Overall, such behaviour is contrary to the usual metallic and paramagnetic characteristics of alkali and alkaline earth metal intercalates of WS_2. Indeed, earlier studies have shown that WS_2 can be successfully intercalated with alkali or alkaline earth metals and that the behaviour of the host material drastically changes from diamagnetic semiconducting to metallic and superconducting [264] [320]. These results were explained on the basis of a charge transfer band model which assumes that, upon intercalation, the conduction band of alkali or alkaline earth metals overlaps with unfilled non-bonding d/p bands of WS_2, and that electrons are transferred from the guest atoms to the host material which thus become metallic due to a large increase in free electron density compared to pure WS_2 [1]. Whereas, to explain the semi-conducting behaviour in In-intercalated TMDs and in a few other compounds such as M_xZrS_2 where

M=Fe, Co, Ni, it has been suggested that in certain cases the electrons given by the guest atoms may be trapped rather than being delocalized in the conduction band of the host crystal, likely due to the higher ionization potential of In as compare to alkali or alkaline metals [321][322]. Later measurements on the fundamental absorption edge of M_xZrS_2, M_xHfS_2 (M=Cu, Fe and $x \leq 0.22$) and Ni_xZrS_2 ($x \leq 0.15$) have revealed that these compounds also retain semiconducting behaviour. It has been proposed that in such cases the intercalated atoms should be regarded as analogous to deep level impurities, leading to an additional energy level near to the top of the valence band or, alternatively, as a modification of the energy band of the host crystal due to the interaction between the intercalate and S atoms [323][324]. Therefore, it has been proposed that the intercalation of TMDs by In atoms may generate an additional energy state at the top of the valence band which leads to a subsequent upward shift of this band [325]. A gradual increase in this shift with increasing amount of intercalating atoms would explain the linear decrease in the energy gap with increasing In content, as observed in In-intercalated $MoSe_2$ compounds via optical absorption measurements [325].

It has been also reported that, unlike their alkali and alkaline earth metal analogues, In-intercalated WS_2 compounds were found to be stable upon exposure to air [258][263][264][316][317][318][326] and that such behaviour is similar to what observed for $M'MX_2$ intercalation compounds (where M'=unsolvated transition or post transition metal, M=Nb, Ta and Ch=S, Se) due to a fairly strong guest-host bonding which hinders deintercalation processes [327].

Further, it has been shown that In intercalation is likely to induce some degree of crystal disorder and variations in the morphological characteristics of the host MoS_2 and $MoSe_2$ crystals, which exhibited a gradual decrease in the crystallite size with increasing In content, and additional In_xSe_y phases in $MoSe_2$ and WSe_2 [316][317][318][319][326]. On the other hand, these effects were significantly less prominent in In_xWS_2 intercalated compounds for all compositions, probably due to the WS_2 larger van der Waal gap than MoS_2, which can permit an easier entry of the incoming guest In atoms, and to a less favourable formation of In_xS_y phases [263][264].

Finally, it has been reported that In-intercalated WS_2 thin films are resistant against oxidation in air and to chemicals. Further, they exhibited higher conductivity and photocurrent than both pure and

doped WS_2 films intercalated with other group III-elements (Ga and Tl), thus proving to be highly photo-active and applicable as photoelectrodes in solar cells [258].

Therefore, the choice of indium as dopant metal has been mainly guided by these interesting and encouraging results and by the fact that it is a representative post-transition element of the group IIIA having lower melting and boiling points than B, Al and Ga. Further, both the ionization potential and electronegativity of In are higher than those of alkali and alkaline earth metals (Table 7.1) and thus it is expected that the properties of In-doped WS_2 would significantly differ from those of other alkali and alkaline earth metal complexes.

Element	Ionization potential* (eV)	Electronegativity (Pauling values) (eV)	Ionic diameter (Å)
Li	5.390	0.98	1.36
Na	5.138	0.93	1.94
K	4.339	0.82	2.66
Rb	4.176	0.82	2.94
Cs	3.893	0.79	3.34
Ca*	6.111	1.00	1.98
Sr	5.692	0.95	2.24
Ba	5.212	0.89	2.68
In	5.785	1.78	2.64

***Calcium is the exception which has a higher ionization potential than indium.**

Table 7.1 *Ionization potential, electronegativity and ionic diameter values of In, alkali and alkaline earth metals. Adapted from Ref. [316].*

7.2. RESULTS

The CVD synthesis of In-doped WS_2 samples was performed by using the optimized conditions for the grow of high-optical quality and high-mobility atomically thin WS_2 described in Chapter 6. In this experiment, $In(OH)_3$ powders were added as indium precursor. H_2WO_4 (0.2g, 99%, Sigma Aldrich), NaCl (0.2g, ≥99.5%, Sigma Aldrich) and $In(OH)_3$ (0.05-0.2g, ≥99.5%, Sigma Aldrich) powders were loaded in the center of a quartz tubular furnace together with SiO_2/Si substrates, while S (0.6g, ≥99.5%, Sigma Aldrich) powders were placed upstream in correspondence to the second independently controlled

heater (Fig. 7.1*a*). The synthesis were carried out at 10^{-1}mbar under vacuum and high-purity Ar gas flowing at 100sccm throughout the entire process. The W and In precursors-controlling furnace was heated up to 850°C at 25°Cmin^{-1}, kept at this temperatures for 15min and then naturally cooled down to room temperature, whereas the S-controlling heater was heated up to 125°C at 5°Cmin^{-1}, kept at this temperature for 15min and then naturally cooled down (Fig. 7.1*b*).

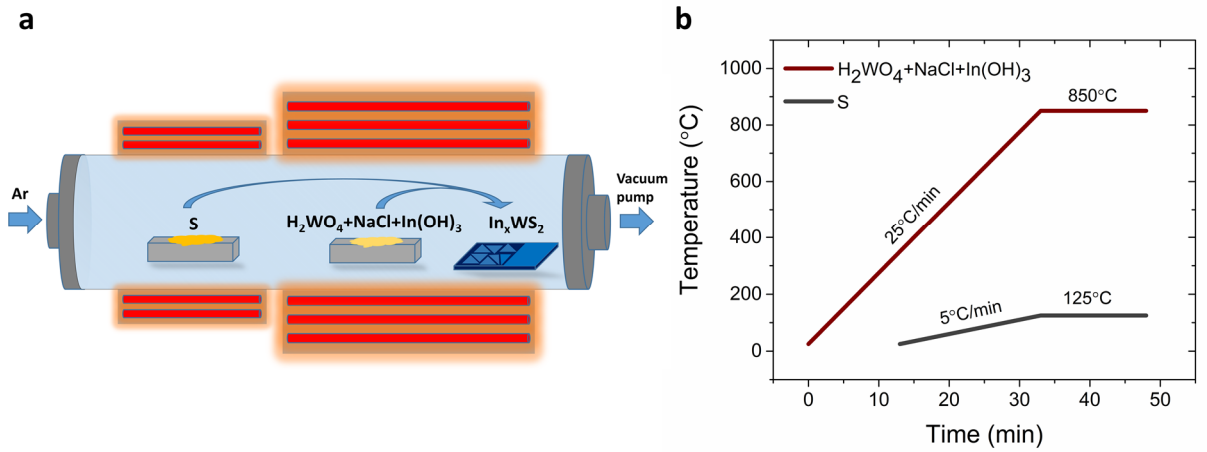


Figure 7.1 *Illustration of the (a) two-zone CVD tubular furnace set-up and (b) temperature profiles of the W and In precursors-furnace and S-heating module. The S reaches 125°C when the main furnace is at 850°C. The SiO_2/Si substrate is loaded downstream at 1-8cm away from the W and In precursors-containing crucible and it is subjected to the same temperature.*

Figure 7.2 shows optical and SEM images of flakes grown by using different $In(OH)_3/H_2WO_4$ weight ratios: In/W=0.25, In/W=0.5, In/W=0.75 and In/W=1 (Table 7.2). It can be seen that the samples In/W=0.25 and In/W=0.5 present triangular morphology with straight edges similar to that of crystalline CVD-grown WS_2 (Chapter 6), whereas the samples In/W=0.75 and In/W=1 show convex and jagged edges, respectively, which might suggest a more significant incorporation of In. Increasing amount of Indium has been confirmed by XRD, Raman, PL and XPS characterizations discussed in the following. Figure 7.3 shows additional optical and SEM images of the sample In/W=1 since it presents different morphologies and a large coverage.

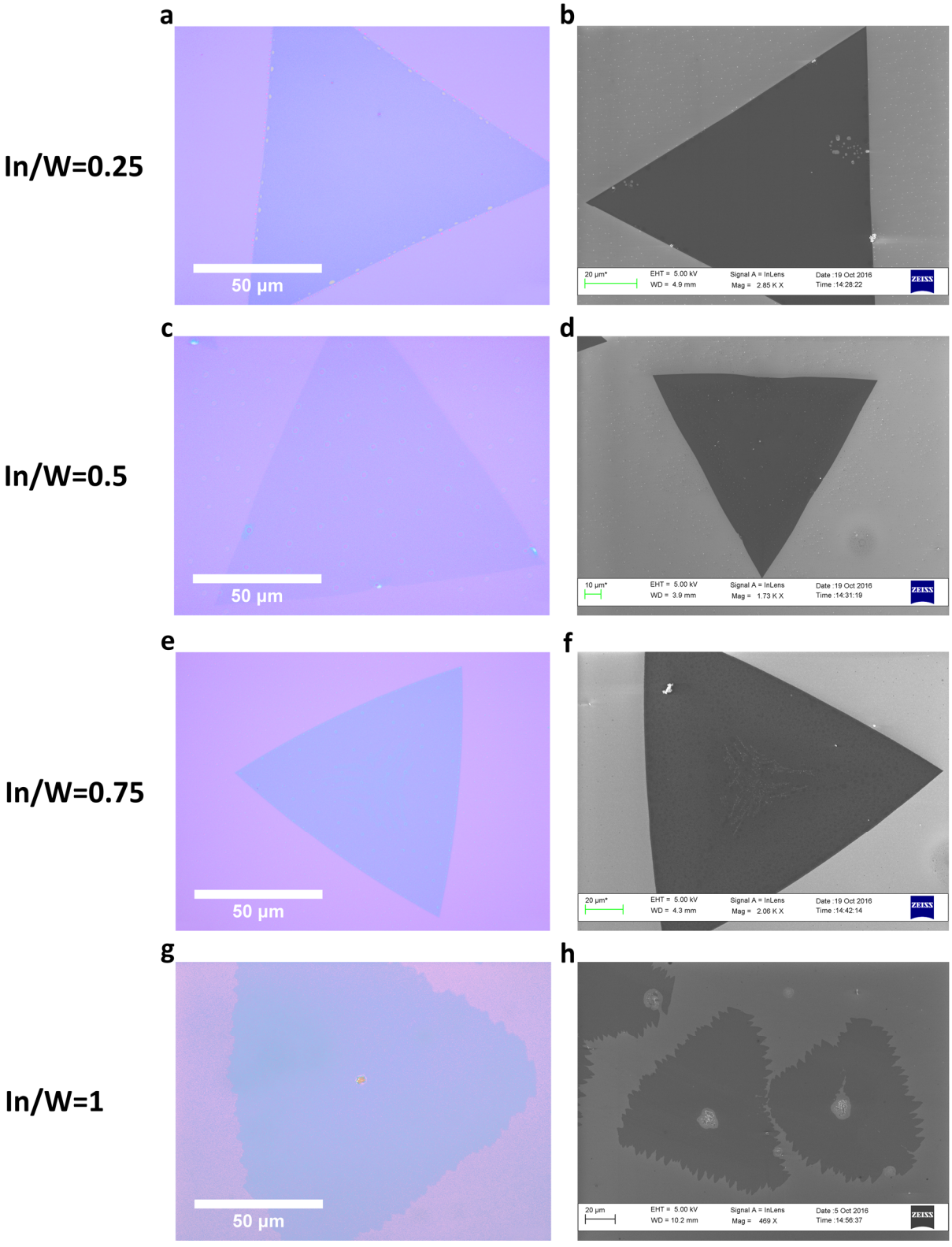


Figure 7.2 *Optical and SEM images of flakes grown by using different $In(OH)_3/H_2WO_4$ weight ratios: (a, b) 0.25, (c, d) 0.5, (e, f) 0.75 and (g, h)=1. All other synthesis conditions and parameters were kept constant as described above (Table 7.2).*

SAMPLE	$In(OH)_3$	H_2WO_4	NaCl	S	Growth Temperature	Growth Time	Growth Pressure
In/W = 0.25	0.05g	0.2g	0.2g	0.6g	850°C	15min	1.3mbar
In/W = 0.5	0.1g	0.2g	0.2g	0.6g	850°C	15min	1.3mbar
In/W = 0.75	0.15g	0.2g	0.2g	0.6g	850°C	15min	1.3mbar
In/W = 1	0.2g	0.2g	0.2g	0.6g	850°C	15min	1.3mbar

Table 7.2 *CVD synthesis conditions for the In-doped WS_2 samples.*

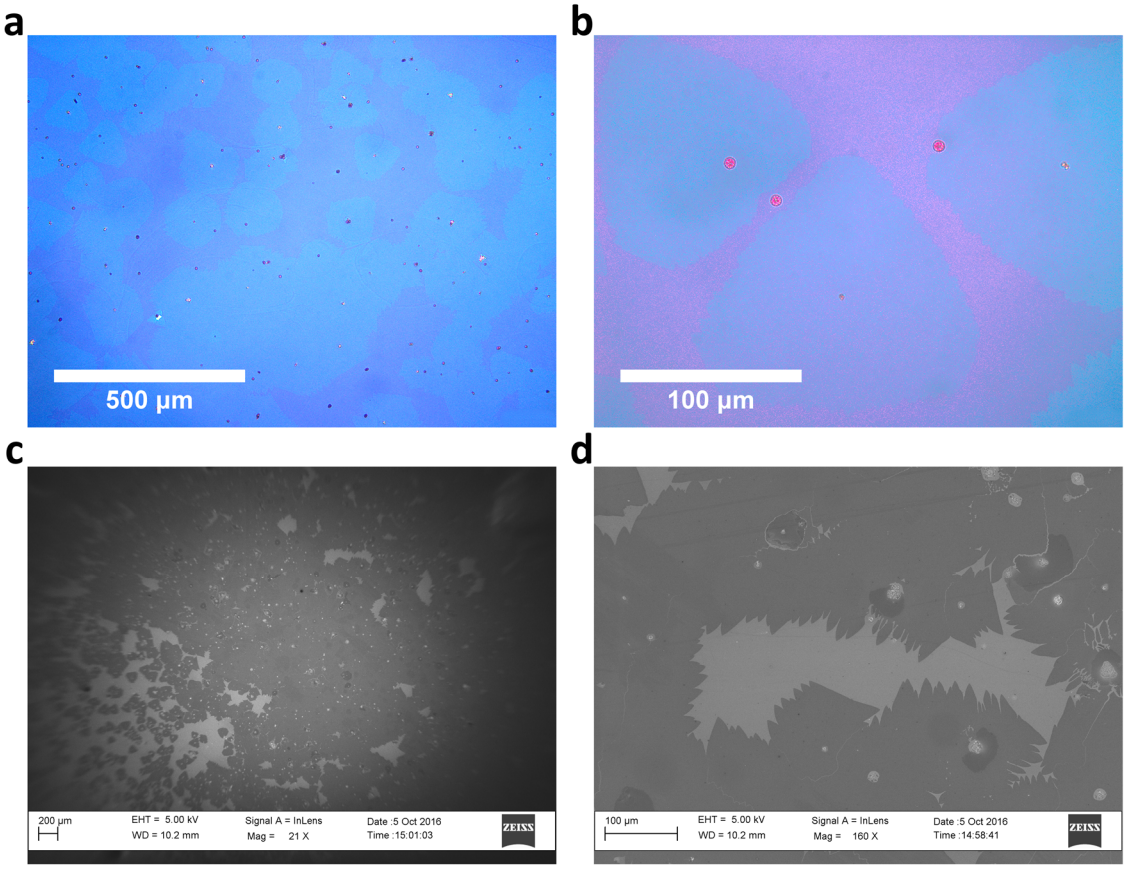


Figure 7.3 *(a, b) Optical and (c, d) SEM images of the sample In/W=1, showing high nucleation density of the flakes and their jagged edges.*

7.3. PHYSICAL CHARACTERIZATION

7.3.1. X-RAY DIFFRACTION

As shown in Figure 7.4, the XRD diffraction patterns of all the In-doped WS_2 samples show a marked analogy to that of 2H-WS_2 and they can all be indexed on a hexagonal unit cell basis. Therefore,

as also previously reported for bulk In_xMoS_2, In_xWS_2, In_xMoSe_2 and In_xWSe_2 [258][263][264][316][317][318][319][325][326], it can be concluded that the crystal arrangement of W and S atoms remains virtually the same as in the host 2H-WS_2 upon indium incorporation, except for a slight expansion of the van der Waals gap (Table 7.3). The crystal structure of all the In-doped WS_2 samples can therefore be referred to the same space group of the host 2H-WS_2 (namely P63/mmc). It is worth noting that these results are in agreement with earlier studies on the intercalation compounds of MoS_2 which revealed that larger metal ions are likely to retain the hexagonal structure of MoS_2 whereas smaller ions mostly lead to a different crystallographic order [328]. Further, it has been suggested that, contrarily to alkali and alkaline earth metals-intercalated layered compounds which exhibit octahedral coordination, In stabilizes a trigonal prismatic coordination. This is due to the presence of d-bands in indium metal which provide an additional contribution to bonding stabilization [264].

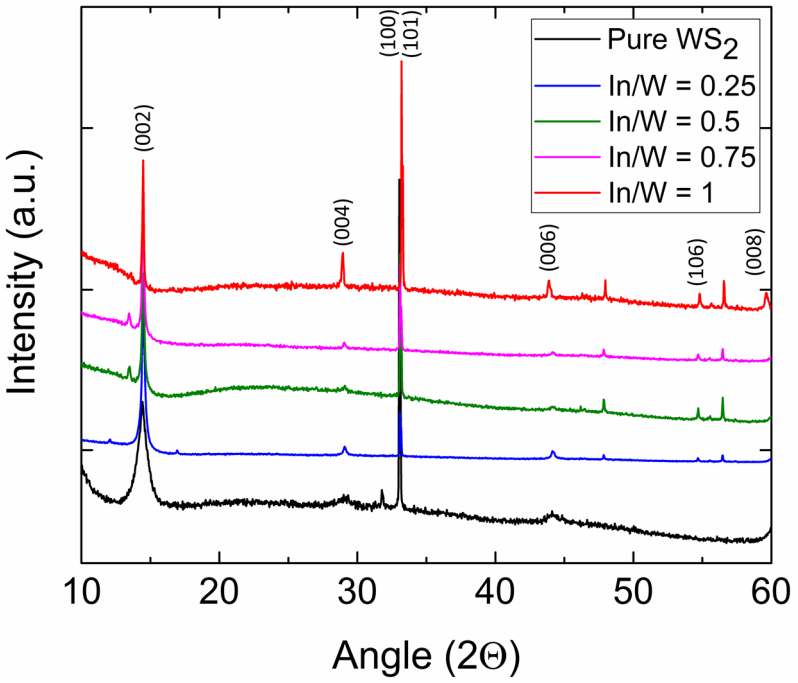


Figure 7.4 *XRD patterns for CVD-grown pure WS_2 and In-doped WS_2.*

Earlier structural studies on the intercalation of layered TMDs (In_xMoS_2, In_xWS_2, In_xMoSe_2, In_xWSe_2, Cu_xNbS_2, Cu_xNbSe_2, AI_xTaS_2, Zn_xTaS_2) and some other compounds (Li_xYCl, Li_xGdCl) have showed that the intercalation process does not necessarily lead to the same significant increase in the interlayer spacing observed for alkali or alkaline earth metal analogues [264]. It has therefore been suggested that there may be no increase in the c-parameter at all in a given intercalation process. This phenomenon

does not have purely geometric origin but is thought to be dependent on the size, concentration, electronic configuration, ionisation potential and electronegativity of the guest atoms and on the structure of the host crystal [329].

SAMPLE	Position (2θ)	FWHM (2θ)	a (Å)	c (Å)	d (Å)
WS_2	14.444	0.703	3.23	11.02	5.51
In/W = 0.25	14.47	0.294	3.23	11	5.50
In/W = 0.5	14.444	0.166	3.22	11.02	5.51
In/W = 0.75	14.479	0.137	3.22	11	5.50
In/W = 1	14.307	0.182	3.21	11.14	5.57

Table 7.3 *Data for the (002) XRD peak and lattice parameters for pure WS_2 and In-doped WS_2 samples.*

By analysing the (002) XRD peak for pure and In-doped WS_2 (Fig. 7.5) it can be seen that the FWHM decreases as the In precursor concentration increases and that the sample In/W=1 exhibits a clear peak shift towards a larger d spacing (Table 7.3). Further, the samples In/W=0.5, In/W=0.75 and In/W=1 show an additional peak at 2θ=13.44 (Fig. 7.5) which we attribute to the incorporation of In atoms into the WS_2 lattice.

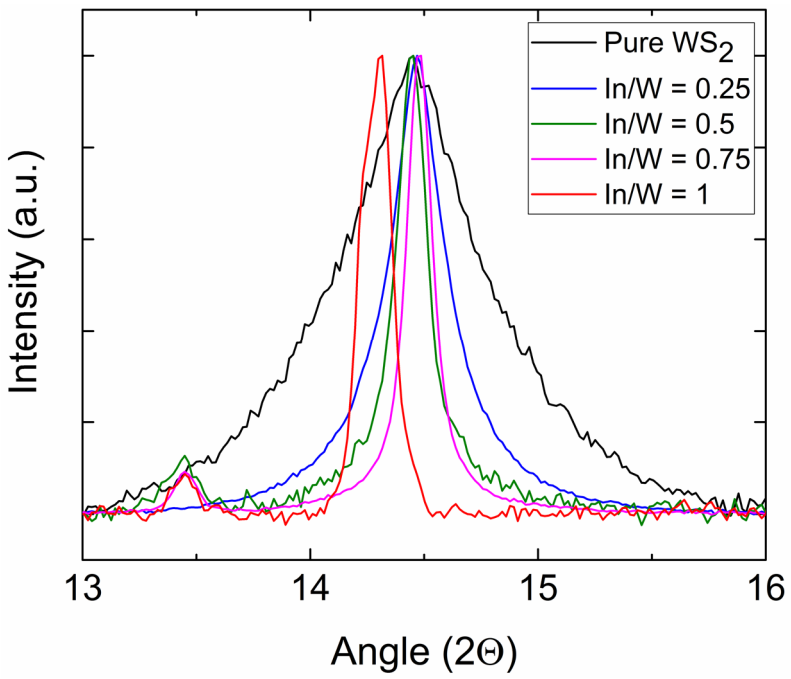


Figure 7.5 *(002) XRD peak for CVD-grown pure WS_2 and In-doped WS_2.*

The XRD spectra were further thoroughly analysed in order to ascertain the presence of any extra phase due to either free In metal and W oxide or binary In sulphides (InS, In_2S_3, In_7S_6). The reflections at 2θ~48 and ~57 have been ascribed to the presence of some In_2S_3 [330]. Indeed, thick crystals are often observed in the centre of thinner flakes (Fig. 7.6*a-c*) and Raman spectroscopy has ascertained that they consists of In_2S_3 (Fig. 7.6*d*). However, the In_2S_3 flakes are relatively small and are scattered across the growth substrate with low nucleation density compared to the WS_2 domains, and they can therefore be considered as secondary reaction products.

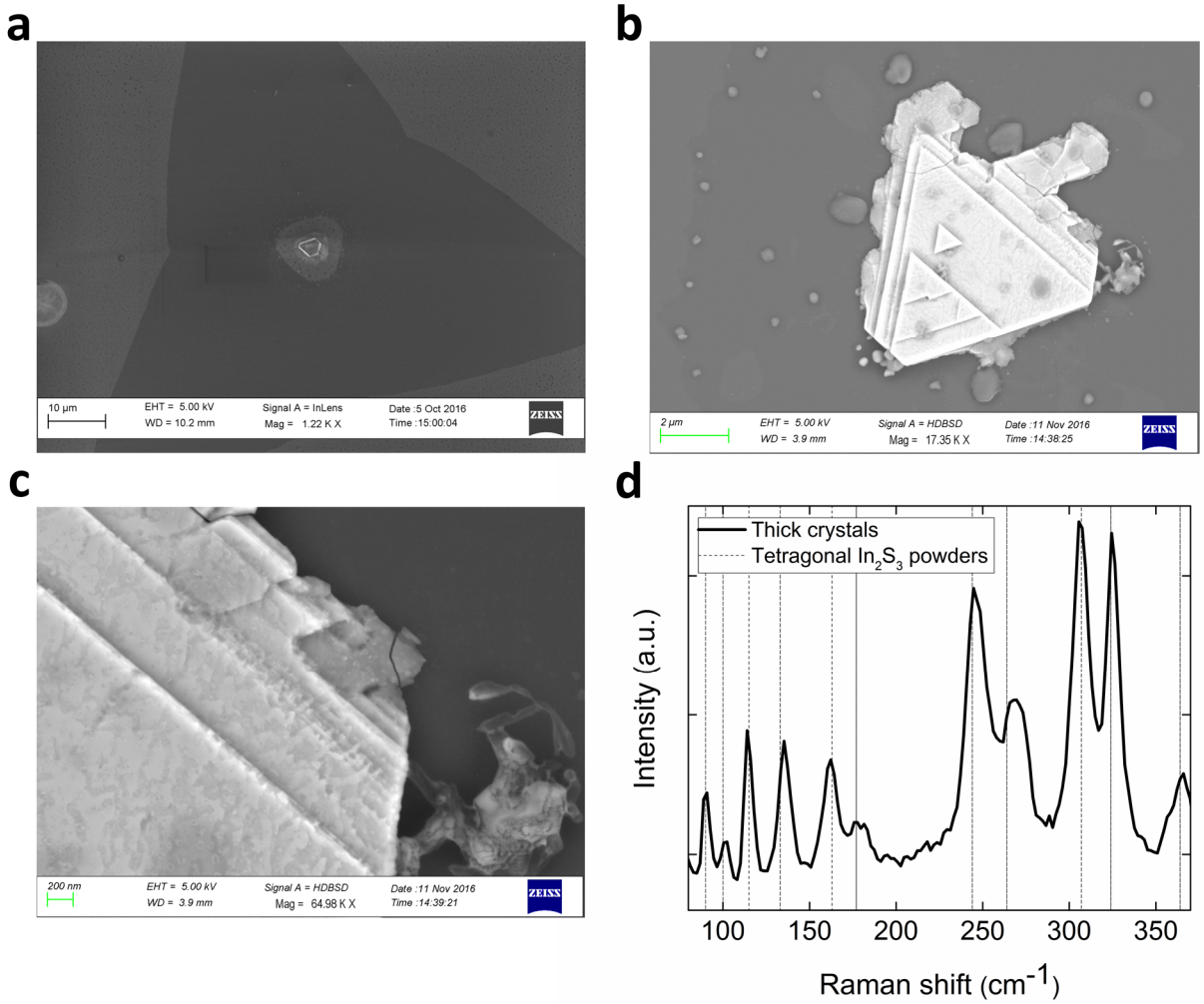


Figure 7.6 *(a) Low- and (b, c) high-resolution SEM images revealing the presence of multilayered In_2S_3 crystals in the centre of the thin In-doped WS_2 domains. (d) Representative Raman spectrum of the thick crystals shown in (b) and (c) confirming that they consist of In_2S_3 [331].*

7.3.2. RAMAN AND PHOTOLUMINESCENCE

Figure 7.7*a* shows representative Raman spectra for undoped WS_2 and In-doped WS_2 samples. It can be seen that, while the samples In/W=0.25, In/W=0.5 and In/W=0.75 show the characteristic in-plane 2LA-E^1_{2g} and out-of-plane A_{1g} vibrational modes for WS_2 [38], the sample In/W=1 is not Raman active. Moreover, PL characterization has revealed that, while the samples In/W=0.25, In/W=0.5 and In/W=0.75 exhibit PL emission peaks at higher energies than pure WS_2 and of lower intensity, the sample In/W=1 does not luminesce (Fig. 7.7*b*). Therefore, the sample In/W=1 shows a significantly different behaviour than pure WS_2 and WS_2 doped at lower In contents, which may be attributed to a very large amount of dopant atoms altering the crystal structure and properties of the host material, as also confirmed by XPS and electrical measurements discussed in the next sessions.

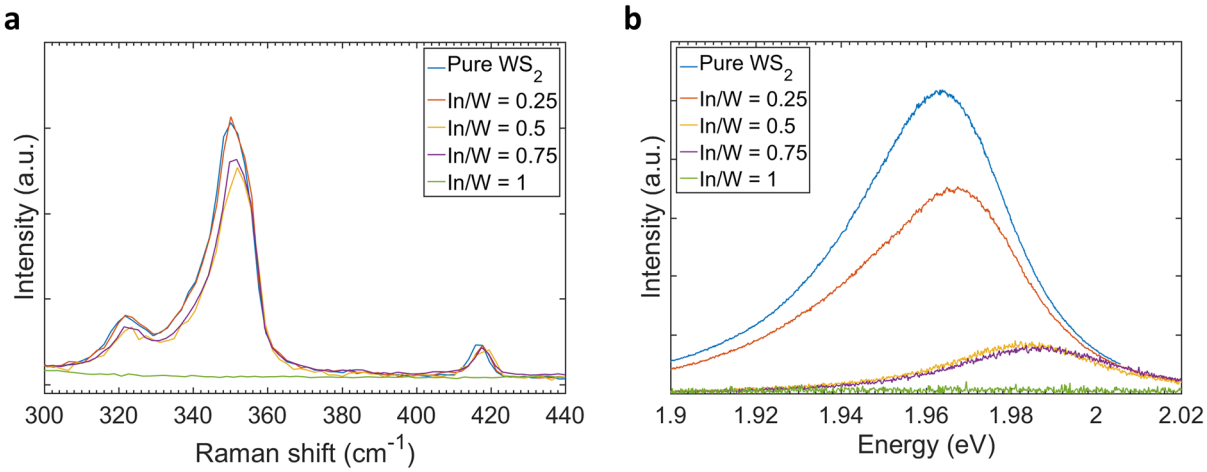


Figure 7.7 *Representative (a) Raman and (b) PL spectra for pure WS_2 (grown by using H_2WO_4 as metal precursor) and In-doped WS_2.*

Figure 7.8 shows that the E^1_{2g} and A_{1g} Raman peaks for all the Raman active In-doped samples (In/W=0.25, In/W=0.5 and In/W=0.75) are shifted towards higher frequencies (E^1_{2g} at ~351.5cm^{-1} and A_{1g} at ~418cm^{-1}) as compared to pure WS_2, which may be caused by differences in the binding energy between W–S and In–S bonds [95]. Nevertheless, the assignment of the shifts in Raman frequencies observed in atomically thin metal-doped TMDs is not yet fully understood and further studies will follow [95]. Figure 7.9 reveals that the excitons-to-trions ratio for all the PL active In-doped samples (In/W=0.25, In/W=0.5 and In/W=0.75) is lower than that of pure WS_2, thus suggesting n-type doping and a gradual increase in

the electron-carrier concentration with increasing In concentration. This trend may be explained considering that the post-transition In metal atoms have fully-filled d-orbitals and an additional third electron in a p-orbital in their most outer shell. This excess electron may thus enhance the concentration of free electrons in n-type WS_2, which may eventually lead to a semiconducting-to-metallic transition of the host material at high In incorporation levels. This trend has been confirmed by electrical characterization on the sample In/W=1 with the highest In content, which showed an increase in the resistance with increasing temperature, thus revealing a metallic behaviour (Fig. 7.10).

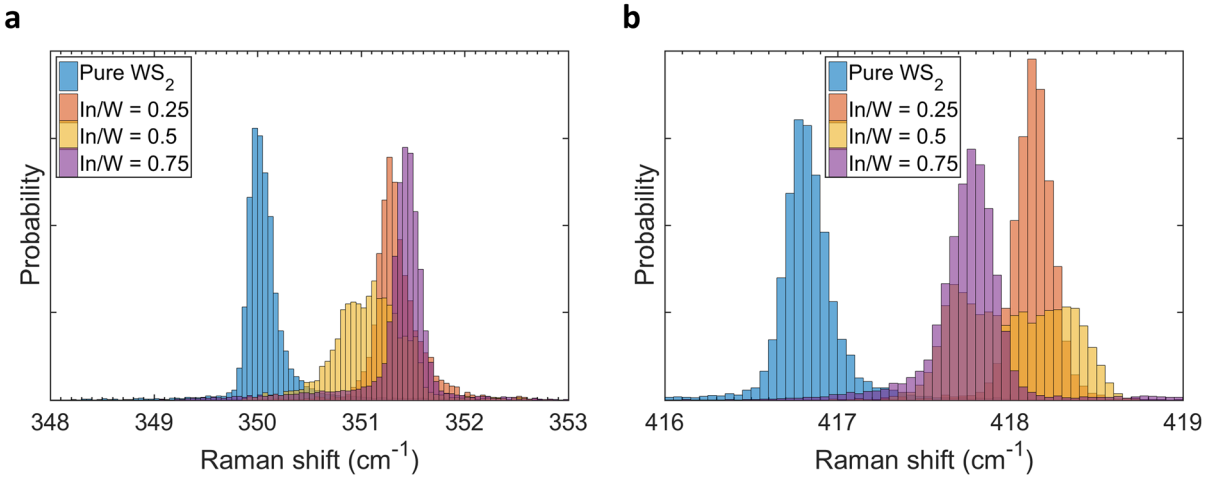


Figure 7.8 *(a) E^1_{2g} and (b) A_{1g} peak positions for pure WS_2 and Raman active In-doped WS_2 samples, obtained by fitting the spectra in Fig. 7.7a with Voigt profiles for both E^1_{2g} and A_{1g} modes.*

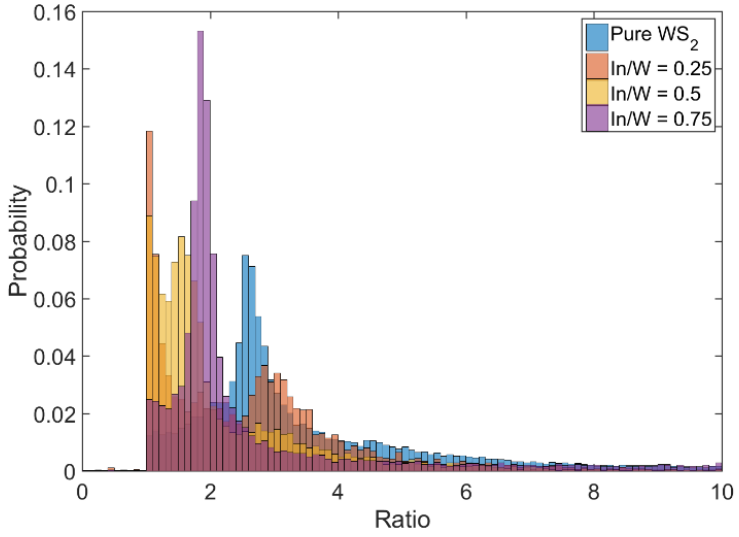


Figure 7.9 *Excitons-to-trions ratio for pure WS_2 and PL active In-doped WS_2 samples, obtained by fitting the spectra in Fig. 7.7b with Voigt profiles for both exciton and trion components.*

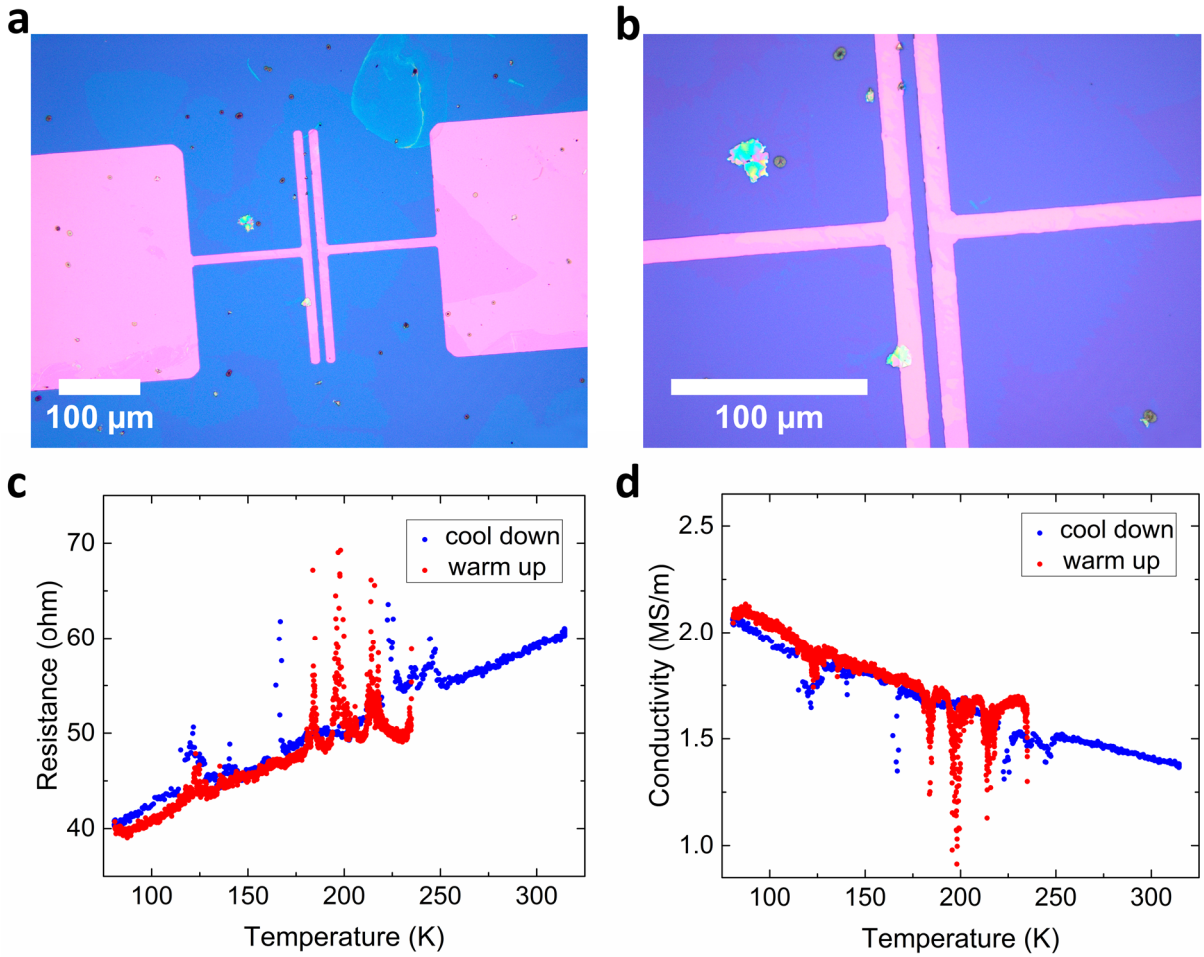


Figure 7.10 *(a, b) Optical micrographs of Ti and Au contacts deposited on In/W=1 flakes. (c) Measured resistance as a function of temperature. (d) Calculated conductivity vs. temperature revealing a semi-metallic behaviour.*

7.3.3. X-RAY PHOTOELECTRON SPECTROSCOPY

Since the sample In/W=1 is not Raman and PL active we have conducted SEM characterization in backscattered electron imaging mode (BSD) to reveal any elemental contrast. As atoms with a greater atomic number have a higher probability of producing elastic electron beam-atoms collisions, and thus a higher number of backscattered electrons reaching the BSE detector, “bright” and “dark” BSE areas can be correlated with higher and lower average atomic numbers in the sample, respectively. Therefore, since the atomic numbers of W and In are 74 and 49, respectively, figure 7.11 shows that the sample In/W=1 is made of different phases (In/W=1(1), In/W=1(2), In/W=1(3)) witch are likely due to a gradient

in the In concentration across the flakes. Figure 7.12 shows the In 3d, W 4f and S 2p core levels XPS spectra for pure WS_2 and In-doped WS_2 (In/W=0.25, In/W=0.5, In/W=1(1), In/W=1(2), In/W=1(3)).

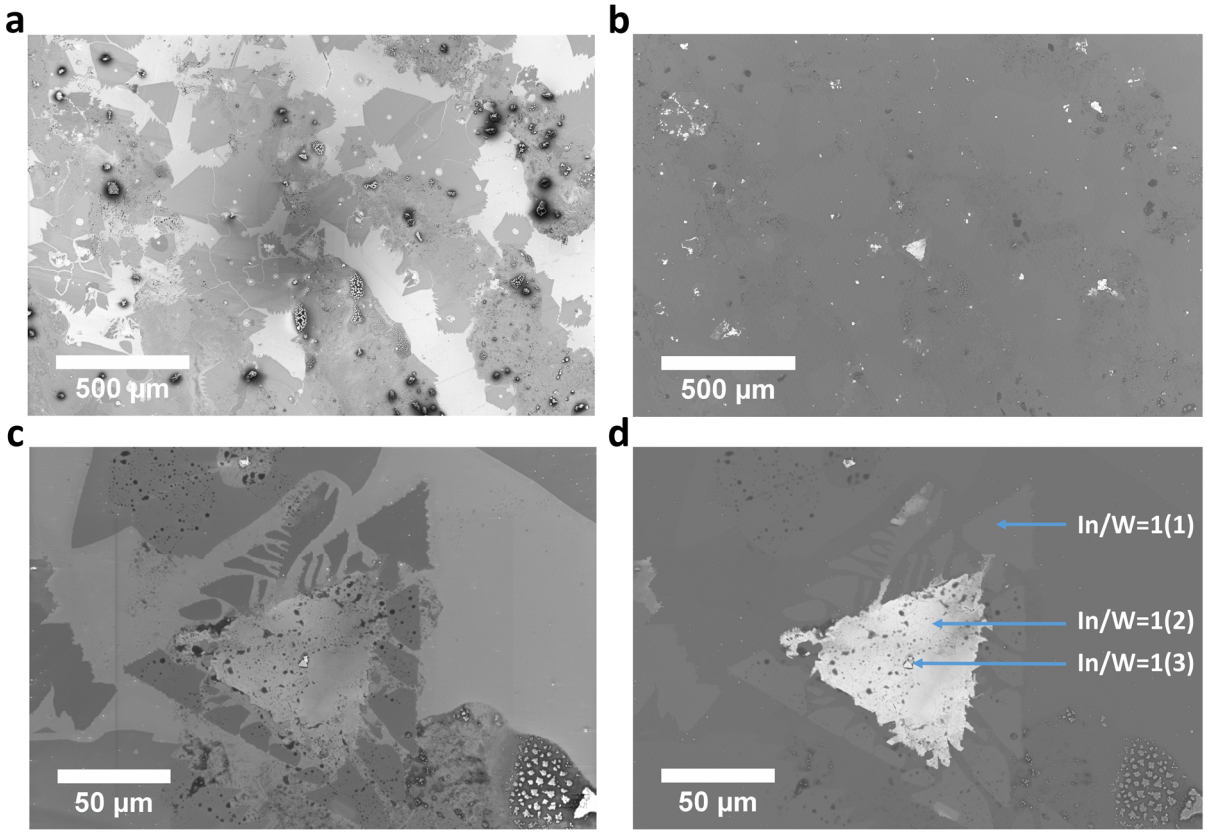


Figure 7.11 *Low-magnification SEM images in (a) SE and (b) BSD imaging mode of the same area of sample In/W=1. High-magnification SEM images in (c) SE and (d) BSD imaging mode of the same area of sample In/W=1, revealing compositional variation across the flakes.*

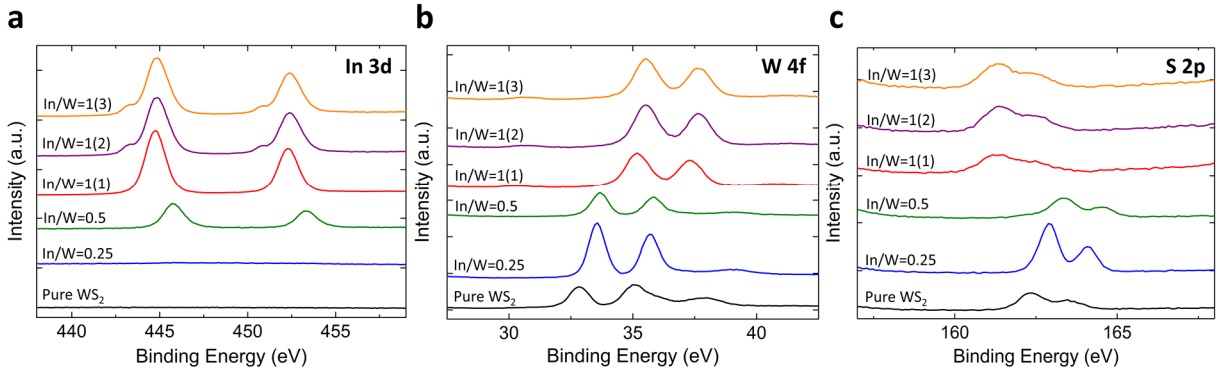


Figure 7.12 *(a) In 3d (b) W 4f and (c) S 2p core levels XPS spectra for undoped WS_2 and In-doped WS_2 (In/W=0.25, In/W=0.5, In/W=1), where In/W=1 (1), In/W=1 (2) and In/W=1 (3) refer to the three areas of the sample In/W=1 highlighted in Fig. 7.11d.*

It can be noticed that, while pure WS_2 and In/W=0.25 do not exhibit any Indium core level peak (Fig. 7.12*a*), the samples In/W=0.5 and In/W=1 show In $3d_{5/2}$ and In $3d_{3/2}$ core levels at binding energies of ~444eV and ~452eV, respectively. Further, it is observed that both In 3d core levels for the sample In/W=1 are slightly shifted to lower binding energies compared to the sample In/W=0.5 (Fig. 7.12*a*), which can be attributed to the presence of $In_xW_yS_z$ compounds [332]. While the peak shoulders at ~443eV and ~451eV observed for both samples In/W=1(2) and In/W=1(3) (Fig. 7.12*a*) are due to the presence of In_2S_3 as previously ascertained by Raman spectroscopy (Fig. 7.6). The W $4f_{5/2}$ and W $4f_{7/2}$ core levels peaks (Fig. 7.12*b*) of the In-doped samples are significantly shifted to higher energies compared to pure WS_2 (W $4f_{5/2}$ and W $4f_{7/2}$ at 32.4eV and 34.7eV respectively) which may suggest the presence of W6+ in the doped samples as opposed to W4+ in pure WS_2 [307]. This suggest a preferential bonding between In and W. Further, the S $2p_{1/2}$ and S $2p_{3/2}$ core levels peaks (Fig. 6.12*c*) of the In/W=1 samples also appear at lower energies than pure WS_2 (S $2p_{1/2}$ and S $2p_{3/2}$ at 162eV and 163.5eV respectively). Thus, we can conclude that In atoms have been successfully interacting with WS_2 as there is a clear In-W interaction based on the In 3d and W 4f peak shifts towards each other. The In atoms are thus likely to be chemisorbed onto the WS_2 or intercalated between multi-layered WS_2 domains. Table 7.4 reports the stoichiometric ratios of In, W and S for the doped samples obtained by calculating the corresponding concentrations from the integrated intensity of the In 3d, W 4f and S 2p core levels. In particular, it can be seen that the In:W ratios for the samples In/W=0.25 and In/W=0.5 are 0.038 and 0.45, respectively, with an associated uncertainty of ±0.2. While the In:W ratio for the sample In/W=1 is 1.2 with an associated uncertainty of ±0.5.

SAMPLE	In:W	S:W
In/W = 0.25	0.038:1	2.32:1
In/W = 0.5	0.45:1	2.22:1
In/W = 1	1.2:1	1.8:1

Table 7.4 *In:W and S:W stoichiometric ratios obtained by calculating the In, W and S concentrations from the integrated intensity of the In 3d, W 4f and S 2p core levels.*

7.4. CONCLUSIONS

In this chapter we have reported the successful chemisorption of indium atoms onto WS_2 atomic layers grown through the molecular precursors CVD approach described in Chapter 6, without sacrificing their lateral extension or the reproducibility/scalability of the synthesis process. Remarkably, the In-doped WS_2 samples exhibit tuneable optical emission and a semiconducting-to-semimetallic transition at high doping levels. Therefore, the present synthesis strategy can be employed to achieve carrier control in atomically-thin WS_2 through a stable incorporation of non-volatile post-transition metal atoms.

8) CONCLUSIONS AND FUTURE WORK

In this work we have demonstrated a novel use of molecular precursors in the controlled CVD synthesis of atomically-thin WS_2, which leads to superior material quality compared to the widely used topotactic transformation of WO_3-based precursors. Record high room-temperature charge carrier mobility up to 52cm^2/Vs and ultra-sharp photoluminescence linewidth of 36meV over submillimeter areas reveal that the crystal quality of the synthesized material supersedes also that of naturally occurring WS_2. Further, the proposed W precursors share some of the advantages of typical oxy-carbon based precursors of W, while not containing any carbon which is known to contaminate the synthesis product and to form toxic sub-products. Finally, by exploiting the surface diffusion kinetics of W and S species adsorbed onto the substrate, a deterministic layer thickness control has also been achieved, thus promoting the design of a scalable synthesis route of WS_2. This work discloses new insights on the synthesis of WS_2 with superior optical and electrical properties to any other mono- and bi-layered material grown via vapour-phase techniques and reveals how the chemical properties of the precursors can be exploited to obtain high quality material via a reproducible and cost effective synthesis method. Furthermore, we believe that the water-assisted halide-mediated growth strategy presented in this work could be adapted to the CVD synthesis of other layered TMDs such as WSe_2, MoS_2 and $MoSe_2$ with superior properties than what reported in the literature.

One of the most promising applications of high-quality WS_2 crystals lies in their heterostructures with graphene towards the development of spintronic devices. Indeed, it has been shown that spin-orbit coupling (SOC) plays a crucial role in condensed matter physics and it can been exploited for designing novel transport phenomena in electronic materials [333]. Depending on its crystalline symmetry, SOC can alter the electronic band structure of a trivial conductor and turn it into a topological insulator where

the transport takes place via surface or edge states along which the electron spin is locked to the kinetic momentum [334]. This minimizes scattering phenomena with non-magnetic impurities while it favours spin-polarized ballistic transport and the propagation of dissipationless spin currents [334]. It has been predicted that graphene could be a promising material for the formation of a 2D topological insulator in the presence of on-site intrinsic SOC [335][336]. In this system SOC leads to the quantum spin Hall state with the opening of a spin-orbit gap around the K and K' points and the formation of chiral spin polarized topological edge states. Further, room temperature ballistic charge transport and gate-tunability make graphene an ideal material for spin-based FETs [333]. However, the extremely weak intrinsic spin-orbit coupling in graphene (24μeV) due to the small atomic number of carbon makes the experimental observation of these phenomena particularly challenging [337]. Previous studies have shown that the weak hydrogenation of graphene and the decoration of its surface with heavy metal adatoms such as gold, indium or thallium, can significantly enhance the SOC [333]. However, these approaches introduces a high degree of disorder and severely limit both charge mobility and spin transport properties. Since group VI-TMDs present SOC orders of magnitude higher than graphene (~100meV), spin split bands and band gaps in a technologically appealing energy range (~1-2eV), they could be ideal materials for spintronics [333][338]. Nevertheless, the unavoidable presence of intrinsic defects in TMDs typically limits their electron mobilities and results in a short spin relaxation length [333].

It has recently been shown that, by forming an interface between monolayered graphene and few-layered WS_2, graphene acquires SOC up to 17meV, which is three orders of magnitude higher than its intrinsic value, while keeping extraordinary high electron mobilities [333]. The combination of the large proximity-induced SOC and high charge mobility results in a gate-tunable spin Hall effect even at room temperature, paving the way for the realization of spin FETs and potentially even quantum spin Hall insulators [333]. Nevertheless, experimental efforts in this direction have almost exclusively focused on developing heterostructures between graphene and multi-layered TMDs, whereas monolayered TMDs have been exploited in a very few cases [339]. Furthermore, no studies have been reported on the direct comparison between mono- and multi-layered TMDs for efficient generation of strong SOC in graphene [339]. As theoretical studies have predicted that monolayered TMDs can potentially induce much stronger SOC in graphene than what achievable by employing multilayered TMDs, the high-quality monolayered

WS_2 synthesized through the water-assisted halide-mediated CVD approach described in this work is expected to induce a considerably strong SOC in graphene, opening the doors to next-generation spin-based devices, and further studies will follow.

A second promising application of atomically thin graphene-WS_2 heterostructures is for light detection devices which have the potential to supersede current state-of-the-art technology. It has been shown that graphene-based transistors can operate as high-speed photodetectors with response times comparable to conventional silicon-based devices [340]. However, the lack of a finite bandgap and the absence of significant gain mechanism in graphene limits their use for ultrasensitive light detection. It has been reported that hybrid structures made of graphene coupled with semiconducting materials such as quantum dots, chlorophyll molecules and MoS_2, exhibit enhanced light absorption and internal gain mechanism [341]. Nevertheless, such detectors typically exhibit slow response times with an operational bandwidth limited to less than 10Hz. This has been attributed to the unavoidable presence of intrinsic and/or extrinsic long-lived charge traps such as SiO_2 surface states and atmospheric contaminations [341]. It has recently been demonstrated that photodetectors based on heterostrucures between graphene and mechanically-exfoliated few-layered WS_2 with an ionic polymer gate exhibit a gate-tuneable responsivity up to $10^6 AW^{-1}$, which surpasses that of graphene- or TMDs-based photodetectors by at least four orders of magnitude [341]. Further, the graphene-WS_2 heterostructure photodetectors reach a -3dB bandwidth of 1.5kHz leading to sub-millisecond rise and fall times. The obtained high gain and fast response have been attributed to the highly mobile ions and nanometre-scale Debye length of the ionic polymer top gate, which screen charge traps and tune the Fermi level of the graphene over an unprecedented range. Finally, these devices exhibit a detectivity of $3.8 \cdot 10^{11}$Jones, which is approaching that of single-photon counters, and are able to operate on a broad spectral range (400-700nm). As WS_2 synthesized via the water-assisted halide-mediated CVD approach described in this work exhibits higher crystal and optical quality than mechanically exfoliated WS_2, we believe that the integration of high-quality CVD-grown WS_2 in ionic-polymer-gated graphene-WS_2 photodetectors would bring the realization of high frame-rate video-imaging applications with two-dimensional materials even closer.

Nevertheless, any industrial-scale applications of WS_2 requires both the synthesis of uniform films over larger length scales than what achieved in this work and a further reduction of the growth

temperature without sacrificing the material proprieties. Contrarily to the successful production of large-scale high-quality graphene films, the synthesis of highly performing atomically thin TMDs over large areas is still an unsolved challenge and some limited success has only been achieved in the case of MoS_2. The main difference between the CVD synthesis of graphene and TMDs is the issue of dispersion uniformity of precursors on the growth substrate, which is significantly limited in the case of TMDs by the use of solid powdered precursors, thus leading to isolated flakes. To achieve large-area WS_2 growth, different strategies have been proposed for improving the W dispersion uniformity onto the substrate, such as atomic layer deposition and pulse laser deposition of thin metal/metal oxide films, or the use of noble metal substrates. It has been shown that some of these strategies can led to continuous WS_2 films but at the expense of the material quality, production cost and complexity.

The large-scale growth of WS_2 directly onto insulating substrates (such as SiO_2/Si) and flexible platforms would enable the batch fabrication of electronic and optoelectronic devices on flexible substrates on a technologically relevant scale without the need of film transferring. However, it has been observed the formation of "pinholes" in the SiO_2 layer after typical syntheses at temperatures $\geq$700°C, which destroy its dielectric capability, whereas flexible substrates such as polymers generally cannot withstand high temperatures. Therefore, any industrial applications of WS_2 require reducing the synthesis temperature without sacrificing the material quality. Further, as another potential application of monolayered WS_2 is to complement or substitute silicon in electronics, its growth temperature should also be lower in order to be compatible with established Si-based fabrication technologies. Therefore, although this challenge is nontrivial since a lower growth temperature generally results in smaller grain size and/or lower degree of crystallinity, alternative precursors and synthesis methodologies have to be investigated to meet the above industrial applications requirements.

APPENDIX

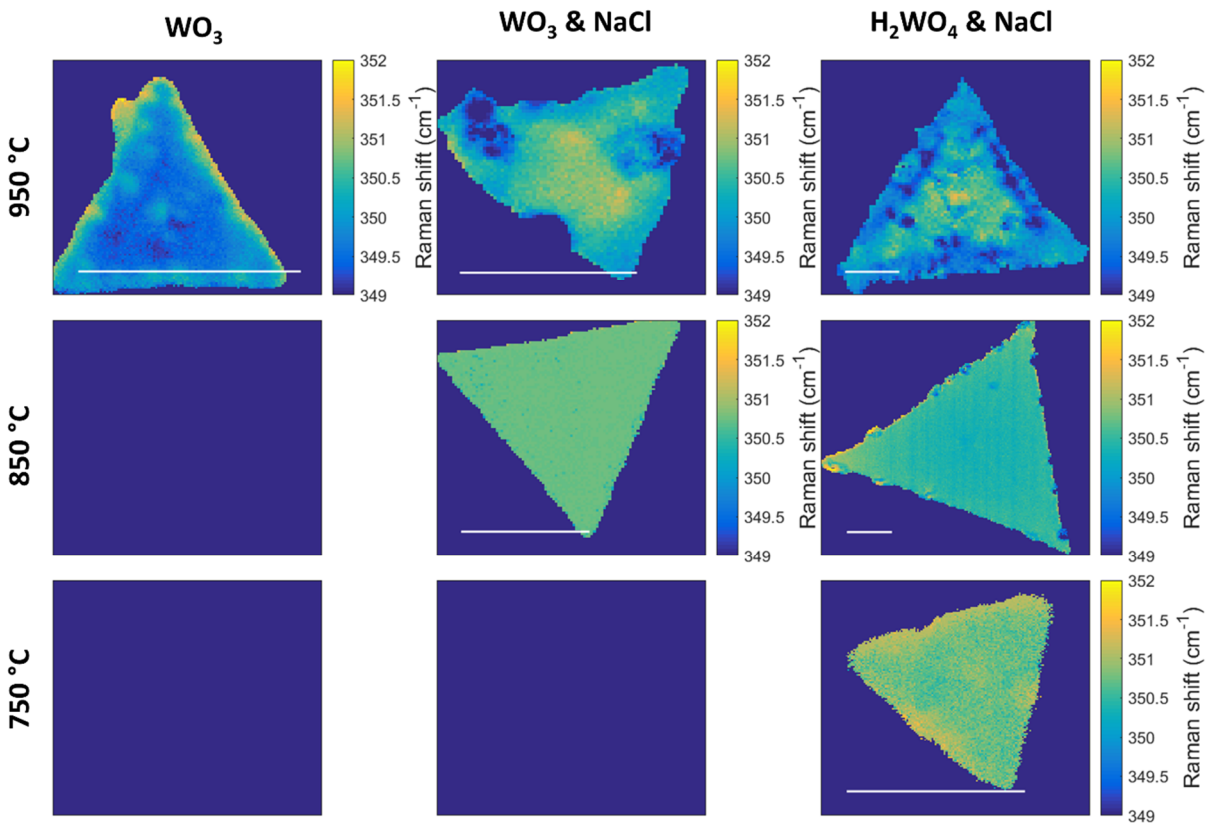


Figure A1 *Raman spectroscopy: $2LA+E^{1}_{2g}$ peak position. Scale bar is 10μm.*

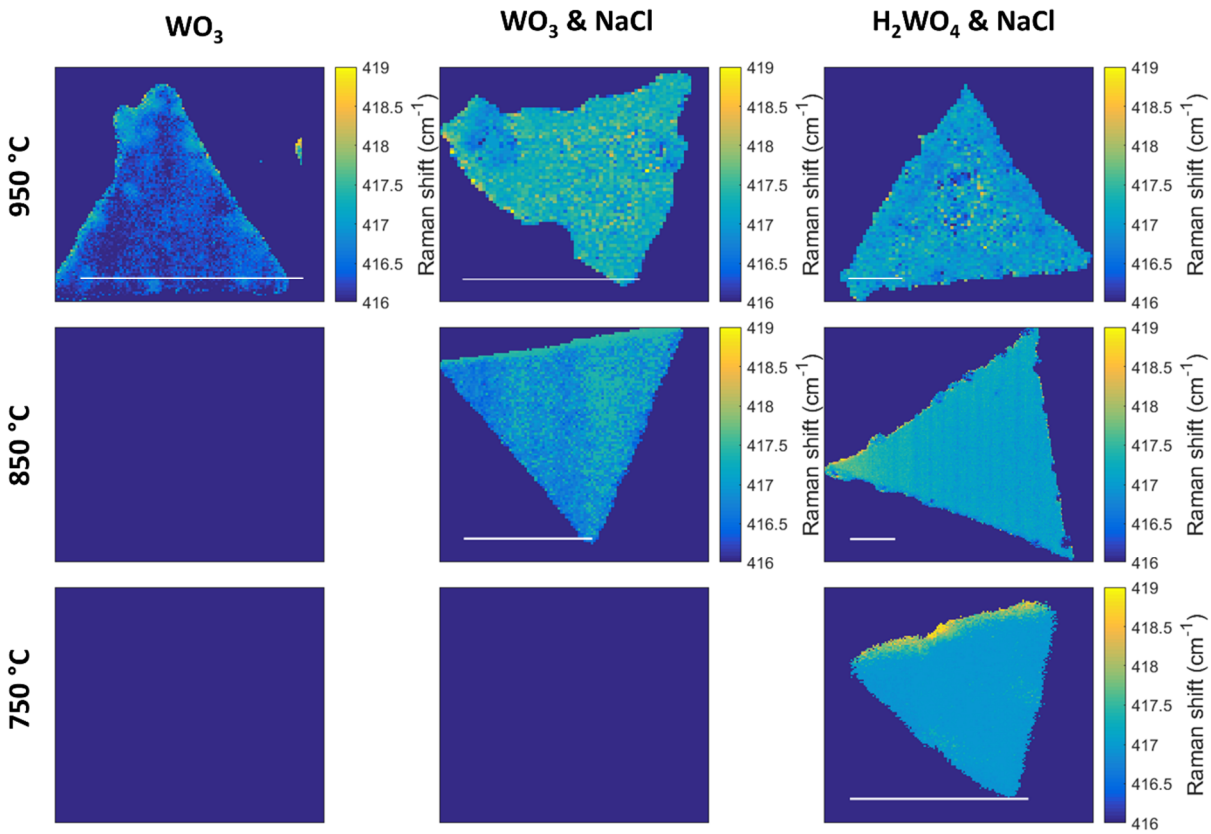


Figure A2 *Raman spectroscopy: A_{1g} peak position. Scale bar is 10μm.*

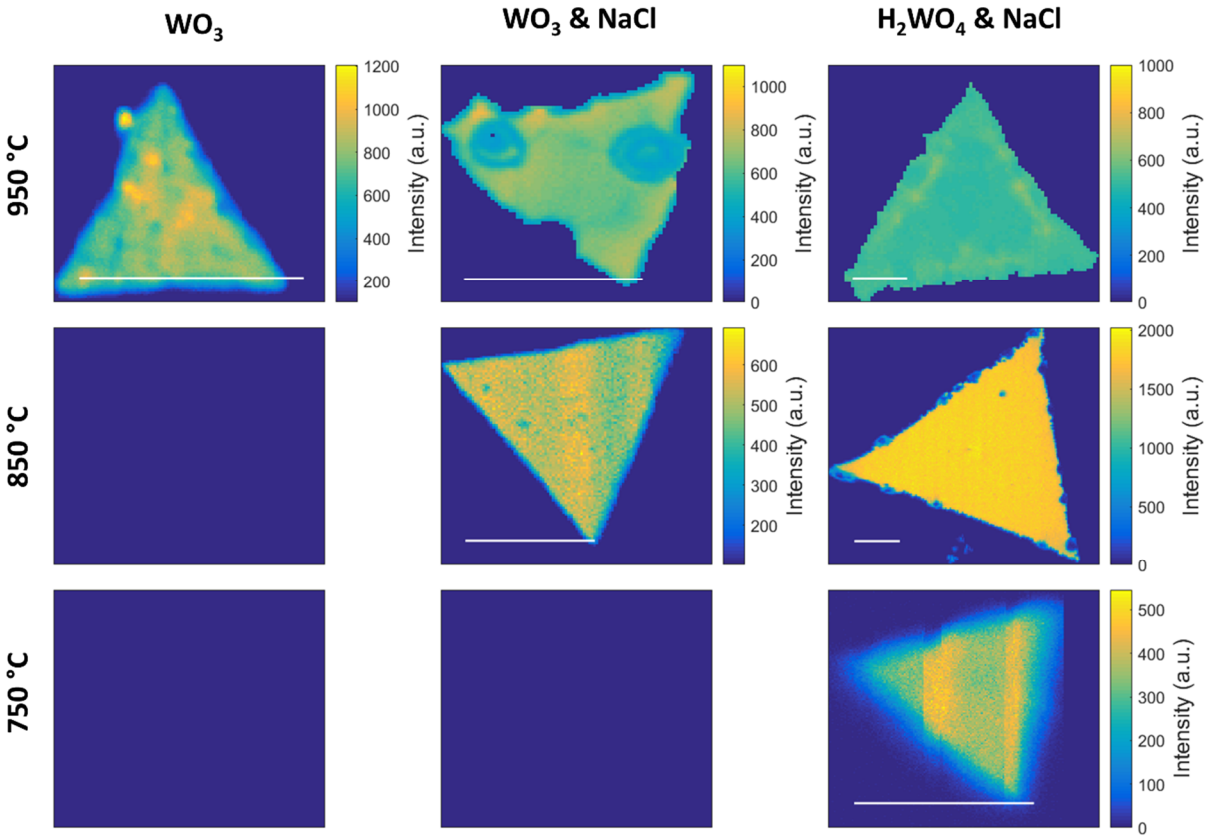


Figure A3 *Raman spectroscopy: $2LA+E^{1}_{2g}$ peak intensity. Scale bar is 10μm.*

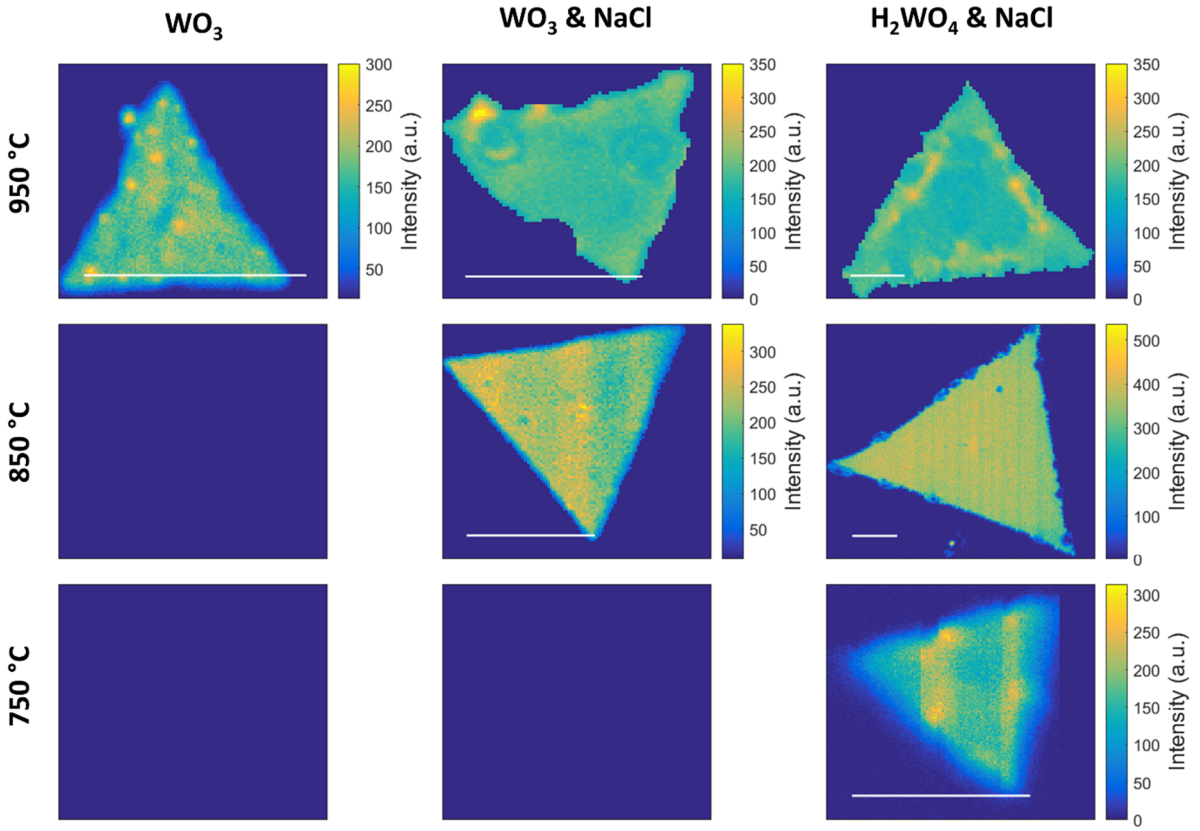


Figure A4 *Raman spectroscopy: A_{1g} peak intensity. Scale bar is 10μm.*

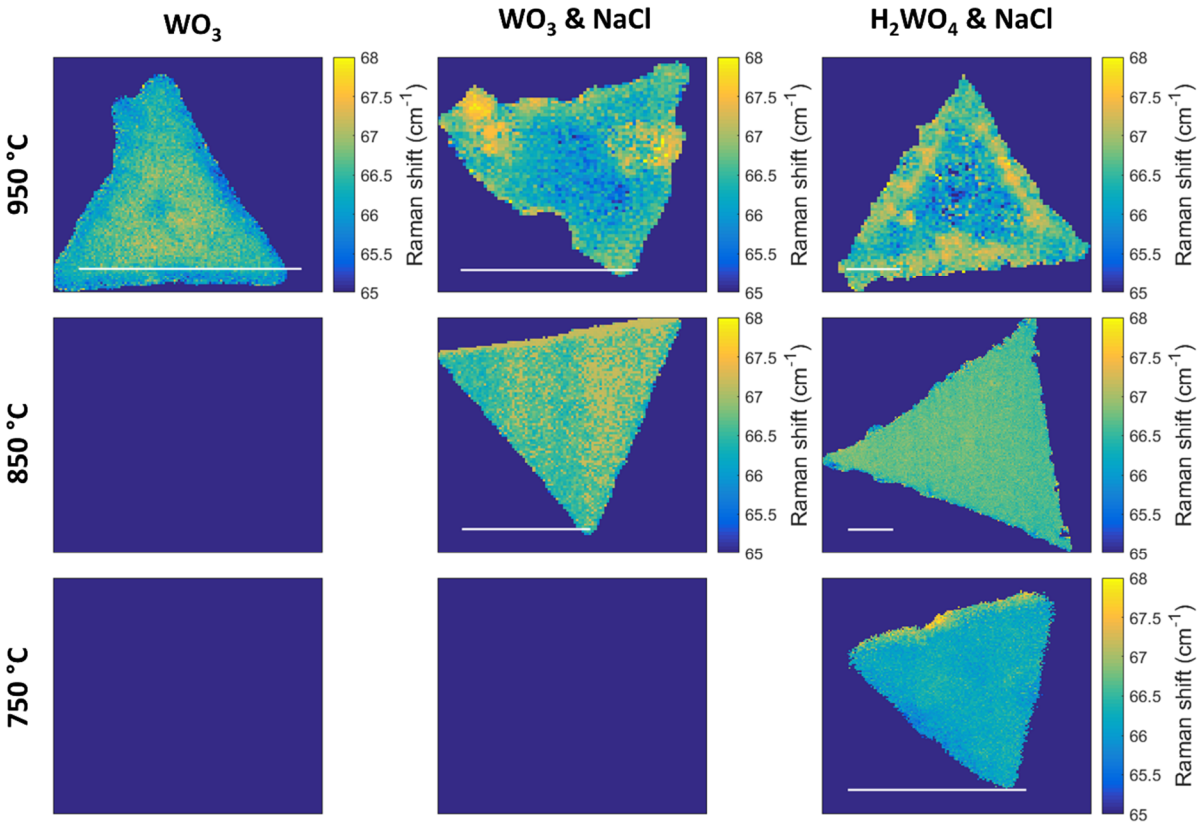


Figure A5 *Raman spectroscopy: 2LA-A_{1g} energy difference. Scale bar is 10μm.*

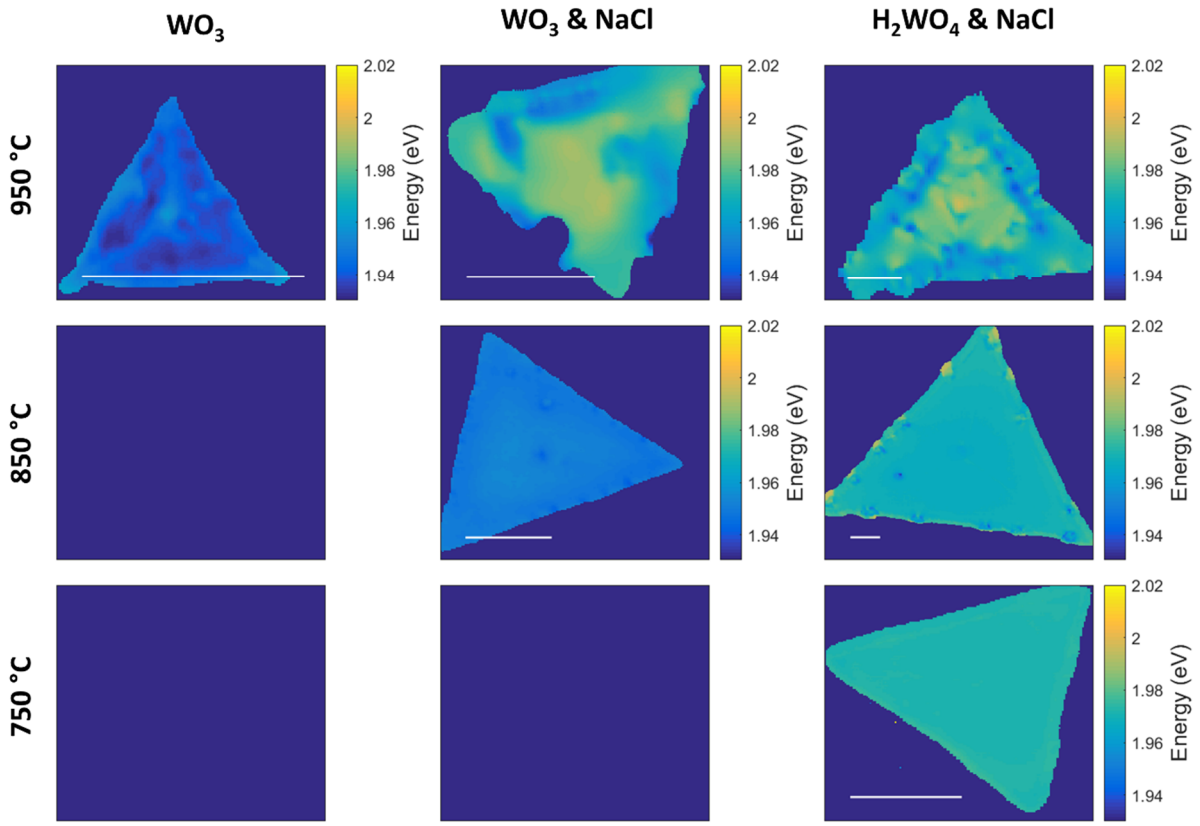


Figure A6 *PL spectroscopy: PL peak position. Scale bar is 10µm.*

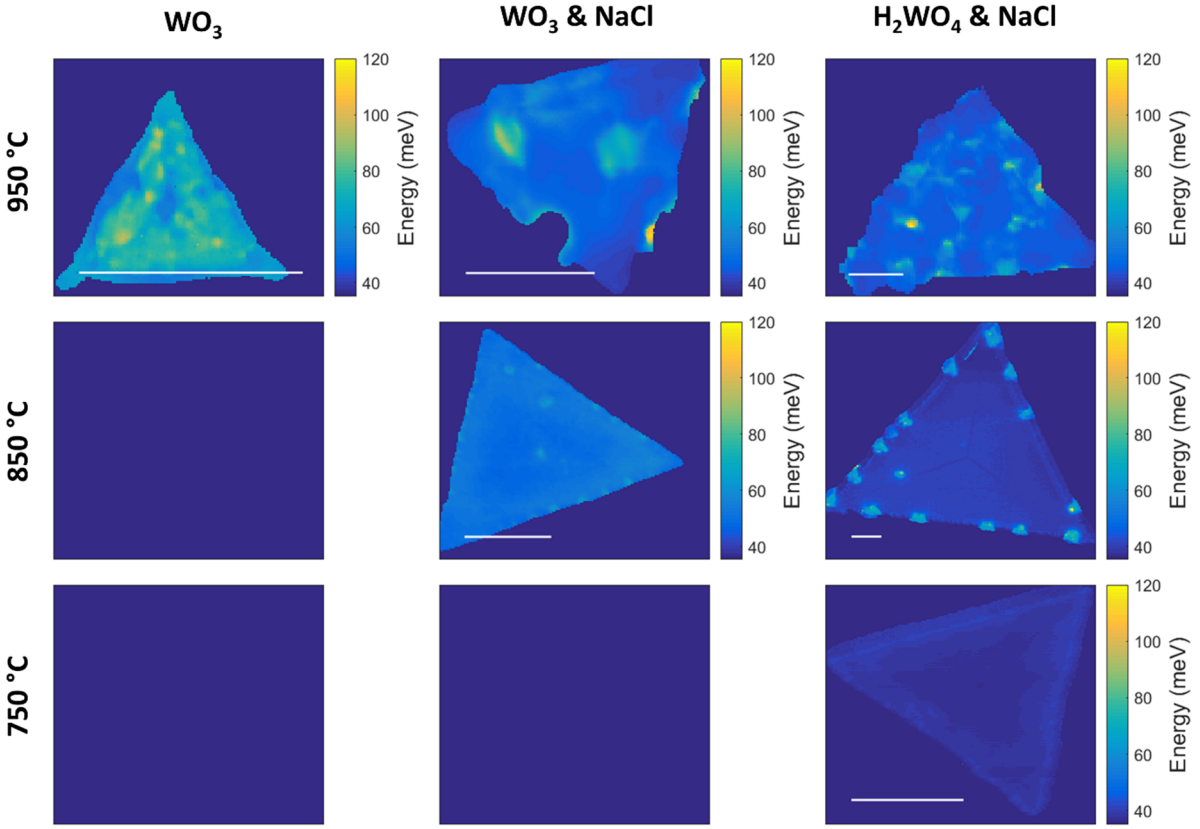


Figure A7 *PL spectroscopy: PL FWHM. Scale bar is 10µm.*

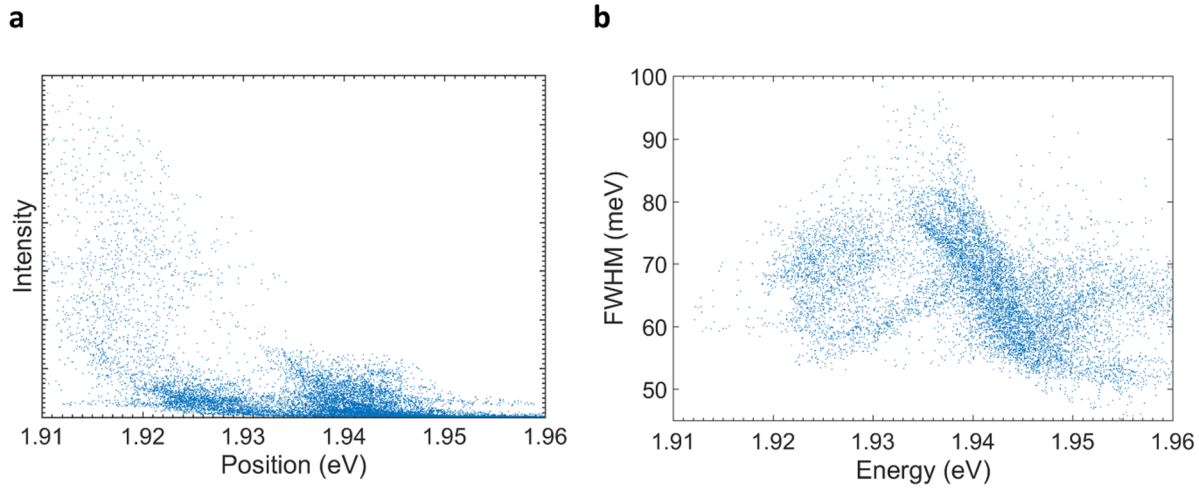


Figure A8 *Data for WO_3 at 950°C: (a) PL intensity vs position; (b) PL FWHM vs position.*

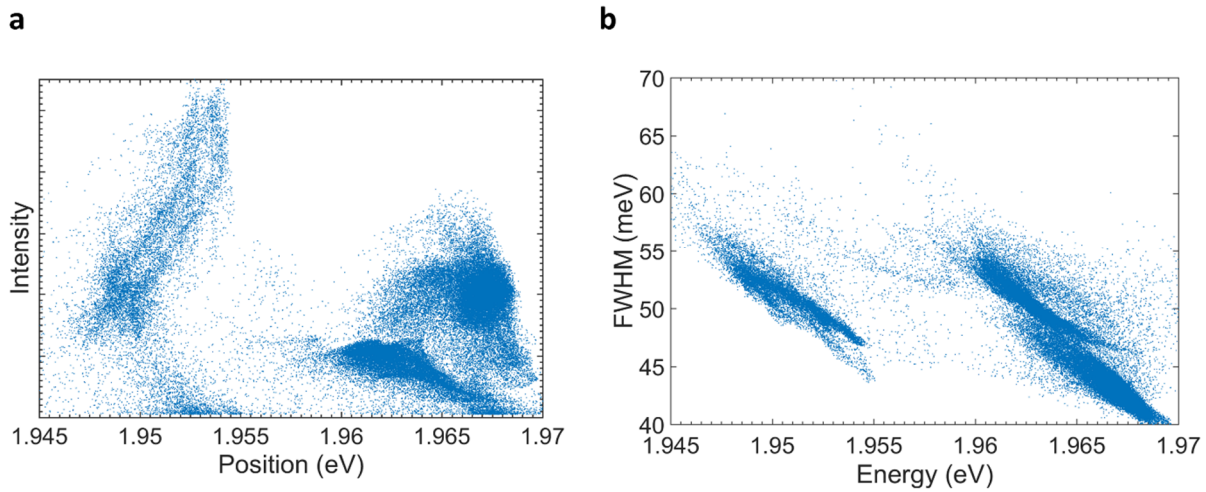


Figure A9 *Data for WO_3+NaCl at 850°C: (a) PL Intensity vs position; (b) PL FWHM vs position.*

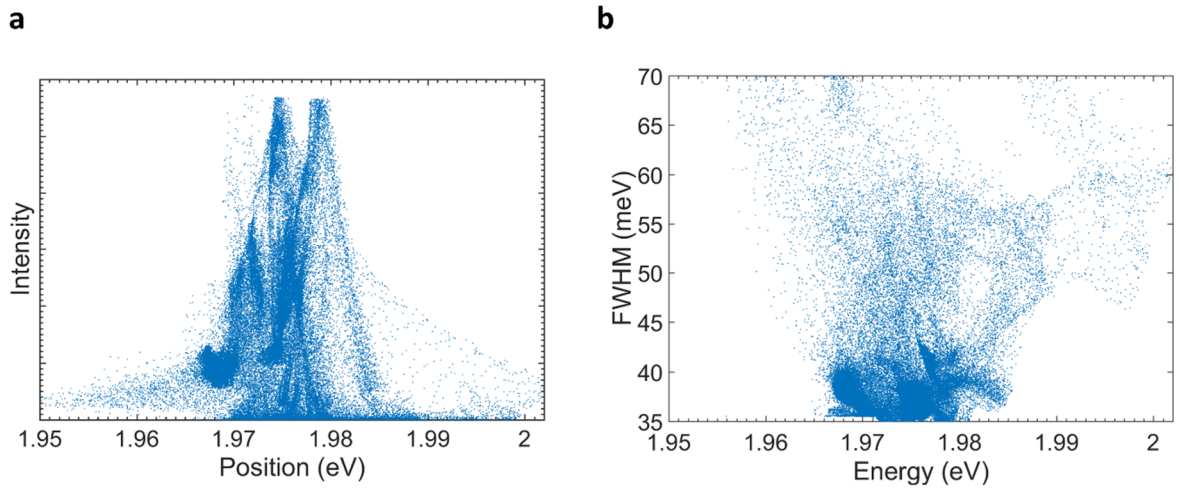


Figure A10 *Data for H_2WO_4+NaCl at 850°C: (a) PL Intensity vs position; (b) PL FWHM vs position.*

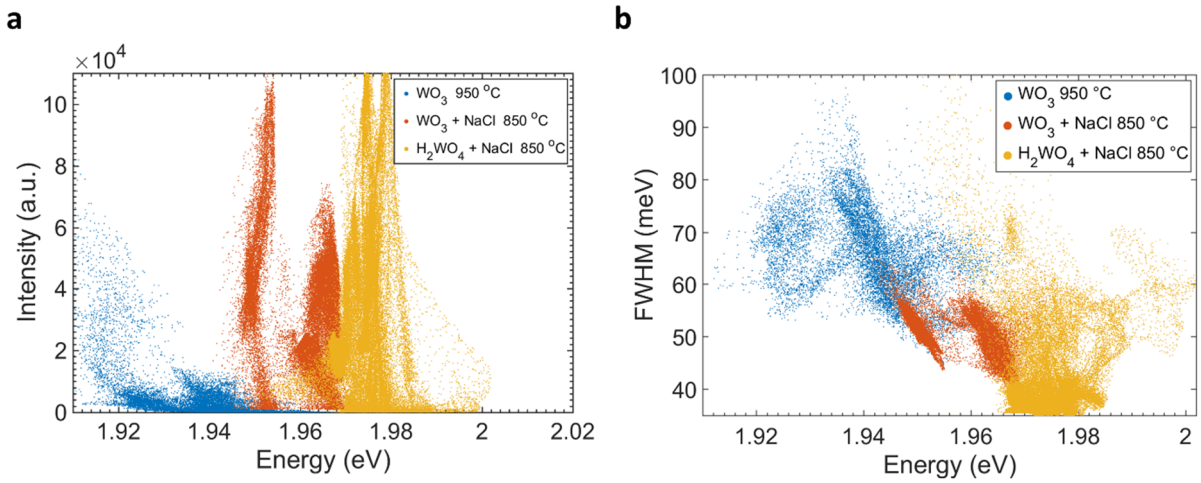


Figure A11 *Data for WO_3, WO_3+NaCl and H_2WO_4+NaCl: (a) PL Intensity vs position; (b) PL FWHM vs position.*

BIBLIOGRAPHY

[1] Wilson, J. A., Yoffe, A. D. The transition metal dichalcogenides discussion and interpretation of the observed optical, electrical and structural properties. *Advances in Physics* **18** *(*1969), 193−335.

[2] Mak, K. F. *et al.* Atomically thin MoS_2: a new direct-gap semiconductor. *Physical Review Letters* 105: 136805 (2010).

[3] Splendiani, A. *et al.* Emerging photoluminescence in monolayer MoS_2. *Nano Letters* **10** (2010), 1271−1275.

[4] Gutiérrez, H. R. *et al.* Extraordinary room-temperature photoluminescence in triangular WS_2 monolayers. *Nano Letters* **13** (2013), 3447−3454.

[5] Bernardi, M. *et al.* Extraordinary sunlight absorption and one nanometer thick photovoltaics using two-dimensional monolayer materials. *Nano Letters* **13** (2013), 3664−3670.

[6] Zhao, W. *et al.* Evolution of electronic structure in atomically thin sheets of WS_2 and WSe_2. *ACS Nano* **7** (2013), 791−797.

[7] Mak, K. F. *et al.* Control of valley polarization in monolayer MoS_2 by optical helicity. *Nature Nanotechnology* **7** (2012), 494−498.

[8] Zeng, H. *et al.* Valley polarization in MoS_2 monolayers by optical pumping. *Nature Nanotechnology* **7** (2012), 490−493.

[9] Li, Y. *et al.* Probing symmetry properties of few-layer MoS_2 and h-BN by optical second-harmonic generation. *Nano Letters* **13** (2013), 3329−3333.

[10] Mak, K. F. *et al.* Tightly bound trions in monolayer MoS_2. *Nature Materials* **12** (2013), 207−211.

[11] Xiao, D. *et al.* Coupled spin and valley physics in monolayers of MoS_2 and other group-VI dichalcogenides. *Physical Review Letters* 108:196802 (2012).

[12] Zhu, Z. Y. *et al.* Giant spin-orbit-induced spin splitting in two-dimensional transition-metal dichalcogenide semiconductors. *Physical Review B* 84:153402 (2011).

[13] Li, T., Galli, G. Electronic Properties of MoS_2 Nanoparticles. *Journal of Physical Chemistry C* **111** (2007), 16192−16196.

[14] Duerloo, K.-A. N. *et al.* Structural phase transitions in two-dimensional Mo- and W-dichalcogenide monolayers. *Nature Communications* 5:4214 (2014).

[15] Ghorbani-Asl, M. *et al.* Electromechanics in MoS_2 and WS_2: nanotubes vs. monolayers. *Scientific Reports* 3:2961 (2013).

[16] Tedstone, A. A. *et al.* Synthesis, properties, and applications of transition metal-doped layered transition metal dichalcogenides. *Chemistry of Materials* **28** (2016), 1965−1974.

[17] Chhowalla, M. *et al.* The chemistry of two-dimensional layered transition metal dichalcogenide nanosheets. *Nature Chemistry* **5** (2013) 263−275.

[18] Lieth, R. M. A., Terhell, J. C. J. M. Transition metal dichalcogenides. *Preparation and crystal growth of materials with layered structures* (1977), 141−223.

[19] Wang, Q. H. *et al.* Electronics and optoelectronics of two-dimensional transition metal dichalcogenides. *Nature Nanotechnology* **7** (2012), 699−712.

[20] Frindt, R. F., Yoffe, A. D., Physical properties of layer structures: optical properties and photoconductivity of thin crystals of molybdenum disulphide. *Proceedings of the Royal Society A: Mathematical, Physical and Engineering Sciences* **273** (1963), 69−83.

[21] Novoselov, K. S. *et al.* Two-dimensional atomic crystals. *PNAS* **102** (2005), 10451−10453.

[22] Geim, A. K., Grigorieva, I. V. Van der Waals heterostructures. *Nature* **499** (2013), 419−425.

[23] Splendiani, A. *et al.* Emerging photoluminescence in monolayer MoS_2. *Nano Letters* **10** (2010), 1271−1275.

[24] Reale, F. *et al.* From bulk crystals to atomically thin layers of group VI-transition metal dichalcogenides vapour phase synthesis. *Applied Materials Today* **3** (2016), 11−22.

[25] Zhou, L. *et al.* Large-area synthesis of high-quality uniform few-layer $MoTe_2$. *Journal of the American Chemical Society* **137** (2015), 11892−11895.

[26] Keum, D. H. *et al.* Bandgap opening in few-layered monoclinic $MoTe_2$. *Nature Physics* **11** (2015), 482−486.

[27] Ali, M. N. *et al.* Large, non-saturating magnetoresistance in WTe_2. Nature **514** (2014), 205−208.

[28] Kuc, A *et al.* Influence of quantum confinement on the electronic structure of the transition metal sulfide TS_2. *Physical Review B* 83:245213 (2011).

[29] Elliott, R. J. Intensity of optical absorption by excitons. *Physical Review* 108:1384 (1957).

[30] Xiao, J. *et al.* Excitons in atomically thin 2D semiconductors and their applications. *Nanophotonics* **6** (2017), 1309−1328.

[31] Eda, G. *et al.* Photoluminescence from chemically exfoliated MoS_2. *Nano Letters* **11** (2011), 5111−5116.

[32] Kozawal, D. *et al.* Photocarrier relaxation pathway in two-dimensional semiconducting transition metal dichalcogenides. *Nature Communications* 5:4543 (2014).

[33] Bernardi, M. *et al.* Extraordinary sunlight absorption and one nanometer thick photovoltaics using two-dimensional monolayer materials. *Nano Letters* **13** (2013), 3664−3670.

[34] Gong, Y. *et al.* Vertical and in-plane heterostructures from WS_2/MoS_2 monolayers. *Nature Materials* **13** (2014), 1135−1142.

[35] Fang, H. *et al.* Strong interlayer coupling in van der Waals heterostructures built from single-layer chalcogenides. *PNAS* **111** (2014), 6198−6202.

[36] Molina-Sanchez, A., Wirtz, L. Phonons in single-layer and few-layer MoS_2 and WS_2. *Physical Review B* 84:155413 (2011).

[37] Zhao, W. *et al.* Lattice dynamics in mono- and few-layer sheets of WS_2 and WSe_2. *Nanoscale* **5** (2013), 9677−9683.

[38] Whiters, F. *et al.* Electron transport of WS_2 transistors in a hexagonal boron nitride dielectric environment. *Scientific Reports* 4:4967 (2014).

[39] Terrones, H. *et al.* New first order Raman-active modes in few layered transition metal dichalcogenides. *Scientific reports* 4:4215 (2014).

[40] Molina-Sanchez, A., Wirtz, L. Phonons in single-layer and few-layer MoS_2 and WS_2. *Physical Review B* 84:155413 (2011).

[41] Han, S. A. *et al.* Synthesis, properties and potential applications of two-dimensional transition metal dichalcogenides. *Nano Convergence* 2:17 (2015).

[42] Li, X. *et al.* Large-area synthesis of high-quality and uniform graphene films on copper foils. *Science* **324** (2009), 1312−1314.

[43] Bosi, M. Growth and synthesis of mono and few-layers transition metal dichalcogenides by vapour techniques: a review. *RSC Advances* **5** (2015), 75500−75518.

[44] Shi, Y. *et al.* Recent advances in controlled synthesis of two-dimensional transition metal dichalcogenides via vapour deposition techniques. *Chemical Society Reviews* **44** (2015), 2744−2756.

[45] Cui, X. *et al.* Multi-terminal transport measurements of MoS_2 using a van der Waals heterostructure device platform. *Nature Nanotechnology* **10** (2015), 534−540.

[46] Kappera, R. *et al.* Phase-engineered low-resistance contacts for ultrathin MoS_2 transistors. *Nature Materials* **13** (2014), 1128−1134.

[47] Liu, Z. *et al.* Strain and structure heterogeneity in MoS_2 atomic layers grown by chemical vapour deposition. *Nature Communications* 5:5246 (2014).

[48] Akinwande, D. *et al.* Two-dimensional flexible nanoelectronics. *Nature Communications* 5:5678 (2014).

[49] He, K. *et al.* Experimental demonstration of continuous electronic structure tuning via strain in atomically thin MoS_2. *Nano Letters* **13** (2013), 2931−2936.

[50] Duerloo, K.-A. N. *et al.* Intrinsic piezoelectricity in two-dimensional materials. *The Journal of Physical Chemistry Letters* **3** (2012), 2871−2876.

[51] Joensen, P. *et al.* Single-layer MoS_2. *Materials Research Bulletin* **21** (1986), 457−461.

[52] Fan, X. *et al.* Pressure evolution of the potential barriers of phase transition of MoS_2, $MoSe_2$ and $MoTe_2$. *Physical Chemistry Chemical Physics* **18** (2016), 12080−12085.

[53] Wang, X. *et al.* Pressure-induced iso-structural phase transition and metallization in WSe_2. *Scientific Reports* 7:46694 (2017).

[54] Li, Y. *et al.* Structural semiconductor-to-semimetal phase transition in two-dimensional materials induced by electrostatic gating. *Nature Communications* 7:10671 (2016).

[55] Wu, Y. *et al.* State-of-the-art graphene high-frequency electronics. *Nano Letters* **12** (2012), 3062−3067.

[56] Radisavljevic, B. *et al.* Single-layer MoS_2 transistors. *Nature Nanotechnology* **6** (2011), 147−150.

[57] Podzorov *et al.* High-mobility field-effect transistors based on transition metal dichalcogenides. *Applied Physics Letters* **84** (2004), 3301−3303.

[58] Braga, D. *et al.* Quantitative determination of the band gap of WS_2 with ambipolar ionic liquid-gated transistors. *Nano Letters* **12** (2012), 5218−5223.

[59] Ovchinnikov, D. *et al.* Electrical transport properties of single-layer WS_2. *ACS Nano* **8** (2014), 8174−8181.

[60] Fang, H. *et al.* High-performance single layered WSe_2 p-FETs with chemically doped contacts. *Nano Letters* **12** (2012), 3788−3792.

[61] Liu, W. *et al.* Role of metal contacts in designing high-performance monolayer n-type WSe_2 field effect transistors. *Nano Letters* **13** (2013), 1983−1990.

[62] Larentis, S. *et al.* Field-effect transistors and intrinsic mobility in ultra-thin $MoSe_2$ layers. *Applied Physics Letters* 101:223104 (2012).

[63] Wang, X. *et al.* Chemical vapor deposition growth of crystalline monolayer $MoSe_2$. *ACS Nano* **8** (2014), 5125−5131.

[64] Bertolazzi, S. *et al.* Stretching and breaking of ultrathin MoS_2. *ACS Nano* **5** (2011), 9703−9709.

[65] Radisavljevic, B. *et al.* Integrated circuits and logic operations based on single-layer MoS_2. *ACS Nano* **5** (2011), 9934−9938.

[66] Wang, H. *et al.* Integrated circuits based on bilayer MoS_2 transistors. *Nano Letters* **12** (2012), 4674−4680.

[67] Furchi, M. M. *et al.* Mechanisms of photoconductivity in atomically thin MoS_2. *Nano Letters* **14** (2014), 6165−6170.

[68] Yin, Z. *et al.* Single-layer MoS_2 phototransistors. *ACS Nano* **6** (2012), 74−80.

[69] Lee, H. S. *et al.* MoS_2 nanosheet phototransistors with thickness-modulated optical energy gap. *Nano Letters* **12** (2012), 446−701.

[70] Zhang, Y. *et al.* Polymer ambipolar MoS_2 thin flake transistors. *Nano Letters* **13** (2013), 1983−1990.

[71] Pospishil, A. *et al.* Solar-energy conversion and light emission in an atomic monolayer p-n diode. *Nature Nanotechnology* **9** (2014), 257−261.

[72] Nipane, A. *et al.* Few-layer MoS_2 p-type devices enabled by selective doping using low energy phosphorus implantation. *ACS Nano* **10** (2016), 2128−2137.

[73] Cheng, R. *et al.* Electroluminescence and photocurrent generation from atomically sharp WSe_2/MoS_2 heterojunction p-n diodes. *Nano Letters* **14** (2014), 5590−5597.

[74] Dietl, T. A ten-year perspective on dilute magnetic semiconductors and oxides. *Nature Materials* **9** (2010), 965−974.

[75] Spalvins, T. Morphological and frictional behavior of sputtered MoS_2 films. *Thin Solid Films* **96** (1982), 17−24.

[76] Regula, M. *et al.* Structural, chemical, and electrical characterisation of reactively sputtered WS_x thin films. *Thin Solid Films* **280** (1996), 67−75.

[77] Donley, M. S. *et al.* Deposition of stoichiometric MoS_2 thin-films by pulsed laser evaporation. *Thin Solid Films* **168** (1989), 335−344.

[78] Mcdevitt, N. T. *et al.* The use of Raman-scattering to study disorder in pulsed-laser deposited MoS_2 films. *Thin Solid Films* **240** (1994), 76−81.

[79] Voevodin, A. A. *et al.* Magnetic field argon ion filtering for pulsed magnetron sputtering growth of two-dimensional MoS_2. *Surface and Coatings Technology* **280** (2015), 260−267.

[80] Stupp, B. C. Synergistic effects of metals co-sputtered with MoS_2. *Thin Solid Films* **84** (1981), 257−266.

[81] Lin, X. Q., Ni, J. Charge and magnetic states of Mn-, Fe-, and Co-doped monolayer MoS_2. *Journal of Applied Physics* 116:044311 (2014).

[82] Cheng, L. *et al.* Bottom-up synthesis of metal-ion-doped WS_2 nanoflakes for cancer theranostics. *ACS Nano* **9** (2015), 11090−11101.

[83] Cammarata, A., Polcar, T. Tailoring nanoscale friction in MX_2 transition metal dichalcogenides. *Inorganic Chemistry* **54** (2015), 5739−5744.

[84] Hsu, W. K. *et al.* Titanium-doped molybdenum disulphide nanostructures. *Advanced Functional Materials* **11** (2001), 69−74.

[85] McCain, M. N. *et al.* Aerosol-assisted chemical vapor deposition of lubricating MoS_2 films. Ferrous substrates and titanium film doping. *Chemistry of Materials* **20** (2008), 5438−5443.

[86] Scharf, T. W. *et al.* Growth, structure and friction behavior of titanium doped tungsten disulphide (Ti-WS_2) nanocomposite thin films. *Thin Solid Films* **517** (2009), 5666−5675.

[87] Ding, X. Z. *et al.* Tribological properties of Cr- and Ti-doped MoS_2 composite coatings under different humidity atmosphere. *Surface and Coatings Technology* **205** (2010), 224−231.

[88] Arslan, E. *et al.* Comparison of structure and tribological properties of MoS_2-Ti films deposited by biased-dc and pulsed-dc. *Progress in Organic Coatings* **74** (2012), 772−776.

[89] Singh, H. *et al.* Tribological performance and coating characteristics of sputter-deposited Ti-doped MoS_2 in rolling and sliding contact. *Tribology Transactions* **58** (2015), 767−777.

[90] Lian, Y. S. *et al.* Friction and wear behavior of WS_2/Zr self-lubricating soft coatings in dry sliding against 40Cr-hardened steel balls. *Tribology Letters* **53** (2014), 237−246.

[91] Conroy, L. E., Park, K. C. Electrical properties of the Group IV disulfides, titanium disulfide, zirconium disulfide, hafnium disulphide and tin disulfide. *Inorganic Chemistry* **7** (1968), 459−463.

[92] Laskar, M. R. *et al.* P-type doping of MoS_2 thin films using Nb. *Applied Physics Letters* 104:092104 (2014).

[93] Suh, J. *et al.* Doping against the native propensity of MoS_2: degenerate hole doping by cation substitution. *Nano Letters* **14** (2014), 6976−6982.

[94] Sun, X. *et al.* Semimetallic molybdenum disulfide ultrathin nanosheets as an efficient electrocatalyst for hydrogen evolution. *Nanoscale* **6** (2014), 8359−8367.

[95] Sasaki, S. *et al.* Growth and optical properties of Nb-doped WS_2 monolayers. *Applied Physics Express* 9:071201 (2016).

[96] Lewis, D. J. *et al.* Thin films of molybdenum disulfide doped with chromium by aerosol-assisted chemical vapour deposition (AACVD). *Chemistry of Materials* **27** (2015), 1367−1374.

[97] Tedstone, A. A. *et al.* Mechanical properties of molybdenum disulfide and the effect of doping: an in situ TEM study. *ACS Applied Materials & Interfaces* **7** (2015), 20829−20834.

[98] Luo, H. X. *et al.* Cr-doped $TiSe_2$ - A layered dichalcogenide spin glass. *Chemistry of Materials* **27** (2015), 6810−6817.

[99] Srivastava, S. K. *et al.* Studies on layer disorder, microstructural parameters and other properties of tungsten-substituted molybdenum disulfide, $Mo_{1-x}W_xS_2$ ($0 \leq x \leq 1$). *Synthetic Metals* **90** (1997), 135−142.

[100] Ho, C. H. *et al.* Temperature dependence of energies and broadening parameters of the band-edge excitons of $Mo_{1-x}W_xS_2$ single crystals. *Journal of Physics*: *Condensed Matter* **10** (1998), 9317−9328.

[101] Thomazeau, C. *et al.* Two cation disulfide layers in the $W_xMo_{(1-x)}S_2$ lamellar solid solution. *Journal of Solid State Chemistry* **160** (2001), 147−155.

[102] Thomazeau, C. *et al.* Predictive approach for the design of improved HDT catalysts: g-Alumina supported (Ni, Co) promoted $Mo_{1-x}W_xS_2$ active phases. *Applied Catalysis A: General* **322** (2007), 92−97.

[103] Nath, M. *et al.* $Mo_{1-x}W_xS_2$ nanotubes and related structures. *Chemical Physics Letters* **352** (2002), 163−168.

[104] Dumcenco, D. O. *et al.* Raman study of 2H-$Mo_{1-x}W_xS_2$ layered mixed crystals. *Journal of Alloys and Compounds* **506** (2010), 940−943.

[105] Dumcenco, D. O. *et al.* Visualization and quantification of transition metal atomic mixing in $Mo_{1-x}W_xS_2$ single layers. *Nature Communications* 4:1351 (2013).

[106] Wang, L. *et al.* $Mo_xW_{1-x}S_2$ solid solutions as 3D electrodes for hydrogen evolution reaction. *Advanced Materials Interfaces* 2:1500041 (2015).

[107] Shi, Y. *et al.* Synthesis and structure of two-dimensional transition-metal dichalcogenides. *MRS Bulletin* **40** (2015), 566−576.

[108] Xie, L. M. Two-dimensional transition metal dichalcogenide alloys: preparation, characterization and applications. *Nanoscale* **7** (2015), 18392−18401.

[109] Wang, H. *et al.* Physical and chemical tuning of two-dimensional transition metal dichalcogenides. *Chemical Society Reviews* **44** (2015), 2664−2680.

[110] Jellinek, F. The structures of the chromium sulphides. *Acta Crystallographica* **10** (1957), 620−628.

[111] Xu, J. *et al.* Facile synthesis of $Mo_{0.91}W_{0.09}S_2$ ultrathin nanosheets/amorphous carbon composites for high-performance supercapacitor. *Materials Letters* **162** (2016), 126−130.

[112] Dumcenco, D. O. *et al.* Piezoreflectance and Raman characterization of $Mo_{1-x}W_xS_2$ layered mixed crystals. *Solid State Phenomena* **170** (2011), 55−59.

[113] Zhao, X. *et al.* Effect of structural defects on electronic and magnetic properties of pristine and Mn-doped MoS_2 monolayer. *Solid State Communications* **220** (2015), 31−35.

[114] Murray, H. H. *et al.* Structure of rhenium disulfide. *Inorganic Chemistry* **33** (1994), 4418−4420.

[115] Drabek, M. *et al.* The Re−Mo−S system: new data on phase relations between 400 and 1200 °C. *European Journal of Mineralogy* **22** (2010), 479−484.

[116] Sigiro, M. *et al.* Influence of rhenium on the structural and optical properties of molybdenum disulfide. *Japanese Journal of Applied Physics* 54:04DH05 (2015).

[117] Benavente, E. *et al.* Intercalation chemistry of molybdenum disulfide. *Coordination Chemistry Reviews* **224** (2002), 87−109.

[118] Zhang, K. *et al.* Doping of monolayer MoS_2: the substrate is critical. *Nano Letters* **15** (2015), 6586−6591.

[119] Enyashin, A. N. *et al.* New route for stabilization of 1T-WS_2 and MoS_2 phases. *Journal of Physical Chemistry C* **115** (2011), 24586−24591.

[120] Kogovsek, J., Kalin, M. Various MoS_2-, WS_2- and C-based micro- and nanoparticles in boundary lubrication. *Tribology Letters* **53** (2014), 585−597.

[121] Chhetri, M. *et al.* Beneficial effect of Re doping on the electrochemical HER activity of MoS_2 fullerenes. *Dalton Transactions* **44** (2015), 16399−16404.

[122] Woo, S. H. *et al.* Fullerene-like Re-doped MoS_2 nanoparticles as an intercalation host with fast kinetics for sodium ion batteries. *Israel Journal of Chemistry* **55** (2015), 599−603.

[123] Al-Dulaimi, N. *et al.* Chemical vapour deposition of rhenium disulfide and rhenium-doped molybdenum disulfide thin films using single-source precursors. *Journal of Materials Chemistry C* **4** (2016), 2312−2318.

[124] Tian, X. *et al.* Effects of 3d transition-metal doping on electronic and magnetic properties of MoS_2 nanoribbons. *Physical Chemistry Chemical Physics* **17** (2015), 1831−1836.

[125] Ma, D. W. *et al.* CO catalytic oxidation on iron-embedded monolayer MoS_2. *Applied Surface Science* **328** (2015), 71−77.

[126] Shu, H. *et al.* Layer-dependent dopant stability and magnetic exchange coupling of iron-doped MoS_2 nanosheets. *ACS Applied Materials & Interfaces* **7** (2015), 7534−7541.

[127] Chen, Z. P. *et al.* Strain control of the electronic structures, magnetic states, and magnetic anisotropy of Fe doped single-layer MoS_2. *Computational Materials Science* **110** (2015), 102−108.

[128] Cheng, Y. C. *et al.* Prediction of two-dimensional diluted magnetic semiconductors: doped monolayer MoS_2 systems. *Physical Review B: Condensed Matter and Materials Physics* 87:100401 (2013).

[129] Wang, S. Y. *et al.* Optical and electrical properties of MoS_2 and Fe-doped MoS_2. *Japanese Journal of Applied Physics* 53:04EH07 (2014).

[130] Deepak, F. L. *et al.* Direct imaging and identification of individual dopant atoms in MoS_2 and WS_2 catalysts by aberration corrected scanning transmission electron microscopy. *ACS Catalysis* **1** (2011), 537−543.

[131] Peng, H. *et al.* Co-doped MoS_2 NPs with matched energy band and low overpotential high efficiently convert CO_2 to methanol. *Applied Surface Science* **353** (2015), 1003−1012.

[132] Xiang, Z. *et al.* Room-temperature ferromagnetism in Co doped MoS_2 sheets. *Physical Chemistry Chemical Physics* **17** (2015), 15822−15828.

[133] Yu, L. *et al.* General formation of M-MoS_3 (M=Co, Ni) hollow structures with enhanced electrocatalytic activity for hydrogen evolution. *Advanced Materials* **28** (2016), 92−97.

[134] Sobczynski, A. *et al.* Catalytic hydrogen evolution properties of nickel-doped tungsten disulphide. *Journal of Physical Chemistry* **93** (1989), 401−403.

[135] Xie, Y. C., Li, Y. M. Preparation of Ni-doped MoS_2 microsphere and its superior electrocatalytic hydrogen evolution ability. *Advanced Materials Research* **871** (2014), 206−210.

[136] Leyral, G. *et al.* Synthesis and structuring of Ni MoS_2 by using an ionic liquid. *European Journal of Inorganic Chemistry* **2012** (2012), 4967−4971.

[137] Deng, J. *et al.* Triggering the electrocatalytic hydrogen evolution activity of the inert two-dimensional MoS_2 surface via single-atom metal doping. *Energy & Environmental Science* **8** (2015), 1594−1601.

[138] Yun, W. S., Lee, J. D. Unexpected strong magnetism of Cu doped single-layer MoS_2 and its origin. *Physical Chemistry Chemical Physics* **16** (2014), 8990−8996.

[139] Hu, A.-M. *et al.* Electronic structures and magnetic properties in Cu-doped two-dimensional dichalcogenides. *Physica E* **73** (2015), 69−75.

[140] Zhao, X. *et al.* Magnetic properties of two nearest Cu-doped monolayer WS_2: A first-principles study. *Solid State Communications* **217** (2015), 66−69.

[141] Xu, S. S. *et al.* Microstructure evolution and enhanced tribological properties of Cu-doped WS_2 films. *Tribology Letters* **55** (2014), 1−13.

[142] Bhimanapati, G. R. *et al.* Recent advances in two-dimensional materials beyond graphene. *ACS Nano* **9** (2015), 11509−11539.

[143] Craciun, M. F. *et al.* Properties and applications of chemically functionalized graphene. *Journal of Physics: Condensed Matter* 25:423201 (2013).

[144] Kuila, T. *et al.* Chemical functionalization of graphene and its applications. *Progress in Materials Science* **57** (2012), 1061−1105.

[145] Georgakilas, V. *et al.* Functionalization of graphene: covalent and non-covalent approaches, derivatives and applications. *Chemical Reviews* **112** (2012), 6156−6214.

[146] Tongay, S. *et al.* Broad-range modulation of light emission in two-dimensional semiconductors by molecular physisorption gating. *Nano Letters* **13** (2013), 2831−2836.

[147] Sarkar, D. *et al.* Functionalization of transition metal dichalcogenides with metallic nanoparticles: implications for doping and gas-sensing. *Nano Letters* **15** (2015), 2852−2862.

[148] Fang, H. *et al.* Degenerate n-doping of few-layer transition metal dichalcogenides by potassium. *Nano Letters* **13** (2013), 1991−1995.

[149] Lin, J. D. *et al.* Electron-doping-enhanced trion formation in monolayer molybdenum disulfide functionalized with cesium carbonate. *ACS Nano* **8** (2014), 5323−5329.

[150] Kang, D.-H. *et al.* Controllable nondegenerate p-type doping of tungsten diselenide by octadecyltrichlorosilane. *ACS Nano* **9** (2015), 1099−1107.

[151] Mouri, S. *et al.* Tunable photoluminescence of monolayer MoS_2 via chemical doping. *Nano Letters* **13** (2013), 5944−5948.

[152] Kiriya, D. *et al.* Air stable surface charge transfer doping of MoS_2 by benzyl viologen. *Journal of the American Chemical Society* **136** (2014), 7853−7856.

[153] Andleeb, S. *et al.* Chemical doping of MoS_2 multilayer by p-toluene sulfonic acid. *Science and Technology of Advanced Materials* 16:35009 (2015).

[154] Yang, L. *et al.* Chloride molecular doping technique on 2D materials: WS_2 and MoS_2. *Nano Letters* **14** (2014), 6275−6280.

[155] Du, Y. *et al.* Molecular doping of multilayer MoS_2 field-effect transistors: reduction in sheet and contact resistances. *IEEE Electron Device Letters* **34** (2013), 1328−1330.

[156] Li, Y. *et al.* Carrier control of MoS_2 nanoflakes by functional self-assembled monolayers. *ACS Nano* **7** (2013), 7795−7804.

[157] Wi, S. *et al.* Enhancement of photovoltaic response in multilayer MoS_2 induced by plasma doping. *ACS Nano* **8** (2014), 5270−5281.

[158] Chen, M. *et al.* Stable few-layer MoS_2 rectifying diodes formed by plasma-assisted doping. *Applied Physics Letters* 103:142110 (2013).

[159] Wu, C.-I. *et al.* Electronic structures and electron-injection mechanisms of cesium-carbonate-incorporated cathode structures for organic light-emitting devices. *Applied Physics Letters* 88:152104 (2006).

[160] Li, H.-M. *et al.* Ultimate thin vertical p-n junction composed of two-dimensional layered molybdenum disulfide. *Nature Communications* 6:6564 (2015).

[161] Shi, Y. *et al.* Work function engineering of graphene electrode via chemical doping. *ACS Nano* **4** (2010), 2689−2694.

[162] Shin, H.-J. *et al.* Control of electronic structure of graphene by various dopants and their effects on a nanogenerator. *Journal of the American Chemical Society* **132** (2010), 15603−15609.

[163] Wildervanck, J. C., Jellinek, F. Preparation and crystallinity of molybdenum and tungsten sulfides *Zeitschrift für anorganische und allgemeine Chemie* **328** (1964), 309−318.

[164] Ehrlich, P. Untersuchungen an Wolframsulfiden. *Zeitschrift für anorganische und allgemeine Chemie* **257** (1948), 247−253.

[165] Shang, J. *et al.* Observation of excitonic fine structure in a 2D transition-metal dichalcogenide semiconductor. *ACS Nano* **9** (2015), 647−655.

[166] Iqbal, M. W. *et al.* High-mobility and air-stable single-layer WS_2 field-effect transistors sandwiched between chemical vapor deposition-grown hexagonal BN films. *Scientific Reports* 5:10699 (2015).

[167] Peimyoo, N. *et al.* Nonblinking, intense two-dimensional light emitter: monolayer WS_2 triangles. *ACS Nano* **7** (2013), 10985−10994.

[168] Danda, G. *et al.* Monolayer WS_2 nanopores for DNA translocation with light-adjustable sizes. *ACS Nano* **11** (2017), 1937−1945.

[169] Dean, C. R. *et al.* Boron nitride substrates for high-quality graphene electronics. *Nature Nanotechnology* **5** (2010), 722−726.

[170] Qiu, H. *et al.* Hopping transport through defect-induced localized states in molybdenum disulphide. *Nature Communications* 4:2642 (2013).

[171] Lu, C.-P. *et al.* Bandgap, mid-gap states and gating effects in MoS_2. *Nano Letters* **14** (2014), 4628−4633.

[172] Yu, Z. *et al.* Towards intrinsic charge transport in monolayer molybdenum disulfide by defect and interface engineering. *Nature Communications* 5:5290 (2014).

[173] Elías, A. L. *et al.* Controlled synthesis and transfer of large-area WS_2 sheets: from single layer to few layers. *ACS Nano* **7** (2013), 5235−5242.

[174] Yuan, L., Huang, L. Exciton dynamics and annihilation in WS_2 2D semiconductors. *Nanoscale* **7** (2015), 7402−7408.

[175] Lin, L. *et al.* Fabrication of luminescent monolayered tungsten dichalcogenides quantum dots with giant spin-valley coupling. *ACS Nano* **7** (2013), 8214−8223.

[176] Amani, M. *et al.* Near-unity photoluminescence quantum yield in MoS_2. *Science* **27** (2015), 1065−1068.

[177] Jo, S. *et al.* Mono- and bilayer WS_2 light-emitting transistors. *Nano Letters* **14** (2014), 2019−2025.

[178] Zeng, L. *et al.* High-responsivity UV-Vis photodetector based on transferable WS_2 film deposited by magnetron sputtering. *Scientific Reports* 6:20343 (2016).

[179] Whiters, F. *et al.* Light-emitting diodes by band-structure engineering in van der Waals heterostructures. *Nature Materials* **14** (2015), 301−306.

[180] Cong, C. *et al.* Synthesis and optical properties of large-area single-crystalline 2D semiconductor WS_2 monolayer from chemical vapor deposition. *Advanced Optical Materials* **2** (2014), 131−136.

[181] Lukowski, M. A. *et al.* Highly active hydrogen evolution catalysis from metallic WS_2 nanosheets. *Energy & Environmental Science* **7** (2014), 2608−2613.

[182] Hofmann, W. K. Thin films of molybdenum and tungsten disulphides by metal organic chemical vapour deposition. *Journal of Materials Science* **23** (1988), 3981−3986.

[183] Rong, Y. *et al.* Controlling sulphur precursor addition for large single crystal domains of WS_2. *Nanoscale* **6** (2014), 12096−12103.

[184] Zhang, Y. *et al.* Controlled growth of high-quality monolayer WS_2 layers on sapphire and imaging its grain boundary. *ACS Nano* **7** (2013), 8963−8971.

[185] Xu, Z. Q. *et al.* Synthesis and transfer of large-area monolayer WS_2 crystals: moving toward the recyclable use of sapphire substrates. *ACS Nano* **9** (2015), 6178−6187.

[186] Fu, Q. *et al.* Controllable synthesis of high quality monolayer WS_2 on a SiO_2/Si substrate by chemical vapor deposition. *RSC Advances* **5** (2015), 15795−15799.

[187] Lee, Y. H. *et al.* Synthesis and transfer of single-layer transition metal disulfides on diverse surfaces. *Nano Letters* **13** (2013), 1852−1857.

[188] Kang, K. *et al.* High-mobility three-atom-thick semiconducting films with wafer-scale homogeneity. *Nature* **520** (2015), 656−660.

[189] Gao, Y. *et al.* Large-area synthesis of high-quality and uniform monolayer WS_2 on reusable Au foils. *Nature Communications* 6:8569 (2015).

[190] Bletskan, D. I. Material synthesis and growth of the single crystals of the type $A^{IV}B^{VI}$ and $A^{IV}B_2^{VI}$. *Chalcogenide Letters* **4** (2007), 1−16.

[191] Schmidt, P. *et al.* Chemical vapor transport reactions – methods, materials, modelling. *Advanced Topics on Crystal Growth* InTech (2013).

[192] Nitsche, R. Kristall zucht aus der Gasphase durch chemische Transport reaktionen. *Fortschritte der Mineralogie* **44** (1967), 231.

[193] Schäfer, H. Thermodynamische Gesichtspunkte bei der Auswahl chemischer Transportvorgänge. *Journal of Crystal Growth* **9** (1971), 17−30.

[194] Kaldis, E. Principles of the vapour growth of single crystals. *Crystal Growth, Theory and Techniques* **1** (1974), 49−191.

[195] Nitsche, R. *et al.* Crystal growth by chemical transport reactions—I: Binary, ternary, and mixed crystal chalcogenides. *Journal of Physics and Chemistry of Solids* **21** (1961), 199−205.

[196] Al-Hilli, A. A., Evans, B. L. The preparation and properties of transition metal dichalcogenide single crystals. *Journal of Crystal Growth* **15** (1972), 93−101.

[197] Brixner, L. H. Preparation and properties of the single crystalline AB_2-type selenides and tellurides of niobium, tantalum, molybdenum and tungsten. *Journal of Inorganic and Nuclear Chemistry* **24** (1962), 257−263.

[198] Lenz, M., Gruehn, R. Developments in measuring and calculating chemical vapor transport phenomena demonstrated on Cr, Mo, W, and their compounds. *Chemical Reviews* **97** (1997), 2967−2994.

[199] Brown, B. E. The crystal structures of WTe_2 and high-temperature $MoTe_2$. *Acta Crystallographica* **20** (1966), 268−274.

[200] Sunil, K., Ittyachen, M. A. The growth and thermodynamical feasibility of tungsten diselenide single crystals using chemical vapour transport technique. *Bulletin of Materials Science* **20** (1997), 231−238.

[201] Schäfer, H. *et al.* Chemischer Transport mit Schwefet als Transportmittel. *Journal of the Less Common Metals* **16** (1968), 290−291.

[202] Binnewies, M. Das Massenspektrum des Systems Te/S und der chemische Transport von Tellur mit Schwefel. *Zeitschrift für anorganische und allgemeine Chemie* **422** (1976), 43−46.

[203] Lenz, M., Gruehn, R. Developments in measuring and calculating chemical vapor transport phenomena demonstrated on Cr, Mo, W, and their Compounds. *Chemical Reviews* **97** (1997), 2967−2994.

[204] Binnewies, M. Chemische Transportreaktionen. *Chemie in unserer Zeit* **32** (1998), 15−21.

[205] Gruehn, R., Glaum, R. Neues zum chemischen Transport als Methode zur Präparation und thermochemischen Untersuchung von Festkörpern. *Angewandte Chemie* **112** (2000)**,** 706−731.

[206] Liu, X. *et al.* High performance field-effect transistor based on multilayer tungsten disulphide. *ACS Nano* **8** (2014), 10396−10402.

[207] Vaidya, R. *et al.* Growth of molybdenum disulphide using iodine as transport material**.** *Pramana - Journal of Physics* **63** (2004), 611−616.

[208] Pradhan, N. R. *et al.* Field-effect transistors based on few-layered α-$MoTe_2$. *ACS Nano* **8** (2014), 5911−5920.

[209] Hu, S.Y. *et al.* Effect of Re dopant on the electrical and optical properties of $MoSe_2$ single crystals. *Journal of Alloys and Compounds* **442** (2007), 249−251.

[210] Tongay, S. *et al.* Monolayer behaviour in bulk ReS_2 due to electronic and vibrational decoupling. *Nature Communications* 5:3252 (2014).

[211] Ubaldini, A. *et al.* Chloride-driven chemical vapor transport method for crystal growth of transition metal dichalcogenides. *Crystal Growth & Design* **13** (2013), 4453−4459.

[212] Dettingmeijer, J. H. *et al.* Chemical transport of tungsten in the heterogeneous systems tungsten-oxygen-hydrogen-iodine/bromine/chlorine. *Journal of the Less Common Metals* **35** (1974) 159−169.

[213] Schäfer, H. *et al.* The chemical transport of molybdenum and tungsten and of their dioxides and sulphides. *Journal of Solid State Chemistry* **8** (1973), 14−28.

[214] Housecroft, C. E. The heavier d-block metals, aspects of inorganic and coordination chemistry. Oxford Chemistry Primers (1999).

[215] Kodas, T., Hampden-Smith, M. The chemistry of metal CVD (2008).

[216] van der Zande, A. M. *et al.* Grains and grain boundaries in highly crystalline monolayer molybdenum disulphide. *Nature Materials* **12** (2013), 554−561.

[217] Ennaoui, A. *et al.* Preparation of textured and photoactive 2H-WS_2 thin films by sulfurization of WO_3. *Thin Solid Films* **261** (1995), 124−131.

[218] Chung, J.-W. *et al.* WS_2 thin films by metal organic chemical vapor deposition. *Journal of Crystal Growth* **186** (1998), 137−150.

[219] Zhan, Y. *et al.* Large-area vapor-phase growth and characterization of MoS_2 atomic layers on a SiO_2 substrate. *Small* **8** (2012), 966−971.

[220] Orofeo, C. M. *et al.* Scalable synthesis of layer-controlled WS_2 and MoS_2 sheets by sulfurization of thin metal films. *Applied Physics Letters* 105:083112 (2014).

[221] Ma, L. *et al.* Epitaxial growth of large area single-crystalline few-layer MoS_2 with room temperature mobility of 192 $cm^2V^{-1}s^{-1}$. *Applied Physics Letters* 105:072105 (2016).

[222] Kong, D. *et al.* Synthesis of MoS_2 and $MoSe_2$ films with vertically aligned layers. *Nano Letters* **13** (2013), 1341−1347.

[223] Hussain, A. M. *et al.* Chemical vapor deposition based tungsten disulfide (WS_2) thin film transistor. *SIECPC* (2013), DOI: 10.1109/SIECPC.2013.6550981.

[224] Yu, Q. *et al.* Control and characterization of individual grains and grain boundaries in graphene grown by chemical vapour deposition. *Nature Materials* **10** (2011), 443−449.

[225] Dumcenco, D. *et al.* Large-area epitaxial monolayer MoS_2. *ACS Nano* **9** (2015), 4611−4620.

[226] Muijsers, J. C. *et al.* Sulfidation study of molybdenum oxide using $MoO_3/SiO_2/Si(100)$ model catalysts and Mo-$^{IV}{}_3$-sulfur cluster compounds. *Journal of Catalysis* **157** (1995), 698−705.

[227] Lin, Y.-C. *et al.* Wafer-scale MoS_2 thin layers prepared by MoO_3 sulfurization. *Nanoscale* **4** (2012), 6637−6641.

[228] Wang, X. *et al.* Controlled synthesis of highly crystalline MoS_2 flakes by chemical vapor deposition. *Journal of American Chemical Society* **135** (2013), 5304−5307.

[229] Diskus, M. *et al.* Growth of thin films of molybdenum oxide by atomic layer deposition. *Journal of Material Chemistry* **21** (2011), 705−710.

[230] Malm, J. *et al.* Atomic layer deposition of WO_3 thin films using $W(CO)_6$ and O_3 precursors. *Chemical Vapor Deposition* **18** (2012), 245−248.

[231] Scharf, T. W. *et al.* Growth, structure, and tribological behavior of atomic layer-deposited tungsten disulphide solid lubricant coatings with applications to MEMS. *Acta Materialia* **54** (2006), 4731−4743.

[232] Grubbs, R. K. *et al.* Gas phase reaction products during tungsten atomic layer deposition using WF_6 and Si_2H_6. *Journal Of Vacuum Science & Technology B* **22** (2004), 1811−1821.

[233] Kim, C.-Y. *et al.* Imaging of atomic layer deposited (ALD) tungsten monolayers on α-TiO_2(110) by X-ray standing wave Fourier inversion. *The Journal of Physical Chemistry B* **110** (2006), 12616−12620.

[234] Song, J.-G. *et al.* Layer-controlled, wafer-scale, and conformal synthesis of tungsten disulphide nanosheets using atomic layer deposition. *ACS Nano* **7** (2013), 11333−11340.

[235] Lee, Y.-H. *et al.* Synthesis of large-area MoS_2 atomic layers with chemical vapor deposition. *Advanced Materials* **24** (2012), 2320−2325.

[236] Ling, X. *et al.* Role of the seeding promoter in MoS_2 growth by chemical vapor deposition. *Nano Letters* **14** (2014), 464−472.

[237] Najmaei, S. *et al.* Vapour phase growth and grain boundary structure of molybdenum disulphide atomic layers. *Nature Materials* **12** (2013), 754−759.

[238] Ji, Q. *et al.* Epitaxial monolayer MoS_2 on mica with novel photoluminescence. *Nano Letters* **13** (2013), 3870−3877.

[239] Zhang, Y. *et al.* Dendritic, transferable, strictly monolayer MoS_2 flakes synthesized on $SrTiO_3$ single crystals for efficient electrocatalytic applications. *ACS Nano* **8** (2014), 8617−8624.

[240] Yu. Y. *et al.* Controlled scalable synthesis of uniform, high-quality monolayer and few-layer MoS_2 films. *Scientific Reports* 3:1866 (2013).

[241] Wang, X. *et al.* Chemical vapor deposition growth of crystalline monolayer $MoSe_2$. *ACS Nano* **8** (2014), 5125−5131.

[242] Shaw, J. *et al.* Chemical vapor deposition growth of monolayer $MoSe_2$ nanosheets. *Nano Research* **7** (2014), 511−517.

[243] Huang, J.-K. *et al.* Large-area synthesis of highly crystalline WSe_2 monolayers and device applications. *ACS Nano* **8** (2013), 923−930.

[244] Tsirlina, T. *et al.* Synthesis and characterization of inorganic fullerene-like WSe_2 material. *Fullerene Science and Technology* **6** (1998), 157−165.

[245] Li, S. *et al.* Halide-assisted atmospheric pressure growth of large WSe_2 and WS_2 monolayer crystals. *Applied Materials Today* **1** (2015), 60−66.

[246] Okada, M. *et al.* Direct chemical vapor deposition growth of WS_2 atomic layers on hexagonal boron nitride. *ACS Nano* **8** (2014), 8273−8277.

[247] Kang, K. N. *et al.* The growth scale and kinetics of WS_2 monolayers under varying H_2 concentration. *Scientific Reports* 5:13205 (2015).

[248] Gong, Y. *et al.* Tellurium-assisted low-temperature synthesis of MoS_2 and WS_2 monolayers. *ACS Nano* **9** (2015), 11658−11666.

[249] Browning, R. *et al.* Atomic layer deposition of MoS_2 thin films. *Materials Research Express* 2:035006 (2015).

[250] Bozheyev, F. *et al.* Preparation of highly (001)-oriented photoactive tungsten diselenide (WSe_2) films by an amorphous solid-liquid-crystalline solid (aSLcS) rapid-crystallization process. *Physica Status Solidi* **211** (2014), 2013−2019.

[251] Jin, Z. *et al.* Novel chemical route for atomic layer deposition of MoS_2 thin film on SiO_2/Si substrate. *Nanoscale* **6** (2014), 14453−14458.

[252] Tan, L. K. *et al.* Atomic layer deposition of a MoS_2 film. *Nanoscale* **6** (2014), 10584−10588.

[253] Kranthi Kumar, V. *et al.* A predictive approach to CVD of crystalline layers of TMDs: the case of MoS_2. *Nanoscale* **7** (2015), 7802−7810.

[254] Carmalt, C. J. *et al.* Atmospheric pressure chemical vapour deposition of WS_2 thin films on glass. *Polyhedron* **22** (2003) 1499−1505.

[255] Park, J. *et al.* Layer-modulated synthesis of uniform tungsten disulfide nanosheet using gas-phase precursors. *Nanoscale* **7** (2015), 1308−1313.

[256] Eichfeld, S. M. *et al.* Highly scalable, atomically thin WSe_2 grown *via* metal–organic chemical vapor deposition. *ACS Nano* **9** (2015), 2080−2087.

[257] Yun, S. J. *et al.* Synthesis of centimeter-scale monolayer tungsten disulfide film on gold foils. *ACS Nano* **9** (2015), 5510−5519.

[258] Hryniewicz, T., Sienicki, W. Preparation and properties of tungsten disulphide polycrystalline thin films intercalated with guest atoms. *Materials Chemistry and Physics* **44** (1996), 211−214.

[259] Kobayashi, Y. *et al.* Bandgap-tunable lateral and vertical heterostructures based on monolayer $Mo_{1-x}W_xS_2$ alloys. *Nano Research* 8:3261 (2015).

[260] Yoshida, S. *et al.* Microscopic basis for the band engineering of $Mo_{1-x}W_xS_2$-based heterojunction. *Scientific Reports* 5:14808 (2015).

[261] Chen, Y. *et al.* Tunable band gap photoluminescence from atomically thin transition-metal dichalcogenide alloys. *ACS Nano* **7** (2013), 4610−4616.

[262] Feng, L.-P. *et al.* Performance of field-effect transistors based on $Nb_{(x)}W_{(1-x)}S_2$ monolayers. *Nanoscale* **8** (2016), 6507−6513.

[263] Srivastava, S. K., Avasthi, B. N. Synthesis and characterization of indium intercalation compounds of tungsten disulphide: In_xWS_2 ($0 \leq x \leq 1$). *Synthetic Metals* **10** (1985), 213−221.

[264] Srivastava, S. K. Structure, properties and morphological studies of indium intercalation compounds of tungsten disulphide, In_xWS_2 ($0 \leq x \leq 1$). *Journal of Materials Science* **23** (1988), 388–394.

[265] Berkdemir, A. *et al.* Identification of individual and few layers of WS_2 using Raman Spectroscopy. *Scientific Reports* 3:1775 (2013).

[266] Chen, Y. *et al.* Composition-dependent Raman modes of $Mo_{(1-x)}W_{(x)}S_2$ monolayer alloys. *Nanoscale* **6** (2014), 2833−2839.

[267] Zheng, S. *et al.* Monolayers of $W_xMo_{1-x}S_2$ alloy heterostructure with in-plane composition variations. *Applied Physics Letters* 106:063113 (2015).

[268] Donald, A. M. The use of environmental scanning electron microscopy for imaging wet and insulating materials. *Nature Materials* **2** (2003), 511−516.

[269] Kochat, V. *et al.* High contrast imaging and thickness determination of graphene with in-column secondary electron microscopy. *Journal of Applied Physics* 110:014315 (2011).

[270] Scrivener, K. L. Backscattered electron imaging of cementitious microstructures: Understanding and quantification. *Cement and Concrete Composites* **26** (2004), 935−945.

[271] Ogura, T. Analysing indirect secondary electron contrast of unstained bacteriophage T4 based on SEM images and Monte Carlo simulations. *Biochemical and Biophysical Research Communications* **380** (2009), 254−259.

[272] Pawley, J. Low voltage scanning electron microscopy. *Journal of Electron* Microscopy **136** (1984), 45−68.

[273] Cappella, B., Dietler, G. Force-distance curves by atomic force microscopy. *Surface Science Reports* **34** (1999), 1−104.

[274] Binnig, G. *et al.* Atomic-force microscope. *Physical Review Letters* **56** (1986), 930−933.

[275] Geisse, N. A. AFM and combined optical techniques. *Materials Today* **12** (2009), 40−45.

[276] Schmitz, I. *et al.* Tapping-mode AFM in comparison to contact-mode AFM as a tool for in situ investigations of surface reactions with reference to glass corrosion. *Analytical Chemistry* **69** (1997), 1012−1018.

[277] Fernando, G. W. Chapter 5 – Probing layered systems: a brief guide to experimental techniques. *Handbook of Metal Physics* **4** (2008), 111−130.

[278] Ferrari, A. C. *at al.* Raman spectrum of graphene and graphene layers. *Physical Review Letters* 97:187401 (2006).

[279] Cardona, M., Güntherodt, G. Light scattering in solids II: basic concepts and instrumentation. *Topics in Applied Physics* **50** (1982), 19−178.

[280] Pierret, R. F. MOSFETs – The essentials. *Semiconductor device fundamentals* (1995), Chapter 17.

[281] Shur, M. Field Effect Transistors. *Physics of Semiconductor Devices* (1990), Chapter 4.

[282] Sze, S. M., Ng, K. K. MOSFETs. *Physics of Semiconductor Devices* (2006), Chapter 6.

[283] Cudennec, Y., Lecerf, A. Topotactic transformations of goethite and lepidocrocite into hematite and maghemite. *Solid State Sciences* **7** (2005), 520−529.

[284] Tonti, D. *et al.* Preparation and photoelectrochemistry of semiconducting WS_2 thin films. *Journal of Physical Chemistry B* **101** (1997), 2485−2490.

[285] Song, X. C. *et al.* Large-scale hydrothermal synthesis of WO_3 nanowires in the presence of K_2SO_4. *Materials Letters* **61** (2007), 3904−3908.

[286] Szabó, M. *et al.* Synthesis and characterization of WO_3 nanowires and metal nanoparticle-WO_3 nanowire composites. *Journal of Molecular Structure* **1044** (2013), 99−103.

[287] Kim, H. *et al.* Activation energy paths for graphene nucleation and growth on Cu. *ACS Nano* **6** (2012), 3614−3623.

[288] Gäggeler, H. W., Türler, A. Gas-phase chemistry of superheavy elements. *The Chemistry of Superheavy Elements* (2th ed.) (2013), 415−483.

[289] Wells, A. F. Structural inorganic chemistry (5th ed.). Oxford [Oxfordshire]: Clarendon Press. (1986).

[290] Yang, J. *et al.* Hydrothermal synthesis and photoelectrochemical properties of vertically aligned tungsten trioxide (hydrate) plate-like arrays fabricated directly on FTO substrates. *Journal of Material Chemistry* **22** (2012), 17744−17752.

[291] Murau, P. C. Dissolution of tungsten by hydrogen peroxide. *Analytical Chemistry* **33** (1961), 1125−1126.

[292] Ramans, G. M. *et al.* Structure of tungstic acids and amorphous and crystalline WO_3 thin films. *Physica Status Solidi (a)* **74** (1982), K41−K44.

[293] Viswanathan, K. Crystal structure of sodium tetratungstate, $Na_2W_4O_{13}$. *Journal of the Chemical Society, Dalton Transactions* **20** (1974), 2170−2172.

[294] Yan, F. *et al.* The ternary system Na_2O–ZnO–WO_3: Compounds and phase relationships. *Journal of Alloys and Compounds* **458** (2008), 138−143.

[295] Chang, L. L. Y., Sachdev, S. Alkali tungstates. Stability relations in the systems alkali monotungstate-tungsten trioxide. *Journal of the American Ceramic Society* **58** (1975), 267−270.

[296] McKone, J. R. *et al.* Hydrogen evolution from Pt/Ru-coated p-type WSe_2 photocathodes. *Journal of the American Chemical Society* **135** (2013), 223−231.

[297] Baglio, J. *et al.* Growth and characterization of n-WS_2 and niobium-doped p-WS_2 single crystals. *Journal of Solid State Chemistry* **49** (1983), 166−179.

[298] Lenz, M., Gruehn, R. Developments in measuring and calculating chemical vapor transport phenomena demonstrated on Cr, Mo, W, and their compounds. *Chemical Reviews* **97** (1997), 2967−2994.

[299] Wu, R. J. *et al.* Determining the thickness of atomically thin MoS_2 and WS_2 in the TEM. *Ultramicroscopy* **147** (2014), 8−20.

[300] Rasmussen, F. A., Thygesen, K. S. Computational 2D materials database: electronic structure of transition-metal dichalcogenides and oxides. *The Journal of Physical Chemistry C* **119** (2015), 13169−13183.

[301] Hu, P. *et al.* Control of radiative exciton recombination by charge transfer induced surface dipoles in $MoS_2$and WS_2 monolayers. *Scientific Reports* 6:24105 (2016).

[302] Peimyoo, N. *et al.* Chemically driven tunable light emission of charged and neutral excitons in monolayer WS_2. *ACS Nano* **8** (2014), 11320−11329.

[303] Hui, Y. Y. *et al.* Exceptional tunability of band energy in a compressively strained trilayer MoS_2 sheet. *ACS Nano* **7** (2013), 7126−7131.

[304] Tongay, S. *et al.* Defects activated photoluminescence in two-dimensional semiconductors: interplay between bound, charged, and free excitons. *Scientific Reports* 3:2657 (2013).

[305] Liu, H. *et al.* Fluorescence concentric triangles: a case of chemical heterogeneity in WS_2 atomic monolayer. *Nano Letters* **16** (2016), 5559−5567.

[306] Zhu, B. *et al.* Anomalously robust valley polarization and valley coherence in bilayer WS_2. PNAS **111** (2014), 11606−11611.

[307] McCreary, K. M. *et al.* Synthesis of large-area WS_2 monolayers with exceptional photoluminescence. *Scientific Reports* 6:19159 (2016).

[308] Cattelan, M. *et al.* New strategy for the growth of complex heterostructures based on different 2D materials. *Chemistry of Materials* **27** (2015), 4105−4113.

[309] Martinez, H. *et al.* Influence of the cation nature of high sulfur content oxysulfide thin films MO_yS_z (M=W, Ti) studied by XPS. *Applied Surface Science* **236** (2004), 377−386.

[310] Iqbal, M. W. *et al.* Tailoring the electrical and photo-electrical properties of a WS_2 field effect transistor by selective n-type chemical doping. *RSC Advances* **6** (2016), 24675−24682.

[311] Georgiou, T. *et al.* Electrical and optical characterization of atomically thin WS_2. *Dalton Transactions* **43** (2014), 10388−10391.

[312] Iqbal, M. W. *et al.* Deep-ultraviolet-light-driven reversible doping of WS_2 field-effect transistors. *Nanoscale* **7** (2015), 747−757.

[313] Alharbi, A., Shahrjerdi, D. Electronic properties of monolayer tungsten disulfide grown by chemical vapor deposition. *Applied Physics Letters* 109:193502 (2016).

[314] Lan, C. *et al.* Large-area synthesis of monolayer WS_2 and its ambient-sensitive photo-detecting performance. *Nanoscale* **7** (2015), 5974−5980.

[315] Cui, Y. *et al.* High-performance monolayer WS_2 field-effect transistors on high-κ dielectrics. *Advanced Materials* **27** (2015), 5230−5234.

[316] Srivastava, S. K., Avasthi, B. N. Indium intercalation compounds of molybdenum disulphide; In_xMoS_2 ($0 \leq x \leq 1$). *Synthetic Metals* **11** (1985), 193−205.

[317] Srivastava, S. K., Avasthi, B. N. Synthesis and characterization of indium intercalation compounds of molybdenum diselenide, In_xMoSe_2 ($0 \leq x \leq 1$). *Journal of Materials Science* **24** (1989), 1919−1924.

[318] Srivastava, S. K. Preparation, structure and properties of indium intercalation compounds of tungsten diselenide, In_xWSe_2 ($0 \leq x \leq 1$). *Materials Research Bulletin* **24** (1989), 1031−1041.

[319] Deshpande, M. P. *et al.* Effect of intercalating indium in WSe_2 single crystals. *Journal of Crystal Growth* **197** (1999), 833−840.

[320] Subba Rao, G. V. *et al.* Superconductivity in alkaline earth metal and Yb intercalated group VI layered dichalcogenides. *Journal of Solid State Chemistry* **9** (1974), 323−329.

[321] Trichet, L. *et al.* Sur les propriétés électriques et magnétiques des phases M_xZrS_2 (M = Fe, Co, Ni). *Journal of Solid State Chemistry* **14** (1975), 283−290.

[322] Rouxel, J. Conductivity problems in two dimensional intercalation compounds. *Materials Research Bulletin* **13** (1978), 1425−1431.

[323] Yacobi, B. G. *et al.* Intercalation-induced shift of the absorption edge in ZrS_2 and HfS_2. *Journal of Physics C: Solid State Physics* **12** (1979), 2189−2196.

[324] Yacobi, B. G. *et al.* The fundamental absorption edge in Ni_xZrS_2. *Materials Research Bulletin* **14** (1979), 1033−1038.

[325] Deshpande, M. P. *et al.* Transport and optical property measurements in indium intercalated molybdenum diselenide single crystals grown by DVT technique. *Synthetic Metals* **123** (2001), 73−81.

[326] Srivastava, S. K. Structural and morphological studies on indium intercalated compounds of molybdenum disulphide; In_xMoS_2 ($0 \leq x \leq 1$). *Materials Research Bulletin* **26** (1991), 631−639.

[327] Subba Rao, G. V., Sunandana, C. S. Layered dichalcogenides and intercalated materials. *Preparation and Characterization of Materials* (1981), 269–282.

[328] Somoano, R. B., Woollam, J. A. Intercalation compounds of molybdenum disulfide. *Intercalated Layered Materials* (1979), 307−319.

[329] Rouxel., J. Reactivity of low dimensional transition metal derivatives towards cationic intercalation chemistry. *Chemical Physics of Intercalation* **172** (1982), 127−147.

[330] Hahn, H., Klingler, W. Über die Kristallstrukturen des In_2S_3 und In_2Te_3. *Zeitschrift für anorganische und allgemeine Chemie* **260** (1949), 97−109.

[331] Sim, Y. *et al.* Simple synthesis of ultra-high quality In_2S_3 thin films on InAs substrates. *Journal of Alloys and Compounds* **685** (2016), 518−522.

[332] Wagner, C. D. The NIST x-ray photoelectron spectroscopy (XPS) database (1991).

[333] Avsar, A. *et al.* Spin–orbit proximity effect in graphene. *Nature Communications* 5:4875 (2014).

[334] Hasan, M. Z.; Kane, C. L. Colloquium: Topological insulators. *Review of Modern Physics* 82:3045 (2010).

[335] Kane, C. L.; Mele, E. J. Quantum spin Hall effect in graphene. *Physical Review Letters* 95:226801 (2005).

[336] Kane, C. L.; Mele, E. J. Z_2 Topological order and the quantum spin Hall effect. *Physical Review Letters* 95:146802 (2005).

[337] Gmitra, M. *et al.* Band-structure topologies of graphene: Spin-orbit coupling effects from first principles. *Physical Review B* 80:235431 (2009).

[338] Xiao, D. *et al.* Coupled spin and valley physics in monolayers of MoS_2 and other group-VI dichalcogenides. *Physical Review Letters* 108:196802 (2012).

[339] Wakamura, T.; Reale, F. *et al.* Strong spin-orbit interaction induced in graphene by monolayer WS_2. Submitted.

[340] Mueller, T. *et al.* Graphene photodetectors for high-speed optical communications. *Nature Photonics* **4** (2010), 297−301.

[341] Mehew, J. D. *et al.* Fast and highly sensitive ionic-polymer-gated WS_2–graphene photodetectors. *Advanced Materials* 29:1700222 (2017).